

**Novel Synthetic Pathways for Tailored  
Covalent Triazine Frameworks with  
Catalytic and Electrochemical Applications**

**DISSERTATION**

Zur Erlangung des akademischen Grades

**Doctor rerum naturalium**

**(Dr. rer. nat.)**

vorgelegt

**dem Bereich Mathematik und Naturwissenschaften**

**der Technischen Universität Dresden**

von

**M. Sc. Erik Troschke**

geboren am 31.05.1989 in Cottbus

eingereicht am 30.08.2018

verteidigt am 20.11.2018

Die Dissertation wurde im Zeitraum März 2015 bis August 2018

am Institut für Anorganische Chemie I angefertigt

---

Erstgutachter: Prof. Dr. Stefan Kaskel (Technische Universität Dresden)

Zweitgutachter: Prof. Dr. Arne Thomas (Technische Universität Berlin)



---

## Acknowledgements

Großer Dank gebührt Prof. Dr. Stefan Kaskel für die Aufnahme in den Arbeitskreis und die Möglichkeit, eigenständig und mit vielen Freiheiten an meinem Thema arbeiten zu können.

Besonders gedankt sei meiner Gruppenleiterin Dr. Irena Senkovska, die stets ein offenes Ohr für die Belange ihrer Doktoranden hatte. Gleiches gilt für Dr. Lars Borchardt, der meinen Blickpunkt auf wissenschaftliche Fragestellungen verändert hat, aber mir vor allem Zielstrebigkeit in der Forschung vermittelte.

Eine besondere Wertschätzung gebührt meinen freundschaftlich verbundenen Bürokollegen (Sebastian Ehrling, Desirée Leistenschneider, Sven Grätz, Simon Krause, Dr. Mirian Casco). Ich danke euch für die persönliche Note, die ihr in den Büroalltag eingebracht habt und habe sowohl wissenschaftlich, als auch außeruniversitär viel von euch lernen können. Simon Krause danke ich speziell für die unzähligen kulturell wertvollen Stunden im Labor; Sven Grätz sei gedankt für alle erdenkbaren Hilfestellungen von der Argon Messung bis zum PC Problem.

Weiterer Dank geht an Dr. Susanne Dörfler, Christian Kensy und Dr. Patrick Strubel (Fraunhofer IWS) für unzählige Projekttreffen und die Verarbeitung meiner Proben. Für die gute Zusammenarbeit danke ich auch Prof. Dr. Bettina Lotsch, Dr. Frederik Haase, Hendrik Schlomberg, Johannes Maschita und Peter Schützendübe (LMU München und MPI Stuttgart)

Ich danke allen Kollegen aus dem Labor: Kerstin für ihr stete Hilfsbereitschaft als gute Fee im Hintergrund; Georg und Christel für die Aufnahme in den Arbeitskreis und anfängliche Betreuung; Steffen, Khoa, Ubed, Claudia, Francesco und Friedrich für die tolle Atmosphäre.

Besonderer Dank gebührt meinen SHKs Tilo Rensch und Annette Zschiesche. Danke, dass ihr meine Ungeduld so gut kanalisiert habt.

Ich danke vielen Personen für die Kooperation und die Durchführung von Messungen: Dr. Danny Haubold, Benjamin Klemmed, Prof. Dr. Eychmüller (TEM, Raman: Physikalische Chemie); Sebastian Ehrling, Andrea Brünner (REM); Dr. Ilka Kunert (TGA); Dr. Silvia Paasch, Prof. Dr. Brunner (Festkörper NMR, Bioanorganische Chemie), Prof. Dr. Yvonne Joseph (XPS, TU Freiberg), Dr. Johannes Schmidt (XPS, TU Berlin); Anett Rudolph, Dr. Tilo Lübken (NMR); Dr. Valeriya Tkachova (MALDI-TOF, Molekulare Funktionsmaterialien).

Dem gesamten AK Kaskel sei für die angenehme Arbeitsatmosphäre gedankt.

Spezieller Dank gebührt meiner Familie und Freunden für die Unterstützung in den letzten Jahren.

Der größte Dank gebührt meinen Kindern und Lea, ihr wart stets meine größte Motivation!

---

## Table of contents

Table of contents.....	2
Abbreviations.....	4
1 Motivation.....	6
2 State of the art.....	9
2.1 Porous polymers.....	9
2.2 Nanoporous organic polymers obtained by metal-free condensation reactions.....	12
2.3 Nanoporous organic polymers obtained by metal-catalysed (-mediated) reactions.....	18
2.4 Covalent triazine frameworks.....	23
2.5 Synthetic pathways towards covalent triazine frameworks.....	27
2.6 Application of covalent triazine frameworks.....	31
3 Characterisation techniques.....	36
3.1 Physisorption.....	36
3.2 X-ray photoelectron spectroscopy.....	45
4 Experimental part.....	51
4.1 Applied chemicals and gases.....	51
4.2 Instrumental setup.....	53
4.3 General information.....	59
4.4 Syntheses of salt templated CTFs in binary salt mixtures.....	59
4.5 Mechanochemical CTF syntheses.....	60
4.6 Synthesis of CTFs containing covalently bound sulfur.....	65
4.6.1 Synthesis of the parent materials.....	65
4.6.2 Synthesis of the S@CTF materials.....	65
4.7 Synthesis of CTFs based on 3,5-dicyanopyridine.....	66
4.7.1 Synthesis of 3,5-dicyanopyridine.....	66
4.7.2 CTF synthesis.....	68
4.8 Synthesis of the imidazolium CTF.....	68
4.8.1 Synthesis of the imidazolium monomer.....	68
4.8.2 Synthesis of the imidazolium CTF.....	70
4.8.3 Catalytic testing of the imidazolium CTF.....	70
5 Results and discussion.....	72
5.1 Salt templated synthesis of hierarchical covalent triazine frameworks.....	72

5.2	Mechanochemical synthesis of covalent triazine frameworks .....	80
5.2.1	Carbazole-based porous organic polymers .....	81
5.2.2	Porous organic polymers from other aromatic monomers .....	89
5.3	Synthesis of pyridine-based CTFs for direct supercapacitor integration.....	92
5.4	Covalent triazine frameworks containing covalently bound sulfur and their evaluation as cathodes in the lithium sulfur battery.....	104
5.5	Integration of an N-heterocyclic carbene precursor into a covalent triazine framework for organocatalysis.....	117
6	Summary, Conclusion and Outlook.....	127
	References.....	132
	Appendix.....	145
	List of tables .....	182
	List of schemes.....	183
	List of figures.....	185

## Abbreviations

abbreviation	meaning
°C	Degree Celsius
1D	one-dimensional
2D	two-dimensional
3D	three-dimensional
Å	Ångström
a. u.	arbitrary units
AC	Anthracene
arom	aromatic
BET	Brunauer-Emmett-Teller
BLP	Borazine linked polymer
BZ	Benzene
ca.	circa
CBZ	Carbazole
CMP	Conjugated microporous polymer
cod	1,5-cyclooctadiene
COF	Covalent organic framework
CP	Cross-polarization
Cp*	Cyclopentadienyl
CTF	Covalent triazine framework
DBU	1,8-Diazabicyclo[5.4.0]undec-7-ene
DCP	3,5-Dicyanopyridine
DFT	Density Functional Theory
DMF	<i>N,N</i> -Dimethylformamide
e.g.	exempli gratia [Latin], for example
EA	Elemental analysis
E <sub>B</sub>	Binding energy
EDG	Electron donating group
EOF	Element organic framework
eq.	Equivalents
Eq.	Equation
ESR	Electron spin resonance
et al.	et alii [Latin], and others
eV	Electron volt
FT-IR	Fourier-transform infrared spectroscopy
FWHM	Full width at half maximum
GC	Gas chromatography
HCP	Hypercrosslinked polymer
HMBC	Heteronuclear multiple-bond correlation
IUPAC	International Union of Pure and Applied Chemistry
K	Kelvin
M	molar
MALDI-TOF	Matrix assisted laser desorption ionisation time of flight
MAS	Magic angle spinning
mg	Milligram

abbreviation	meaning
MOF	Metal-organic framework
MW	Microwave
n. s.	not specified
NHC	<i>N</i> -heterocyclic carbene
nm	Nanometer
NMR	Nuclear magnetic resonance
NPOP	Nanoporous organic polymer
NT	Naphthalene
ORR	Oxygen reduction reaction
p. a.	pro Analsi [Latin], for analysis
PAF	Porous aromatic framework
PIM	Polymer of intrinsic microporosity
POP	Porous organic polymer
PP	Polyphenylene
ppm	Parts per million
PPN	Porous polymer network
pTsOH	<i>para</i> -Toluenesulfonic acid
PXRD	Powder X-ray diffraction
q.	quaternary
QSDFT	Quenched Solid Density Functional Theory
Ref.	Reference
rpm	Rotations per minute
RT	Room temperature
$S_{\text{BET}}$	Specific surface area (calculated using the BET equation)
SCD	Supercritical drying
SEM	Scanning electron microscopy
STP	Standard temperature and pressure
TEM	Transmission electron microscopy
TGA	Thermogravimetric analysis
THF	Tetrahydrofuran
TPB	1,3,5-Triphenylbenzene
TPM	Tetraphenylmethane
UV	ultraviolet
UV/VIS	ultraviolet/visible
$V_{\text{ads}}$	adsorbed volume
$V_{\text{Meso}}$	Mesopore volume
$V_{\text{Micro}}$	Micropore volume
$V_{\text{Smicro}}$	Supermicropore volume
$V_{\text{Total}}$	Total pore volume
$V_{\text{Umicro}}$	Ultramicropore volume
w%	Weight percent
XPS	X-ray photoelectron spectroscopy

# 1 Motivation

Who can see more beauty in a flower – an artist or a scientist? This question was raised by the American physicist and Nobel Prize winner Richard Feynman while being interviewed by the BBC. He claimed that a scientist can see more beauty in a flower, whereas a friend of his argued that knowledge detracts from beauty. Basically, the answer to this question does not matter since it eventually lies in the eye of the beholder. It is more important to realise that even small objects that seem to be meaningless comprise different perspectives of the very same little thing. When Feynman introduced this little anecdote, he was referring to the “beauty at smaller dimensions” which became visible through modern microscopy. In contrast to physicists, who can see new aspects of objects by highly magnified images and observations of those, for synthetic chemists beauty lies in the rational construction of new and tailored molecules or materials. It is the unlimited repertoire of building blocks that can be assembled by synthetic chemistry in an infinite number of possibilities that is a source of inspiration for scientists throughout the past centuries and decades. Exemplarily, porosity is known in nature from common objects like honeycombs or aquatic sponges, which both provide a structure that comprises pores. The goal of synthetic scientist is to mimic natural porosity in an artificial way in order to benefit from such structural features. In consequence, very often scientific discoveries gained from synthetic chemistry also promised remarkable merits for industrial processes where materials with intrinsic porosity play a key role. To mention just a few, processes such as gas separation or catalysis must necessarily be associated with porous materials such as active carbons or zeolites that have been cornerstones of industrial development in the past century. In the course of the last decade, the toolbox in the subdiscipline of porous materials has expanded significantly. Prominent and relatively new examples are highly porous materials such as metal-organic frameworks (MOFs) and porous organic polymers (POPs). The thesis at hand will in particular deal with the latter group of porous materials that are exclusively constructed from organic matter on a rational basis – namely the group of nanoporous organic polymers (NPOPs). The term nanoporous is thereby referring to the type of porosity exhibited by these materials, since the pores within these porous polymers lie in the range of a few nanometers ( $\leq 100$  nm). As a result of such small pores, these materials exhibit extraordinary high intrinsic surface areas which are valuable for applications such as heterogeneous catalysis (in order to increase the number of

catalytically active sites) or adsorptive processes (in order to enhance the number of adsorption sites). The diversity of potential synthetic methods opens up novel pathways towards the most different subgroups within the wide field of NPOPs, which can differ according to their construction strategy or the building blocks that have been applied. This synthetic diversity also led to a class of materials called covalent triazine frameworks (CTFs) that consist of organic linking units which are connected via triazine nodes (1,3,5-triazabenzene). CTFs are remarkable materials since they outperform many other porous organic polymers by their extraordinary high chemical and thermal stability. This circumstance, in addition to their synthetic richness allowing for adjustable properties, makes CTFs auspicious candidates for applications suffering from harsh conditions, e.g. at elevated temperatures or the presence of strong basic or acidic media. However, besides all of the strengths, these materials have to be tailored individually for every single application. Therefore, it was one main concern of the thesis at hand to tackle different demands that are specifically governed by their respective application. High specific surface areas provided by micropores ( $< 2$  nm) in porous materials are often considered as the “Holy Grail” in materials chemistry but are in fact less valuable for many applications without the presence of mesopores (2 – 50 nm), which serve to enhance the transport kinetics within the material. To this end, a part of this thesis deals with the targeted introduction of mesopores into formerly microporous CTF materials to give access to hierarchical (containing interconnected micro- and/or mesopores) CTFs. Another aspect of the thesis is dedicated to the development of a sustainable synthetic procedure to generate CTFs. The chemical and thermal stability of CTFs comes at a cost, since the conventional synthesis route requires temperatures of at  $400$  °C for more than two days. Therefore, a novel mechanochemical approach to synthesise CTFs was developed that can be performed at room temperature and within two hours. In addition, this approach extends the possibility to introduce chemical functionalities into CTF materials and enables facile synthesis on a gram scale. Whereas the first two aspects deal with novel synthesis routes, three other chapters cover the vast field of characterisation and application. Owing to elevated synthesis temperatures that have been previously mentioned, CTFs undergo structural changes and in consequence, an idealised structure is far away from a realistic picture. Therefore, the novel CTFs that will be described within the thesis at hand have been intensively studied by X-ray photoelectron spectroscopy in order to get a more profound understanding of the processes occurring at high reaction temperatures. In parallel, those materials will be assessed

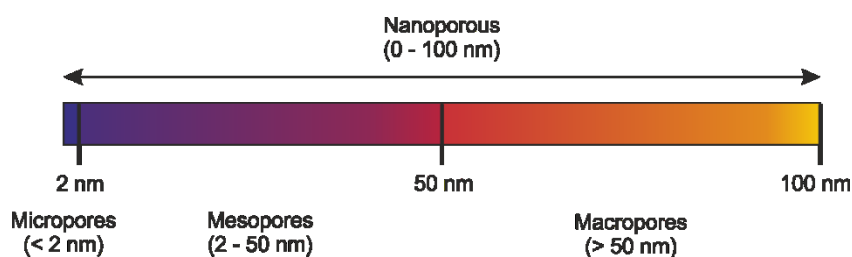
towards their application in energy storage systems such as in the lithium sulfur battery or as supercapacitor. To complete the field of potential applications, the last chapter describes the synthesis of a novel covalent triazine framework that intrinsically contains catalytically active sites. Thus, this thesis is written to provide both, a substantial synthetic understanding that allows for a tailored design of novel CTF materials as well as a widespread characterisation part in order to explain and investigate the materials' properties.



## 2 State of the art

### 2.1 Porous polymers

For many applications of industrial relevance solids providing enhanced porosity have been the key drivers of progress in the past century.<sup>1</sup> Such porous solids have been applied in diverse processes ranging from gas sorption and separation to heterogeneous catalysis.<sup>2</sup> Porosity if considered very schematically describes the existence of cavities or channels within or close to the surface of a solid that are deeper than they are wide. In consequence, such materials exhibit an internal surface which often excels the external surface area by far.<sup>3</sup> Following IUPAC recommendations, such materials are classified according to their pore size.<sup>4</sup> Macroporous solids have pore widths greater than 50 nm; mesoporous solids have pore widths between 2 nm and 50 nm; whereas microporous solids exhibit pores of less than 2 nm.

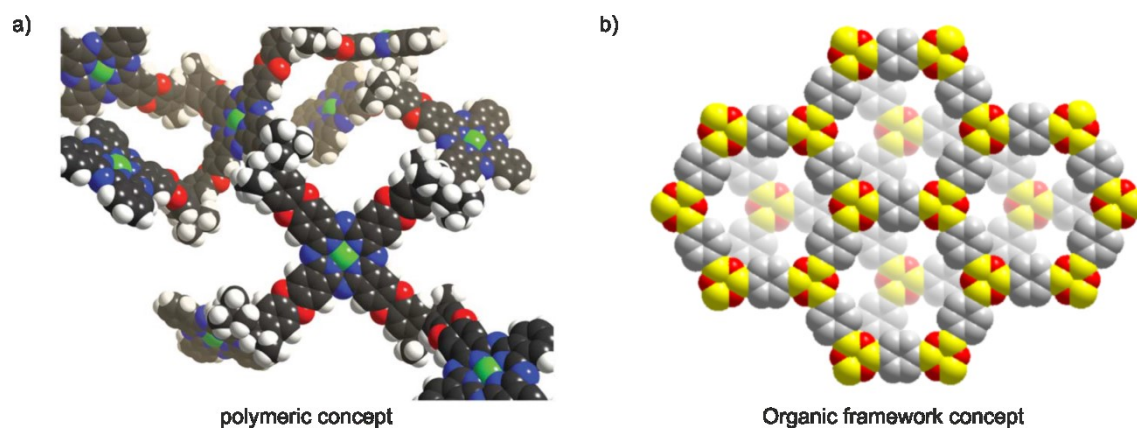


**Scheme 1** Schematic representation of different pores sizes in porous solids (according to IUPAC).<sup>4</sup>

The term nanoporous (pore widths < 100 nm) could in theory be applied to categorise all of the aforementioned kinds of porous materials, but here the main focus will lie on solids comprising micro- and/or mesoporosity. In particular, the presence of micropores leads to a high internal surface area. This property of a solid promotes adsorptive processes or increased turnover numbers of a heterogeneous catalyst, which is of utmost importance for those industrially relevant processes mentioned earlier. For a long time, activated carbons and zeolites have been considered as benchmark materials in the field of microporous solids. Albeit these sometimes even naturally occurring materials marked an entire era of research, scientists have contributed immense effort to mimic porosity in an artificial way. A rich field to address this challenge is polymer chemistry. Especially nanoporous organic polymers (NPOPs), which are exclusively built up from organic matter connected by covalent bonds (in contrast to metal-organic frameworks),<sup>5,6</sup> have proliferated tremendously in the last 15 years.<sup>7</sup> Since many different types of

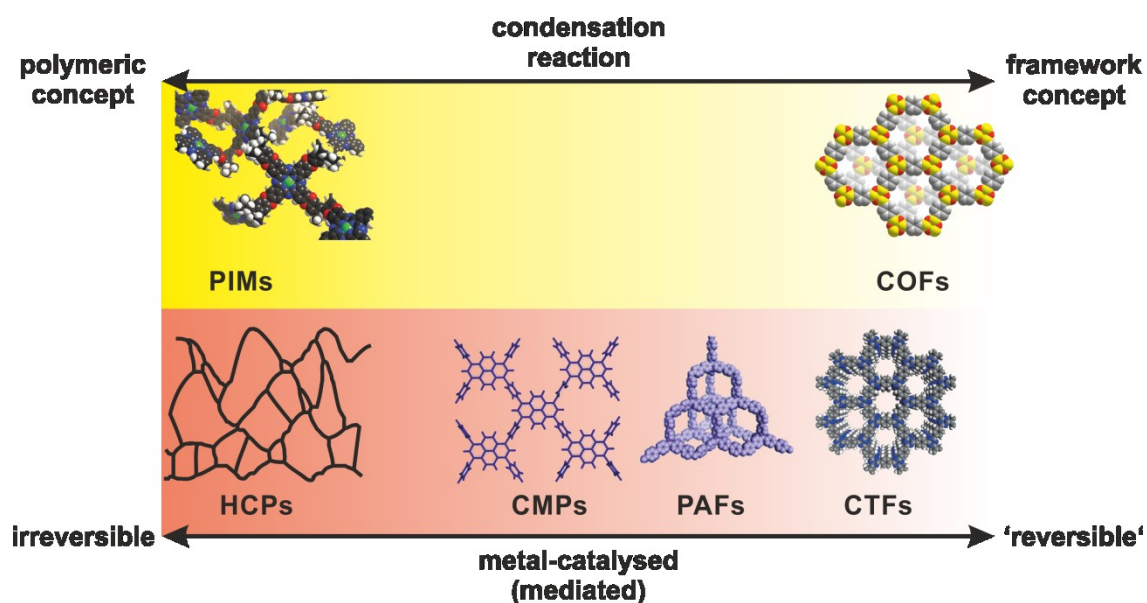
nanoporous polymers have climbed their way into scientific interest, it is necessary to find categories which are suitable to encompass the variety within the field of NPOPs.

Nanoporous organic polymers mainly consist of the lighter elements of the periodic table such as carbon, nitrogen and hydrogen. Prior to classify NPOPs, it is crucial to initially consider the origin of porosity within this class of materials. Regarding NPOPs, it is a pivotal feature that porosity is a function of the molecular structure rather than a result of templating methods.<sup>8</sup> Thus, an interconnected network has to be created on a rational basis which contains cavities and channels in order to achieve a porous material. There are some prerequisites that have to be respected that allow the creation of porosity. Basically, two main concepts (see Scheme 2) have emerged in order to “design” NPOPs: 1) a network built up from rigid building blocks, henceforth denoted to as “tectons”, must be constructed in a way that a collapse of the network is prevented in order to retain porosity. While a collapse would use space in a more effective way, the network necessarily has to be constructed from (potentially crosslinked) rigid and sterically hindered units that avoid close packing and can be seen as the origin of porosity.<sup>9-12</sup> This approach can be considered as a **polymeric concept** yielding porous polymeric networks. 2) A modular construction principle as known for metal-organic frameworks<sup>13,14</sup> can be applied by means of a well-defined assembly of multifunctional rigid tectons to form two-(2D) or three-dimensional (3D) covalently connected porous organic framework structures. This approach can be considered as an **organic framework concept** yielding porous organic framework structures. Both approaches are united by the fact that they benefit from rigid “tectons”. Rigidity often stems from stiff aromatic monomers which are either directly linked or linked by other rigid groups/functions. For 2D materials, a connectivity of the tectons of at least 2 is obligatory, for 3D materials a connectivity of >2 is required. Sometimes tectons are also connected by a different “tecton” which is then called a “node”.



**Scheme 2** Comparison of two opposite concepts to create porosity in nanoporous organic polymers: a) porosity as a result of ineffective packing of polymer chains<sup>15</sup> and b) porosity as a result of a modular construction principle yielding organic frameworks.<sup>16</sup>

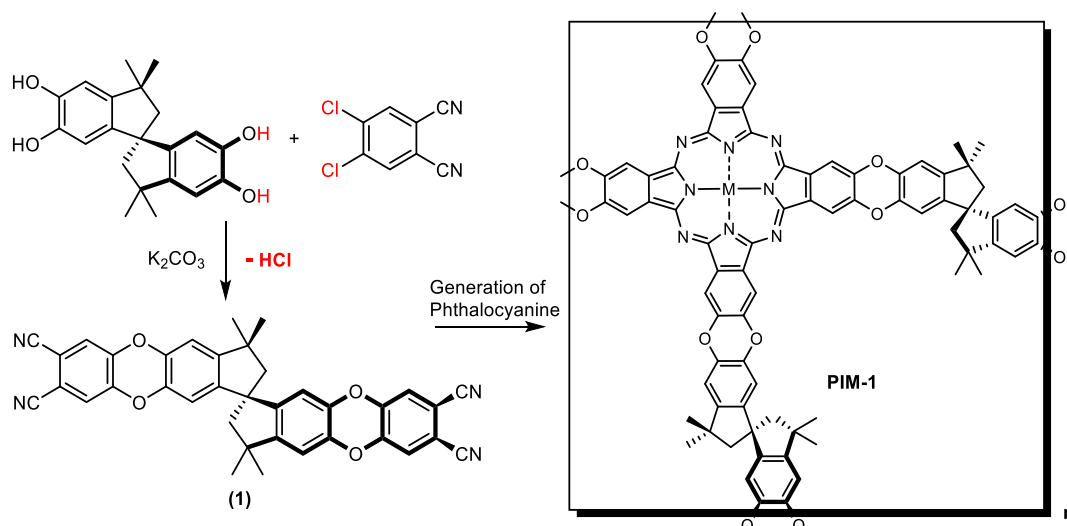
A further differentiation of the polymeric and the organic framework concept is possible due to the degree of order the polymer structures exhibit. Any kind of order (long- or short-range) is the result of a thermodynamically controlled reaction, whereas an amorphous structure is often caused by a kinetically controlled process, although a proper discrimination remains difficult.<sup>6</sup> As it is also known for metal-organic frameworks, a key of a thermodynamically controlled reaction is the reversibility of the network formation, thus ideally crosslinking of the tectons has to be reversible. If the network formation runs under thermodynamic control, a highly ordered NPOP can result, since repeated bond-formation and -breaking can lead to a sufficient reorganisation that initially enables long-range order. As it has been illustrated, the question of reversible or irreversible crosslinking (or network formation) has a crucial impact. In consequence, it is advisable to classify NPOPs towards the crosslinking reaction that creates the polymer since this step determines the properties of the resulting material to a high extent. Thus, most of the reactions that are applied for the synthesis of NPOPs can be either roughly sorted into the general group of condensation or metal-catalysed (or mediated) reactions.<sup>6,17</sup> An essential point of the considerations within this chapter is that an absolute deterministic categorisation that encompasses the variety of NPOPs remains difficult since the classification absolutely depends on the criteria that have been chosen for that purpose. Nevertheless, the following chapters will distinguish a few of the most important NPOP representatives with respect to their synthesis by means of a condensation- or metal-catalysed (or -mediated) reaction (see also Scheme 3 for a rough classification of some of the most representative nanoporous organic polymers which will be discussed within the thesis at hand).



**Scheme 3** Classification of the most prominent representatives of nanoporous organic polymers according to their synthesis concept (organic vs. polymeric), the requirement of metals for their synthesis (metal-free condensation vs. metal-catalysed/-mediated) and the degree of reversibility (reversible vs. irreversible) provided by their synthesis protocol. Figures adapted from reference: PIMs [15]; COFs [16]; HCPs [18]; CMPs [19]; CTFs [20]; PAFs [21].

## 2.2 Nanoporous organic polymers obtained by metal-free condensation reactions

Polymers of intrinsic microporosity (PIMs), obtained by a condensation reaction of aromatic *ortho*-diols with vicinal fluoro- or chloro-containing monomers, are ideally suited to illustrate the polymeric approach to generate porosity (see Scheme 4). Initially, this class of materials was described by Neil McKeown *et al.* in 2002 and is based on a space-inefficient packing of polymer chains that causes intrinsic microporosity.<sup>15</sup> To ensure this demand, it was essential to find a rigid polymer structure that is intrinsically hindered to relaxate, which would cause a structural collapse and thus a loss of microporosity. The first PIM was based on planar phthalocyanine units, which were connected by the rigid and contorted condensation product (1) of hydroxyl-functionalised spirobisindane monomers and 1,2,4,5-tetrachlorobenzene, which provides both rigidity and a non-linear shape.<sup>9</sup> Commonly, the phthalocyanine units are prepared from aromatic nitriles that undergo a cyclotetramerisation reaction.



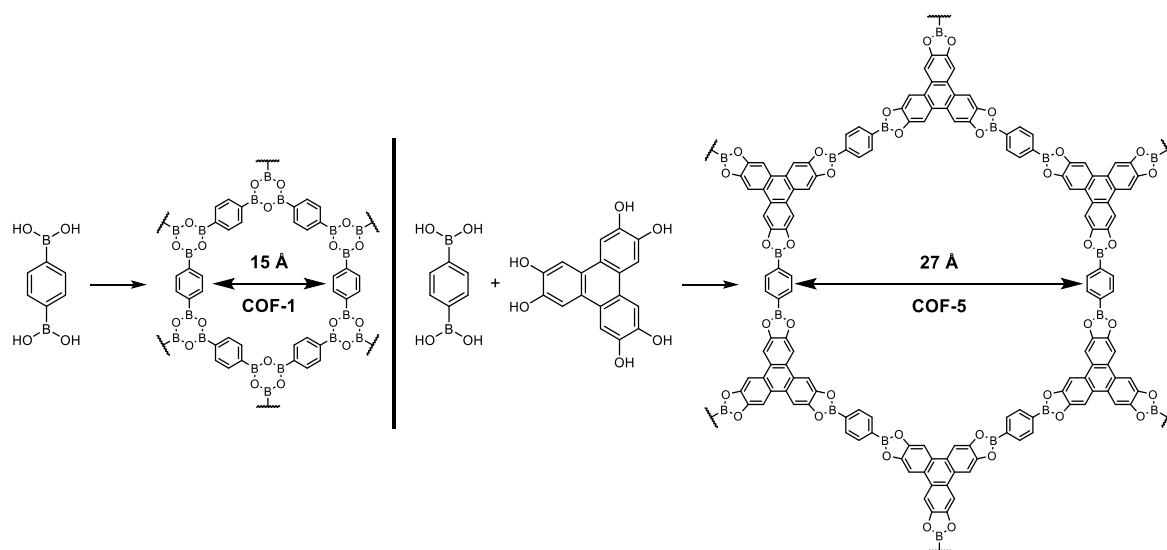
**Scheme 4** Synthesis of PIM-1 by a condensation reaction to yield the spirocyclic bis(phthalonitrile) (1) which undergoes tetramerisation to form phthalocyanine-based PIM-1.<sup>9</sup>

ESR spectroscopy as well as X-ray diffraction revealed that the spirocyclic crosslinks prevent a close packing of the phthalocyanine components which usually tend to extensive  $\pi$ -stacking. The resulting material is amorphous and has a specific surface area ranging from  $450 \text{ m}^2 \text{ g}^{-1}$  –  $950 \text{ m}^2 \text{ g}^{-1}$  depending on the metal center used to stabilise the phthalocyanine unit. The relation of structure and porosity as well as the limits in the characterisation of the accessible porosity in imide-based PIMs were investigated in detail by the groups of Weber and Kaskel.<sup>22–24</sup> PIMs are unique since they are processable in solution. Thus, porosity can be maintained upon dissolving and consequent removal of the solvent which enable for instance the fabrication of membranes that showed beneficial permeability properties in the separation of e.g. oxygen over nitrogen.<sup>25</sup> Based on triptycene monomers that possess alkyl groups attached to their bridgehead positions it was possible to tune the porosity of these materials in a range of  $1060 \text{ m}^2 \text{ g}^{-1}$  –  $1760 \text{ m}^2 \text{ g}^{-1}$  by simply varying the respective alkyl chain.<sup>26,27</sup> These values still set the record in terms of specific surface area to date for this class of materials.

In contrast to PIMs which are perfect representatives of the polymeric concept, covalent organic frameworks (COFs) can be considered as a candidate pursuing the organic framework concept to generate porosity. As it has been previously introduced (chapter 2.1), order is a structural feature that may preferably occur upon a reversible network formation – that can in fact be almost exclusively realised by particular condensation reactions.<sup>28</sup> In 2005, Yaghi and co-workers presented the ground-breaking synthesis of porous crystalline covalent organic frameworks (COFs), which are obtained by self-condensation reactions of multifunctional

aromatic boronic acids yielding materials whose aromatic tectons are connected through boroxine ( $B_3O_3 \rightarrow COF-1$ ) nodes that are generated in course of the condensation (see Scheme 5).<sup>28</sup> If a co-monomer – as for instance hydroxy-functionalised aromatic monomers – is applied, co-condensation occurs and leads to connecting five-membered  $BC_2O_2$  rings ( $\rightarrow COF-5$ ). In course of the condensation reaction, water is eliminated and due to the reversibility of the crosslinking reactions under solvothermal conditions, highly crystalline materials could be obtained. Moreover, COF-1 and COF-5 exhibited permanent porosity and specific surface areas of  $710 \text{ m}^2 \text{ g}^{-1}$  and  $1590 \text{ m}^2 \text{ g}^{-1}$ , respectively. The structure of COF-1 can be described therefore as AB stacked planar 2D sheets formed by hexagonal arrays. The porosity of COF-1 can be ascribed to a 1D pore that exists throughout the material defined by the van der Waals distance between adjacent layers. In contrast, COF-5 displays an eclipsed stacking, nitrogen sorption measurements revealed a mesoporous material showing a Type IV isotherm (according to IUPAC, see chapter 3.1 for detailed information) which results from a  $27 \text{ \AA}$  mesopore that can be explained by the width of the hexagonal channels along the c axis (thus, orthogonal to the 2D COF sheets).

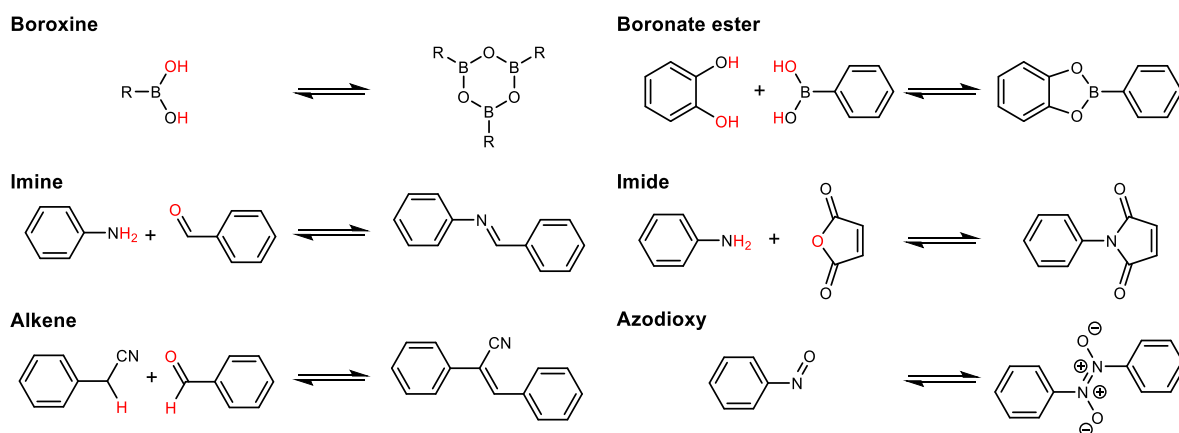
Starting from this breakthrough, COF research was heading into multiple directions.<sup>29</sup> The evolution of a class of materials often starts with an expansion of the structural variety and in the case of porous materials this also includes the quest of pushing the limits of porosity.<sup>16</sup> Hence, one major progress was the introduction of tetrahedral (thus 3D) monomers into the field of COF science.<sup>30</sup> The synthesis of such 3D COFs was afforded by self-condensation of tetra-



**Scheme 5** Synthesis of COF-1 obtained by a condensation of 1,4-diboronic acid and COF-5 obtained by co-condensation of 1,4-diboronic acid and hexahydroxy triphenylene.<sup>28</sup>

dral *tetra*(4-dihydroxyborylphenyl)methane and its silane analogue yielding specific surface areas of up to 3470 m<sup>2</sup> g<sup>-1</sup> and 4210 m<sup>2</sup> g<sup>-1</sup> for COF-102 (containing a tetrahedral carbon) and COF-103 (containing a tetrahedral silicon), respectively.<sup>30</sup> Modular construction of COFs has been expanded towards variations of linker connectivity, linker size and character of the linkage. Nowadays, there are examples of (1) B–O (boroxine, boronate ester, borosilicate, and spiroborate),<sup>28,31,32</sup> (2) C=N (imine, hydrazone, and squaraine)<sup>33–35</sup> as well as (3) C–N ( $\beta$ -ketoenamine, imide, and amide)<sup>36–38</sup> or (4) O $\leftarrow$ N=N $\rightarrow$ O (azodioxy)<sup>39</sup> linkages that have been reported (see Scheme 6).

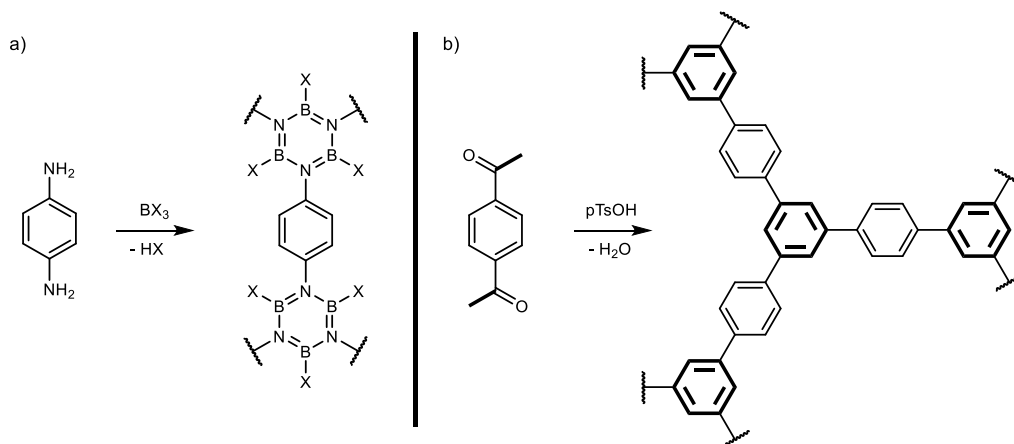
At present, more than 100 COF structures are known and a major focus of COF research was directed towards application or advanced synthetic pathways.<sup>29</sup> COFs turned out to be promising platform materials for heterogeneous catalysts as for instance in a size-selective Knoevenagel condensation reaction demonstrated for base-functionalised COFs reported by Fang *et al.*<sup>40</sup> Also optoelectronic properties were intensively investigated and led to the discovery of conductive and photoactive COF materials,<sup>41</sup> which were applied for e.g. photocatalytic water splitting.<sup>42</sup> Lately, the issue of a maximum degree of long-range order, which remained a major challenge for those optoelectronic properties mentioned before, has been successfully tackled.<sup>43,44</sup> To this end, a concept to minimise stacking faults and resulting defects was presented that benefits from substituted pyrene-based tectons that act as defined molecular docking sites for the attachment of adjacent COF layers.<sup>43</sup> The major advantage of COFs (crystallinity) however, in parallel causes their greatest drawback. The reversibility of condensation reaction that induces long-range order enables also the reverse reaction, e.g. decomposition of the



**Scheme 6** Significant reversible reactions for the synthesis of covalent organic frameworks. All reactions belong to the group of condensation reactions except for the formation of azodioxy compounds. Red atoms indicate atoms that form water in course of the reaction.

framework upon hydrolysis. Therefore, research was striving to close this gap and currently there are examples of phenazine- and  $\beta$ -ketoenamine-based COFs that maintain their structure and porosity in strong acids and bases, respectively.<sup>29</sup>

It is important to recognise that within the thesis at hand, COFs are considered as frameworks that are exclusively constructed from condensation reactions offering a certain degree of reversibility that allows for crystallinity. Therefore, different materials closely related to COFs are known, which in fact differ due to the fact that the network forming reaction cannot be considered as highly reversible. As such, borazine (B=N) linked polymers (BLP) which are obtained by a condensation reaction of aromatic amines and boron trihalides have garnered attention.<sup>45,46</sup> The initial report by Thomas Reich *et al.* describes the synthesis of BLPs starting from 1,4-phenylenediamine or 1,3,5-tris-(4'-aminophenyl)benzene with boron trichloride (or -bromide) to yield totally amorphous NPOPs showing pronounced microporosity with specific surface areas ranging from  $500 \text{ m}^2 \text{ g}^{-1}$  and  $1360 \text{ m}^2 \text{ g}^{-1}$ .<sup>45</sup> The striking difference to classical COFs is the reactivity of the boron trihalides that irreversibly react with amines to a robust B=N bonding motif. This circumstance is the reason for a kinetically controlled reaction product and thus explains the amorphous nature of the polymers. A similar approach that describes the cyclotrimerization of bifunctional acetyl compounds in molten 4-toluene sulfonic acid to afford specific surface areas as high as  $830 \text{ m}^2 \text{ g}^{-1}$  was reported by the group of Stefan Kaskel.<sup>47</sup> This procedure was extended by the same group enabling pore size control as well as the application of such NPOPs as chemiresistive gas sensors.<sup>48,49</sup>



**Scheme 7** Synthesis of borazine linked polymer (a) presented by Reich *et al.*<sup>45</sup> and synthesis of a nanoporous organic polymer by cyclotrimerization of aromatic bi-acetyl compounds (b) from Kaskel and co-workers.<sup>47</sup>



The transition between a condensation and a metal-catalysed (-mediated or -induced) reaction to synthesise NPOPs is gradual. The group of aza-based conjugated microporous polymers (aza-CMPs) is nicely suited to illustrate the limits of categorising such materials.<sup>50</sup> These materials consist of an extended conjugated aromatic system, which is obtained upon condensation reaction of benzene tetraamine and hexahydroxybenzene. In course of the synthesis water as a by-products is formed (thus matching the term condensation), but the condensation is triggered by means of a Lewis acid activation (thus matching the term metal-induced). In consequence, the following chapter will deal with NPOPs obtained by metal-catalysed or mediated reactions and tries to outline the most remarkable examples in this emerging field.

## 2.3 Nanoporous organic polymers obtained by metal-catalysed (-mediated) reactions

For the generation of NPOPs, a myriad of metal-catalysed (-mediated) synthetic methods is available<sup>7</sup> – including but not limited to Sonogashira,<sup>51,52</sup> Suzuki,<sup>53</sup> Yamamoto,<sup>54</sup> Buchwald-Hartwig,<sup>55</sup> Eglinton<sup>56</sup> or Heck reactions<sup>57</sup> (see Table 1 for some important examples). Most commonly, connecting of the tectons by strong covalent bonds as a result of irreversible – and thus kinetically controlled – coupling reactions yields NPOPs of total amorphicity. Hence, these amorphous networks have a statistically disordered structure which in theory causes a broader pore size distribution,<sup>6</sup> although narrow pore size distributions are in fact existing and can be tailored to some extent as will be illustrated later in this chapter.

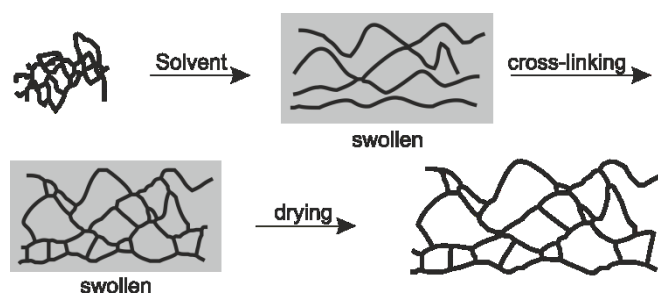
**Table 1** Significant reactions employed in the metal-catalysed (-mediated) synthesis of NPOPs.

reaction type	reaction scheme	$S_{\text{BET}}$ $\text{m}^2 \text{g}^{-1}$	Ref.
Friedel-Crafts alkylation		up to 2500 (PSN-5)	[58]
Suzuki coupling		up to 1080 (PP-CMP)	[59]
Sonogashira-Hagihara coupling		up to 1020 (CMP-0)	[60]
Yamamoto coupling		up to 6460 (PPN-4)	[61]
Oxidative coupling		up to 1060	[62]

X = Ph or other EDG

**EDG**      electron donating group.

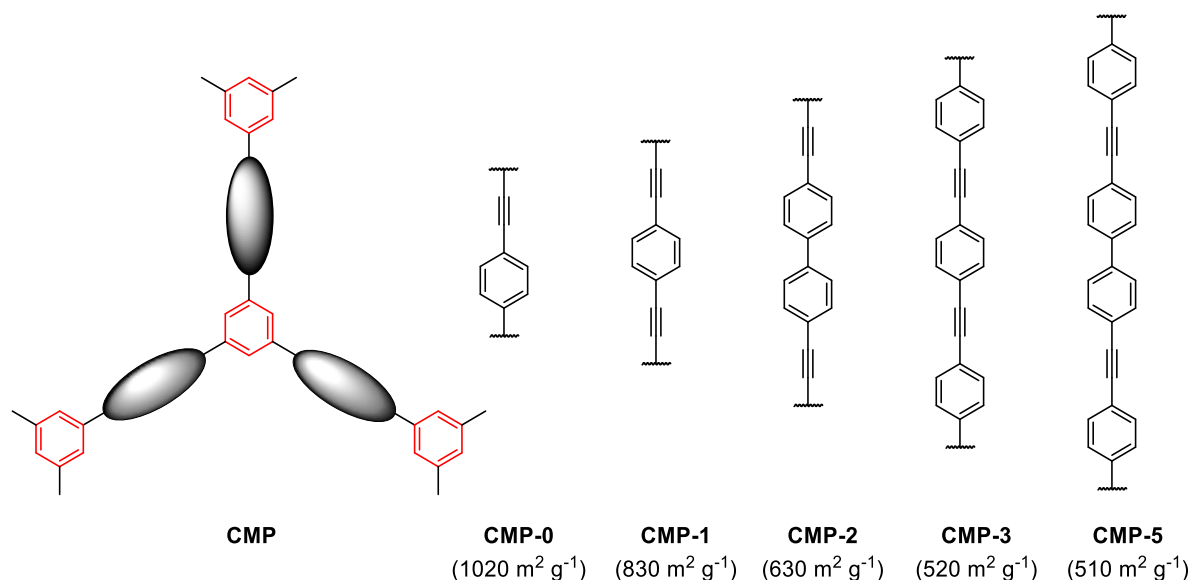
**Hypercrosslinked polymers (HCPs)** can be considered as the oldest NPOP representative since this class of materials has been initially described by Davankov *et al.* in the early seventies.<sup>11</sup> In principal, HCPs are synthesised by metal-mediated crosslinking of polymer chains. In consequence, a highly interconnected and rigid network results that is unable to collapse, thus providing small pore sizes (in the range of micropores) and high surface areas. Based on the previously given classification (chapter 2.1), HCPs can be regarded as a representative of the polymeric approach. The Davankov HCPs (also referred to as “Davankov resins”) are obtained by polymerising vinylbenzylchloride with a small amount of divinylbenzene to generate the corresponding copolymer.<sup>6</sup> The polymer, if swollen in a thermodynamically compatible solvent, can be hypercrosslinked by e.g. iron(III)-chloride mediated Friedel-Crafts alkylation (see Table 1) to lock the polymer chains in the swollen state and yield the HCP (see Scheme 8).<sup>18</sup> By slight modifications of the synthetic protocol to perform the crosslinking it is possible to obtain specific surface areas from  $600 \text{ m}^2 \text{ g}^{-1}$  up to  $2000 \text{ m}^2 \text{ g}^{-1}$ .<sup>63,64</sup> Further research was heading towards the introduction of elongated linker systems and an extended investigation of copolymers for the synthesis of HCPs. Kaskel and co-workers presented an approach to statistically copolymerise 4,4'-bis(chloromethyl)biphenyl with a series of non-functionalised fluorene-based monomers to yield nanoporous polymers exhibiting high specific surface areas of up to  $1800 \text{ m}^2 \text{ g}^{-1}$ .<sup>65</sup> If considering HCPs, it is important to distinguish between external or internal electrophiles to perform the hypercrosslinking by Friedel-Crafts alkylation. To this end, external bifunctional alkylation agents such as 1,4-bis-(chloromethyl)-diphenyl were applied to introduce chloromethyl groups to the polymer which can consequently react with other phenyl rings forming methylene bridges.<sup>18</sup> Vice versa, internal alkylation profits from reactive groups on the monomers such as chloromethylene electrophiles.<sup>66</sup>



**Scheme 8** Schematic synthesis of a hypercrosslinked polymer (adapted from reference [18]).

As it has been mentioned previously in this chapter, in particular metal-catalysed (cross-)coupling reactions are ideally suited to construct NPOPs. There is a plethora of methods available but in general they all consist of multiple carbon-carbon and/or aromatic rings that form an extended  $\pi$ -conjugated network.<sup>6,7,17</sup> Initially, this class of materials was described as conjugated microporous polymers (CMPs) in 2007 by the group of Andy Cooper.<sup>51</sup> Their earliest publication dealt with poly(aryleneethynylene) networks obtained by Sonogashira-Hagihara palladium cross-coupling to link aromatic halides to aromatic alkynes. The so called series of materials denoted to as CMP-1 to CMP-3 was extended to materials with shorter as well as longer “tecton” length.<sup>60</sup> This isorecticular series illustrated the crucial impact of the tecton length on the pore size and the pore volume. Most importantly, this publication proved that the shortest tectons yielded the smallest pores and in consequence the highest micropore volume. The inverse effect could be observed for the longest tecton. Thus, these results gave rise to a controllable and predictable synthesis pathway which was exclusively known for crystalline materials like MOFs<sup>67</sup> and COFs formerly.<sup>31</sup> Pursuing this isorecticular approach Cooper and co-workers could synthesise CMPs with specific surface areas ranging from  $510 \text{ m}^2 \text{ g}^{-1}$  to  $1020 \text{ m}^2 \text{ g}^{-1}$ .<sup>60</sup> (see Scheme 9)

As a general principle that allows for constructing a  $\pi$ -conjugated skeleton, the synthetic reaction must covalently link building blocks with a  $\pi$ -conjugated bond.<sup>17</sup> It is important to notice that only CMPs obtained by metal-catalysed (cross-)coupling reactions are discussed within



**Scheme 9** Isorecticular synthesis of CMPs with varying tecton length by Cooper and co-workers.<sup>60</sup>

this chapter. This excludes for instance Schiff-base reactions (see COFs in chapter 2.2) or cyclotrimerization reactions (which will be discussed intensively in chapter 2.4).

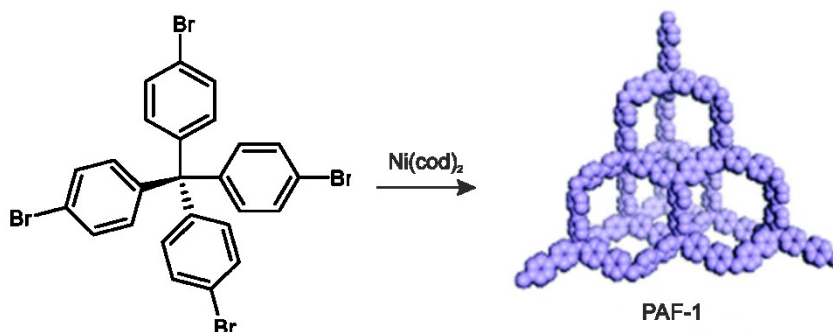
As it has been shown by Arne Thomas and co-workers, the geometry of the linker unit plays a key role in the development of a porous structure.<sup>68</sup> In this work, the nickel catalysed Yamamoto reaction was introduced into the wide field of CMP syntheses. This reaction is beneficial since only one functionality is required (that is a halide-functionalised monomer). When coupling a symmetrically substituted tetrabromo-spirobifluorene with differently substituted dibromobenzenes (*ortho*, *meta*, *para*) the specific surface area of the resulting polymers differed significantly, ranging from 880 m<sup>2</sup> g<sup>-1</sup> (*para*) to 360 m<sup>2</sup> g<sup>-1</sup> (*meta*) and finally 5 m<sup>2</sup> g<sup>-1</sup> in case of the *ortho*-substituted benzene.

Some remarkable examples of CMPs obtained by Suzuki cross-coupling led to their application in optoelectronic devices.<sup>53,59,69</sup> Donglin Jiang and co-workers presented the synthesis of CMPs based on conjugated polyphenylene units (PP-CMP).<sup>59</sup> After confining a coumarin dye within the narrow micropores of the PP-CMP, an energy transfer from the PP-CMP towards the dye was proven spectroscopically. In consequence, excitation of the confined coumarin dye was observed, which is a result of the donor-acceptor interaction within the polymer. Even more extraordinary is the synthesis of soluble CMPs presented by Cooper and co-workers in 2012.<sup>69</sup> To that purpose, tetrabromopyrene was coupled with a *tert*-butyl-functionalised dibromopyrene co-monomer whose solubilising alkyl groups effect the solubility of the resulting polymer. The polymers are processable in solution and can be precipitated as thin films which show green luminescence upon UV irradiation.

Very close to CMPs, but not ideally matching the requirement of a fully conjugated polymeric backbone are polymers that are obtained by metal-catalysed (cross-)coupling reactions but contain nodes such as sp<sup>3</sup> carbon (or silicon),<sup>70</sup> sp<sup>2</sup> boron<sup>71</sup> or, interestingly, cationic tetrahedral phosphorus,<sup>72</sup> which interrupt the conjugated system. Nevertheless, some of these materials provide the most remarkable features in the field of NPOPs.

One outstanding example is a porous aromatic framework (PAF) synthesised from a tetrahedral monomer, tetrakis(4-bromophenylmethane), by a Yamamoto-type Ullmann coupling (denoted to as PAF-1, see Scheme 10).<sup>73</sup> Again the introduction of a tetrahedral node led to an unprecedented specific surface area of 5640 m<sup>2</sup> g<sup>-1</sup>, which even showed a limited

degree of long-range order as reflected by broad reflections in the X-ray diffractograms. Further research was conducted to investigate the origin of porosity within PAF-1. Whereas the initial publication by Ben *et al.* proposed a diamond-like crystalline structure which matched the experimental findings,<sup>73</sup> Cooper and co-workers suggested a structure by computational methods that did not invoke a periodic crystalline structure but also nicely represented the experiments.<sup>74</sup> Cooper's work was also strongly supported by another computational approach which strengthened the hypothesis that the relatively rigid PAF-1 linker prevents the system from interpenetration and causes the high specific surface area.<sup>75</sup> Particularly the latter arguments give rise to the assumption that very high specific surfaces areas may potentially not alone be accessible by means of molecular networks with high degrees of long-range crystalline order.<sup>74</sup> This early work was extended by the group of Hong-Cai Zhou and the synthesis of PAF-1 derived PPN (porous polymer network) materials in 2011.<sup>61</sup> Replacing the central tetrahedral carbon of the monomer with other quadricovalent building centers (adamantane, silicon, and germanium) yielded a material named PPN-4 (based on a tetrahedral silicon center)<sup>61</sup>, which outperforms PAF-1 by exhibiting a specific surface area of  $6460 \text{ m}^2 \text{ g}^{-1}$  which is close to the current record holder in the field of MOF materials (NU-110E:  $7140 \text{ m}^2 \text{ g}^{-1}$ )<sup>76</sup> or COFs (COF-103:  $4210 \text{ m}^2 \text{ g}^{-1}$ )<sup>30</sup> at the time of writing.



**Scheme 10** Synthesis of porous aromatic framework (PAF-1) starting from tetrakis(4-bromophenylmethane).<sup>21</sup>

A very recent approach published by the group of Arne Thomas succeeded with encumbering of triphenylphosphine motifs in a non-conjugated CMP, mimicking the basic sites in a frustrated Lewis pair.<sup>54</sup> By immobilising the strong Lewis acid tris(pentafluorophenyl)borane as counterpart in the porous framework, a semi-immobilised frustrated Lewis pair could be generated that enabled activation of hydrogen at room temperature.

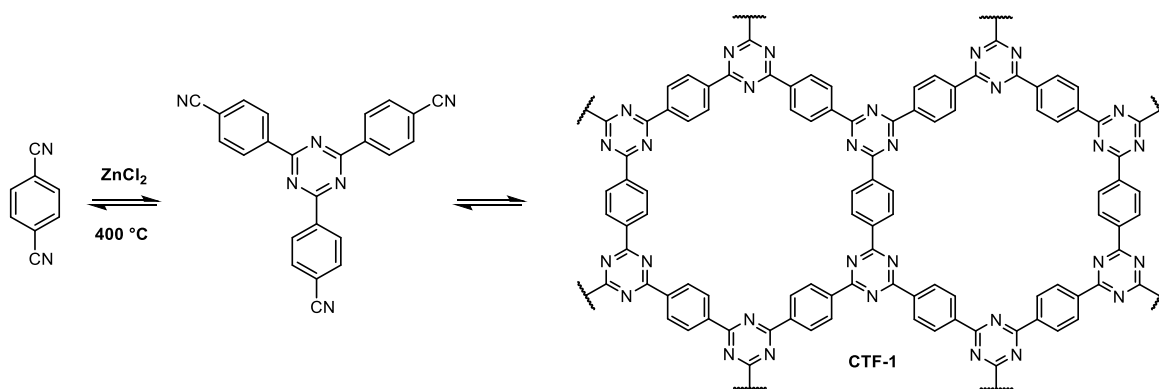
Whereas the group of non-conjugated CMPs is constructed from tectons with an incorporated element as geometry defining feature (as mentioned carbon, silicon or other elements) by means of metal-catalysed coupling reactions, element organic frameworks (EOFs) may be considered very similar but differ in their synthetic approach. This group of materials, introduced by the group of Stefan Kaskel in 2008, is synthesised by an organolithiation route. To this end, multifunctional halide substituted tectons are converted into nucleophilic organolithium species which consequently attack electrophilic precursors to form direct element-carbon bonds as connecting node. Those elements can either be non-metals (phosphor),<sup>77</sup> light weight metalloids like silicon<sup>78</sup> or antimony,<sup>79</sup> but even typical metals (tin, bismuth)<sup>79</sup> were applied. In course of the reaction, EOFs precipitate as amorphous materials and can reach specific surface areas up to 1000 m<sup>2</sup> g<sup>-1</sup>.<sup>66</sup>

A prominent group of NPOPs whose syntheses are performed by the aid of metal compounds has been mostly omitted within this chapter. Those materials belong to the class of CMPs but are obtained by cyclisation reactions instead of (cross-)coupling reactions. This for instance includes examples like the cobalt-catalysed cycloaddition of di- and tri-alkyne monomers for the generation of polyphenylenes (PP-CMPs).<sup>80</sup> More importantly, an exceptional class of materials could be generated by ionothermal trimerization of aromatic nitriles in molten ZnCl<sub>2</sub> – namely the group of covalent triazine-based frameworks (CTFs).<sup>81</sup>

## 2.4 Covalent triazine frameworks

Covalent triazine frameworks are based on aromatic multifunctional nitriles, which undergo a metal-mediated trimerization and consequent oligomerisation to yield porous, chemically and thermally stable polymers. Albeit this class of materials had their scientific breakthrough only 10 years ago in 2008,<sup>81</sup> the roots of these materials can be even backdated to the early 60s of the last century.<sup>82</sup> It was found already in 1962 that 1,3,5-triazines can be obtained from aromatic mono-nitriles at elevated temperatures (e.g. up to 400 °C) by the aid of metal salts as catalyst. In 1973, this approach was extended by G. H. Miller (Texaco Inc.) to a variety of aromatic nitriles with at least two nitrile groups, thus providing highly crosslinked and stable polymers based on triazine motifs.<sup>83</sup> He already discovered that “the products formed in the early stages of this process are at elevated temperatures highly fluid liquid polymers” whereas in course of the

polymerisation “they become soft materials and finally rigid, infusible, insoluble polymeric products result”. Moreover, Miller further mentioned potential metal halides that enable the trimerization reaction at high temperatures such as  $\text{ZnCl}_2$ . With recourse to these early investigations, Kuhn, Antonietti and Thomas took up this concept in 2008 and reported about the synthesis of covalent triazine-based frameworks (CTFs) prepared by ionothermal synthesis under inert conditions.<sup>81</sup> To this end, multifunctional aromatic nitriles e.g. 1,4-dicyanobenzene were converted into highly robust and porous CTF-1 by means of an ionothermal trimerization reaction conducted in molten  $\text{ZnCl}_2$  (see Scheme 11).



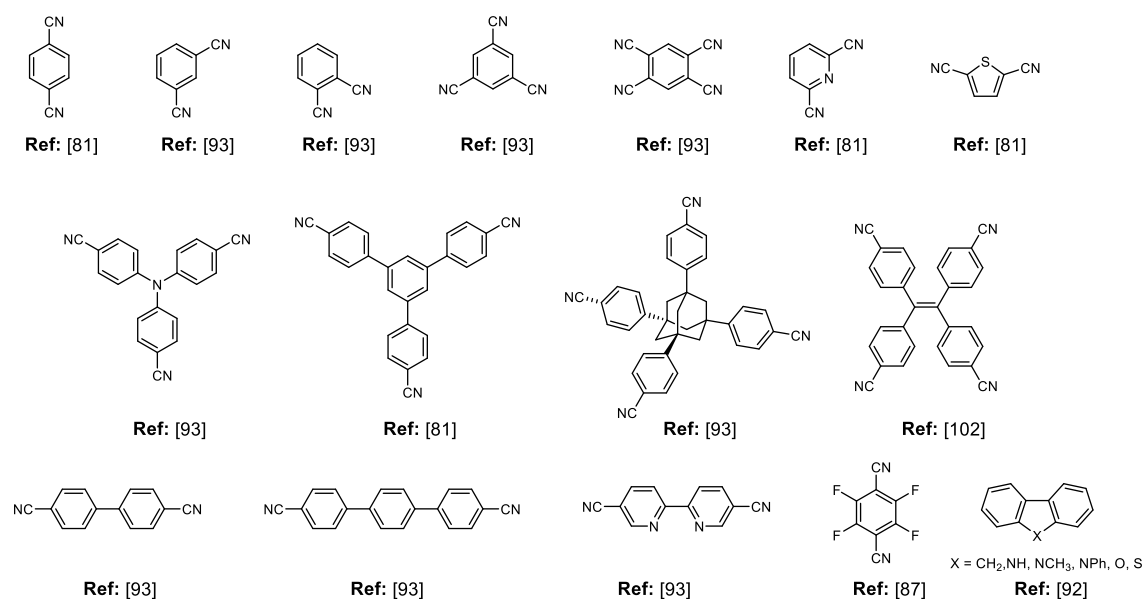
**Scheme 11** Ionothermal trimerization reaction to synthesise CTF-1 from 1,4-dicyanobenzene.

Due to the tendency of low-molecular aromatic nitriles to sublime, the syntheses of those reported CTF materials were conducted in sealed ampoules in order to retain the stoichiometry (with respect to  $\text{ZnCl}_2$ ) of the reaction. Furthermore, both the monomer as well as  $\text{ZnCl}_2$  are highly hygroscopic, thus inert conditions are inherently obligate.  $\text{ZnCl}_2$  acts as a solvent and is activating the nitrile groups serving as a Lewis acid. More importantly, it is also a pore forming agent causing temperature-induced chemical activation.<sup>84</sup> CTF-1, synthesised with an equimolar ratio of 1,4-dicyanobenzene/ $\text{ZnCl}_2$ , displayed a specific surface area of  $790\text{ m}^2\text{ g}^{-1}$  and even a limited degree of crystallinity was observed as reflected by broad peaks in the X-ray diffractogram. The formation of long-range order was ascribed to the reversibility of the trimerization reaction at elevated reaction temperatures, although crystallinity (or long-range order) is just an exceptional case for CTF materials. At the time of writing, only four examples (CTF-0;<sup>85</sup> CTF-1;<sup>81</sup> CTF-2;<sup>86</sup> FCTF-1<sup>87</sup>) are known which exhibit at least a certain degree of long-range order.<sup>88</sup> Nevertheless, it is advisable to mention that there are different synthetic methods available to generate long-range ordered CTF-1 which mostly relies on the reaction that generates the triazine (see chapter 2.5 for more details).<sup>20,88,89</sup> However, this chapter will



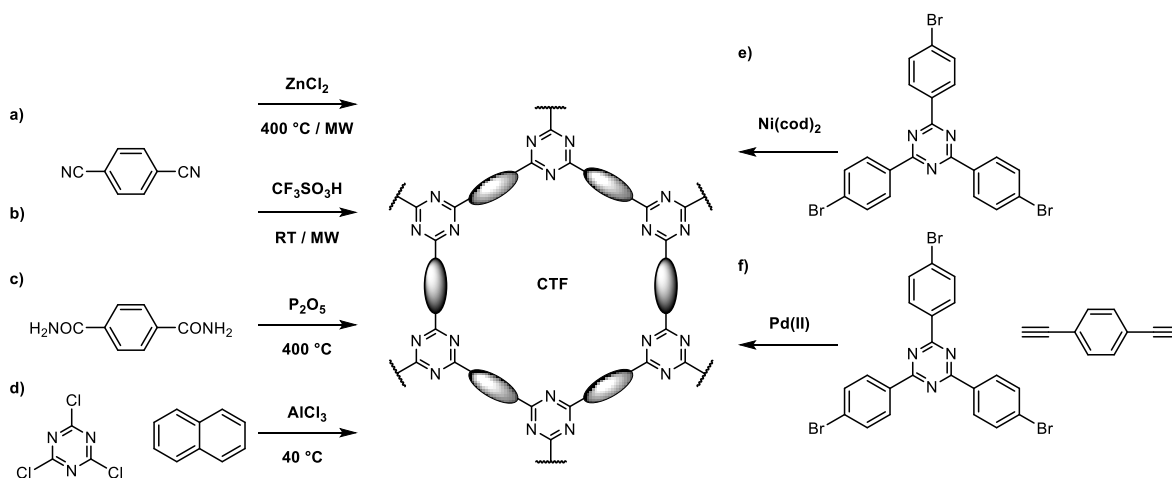
exclusively deal with CTFs derived from aromatic nitriles under ionothermal conditions. Coming back to CTF-1, a hexagonal packing of pores with a layered structure as known for COFs (see chapter 2.2) with an interlayer distance of 3.4 Å was deduced from PXRD. Based on nitrogen physisorption, CTF-1 – synthesised with one equivalent  $\text{ZnCl}_2$  – is a microporous material with pore sizes of 0.7 nm and 1.2 nm. Whereas the pore of 1.2 nm can be ascribed to the pores stemming from eclipsed stacking, the smaller pore can be caused by a layer offset. Higher amounts of  $\text{ZnCl}_2$  (5 or 10 eq.) yielded more porous (up to  $1120 \text{ m}^2 \text{ g}^{-1}$ ) but amorphous materials. Especially the lower density of the amorphous state as compared to the crystalline state can be considered as a main reason of pronounced porosity. Additionally, these observations should be attributed to the crucial role of  $\text{ZnCl}_2$  and its impact on the evolution of porosity due to chemical activation. In consequence, the majority of CTF materials can be described more appropriately as amorphous triazine frameworks or even N-doped carbon materials if obtained at temperatures above  $400^\circ\text{C}$ . Further research was heading towards tailored synthetic approaches to incorporate adjustable structural elements (by the choice of other monomers, see Scheme 12) and/or to control the porosity, pore size and polarity of the surface.<sup>90</sup> In a consecutive study, again Kuhn *et al.* investigated the influence of different temperature/time protocols on structural features of CTF-1.<sup>91</sup> They succeeded with synthesising high surface area hierarchical CTF-1 derived materials (up to  $3300 \text{ m}^2 \text{ g}^{-1}$  and a pore volume of  $2.4 \text{ g cm}^{-3}$ ) when applying a modified temperature protocol (1<sup>st</sup>:  $400^\circ\text{C}$ , then 2<sup>nd</sup>:  $600^\circ\text{C}$ ).<sup>91</sup> They also conducted an insightful series of experiments comparing the impact of the reaction temperature ranging from  $400^\circ - 700^\circ\text{C}$ . At  $400^\circ\text{C}$ , the trimerization reaction has been considered as moderately reversible as supported by long-range order (thus a thermodynamically controlled reaction type). At increased temperatures ( $\geq 500^\circ\text{C}$ ), irreversible reaction pathways like carbonisation and thermal decomposition take place in parallel, thus causing defects (that create porosity) and nitrogen loss. This could be experimentally proven by an increasing specific surface area starting from  $500^\circ\text{C}$  to  $700^\circ\text{C}$  ( $1600 \text{ m}^2 \text{ g}^{-1}/500^\circ\text{C}$  up to  $2530 \text{ m}^2 \text{ g}^{-1}/700^\circ\text{C}$ ).<sup>91</sup> Nevertheless, these observations emphasise the superior thermal stability of most CTF materials (up to  $400^\circ\text{C}$ ) in contrast to other NPOPs. Additionally, these nitrogen-rich porous polymers also feature enhanced chemical stability under strong basic as well as acidic conditions. Certainly, these attributes substantiate the growing interest in CTF materials in the last decade (at the time of writing, more than 220

publications exist that deal with CTFs). In consequence, several monomers comprising a variety of different tecton lengths, building blocks (aromatic and heteroaromatic),<sup>92</sup> geometries (linear, trigonal, tetrahedral)<sup>93</sup> and functionalities have been introduced into CTF materials.<sup>90,94</sup> Despite all these synthetic options, potential and promising monomers necessarily have to withstand harsh conditions during the synthesis. This fact excludes many possible monomers since they decompose at elevated temperatures. Therefore, alternative synthetic concepts towards covalent triazine frameworks have been developed and will be discussed within the next chapter.



**Scheme 12** Representative aromatic nitrile monomers which have been applied for the ionothermal synthesis of CTF materials and the respective reference of first report. For a complete overview find more information in a very recent review that has summarised all applied nitrile monomers until 2016.<sup>94</sup>

## 2.5 Synthetic pathways towards covalent triazine frameworks



**Scheme 13** Different synthetic procedures towards CTF materials including a) ionothermal synthesis in molten  $\text{ZnCl}_2$ /<sup>81</sup>microwave,<sup>95</sup> b) Brønsted acid catalysed trimerization (solution/microwave)<sup>96</sup> c)  $\text{P}_2\text{O}_5$  triggered dehydration and consequent trimerization,<sup>20</sup> d) Friedel-Crafts reaction,<sup>97</sup> e) Yamamoto homo-coupling<sup>98</sup> and f) Sonogashira-Hagihara cross-coupling.<sup>99</sup>

Ionothermal CTF syntheses conducted at 400 °C are most often accompanied by a substantial degree of carbonisation. This might be attributed to an intrinsic decomposition but also  $\text{ZnCl}_2$  strongly contributes and triggers an additional chemical activation which becomes even more pronounced at temperatures above 400 °C.<sup>91</sup> These processes can be indicated by e.g. increasing C/N and C/H ratios as compared to ideal values and also an increased porosity might point to a structural loss. Incipient carbonisation yields black products which is in particular detrimental for photocatalytic applications (see chapter 2.6 for a more detailed overview of potential applications).<sup>100</sup> To overcome these limitations, the group of Lotsch reported about a synthesis route to prevent CTF-1 materials from being partially carbonised by lowering the reaction temperature to 300 °C.<sup>101</sup> It turned out that longer reaction times were necessary to achieve sufficient polymerisation degrees. In consequence, the reaction time was increased from conventionally used 40 h to more than 150 h. Still, the resulting polymers were identified to feature a rather oligomeric (phenyl-triazine oligomers, PTOs) than polymeric character as indicated by the presence of nitrile vibrations in the FT-IR spectra. Another drawback of the ionothermal approach is the time scale of the reaction (40 h and more). In order to tackle this issue a smart energy- and time-efficient microwave-assisted synthesis of CTFs was reported by Zhang *et al.*<sup>95</sup> Their synthesis route avoids the synthesis in sealed quartz ampoules and makes use of a physical property of  $\text{ZnCl}_2$  –which has been shown to be a good microwave absorber. Thus, by irradiat-

ing a mixture of 1,4-dicyanobenzene and  $\text{ZnCl}_2$  it was possible to obtain highly porous CTF-1 samples after 10 min. However, in course of the irradiation of  $\text{ZnCl}_2$  very high temperatures occur and thus, significant carbonisation (as indicated by low nitrogen contents) was observed for these samples.

As it has been mentioned in the previous chapter, there are monomers which do not withstand harsh synthetic conditions as necessary for an ionothermal synthesis conducted at  $400^\circ\text{C}$ . Moreover,  $\text{ZnCl}_2$  is embedded within the pores in course of the reaction and has to be removed by a thorough washing procedure. Most often, work-up fails to remove all of the residual salt and thus a permanent contamination of ca. 5 w% remains within the porous polymer. To overcome these issues and expand the toolbox of accessible monomers, Cooper and co-workers developed a room temperature synthesis including trifluoromethanesulfonic acid ( $\text{CF}_3\text{SO}_3\text{H}$ ) as strong Brønsted acid catalyst to activate nitrile groups and subsequently trigger trimerization.<sup>96</sup> To this end, unreactive solvents like chloroform (or dichloromethane) have to be applied, which do not interact with the acid. In consequence, this method is limited to those monomers well soluble in such unreactive solvents. However, this synthetic strategy shows great advantages since the reactions can be conducted at moderate reaction conditions ( $0^\circ\text{C}$  – RT) and avoids incipient carbonisation.<sup>102,103</sup> Therefore, even monomers such as 4,4'-oxydibenzonitrile, which was previously seen to be not accessible by the ionothermal procedure, could be generated. In addition, this Brønsted acid catalysed protocol also allowed for a microwave-assisted synthesis. In addition to limitations due to the solubility of the respective monomer in chloroform, also the porosities of CTFs obtained from polymerisation triggered by trifluoromethanesulfonic acid are much lower (or sometimes even non-porous) as compared to materials obtained by the ionothermal approach. This finding can be rationalised by the absence of  $\text{ZnCl}_2$  (porogen and chemical activation agent) and/or by an incomplete conversion of nitrile groups into triazine rings (as indicated by the given FT-IR spectra). An elegant approach that combines the Brønsted acid ( $\text{CF}_3\text{SO}_3\text{H}$ ) and the Lewis acid ( $\text{ZnCl}_2$ ) approach was presented by Kuecken *et al.*<sup>88</sup> By applying  $\text{CF}_3\text{SO}_3\text{H}$ , an amorphous, non-porous polymeric pre-CTF network was synthesised in a first step. In consequence, the polymeric precursor (pre-CTF) can be easily processed under ionothermal conditions by adding  $\text{ZnCl}_2$ . Since the pre-CTF has a much higher molecular weight as compared to the monomer, the pre-CTF does not tend to sublime and can be processed in open crucibles under inert atmosphere. Thereby, the

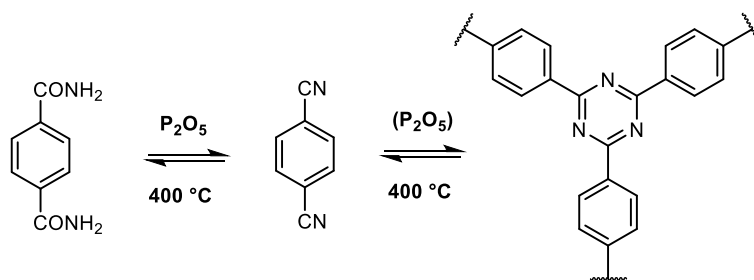
synthesis in quartz ampoules can be bypassed and an efficient up-scaling becomes possible. Moreover, the porosity of the CTF materials obtained by this combined approach stayed comparable to conventionally synthesised materials ( $910 \text{ m}^2 \text{ g}^{-1}$ ). Beneficially, also long-range order was observed for CTF-1 synthesised in an open crucible thus rendering this method highly competitive.

Nevertheless, both synthetic pathways (Lewis acid and Brønsted acid) are strongly restricted to aromatic nitriles of which just a few are commercially available. More complex compounds, required for tailored applications, involve complex and time-consuming organic synthesis which often contains a cyanation using hazardous inorganic metal cyanides in the last sequence.<sup>104</sup> Therefore, a few methods will be presented next which benefit from readily available triazine-based building blocks to generate CTF materials. A very recent approach that circumvents the requirement of aromatic nitriles is the Friedel-Crafts reaction (see chapter 2.3 for mechanistic insights) mediated by anhydrous aluminium chloride.<sup>97,105–107</sup> This methodology includes the nucleophilic attack of an unsubstituted (electron-rich) aromatic monomer at  $\text{AlCl}_3$  activated cyanuric chloride that itself introduces the triazine motif. After multiple reaction steps, a triazine-based polymer can be obtained from a plethora of organic monomers, which do not require a functionalisation with nitrile groups. Several monomers comprising benzene,<sup>105</sup> naphthalene,<sup>105</sup> anthracene,<sup>105</sup> 1,3,5-triphenylbenzene,<sup>106</sup> *trans*-stilbene,<sup>106</sup> 1,1,2,2-tetraphenylethylene,<sup>107</sup> tetraphenylsilane,<sup>107</sup> triptycene<sup>97</sup> and fluorene<sup>97</sup> have been incorporated into a Friedel-Crafts CTF material. At the time of writing, the highest specific surface area achieved by this method is  $1660 \text{ m}^2 \text{ g}^{-1}$  for a triptycene-based CTF.<sup>97</sup>

Also metal-catalysed cross-coupling reactions were investigated to synthesise materials similar to CTFs. In 2012, Cooper and co-workers continued on their work on CMPs (see chapter 2.3) and introduced triazine-nodes by Sonogashira-Hagihara cross-coupling.<sup>99</sup> These so-called triazine-based CMPs exhibited specific surface areas up ranging from  $490 \text{ m}^2 \text{ g}^{-1}$  to  $990 \text{ m}^2 \text{ g}^{-1}$  obtained from 2,4,6-tris(4-bromophenyl)-1,3,5-triazine with various di- and tri-acetylenes. In a similar manner, homo-coupling of a 2,4,6-tris(4-bromophenyl)-1,3,5-triazine yielded a triazine-based polymer by nickel-catalysed Yamamoto-type Ullmann cross-coupling reaction.<sup>98</sup> For this method, specific surface areas as high as  $2010 \text{ m}^2 \text{ g}^{-1}$  were reported which are amongst the highest values for all CTF materials without regard to the specifically applied synthesis route (see Table 2).

---

Very recent approaches to synthesise CTFs without the need for aromatic nitriles deal with cyclisation (or cyclocondensation) reactions which can be considered very similar to COF chemistry.<sup>20,108</sup> As reported by Yu *et al.* in 2018, CTFs with remarkable porosity are accessible via a phosphorus pentoxide ( $P_2O_5$ ) catalysed cyclisation of aromatic amides (see Scheme 14).<sup>20</sup> The synthesis proceeds via a one-pot tandem process in which  $P_2O_5$  serves two different purposes. First,  $P_2O_5$  triggers the dehydration of the primary amide groups of 1,4-benzenedicarboxamide to give intermediary nitriles which consequently undergo a  $P_2O_5$ -mediated trimerization to yield a CTF. The resulting material can be considered as a CTF-1 analogue (denoted to as *p*CTF-1) and featured both long-range order (as reflected by broad reflections in the PXRD) and enhanced porosity as displayed by a specific surface area of  $2030\text{ m}^2\text{ g}^{-1}$ . The main benefit of this work is the smart integration of very old chemistry (dehydration of amides) into the wide field of CTF synthesis. Hence, this method extends the variety of applicable monomers and avoids an additional synthetic step to obtain the respective nitrile. It also bypasses the need for  $ZnCl_2$ , but also  $P_2O_5$  will remain as a residue within the pores. Determining the quantity of  $P_2O_5$  becomes even more complicated, since  $P_2O_5$  sublimates at  $362\text{ }^\circ\text{C}$  at ambient pressure, thus excluding TGA experiments which are conventionally conducted for such investigations.



**Scheme 14** Synthesis of ordered CTF materials starting from aromatic amides according to Yu *et al.*<sup>20</sup>

**Table 2** Synopsis of applied methods to synthesise CTF materials and their respective main features including the highest reported surface areas for each method.

Method	Monomer	Temp. ° C	Time h	ZnCl <sub>2</sub> eq.	S <sub>BET</sub> m <sup>2</sup> g <sup>-1</sup>	Reference
Ionothermal ampoule	1,4-dicyanobenzene	400/600	116	5	3300	[91]
Ionothermal micro-wave	1,4-dicyanobenzene	MW	1	7.5	2390	[95]
Brønsted acid	MTTB <sup>a</sup>	RT	over-night	-	1152	[96]
Pre-CTF in an open crucible	1,4-dicyanobenzene	40/400	12/40	0.8	910	[88]
Friedel-Crafts	tritycene	40	16	-	1660	[97]
Sonogashira-Hagihara	TBPT <sup>b</sup> + TEPA <sup>c</sup>	100	72	-	990	[99]
Yamamoto	TBPT <sup>b</sup>	105	over-night	-	2010	[98]
Amide trimerization	1,4-benzenedicarboxamide	400	n. s.	-	2030	[20]

**a** 4,4',4'',4'''-methanetetrayltetrabenzonitrile.

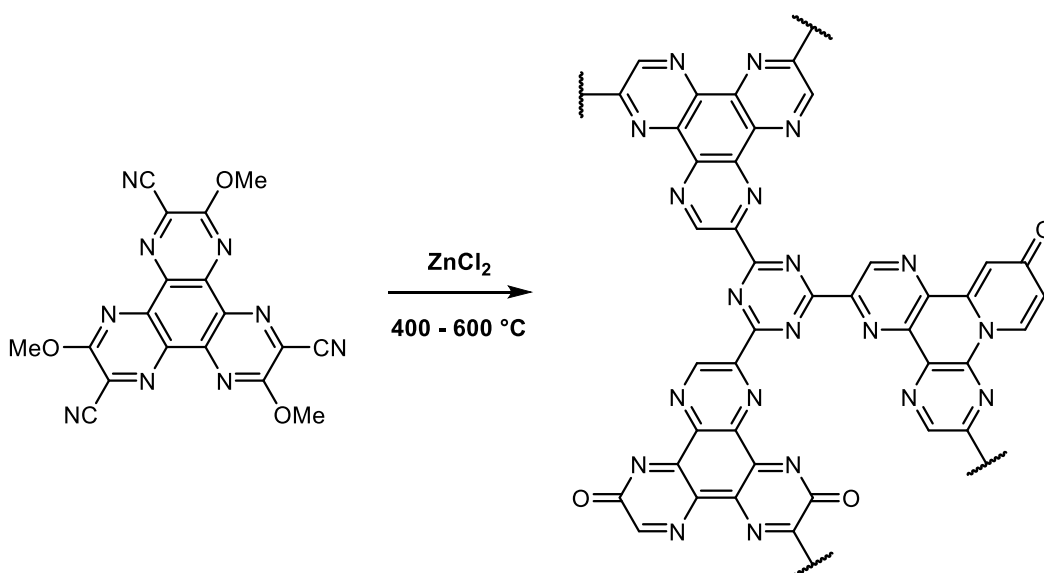
**b** 2,4,6-tris(4-bromophenyl)-1,3,5-triazine.

**c** tris(4-ethynylphenyl)amine.

## 2.6 Application of covalent triazine frameworks

As it has been outlined in the previous chapter, CTFs strongly benefit from a remarkable synthetic richness thus enabling the synthesis of tailored materials which can be finely tuned for different applications. The most obvious field of application for a porous material covers all areas where porosity plays a key role such as gas sorption or separation processes.<sup>90</sup> In course of the last decade, research targeted in particular the adsorption of hydrogen, carbon dioxide and methane. In times of the climate change, the question for efficient CO<sub>2</sub> capture and separation emerged to be a major issue and therefore plenty of publications are available at the time of writing.<sup>87,102,109–115</sup> It turned out that especially CTFs which exhibit pronounced ultramicroporosity in addition to the presence of polar surface groups as provided by heteroatom-rich CTFs (nitrogen, oxygen or sulfur) significantly improved the adsorption properties of CTFs.<sup>111</sup> Two promising CTFs were synthesised via a co-polymerisation of 1,4-dicyanobenzene with either fumaronitrile (CTF-FUM) or 1,4-dicyanonaphthalene (CTF-DCN) exhibiting ultramicropores of 5.2 and 5.4 Å, respectively.<sup>111</sup> In particular CTF-FUM has a high nitrogen content

(27.64 %), which allows for a CO<sub>2</sub> adsorption capacity of 78.2 cm<sup>3</sup> g<sup>-1</sup> (3.5 mmol g<sup>-1</sup>; at 273 K and 1 bar). Even superior CO<sub>2</sub> uptakes (273 K, 1 bar) were reported by the groups of Lotsch and Dai.<sup>110,112</sup> By synthesising CTFs treated at higher temperature (600 °C) thus triggering partial carbonisation, both groups pursued a similar approach to further increase adsorption capacities. In 2015, the group of Lotsch presented the synthesis of a bipyridine-based CTF that displayed a CO<sub>2</sub> capacity of 5.58 mmol g<sup>-1</sup> at 273 K (at 1 bar).<sup>112</sup> This value is even exceeded (6.3 mmol g<sup>-1</sup> at 273 K) by a hexaazatriphenylene-based CTF (HAT-CTF) that benefits from an *in situ* doping strategy to parallel incorporate N/O surface functionalities to enhance the CO<sub>2</sub> affinity (see Scheme 15).<sup>110</sup> At the time of writing, the CO<sub>2</sub> uptake capacity (at 273 K and 1 bar) of HAT-CTF is among the highest of all known NPOPs.<sup>116,117</sup>



**Scheme 15** Synthesis of HAT-CTF and incorporation of oxygen in the structure by *in situ* cleavage of methoxy-groups as proposed by Zhu *et al.*<sup>110</sup>

A fundamental aspect of current research in the area of CO<sub>2</sub> capture comprises also the capability of a porous adsorbent to selectively retain (adsorb) CO<sub>2</sub> in the presence of other gases, thus displaying a more realistic scenario. To this end, several concepts have been reported;<sup>87,111,118</sup> here solely two representative publications will be presented. The synthesis of a hydrophobic perfluorinated CTF was reported by Zhao *et al.*<sup>87</sup> By using tetrafluoroterephthalonitrile a fully fluorinated CTF (FCTF-1) was obtained that exhibited a significant amount of ultramicropores, which offered not only high gas adsorption potential but also kinetic selectivity for CO<sub>2</sub>/N<sub>2</sub> (CO<sub>2</sub>/N<sub>2</sub>: 77) separation. Moreover, due to the hydrophobicity of the material provided by fluorination, the CO<sub>2</sub> capture performance of FCTF-1 remained excellent in the pres-



ence of humidity in the gas mixture. High selectivity was also obtained by previously mentioned CTF-FUM (CO<sub>2</sub>/N<sub>2</sub>: 102) which is among the leading NPOPs regarding this application.<sup>111</sup>

CTFs were also discussed for the adsorption of organic compounds which might be beneficial due to enhanced porosity and favourable interactions provided by the porous adsorbent. Thus, CTFs were applied in a variety of adsorption problems including dyes,<sup>119,120</sup> aromatic compounds<sup>121</sup>, surfactants<sup>122</sup> as well as iodine adsorption.<sup>115</sup>

It is the stability of the triazine motif that causes the chemical and thermal stability of covalent triazine frameworks. Moreover, the opportunity to finely adjust the porosity properties and surface functionalities by choice of suitable monomers makes these materials attractive for heterogeneous catalytic applications. CTFs intrinsically contain basic functionalities which stem from pyridinic nitrogen atoms that already hold a lot of promise for catalytic applications. Thus, the pristine CTF material itself can already serve as a suitable metal-free catalyst as it has been presented by the group of Arne Thomas.<sup>85,123</sup> Owing to the high CO<sub>2</sub> affinity of CTF materials, cycloaddition of CO<sub>2</sub> to various epoxides was reported.<sup>85,123</sup> It is also possible to utilise CTFs as porous support material for metal nanoparticles that have been precipitated within the porous host. The embedding of finely dispersed nanoparticles with a homogeneous size distribution is beneficial for catalytic processes since embedding can prevent the nanoparticles from leaching or agglomerating. In 2010, Prati and co-workers were the first to apply CTF-1 as support for palladium nanoparticles via sol immobilisation and consequent reduction by means of hydrogen to form catalytically active palladium(0).<sup>124</sup> In the meantime, many examples using palladium have been published on this topic<sup>125,126</sup> but also non-noble metals have been described.<sup>127</sup> By using nano-sized cobalt supported in CTF the catalytic hydrolysis of ammonia borane (NH<sub>3</sub>BH<sub>3</sub>) was reported, which is considered as a promising hydrogen storage material since 3 mol hydrogen are generated by the hydrolysis of 1 mol NH<sub>3</sub>BH<sub>3</sub>.<sup>127</sup> In contrast to these very unspecific applications of CTFs as support material, a postsynthetic chemical modification of CTFs by coordinating molecular metal-complexes directly benefits from structural features of CTFs such as pyridinic coordination sites and can be regarded as rather specific.<sup>128</sup> A remarkable example for the aforementioned is the development of a heterogeneous Periana catalyst to convert methane to methanol based on a 2,6-dicyanopyridine CTF presented by Palkovits *et al.* in 2009.<sup>128</sup> Incorporation of 2,6-dicyanopyridine yielded bipyridylic coordination sites for platinum(II), resembling the molecular platinum bipyrimidine complexes by Periana *et al.*<sup>129</sup> Most

remarkably, the catalysis could be run at 200 °C in the presence of SO<sub>3</sub> in concentrated sulfuric acid, which once again demonstrates the distinguished stability of CTFs in contrast to other NPOPs. The group of Lotsch extended the previous work by introducing bipyridine moieties into CTFs and demonstrated the capability to coordinate various metals including copper, nickel, platinum and palladium.<sup>130</sup> The amount of coordinated metals was extensively studied with respect to the synthesis temperature and different metals providing profound insights into the correlation of structure and metal coordination. Later on, Bavykina *et al.* published on a mixed monomer CTF constructed from biphenyl- and pyridinecarbonitrile units.<sup>131</sup> Whereas the biphenyl moieties induce mesoporosity in order to enhance diffusion, the pyridinic units serve the coordination of an Ir<sup>III</sup>Cp\* complex to efficiently produce hydrogen from formic acid.<sup>132</sup>

Covalent triazine frameworks also offer the opportunity to shift the absorption spectrum of the materials into the visible region by careful variation of the synthetic conditions. This paves the way towards photocatalytic applications as shown in a great number of different metal-free CTF photocatalysts for the hydrogen evolution reaction.<sup>100,101,103,133–135</sup> Kuecken *et al.* demonstrated a combined Brønsted acid (CF<sub>3</sub>SO<sub>3</sub>H) and Lewis acid (ZnCl<sub>2</sub>) synthetic approach to finely tune the photocatalytic activity of CTF-1 by varying the reaction time.<sup>100</sup> To this end, the pre-CTF was converted into a photoactive material by treating the material in molten ZnCl<sub>2</sub> for different times between 2.5 – 30 min. After 10 min, the CTF material provided the highest hydrogen evolution rate within the set of samples, thus rendering this method a fast and facile route. A study of Cooper and co-workers compared the monomer length of CTFs with (multiple) phenylene units ranging from 1 – 4 with respect to their photocatalytic properties.<sup>134</sup> By linker length variation, the optical band gap could be finely adjusted in order to find the optimal spacer length towards a maximum hydrogen evolution rate (which was found to be two phenylene units).

Using both noble and non-noble metal modified CTFs, many efforts have been devoted to illustrate the electrocatalytic activity towards oxygen reduction reaction,<sup>136,137</sup> hydrogen oxidation,<sup>138</sup> and alcohol oxidation.<sup>139</sup> Also the contemporary quest of electrochemical energy storage has been a focus of current research in the field of CTFs. In this regard, it is advisory to mention supercapacitors and batteries which could be considered quite complimentary.<sup>140</sup> A publication of Zhu *et al.* presented the synthesis of graphene-coupled 2D CTF sandwich

materials comprising high specific surface area (up to  $1584 \text{ m}^2 \text{ g}^{-1}$ ) exhibiting specific capacities as high as  $340 \text{ F g}^{-1}$ .<sup>141</sup> Tetracyanoquinodimethane-derived conductive CTFs synthesised in a temperature range from  $400 \text{ }^\circ\text{C}$  –  $900 \text{ }^\circ\text{C}$  delivered a specific capacitance of even  $380 \text{ F g}^{-1}$  (at  $800 \text{ }^\circ\text{C}$ ) although one should be aware that these high temperatures yield carbon materials rather than CTFs.<sup>142</sup> CTF-1 synthesised in molten sulfur instead of  $\text{ZnCl}_2$  gave a material with high amounts of embedded sulfur (62 w%) and has been applied as cathode material in a lithium sulfur battery.<sup>143</sup> This strategy has been refined by the same group and nucleophilic aromatic substitution has been employed to introduce sulfur (up to 86 w%) in CTF-1 by replacing the fluorine atoms of fluorinated 1,4-dicyanobenzene against sulfur.<sup>144</sup> Basically the same approach was in parallel published by the group of Xu *et al.*<sup>145</sup> According to their investigations, the application of fluorinated linkers causes both an exchange of fluorine atoms against sulfur but also a confinement of sulfur within the pores thus providing materials with superior electrochemical performance in contrast to non-fluorinated samples.

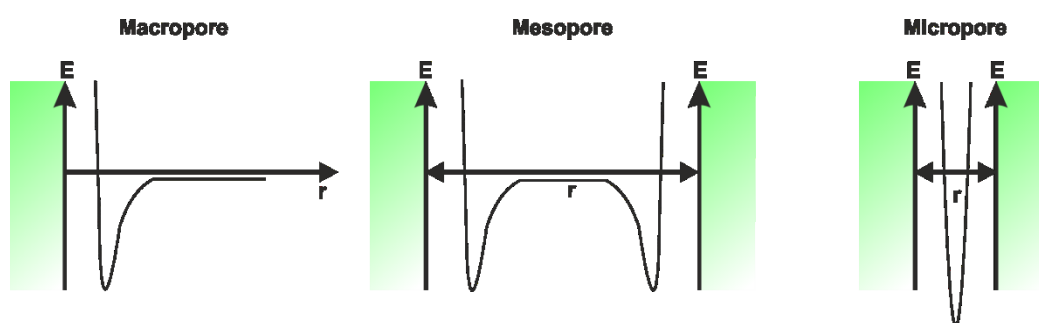
## 3 Characterisation techniques

### 3.1 Physisorption

The development of nanoporous materials providing pores in the micro- and mesopore range (thus up to 50 nm) entails their structural characterisation. In this field, in particular physisorption is the most frequently used technique to investigate surface and textural properties of such materials since it is a non-destructive and reversible method.<sup>146</sup> Gas adsorption occurs whenever an adsorbable gas (the adsorptive) is enriched in the vicinity of a solid surface (the adsorbent). If the adsorptive is adsorbed and thus an increase of its density due to adsorption has occurred, the adsorbed phase is described as adsorbate.<sup>4</sup> According to the intermolecular forces between adsorbate and adsorbent, adsorption can be physical (physisorption) or chemical (chemisorption). Physisorption describes the process of adsorption as a result of physical (non-covalent) interactions like *Van-der-Waals* and intermolecular repulsion forces but also specific molecular interactions (e.g., polarisation, field-dipole, field gradient-quadrupole) contribute. In contrast, chemisorption is dominated by the formation of chemical (covalent) bonds between adsorbate and adsorbent. Exemplarily, the adsorption of hydrogen on palladium surfaces leads to covalently bound dissociated hydrogen atoms. The responsible forces for chemisorption are much stronger, thus the energy required for chemisorption ( $> 40 \text{ kJ mol}^{-1}$ ) is higher as for physisorption ( $< 40 \text{ kJ mol}^{-1}$ ). Physisorption is mainly governed by the interplay between the strength of fluid-wall and fluid-fluid interactions as well as the effects of confined pore space on the state and thermodynamic stability of fluids in narrow pores.<sup>146</sup> Pores are present whenever a (porous) solid has cavities which are deeper than wide.<sup>3</sup> If considered with respect to their morphology, pores can be differentiated into closed (not accessible) and open pores (accessible). Open pores can be blind pores (with a dead-end), interconnected or permeate throughout the entire porous solid (through pore). If differentiated according to the pore size, there are micropores of widths less than 2 nm, mesopores of widths between 2 and 50 nm and macropores of widths greater than 50 nm.<sup>4</sup> Many porous solids comprise pores of varying sizes in different pore size regimes (e.g. combinations of micro- and mesoporosity) and are denoted to as materials with hierarchical pore systems. It is advisory to notion that the sole presence of different pore types

in a material is not enough to qualify it as a hierarchical. Moreover, different pores necessarily have to display synergistic interactions thus influencing the adsorption properties.

The most conventional technique for the characterisation of porous solids is manometric nitrogen ( $N_2$ ) physisorption performed at 77 K, which is the boiling point of nitrogen (1.013 bar). Briefly, a carefully degassed sample is set under vacuum and cooled to 77 K. A known amount of gas is dosed to the sample, which is confined in the measuring cell (with a known volume). If adsorption occurs within the pores of the sample, the pressure will fall until equilibrium conditions are established and the pressure remains constant. The amount of adsorbed gas at equilibrium pressure can be calculated from the expected and the real pressure drop in the cell by application of the respective gas laws. An adsorption isotherm is obtained if the adsorbed volume of  $N_2$  is plotted against the relative pressure  $p/p_0$ . Conventionally, the adsorbed volume is given at 273 K and 1.013 bar which are defined as standard temperature and pressure (STP). At an adsorption temperature below the critical point of the respective adsorptive,  $p$  is the equilibrium pressure and  $p_0$  the saturation vapour pressure at the adsorption temperature (e.g. for  $N_2$ ,  $p_0$  at 77 K is 1.013 bar). The phenomenon of adsorption strongly depends on the pore size of the porous solid that significantly influences the adsorption process. To illustrate the processes during adsorption, the Lennard-Jones potential (LJP) is suitable since it enables a description of the free energy of a gas molecule in dependence of its distance to the pore wall (see Scheme 16).<sup>147</sup>

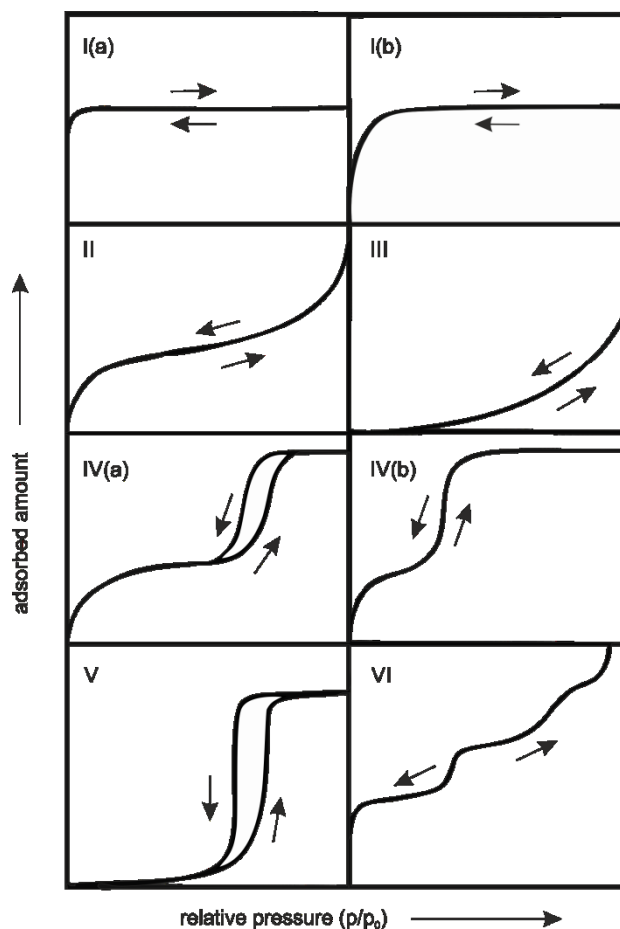


**Scheme 16** Schematic representation of Lennard-Jones potentials in different pore types.

For non- or macroporous materials a typical shape can be assumed that represents the interplay of attractive and repulsive forces to give a minimum for a certain distance between the wall and the gas molecule. In consequence, adsorption of gas molecules occurs on the pore wall by the formation of a monolayer and subsequently multilayers. Monolayer formation is governed by fluid–solid interactions, whereas multilayer formation is dominated by fluid–fluid interactions.

For mesopores, fluid–solid interactions dominate first, but multilayer formation (fluid–fluid interaction) takes place as well. In course of the multilayer formation (thus an increasing layer thickness), surface tension/curvature becomes more pronounced. Since the volume of the mesopore is finite, multilayers of opposite pore walls are approximating. The multilayer cannot be stabilised and a gas–liquid phase transition occurs, which leads to the formation of a concave meniscus. Thus, the gas condenses at lower pressures than the actual saturation pressure  $p_0$  which is caused by attractive fluid–wall interactions. The relative pressure  $p/p_0$  where capillary condensation occurs depends on the pore size and can be described by the Kelvin equation but is only valid for uniform pore sizes (or radii) and shapes. In micropores, the situation is significantly different. Here, the pore walls lie close together, thus an overlapping of the LJPs for the opposite pore walls results, which causes an enhanced adsorption potential and the exclusive domination of fluid–solid interactions. In consequence, pores are filled continuously at low relative pressures. Since a multilayer formation is hindered in micropores, after complete pore filling, no further adsorption takes place, which is displayed in a plateau of the adsorbed volume in the adsorption isotherm. The previous explications illustrate that adsorption isotherms may look totally different with respect to the pore size of the investigated porous solid. Therefore, IUPAC has defined typical isotherm shapes which represent most of the existing characteristics for different porous materials. In 2015, the latest IUPAC recommendation was reported which groups isotherms into six types (see Scheme 17).<sup>4</sup> Since the IUPAC recommendation are widely known and accepted, within the thesis at hand, exclusively those isotherm shapes will be discussed, which will occur in the results and discussion part. Type I isotherms are measured for microporous solids with small external surfaces. According to the described adsorption mechanism for micropores, a steep increase due to micropore filling leads into a plateau at very low relative pressures. It can be distinguished between Type I(a) and Type I(b). For Type I(a), very small and narrow micropores (width < 1 nm) are assumed, thus shifting the uptake to very low relative pressures. In contrast, Type I(b) displays an isotherm for solids comprising larger micropores or narrow mesopores (width < 2.5 nm), resulting in a less steep uptake due to pore filling at different relative pressures of pores in different size regimes. Type IV isotherms occur for mesoporous adsorbents. As it has been illustrated, adsorption in mesopores is governed by fluid–solid interaction and secondly by fluid–fluid interactions that lead to condensation in the

pore. In consequence, after an increase due to mesopore filling, a plateau is reached which is induced by a complete pore filling.



**Scheme 17** Classification of physisorption isotherms according to IUPAC (adapted from reference [4]).

So far, desorption has been totally neglected here. After adsorption, desorption is the reverse process, in which the adsorbate is removed and thus its amount progressively decreases. For Type IV(a) isotherms, adsorption and desorption branch do not coincide, this effect is called hysteresis. Hysteresis is a result of a delayed vapour–liquid phase transition, thus an adsorption that is not in thermodynamic equilibrium. In consequence, delayed condensation is a result of metastability of the adsorbed multilayer and nucleation of liquid bridges. In contrast, desorption processes are in the equilibrium state since evaporation does not include nucleation (as required for condensation), thus representing a reversible liquid–vapour transition. Therefore, the desorption branch is sometimes more appropriate to investigate pore characteristics (pore size), since desorption reflects equilibrium states and thus relative pressures which are closer related to the actual pore size (at least for mesopores displaying hysteresis). Type IV(b) is valid for smaller mesopores (for nitrogen at 77 K: pores < 4 nm) which show no capillary condensa-

tion and thus reversible isotherms. Also the shapes of hysteresis loops have been classified into six types by IUPAC. They differ in their origin which can be related to different (not uniform) pore sizes or effects like pore blocking or cavitation. Pore blocking occurs, if pores have smaller pore windows (or entrances) than their actual width is. The relative pressure at which the pore is emptied is thus determined by the smaller pore window (or neck) and evaporation of the condensate in the mesopores may be hindered until the respective relative pressure is low enough to empty the pore neck. Cavitation occurs, if the pore size of a neck is smaller than a critical (temperature depending) size. In that case, emptying of the pore occurs via a spontaneous nucleation of the metastable fluid to give a gas bubble. The behaviour of the condensed metastable fluid within the mesopore is governed by thermo-physical properties and not by the pore size itself. Thus, for each adsorptive and temperature a minimum relative pressure exist that constitutes the lowest relative pressure where hysteresis can occur (for  $N_2$  at 77 K:  $p/p_0 : 0.42$ ).

Since physisorption methods are most commonly used to determine the surface area and the porosity of solid materials, it is necessary to address the actual surface that is accessible by gas phase adsorption. One of the earliest theories proposed by Gibbs describes adsorption as a process that occurs on a two-dimensional surface. The difference between the total amount introduced ( $n$ ) and the remaining amount of adsorptive in the gas phase ( $n^g$ ) is assumed to be the surface excess amount ( $n^e$ ). For low pressure adsorption (up to 1 bar), the amount of adsorbed gas ( $n^a$ ) can be assumed to be identical to the surface excess amount ( $n^e$ ). In contrast, at high pressures there might be a significant difference between the surface excess amount and the total amount of adsorbed gas. Another theory was proposed by Langmuir in 1916.<sup>148</sup> The theory assumes the presence of a defined number of identical and independent adsorption sites for the adsorptive molecules. It further assumes the exclusive formation of monolayers and is thus not suitable for mesoporous materials since multilayer adsorption plays a crucial role in such pores. In consequence, the Langmuir theory would lead to a significant overestimation of the probe accessible surface. A theory that more accurately represents a realistic scenario is the Brunauer-Emmett-Teller (BET) equation presented in 1938.<sup>149</sup> The BET theory assumes the formation of multilayers on existing monolayers with increasing pressure. Each molecule in an adsorbate layer can be an adsorption site for the next layer. Moreover, the BET theory considers an infinite number of adsorption layers and the distinction between the adsorption energy of the first



layer and the following (all layers except for the first have an equal adsorption energy). From these very basic assumptions, the BET equation was derived (see Eq. 1):

$$\frac{p/p_0}{n(1-p/p_0)} = \frac{1}{n_m C} + \frac{C-1}{n_m C} (p/p_0) \quad (\text{Equation 1})$$

$n$  = specific amount adsorbed at relative pressure;  $n_m$  = specific monolayer capacity;  $C$  = adsorption constant.

If  $\frac{p/p_0}{n(1-p/p_0)}$  is plotted against  $p/p_0$  (denoted to as BET plot) the monolayer capacity ( $n_m$ ) can be determined by extrapolation. If done so, the intersection with the y-axis gives  $\frac{1}{n_m C}$  and  $n_m$  can be calculated. It is of utmost importance to calculate the monolayer capacity in the linear range of the BET plot which is always restricted to a limited part of the isotherm, most commonly in a  $p/p_0$  range of 0.05 – 0.3 for materials with unrestricted multilayer formation (Type II and Type IV(a) isotherms). It becomes apparent that the BET theory is in principal not very well suited to describe microporous materials where no multilayer formation occurs. For microporous materials, the linear range of the BET plot will be shifted to lower relative pressures. To address these issues, Rouquerol *et al.* proposed a protocol comprising three criteria that enables a consistent (and most importantly, comparable) determination of BET surface areas for microporous solids.<sup>150</sup> According to this, the intercept on the ordinate in the BET plot should be positive, thus indicating also a positive  $C$  value.  $C$  is called adsorption constant and is exponentially related to the energy of monolayer adsorption. Very schematically, for high  $C$  values ( $> 80$ ), a clear distinction between completion of monolayer adsorption and consecutive multilayer formation can be assumed. In contrast, for low  $C$  values ( $< 50$ ) a significant amount of overlap of monolayer coverage and the onset of multilayer adsorption is assumed. Second, the BET equation should be restricted to the range where  $n(1-p/p_0)$  continuously increases with  $p/p_0$ . Third,  $p/p_0$  corresponding to  $n_m$  should be within the selected BET range. It is important to notice that these criteria do not lead to a full validity of the BET theory for microporous materials. Nevertheless, application of the three criteria yields a specific surface area (or apparent surface area) that may not be considered as a realistic probe accessible area. If those three criteria have been taken into account and a suitable  $n_m$  is calculated, the specific (mass-related) surface area is given by (see Eq. 2):

$$S_{\text{BET}} = \frac{n_m \cdot N_A \cdot \sigma_{\text{N}_2}}{m} \quad (\text{Equation 2})$$

$N_A$  = Avogadro constant;  $\sigma_{\text{N}_2}$  = cross-sectional area of one nitrogen molecule in a close-packed monolayer;  $m$  = mass of the adsorbent.

In addition to the specific surface area, the pore size distribution is also of peculiar interest. Lately, in particular the density functional theory (DFT) and Monte Carlo simulations became widely accepted methods to provide a reliable picture of real pore size distributions.<sup>151,152</sup> These approaches, based on statistical mechanics, describe the distribution of adsorbed molecules in pores on a molecular level thus representing the behaviour of confined fluids. In simple terms, DFT methods allow for the calculation of a series of theoretical isotherms for pores of different widths and a given pore shape. For each pore width of a given adsorptive/adsorbent pair, a theoretical isotherm  $N(p/p_0, W)$  is calculated. After having measured a real isotherm  $N(p/p_0)$ , a numerical algorithm fits the individual theoretical isotherms to the measured isotherm. The calculated pore size distribution is a result of the respective weighting of each individual isotherm which is given by the pore size distribution function  $f(W)$  that is a solution of the general adsorption isotherm (GAI) equation (see Eq. 3):

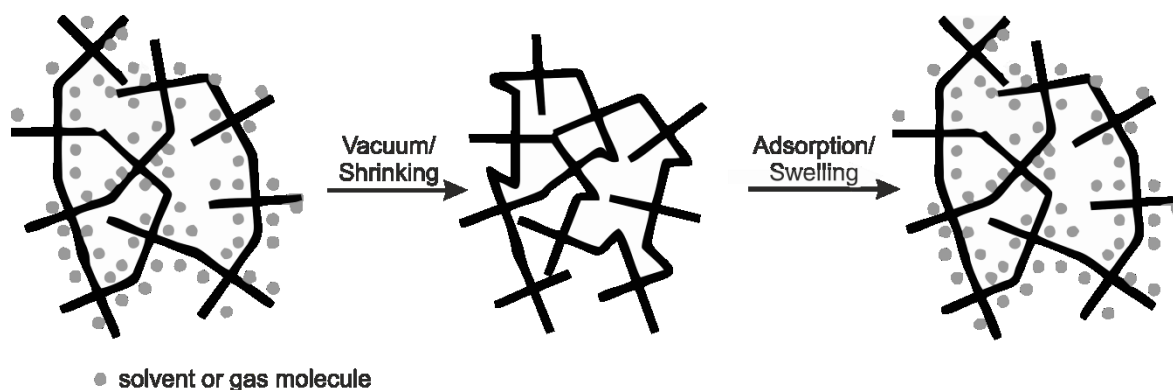
$$N(p/p_0) = \int_{W_{\text{min}}}^{W_{\text{max}}} N(p/p_0, W) f(W) dW \quad (\text{Equation 3})$$

Prior to a physisorption experiment, a careful choice of the respective adsorptive is necessary since each individual adsorptive provides different specifics. Nitrogen adsorption at 77 K is the most frequently used adsorptive but in particular for the analysis of micropores nitrogen is not fully satisfactory.<sup>4</sup> This can be ascribed to the quadrupole moment of nitrogen that causes enhanced interactions with especially polar surface functionalities or adsorbed ions. Thus, the orientation of the nitrogen molecule on the adsorbent surface will be strongly affected. In consequence, misleading amounts of adsorbed gas may be determined. As another consequence of those previously mentioned quadrupole interactions, the relative pressures where micropore filling occurs will be dramatically changed and will be shifted towards very low relative pressures ( $\approx 10^{-7}$ ). At these low pressures, the thermodynamics (extremely low diffusion rates) as well as the instrumentation (the measurement of equilibrated isotherms will be complicated) will reach their limits. To circumvent these issues, argon physisorption conducted at the cryogenic temperature of 87 K has been discussed. Argon does not exhibit specific surface interactions and is a monatomic gas. Hence, argon physisorption features some benefits. Due to the slightly

increased adsorption temperature, argon at 87 K fills micropores at higher relative pressures as compared to nitrogen at 77 K. Also the diffusion and in consequence, equilibrium times are fastened at 87 K. In summary, argon physisorption provides a more exact picture of the adsorbed amount of adsorptive (just one orientation is possible) and reduced electrostatic interactions with the adsorbent allow for a more correct correlation between pore filling pressure and pore width. In particular for materials comprising narrow micropores (ultramicropores) of pore widths smaller than 0.7 nm, nitrogen as well as argon physisorption turned out to be not fully satisfactory due to restricted diffusion at low temperatures. In contrast, CO<sub>2</sub> adsorption can overcome these limitations, since the experiments are conducted at significantly higher adsorption temperatures. CO<sub>2</sub> also has the drawback of a quadrupole moment but has a very high saturation pressure (ca. 35 bar) at for instance 273 K, which is a conventionally used. In consequence, the relative pressures required for micropore size analysis are easier accessible by the instrumentation (up to 1 bar). Nevertheless, by measuring up to a maximum pressure of 1 bar only 3 % of the full isotherm ( $p/p_0 = 0.03$ ) can be measured and hence only pores of < 1 nm can be accessed. For ultramicroporous carbons, CO<sub>2</sub> adsorption might be the right choice.

#### **Adsorption on nanoporous organic polymers.**

The application of physisorption methods for nanoporous organic polymers to determine characteristics such as the specific surface area or the pore size distribution is challenging and features some difficulties. NPOPs are sometimes rather soft and flexible than rigid or stiff materials.<sup>6</sup> Thus, even degassing prior to the adsorption may change the porous polymer since it can significantly shrink upon thermal treatment, which can be classified as a collapsed structure. Moreover, in the course of the adsorption process, the polymer will change its pore morphology due to adsorption induced swelling processes (Scheme 18).



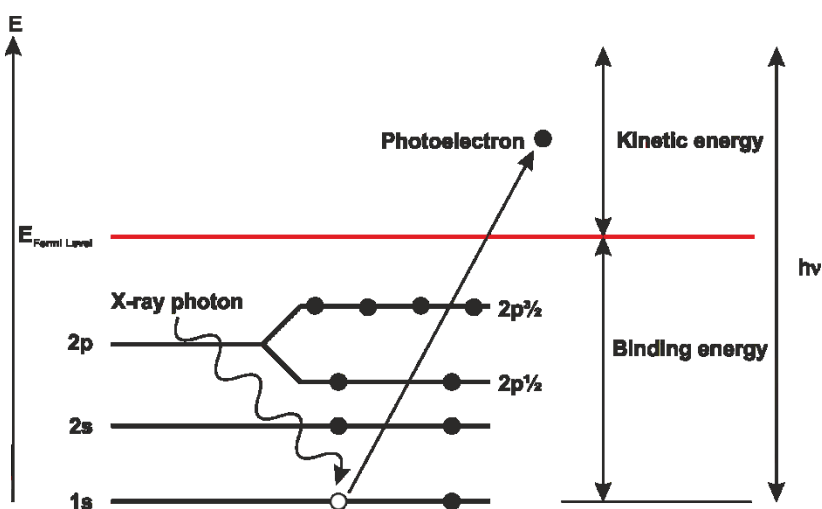
**Scheme 18** Schematic representation of the processes occurring while degassing a flexible nanoporous organic polymer and the change of pore morphology upon adsorption (adapted with slight modification from [153]).

This can be ascribed to the adsorbate which can be regarded as a confined fluid.<sup>153</sup> The fluid-like adsorbate enables a swelling of the flexible network structures, thus changing the pore environment continuously while adsorbing. In addition, a steady increase of the uptake of the adsorptive (say nitrogen) in the whole pressure range is observed, which is a result of the growing pore volume caused by the flexibility of the polymer. Not only adsorption is affected, also desorption features some special characteristics. Very often, a broad hysteresis is observed whose interpretation is often misleading and assigned to mesoporosity. Instead, these observations are in fact a result of the irreversible swelling induced by adsorption.<sup>154</sup> The inverse behaviour (shrinking) cannot be triggered by desorption, thus resulting in a very broad hysteresis. In summary, physisorption methods still represent a valuable tool for the determination of porosity within porous polymers, but the derived results may be regarded with absolute care. In particular calculations to determine the specific surface area (BET model) and/or pore size distributions should be applied by taking limitations into account, since the respective calculations for the BET equation or a DFT kernel do not consider swelling and/or shrinking. To circumvent those limitations, also a comparison of primary data may be suitable to evaluate different materials. Nevertheless, if measured similarly, specific surface areas may be suitable to compare different porous and flexible polymers.

### 3.2 X-ray photoelectron spectroscopy

X-ray photoelectron spectroscopy (XPS) or electron spectroscopy for chemical analysis (ESCA) is a surface analysis technique that measures electrons to gain structural information as it is also prominently known for Auger electron spectroscopy or high-resolution electron energy loss spectroscopy.<sup>155</sup>

XPS is an analytical technique that is based on the photoelectric effect discovered by Albert Einstein in 1905. By applying the concept of the quantisation of energy – introduced by Max Planck in 1900 – Einstein explained that photons of light directly transfer their energy to electrons within an atom, resulting in the emission of electrons without energy loss. For these fundamental discoveries Planck as well as Einstein received the Nobel Prize in physics in 1918 and 1921, respectively. The basic XPS experiment is using an X-ray source to generate photons which are used to irradiate the surface of a sample that is placed in a vacuum environment (see Scheme 19). The resulting photoelectrons escape into the vacuum chamber. According to their energy, the electrons are separated and counted to gain chemical information about the sample.



**Scheme 19** The basic principle of an XPS experiment: An irradiated surface emits electrons via the photoelectric effect (according to reference [155]). Other relevant quantities present in a real setup such as the work function are omitted in this scheme.

The photoelectric effect which is the basis of X-ray photoelectron spectroscopy is a specific case that can be considered as just one case that is possible upon irradiation of a sample. Thus, the photon can either (1) pass the sample with no interaction or (2) can be scattered leading to a partial energy loss or (3) can transfer its energy completely to an atomic orbital electron which

exactly describes the photoemission of electrons. Also this third case depends on particular prerequisites. A certain energy (thus a frequency that is high enough) is required to induce photoemission. After reaching an element specific threshold (in terms of energy) photoemission can be observed. Once this energy threshold is exceeded, the number of emitted electrons will be proportional to the intensity of the illumination. Thus, the more photons are present, the more electrons will be emitted. The kinetic energy of the electrons is linearly proportional to the frequency of the exciting photons. Once the photons have a higher energy than necessary to reach the threshold of photoemission, the excess photon energy will be transferred to the emitted electrons. The process of photoemission is extremely fast ( $10^{-16}$  s). Basically, the ongoing process can be described by the Einstein equation (see Eq. 4).

$$E_B = h\nu - E_{\text{kin}} \quad (\text{Equation 4})$$

The binding energy of the electron in the atom is described by  $E_B$ , whereas  $h\nu$  is the energy of the X-ray source (a known value) and  $E_{\text{kin}}$  is the kinetic energy of the emitted electron. From  $E_{\text{kin}}$  (detected) and  $h\nu$  (known), the interesting quantity of  $E_B$  can be easily calculated.  $E_B$  is usually in the range of electron volts ( $1 \text{ eV} = 1.6 \times 10^{-19} \text{ J}$ ). The value of  $E_B$  is strongly affected by the environment of the electron. It varies with the type of the atom but also the distance to the nucleus or the presence of other atoms in the surrounding will alter the electronic environment. While weak interactions between atoms like hydrogen bonding will not effectively influence the electron distribution, variations of the binding energy will be caused by covalent or ionic bonds between atoms. As mentioned,  $E_B$  is the most interesting quantity that is used to characterise solid materials as performed within the thesis at hand. Briefly,  $E_B$  can be considered as the energy difference of the electrons in the final state  $E_f(n-1)$  (thus after photoemission) and before  $E_i(n)$  (see Eq. 5).

$$E_B = E_f(n-1) - E_i(n) \quad (\text{Equation 5})$$

If no rearrangement of other electrons in the surrounding occurs, then the observed  $E_B$  can be seen as the negative orbital energy  $-\varepsilon_k$  for the emitted electrons. This correlation is also known as Koopman's theorem (see Eq. 6).

$$E_B \approx -\varepsilon_k \quad (\text{Equation 6})$$

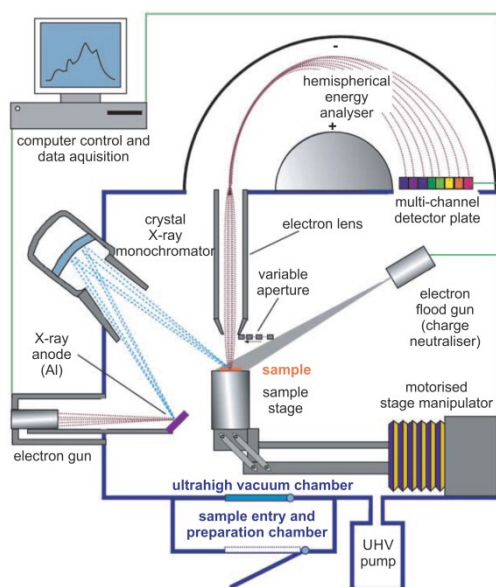
This theorem can be considered as a first approximation of the  $E_B$  value but is not totally sufficient since it does not take into account other contributions that influence  $E_B$ . Exemplarily, rear-

relaxation processes after emission may occur which are commonly denoted as relaxation energy.

Especially in the case of insoluble and coloured (or black) solids like in the case of covalent triazine frameworks XPS turned out to be a powerful characterisation tool since it allows for the discrimination of different chemical environments. The physical basis that enables the analysis of different electron environments can be ascribed to initial state effects (as expressed in  $E_i(n)$ ) and final state effects (as expressed in  $E_f(n-1)$ ) that both contribute to  $E_B$  (see Eq. 5). The initial state  $E_i(n)$ , thus the ground state prior to the photoemission, will be affected by changes of the chemical environment, for instance by the generation of new bonds as it can occur for oxidation reactions or others. Thus, an energy difference  $\Delta E_B$  results between electrons in an unmodified atom ( $\text{Atom}^0$ ) and the same electrons of the respective atom that has undergone an oxidation ( $\text{Atom}^{X+}$ ). In simplified terms, this effect can be illustrated by considering carbon atoms with an increasing number of bound oxygen atoms:  $\text{C-C} < \text{C-O} < \text{C=O} < \text{O-C=O} < \text{O-(C=O)-O}$ . Since oxygen is more electronegative than carbon, the carbon becomes more positively charged, which affects the interaction of the electrons with the nuclei and results in an increase of  $E_B$  for C 1s. However, the shift of  $E_B$  cannot be exclusively ascribed to initial state effects. Also relaxation effects will have an impact on the measured  $E_B$ . Nonetheless, these approximations provide a good picture and emphasise the impact of the chemical environment of the atom and its influence on the respective chemical shift of  $E_B$ . If an atom becomes more positively charged, for instance upon the formation of a chemical bond or in a different chemical surrounding,  $E_B$  will increase. For CTF materials, especially the broad range of N 1s and C 1s binding energies is valuable, since it gives access to structural information that cannot be obtained by other methods. As explained earlier, the chemical environment strongly influences  $E_B$ . Thus, it becomes apparent that a discrimination between pyridinic, pyrrolic or quaternary nitrogen atoms is possible, since the electronic environment is different in all these bonding motifs. The latter is also valid for C 1s and hence, it is possible to distinguish between  $sp^2$  or  $sp^3$  carbons as well as different oxidation states. Thus, XPS is an information-rich and non-destructive technique that allows for detection of almost every element (except for H and He) at very low concentrations. Furthermore, it can be used as an additional tool to determine the elemental composition. However, it is crucial to mention that XPS is only a surface technique with a maximum penetration depth of 10 nm.

### Instrumentation

An XPS apparatus requires complex instrumentation but very simplified the main components are the vacuum system, X-ray source, electron energy analyser and the data system (see Scheme 20).



**Scheme 20** Schematic representation of an XPS spectrometer (adapted from reference [155]).

As it was mentioned earlier in this chapter, the heart of an XPS instrument is the vacuum chamber where the sample is irradiated. Ultrahigh vacuum (ca.  $10^{-9}$  –  $10^{-10}$  bar) is a necessary prerequisite of an XPS experiment since the emitted photoelectrons have to reach the analyser and the detector without colliding with gas phase molecules. Also the X-ray source requires vacuum conditions to work in the operation mode. Most importantly, any molecules in the analysis chamber could influence the surface and thus the chemical information gained by the XPS experiment. Thus, a sample has to be introduced into the vacuum chamber prior to the measurement. Once the sample is evacuated, it can be irradiated by the X-ray source. Conventionally, an Al X-ray source is applied and a monochromator is used to receive monochromatic  $K\alpha$  radiation with an energy of 1486.6 eV. Recently, synchrotron radiation has been established as an alternative source of X-rays. The benefits of this are the monochromatic irradiation in a continuous energy range, which provides a higher intensity and thus allows for shorter data acquisition times and improved resolutions.<sup>155</sup> Upon irradiation, photoelectrons will be generated and collected by means of a lens system. They will be directed towards the energy analyser which is an electrostatic hemispherical analyser in most cases. This part is of utmost importance since it



determines the pass energy of the emitted electrons. The system consists of two concentric hemispheres with different radii which are positively charged at the inner hemisphere and negatively charged at the outer hemisphere. As a consequence of this setup, a constant pass energy of the electrons can be adjusted that maintains a constant absolute resolution for all measured spectra. Typically, the pass energy is in the range of 100 – 200 eV for survey XPS spectra and 5 – 25 eV for high resolution XPS spectra, respectively. Once the electrons have left the energy analyser, they are counted and sorted by their respective energy, which is most commonly realised by a multichannel array.

### Data processing

Once a spectrum is recorded, it is crucial to perform a consistent peak fitting which is necessary to extract reliable information out of the raw data. Therefore, the area and the respective binding energy for each contribution have to be determined. In order to achieve a reliable interpretation it is important to be aware of potential bonding motifs which can be present within the sample. A careful interpretation/peak fitting requires several conventions that have to be regarded. The first step of data processing is charge referencing.<sup>155</sup> For insulating materials, the measured  $E_B$  are usually shifted to higher energies than the correct values. This is due to reduced number of electrons as a result of a loss of photo-emitted electrons (positive shift). In consequence, the kinetic energy of the emitted electrons decreases and higher binding energies are observed. To avoid this effect, a low energy electron source is applied in order to compensate the electron shortage. If the charge is overcompensated, observed binding energies will shift to lower values. In order to obtain correct values, a referencing is conventionally performed by setting the value of C 1s (C 1s or adventitious carbon is present as impurity on almost every surface) to a fixed  $E_B$  (usually between 284.5 and 285.5 eV). Subsequently, the whole spectrum is corrected by subtracting or adding the respective difference of the measured C 1s  $E_B$  and the fixed  $E_B$ . After referencing, the measured peaks can be further interpreted. Therefore, the full width at half maximum (FWHM) is typically kept constant for each contribution. Related to the FWHM is the peak width which is determined by the lifetime of the core hole that is created upon photoemission of electrons, the instrumental resolution and satellite features. Heisenberg's uncertainty relationship is suitable to calculate the peak width  $\Gamma$  dependant on the core hole lifetime  $\tau$  (see Eq. 7).

$$\Gamma = \hbar/\tau \quad (\text{Equation 7})$$

Typically, the core hole lifetime is shorter for inner shell orbitals since they can be reoccupied by electrons from outer shells. It becomes apparent that the latter causes larger peak widths for inner shell orbitals. The line shape due to the core hole lifetime is Lorentzian. In contrast, broadening of the photoemission peak can be ascribed to contributions of instrumental effects as for instance the energy spread of the X-rays or the resolution of the analyser. It is assumed that effects contribute with a Gaussian line shape. Thus, a careful choice of the respective line shape is necessary. Moreover, it is important to consider the peak shape (as mentioned Gaussian, Lorentzian, asymmetric or a mixture thereof), peak position, peak height and peak width, which are often correlated to each other. Also the right procedure to define the background is relevant. Commonly used methods subtract either a linear background or make use of a method proposed by Shirley.<sup>156,157</sup> Briefly Shirley's method implies that the background increases with an increasing signal intensity due to inelastic scattering of the electrons. In addition, elastic scattering is neglected within this method. After having considered all of these preconditions, a least-square fitting routine is performed to iterate the final values.

## 4 Experimental part

### 4.1 Applied chemicals and gases

**Table 3** List of applied chemicals.

compound	formula	purity	supplier
1,3,5-triphenylbenzene <sup>c</sup>	(C <sub>6</sub> H <sub>5</sub> ) <sub>3</sub> C <sub>6</sub> H <sub>3</sub>	99 %	Alfa Aesar
1,4-dicyanobenzene <sup>c</sup>	C <sub>8</sub> H <sub>4</sub> N <sub>2</sub>	98 %	Sigma Aldrich
1,8-diazabicyclo[5.4.0]undec-7-ene <sup>a</sup>	C <sub>9</sub> H <sub>16</sub> N <sub>2</sub>	98 %	Sigma Aldrich
2,2,2-trifluoroacetophenone <sup>a</sup>	CF <sub>3</sub> COC <sub>6</sub> H <sub>5</sub>	99 %	Sigma Aldrich
4,4'-dicyano-1,1'-biphenyl <sup>c</sup>	C <sub>14</sub> H <sub>8</sub> N <sub>2</sub>	98 %	ABCR
4-bromo-2,6-dimethylaniline <sup>c</sup>	C <sub>8</sub> H <sub>10</sub> BrN	98 %	ABCR
aluminium chloride, anhydrous <sup>a</sup>	AlCl <sub>3</sub>	99 %	Acros
anthracene <sup>c</sup>	C <sub>14</sub> H <sub>10</sub>	97 %	Alfa Aesar
aqueous ammonia (25 w% in H <sub>2</sub> O)	NH <sub>4</sub> OH	p. a.	HONEYWELL
barium sulfate	BaSO <sub>4</sub>	99 %	Grüssing
benzene, anhydrous <sup>a</sup>	C <sub>6</sub> H <sub>6</sub>	99.8 %	Sigma Aldrich
carbazole <sup>b,c</sup>	C <sub>12</sub> H <sub>9</sub> N	>95 %	Sigma Aldrich
copper(I)-iodide <sup>c</sup>	CuI	>99.5 %	Sigma Aldrich
cyanuric chloride <sup>c</sup>	C <sub>3</sub> Cl <sub>3</sub> N <sub>3</sub>	99 %	Sigma Aldrich
glyoxal (40 w% in H <sub>2</sub> O)	C <sub>2</sub> H <sub>2</sub> O <sub>2</sub>	n. s.	Grüssing
hydrochloric acid (37 w% in H <sub>2</sub> O)	HCl <sub>(aq)</sub>	p. a.	VWR Chemicals
hydrogen peroxide (30 w% in H <sub>2</sub> O)	H <sub>2</sub> O <sub>2</sub>	n. s.	Fisher scientific
lithium chloride, anhydrous	LiCl	99 %	chemPUR
magnesium sulfate	MgSO <sub>4</sub>	99 %	Grüssing
mesitylene	C <sub>9</sub> H <sub>12</sub>	>98 %	Merck
<i>N,N'</i> -dimethylethane-1,2-diamine <sup>a</sup>	C <sub>4</sub> H <sub>12</sub> N <sub>2</sub>	99 %	Sigma Aldrich
naphthalene <sup>c</sup>	C <sub>10</sub> H <sub>8</sub>	99.9 %	AppliChem
paraformaldehyde	(CH <sub>2</sub> O) <sub>n</sub>	95 %	Merck
phosphoryl trichloride <sup>d</sup>	POCl <sub>3</sub>	99 %	Aldrich
poly(tetrafluoroethylene)	(C <sub>2</sub> F <sub>4</sub> ) <sub>n</sub>	n. s.	ABCR
potassium chloride	KCl	99.5 %	Grüssing
potassium iodide <sup>c</sup>	KI	99.5 %	Grüssing
pyridine-3,5-dicarboxylic acid	C <sub>7</sub> H <sub>5</sub> NO <sub>4</sub>	98 %	Alfa Aesar

compound	formula	purity	supplier
sodium chloride	NaCl	99 %	CHEMSOLUTE
sodium cyanide <sup>c</sup>	NaCN	97 %	Sigma Aldrich
sodium hydrogen carbonate	NaHCO <sub>3</sub>	>99.5 %	Chemsolute
sodium sulfate	Na <sub>2</sub> SO <sub>4</sub>	>99 %	VWR Chemicals
sulfur	S <sub>8</sub>	99.5 %	Grüssing
tetraphenylmethane <sup>c</sup>	C <sub>25</sub> H <sub>20</sub>	96 %	Alfa Aesar
thionyl chloride <sup>d</sup>	SOCl <sub>2</sub>	>99 %	Merck
<i>trans</i> -cinnamaldehyde <sup>a</sup>	C <sub>9</sub> H <sub>8</sub> O	≥99 %	Sigma Aldrich
zinc chloride, anhydrous <sup>a</sup>	ZnCl <sub>2</sub>	98 %	ABCR

**a** stored in a glove box and used as received.

**b** recrystallised from toluene/ethanol and dried prior to use it in a glovebox.

**c** prior to use, the compounds were activated in vacuum at RT and transferred in a glovebox.

**d** freshly distilled prior to use.

**Table 4** Solvents applied in this thesis

compound	formula	purity	supplier
1,2-dichlorobenzene, anhydrous <sup>b</sup>	C <sub>6</sub> H <sub>4</sub> Cl <sub>2</sub>	99 %	Sigma Aldrich
1,4-dioxane	C <sub>4</sub> H <sub>8</sub> O <sub>2</sub>	>99 %	HONEYWELL
acetone	C <sub>3</sub> H <sub>6</sub> O	98 %	BCD Chemie
acetone, anhydrous	C <sub>3</sub> H <sub>6</sub> O	>99.9 %	VWR Chemicals
acetonitrile, anhydrous <sup>a</sup>	C <sub>2</sub> H <sub>3</sub> N	HPLC grade	Fisher scientific
benzene	C <sub>6</sub> H <sub>6</sub>	100 %	VWR Chemicals
chloroform	CHCl <sub>3</sub>	>98 %	Fisher scientific
chloroform d <sub>1</sub>	CDCl <sub>3</sub>	99.8 %	Sigma Aldrich
dichloromethane, anhydrous <sup>a</sup>	CH <sub>2</sub> Cl <sub>2</sub>	HPLC grade	Roth
diethyl ether	C <sub>4</sub> H <sub>10</sub> O	>98 %	Fisher scientific
dimethylsulfoxide d <sub>6</sub>	C <sub>2</sub> D <sub>6</sub> OS	99.9 %	Sigma Aldrich
ethanol <sup>a</sup>	C <sub>2</sub> H <sub>5</sub> OH	99.9 %	VWR Chemicals
ethyl acetate	C <sub>4</sub> H <sub>8</sub> O <sub>2</sub>	98 %	BCD Chemie
isohexane	C <sub>6</sub> H <sub>14</sub>	98 %	BCD Chemie
<i>N,N</i> -dimethylformamide	C <sub>3</sub> H <sub>7</sub> NO	>98 %	Fisher scientific
<i>N,N</i> -dimethylformamide, anhydrous	C <sub>3</sub> H <sub>7</sub> NO	99.8	Sigma Aldrich
pentane	C <sub>5</sub> H <sub>12</sub>	>98 %	Fisher scientific
<i>tert</i> -butanol, anhydrous <sup>b</sup>	C <sub>4</sub> H <sub>10</sub> O	>99.5 %	Sigma Aldrich

compound	formula	purity	supplier
tetrahydrofuran	C <sub>4</sub> H <sub>8</sub> O	>98 %	Fisher scientific
toluene, anhydrous <sup>a</sup>	C <sub>7</sub> H <sub>8</sub>	HPLC grade	VWR Chemicals

a purified by a solvent purification system (SPS)

b stored in a glove box and used as received.

## 4.2 Instrumental setup<sup>\*\*\*</sup>

### Argon/Nitrogen physisorption

Argon physisorption measurements were performed at 87 K on an Autosorb-IQ-C-XR (Quantachrome Instruments). Nitrogen physisorption measurements were performed at 77 K either on a Quadrasorb apparatus or an Autosorb-IQ-C-XR (Quantachrome Instruments). If not stated differently, 20 - 40 mg of the sample was activated in vacuum at 150 °C for at least 16 hours. The pyridine-derived CTF samples were activated at 230 °C for at least 16 hours. High purity gases were used for physisorption measurements (N<sub>2</sub>: 99.999 %, Ar: 99.999 %). Specific surface areas ( $S_{\text{BET}}$ ) were calculated using the Multipoint BET Method from Brunauer, Emmet and Teller (BET) in a relative pressure range that fits to the consistency criteria proposed by Rouquerol and Llewellyn.<sup>150</sup> Pore size distributions and cumulative pore volumes were calculated using the Quenched Solid Density Functional Theory (QSDFT) method for carbon (slit pores, equilibrium kernel) on the adsorption branch. Ultramicropore volumes were calculated from the cumulative pore volumes at a pore diameter of less or equal to 0.7 nm. Supermicropore volumes were determined by subtracting the respective ultramicropore volume from the cumulative pore volume at a pore diameter of 2 nm (or micropore volume). Mesopore volumes were determined by subtracting the respective micropore volume from the cumulative pore volume at a pore diameter of 36 nm (for argon) or 26 nm (nitrogen). Total pore volumes were determined from the adsorption branch at  $p/p_0 = 0.95$  if not stated differently.

### Water and carbon dioxide physisorption

Water physisorption measurements were performed at 298 K on an Autosorb-IQ-C-XR (Quantachrome Instruments). CO<sub>2</sub> physisorption measurements were performed at 273 K (or 195 K and 298 K) on an Autosorb 1C (Quantachrome Instruments, USA) using high purity gas

<sup>\*\*\*</sup> Parts of this chapter have been adopted verbatim from my publications.<sup>104,158</sup>

(CO<sub>2</sub>: 99.995 %, Air Liquide). If not stated differently, 20 - 40 mg of the sample was activated in vacuum at 150 °C for at least 16 hours.

### **Vapour sorption**

Vapour sorption experiments were carried out on a BELSORP-max (MicrotracBEL Corp.). For adsorption of vapours the corresponding liquids were degassed following the automated BELSORP-max routine. Anhydrous solvents of HPLC grade (purity > 99.9 %) were used.

### **Elemental analyses**

Elemental analyses were carried out by Philipp Lange (Inorganic Molecular Chemistry, Technische Universität Dresden) on a vario MICRO cube Elemental Analyzer by Elementar Analysensysteme GmbH in CHNS modus. The pyridine-derived CTF samples were activated at 200 °C and processed in the glovebox prior to the measurement.

### **Fourier transformed infrared spectroscopy**

FT-IR spectra were recorded with a Bruker Vertex 70 using a SPECAC Golden gate ATR unit in the range from 4000 – 600 cm<sup>-1</sup> (resolution 2 cm<sup>-1</sup>). A background as well as a CO<sub>2</sub> and H<sub>2</sub>O correction was conducted by the aid of the software OPUS 6.5

### **Raman spectroscopy**

Raman spectra were recorded with a RM-2000 from Renishaw with a 50x objective (NA = 0.75) and a wavelength of 532 nm. The measurements were carried out by M. Sc. Benjamin Klemmed (Physical Chemistry, TU Dresden).

### **Gravimetric powder resistivity**

Electric powder resistivities were measured with an Agilent 34420A combined with a self-constructed cell with a diameter of 1 cm. The powder was pressed with 2 t. The measurements were carried out by M. Sc. Christian Kensy (Fraunhofer IWS, Dresden).

### **Heating device for CTF syntheses**

A Nabertherm P330 oven was used as heating device for all CTF syntheses. For covalent attaching of sulfur, an argon purged tubular furnace (Gero 30 – 3000 °C) equipped with a quartz tube was applied.

### **Powder X-ray diffraction**

Powder X-ray diffraction (PXRD) patterns were collected in transmission geometry (MYTHEN 1K detector) with a STOE STADI P diffractometer operated at 40 kV and 30 mA with a Ge monochromator using Cu-K $\alpha$ 1 radiation ( $\lambda = 0.15405$  nm).

### **Scanning electron microscopy**

Scanning electron microscopy (SEM) images were obtained using a Hitachi SU8020 SEM equipped with a secondary electron (SE) detector. Prior to the measurement the samples were prepared on an adhesive carbon pad and sputtered with gold to obtain the necessary electron conductivity. All SEM measurements were conducted by M. Sc. Sebastian Ehrling or Dipl.-Chem. Andrea Br nner.

### **Transmission electron microscopy**

TEM measurements were performed on a FEI TECNAI F30 equipped with a field emitter at 300 kV and a FEI TECNAI F20 equipped with a LaB<sub>6</sub> cathode at 200 kV. Samples have been prepared by drop-casting onto a Lacey Copper Grid. All TEM measurements were conducted by Dr. Danny Haubold (Physical Chemistry, TU Dresden).

### **Thermogravimetric analyses**

Thermogravimetric analyses (TGA) were carried out with a ramp rate of 5 K / min in either a flow of synthetic air or Argon with a Netzsch STA 409 PC Luxx. All TGA measurements were conducted by Dr. Ilka Kunert.

### **Solid-State UV-VIS spectroscopy**

Solid-State UV-VIS spectroscopy measurements were conducted on a Cary 4000 (VARIAN) with a HARRICK Praying Mantis unit. The step width was set to 1 nm and the sources were switched at 350 nm. The crude samples were mixed with an excess of BaSO<sub>4</sub> prior to measuring. The optical band gap was determined by using Tauc plot calculation:  $\alpha h \nu = C (h \nu - E_g)^n$  with  $n = 1/2$  for a direct allowed transition.

### **X-ray photoelectron spectroscopy**

X-ray photoelectron spectroscopy measurements were carried out by means of an Axis Ultra photoelectron spectrometer (Kratos Analytical, Manchester, UK) or a Theta Probe photoelectron spectrometer (Thermo Scientific). The spectrometer was equipped with a monochromatic

Al K $\alpha$  ( $h\nu = 1486.6$  eV) X-ray source of 300 W at 15 kV or a monochromatic Al K $\alpha$  X-ray source of 100 W at 15 kV. The kinetic energy of photoelectrons was determined with hemispheric analyser set to pass energy of 160 eV/200 eV for wide-scan spectra and 20 eV/50 eV for high-resolution spectra. During all measurements, electrostatic charging of the sample was avoided by means of a low-energy electron source working in combination with a magnetic immersion lens. Later, all recorded peaks were shifted by the same value that was necessary to set the C 1s component peak showing the carbon atoms involved in conjugated  $\pi$ -electron systems of the phenyl rings to 284.70 eV.

High-resolution spectra were deconvoluted by means of the Casa XPS deconvolution software. A linear spectrum background was subtracted. The deconvolution of spectra was performed using a mixed Gauss-Lorentz function where the Lorentzian contribution was set to 30 % and a full width at half maximum that was kept constant within one sample. Free parameters of component peaks were their binding energy (BE) and height. Quantitative elemental compositions were determined from the integrals of the Gauss-Lorentz fit functions.

XPS measurements were conducted by Dr. Frank Simon (IPF Dresden), Dipl.-Ing. Peter Schützendübe (MPI IS Stuttgart) and Dr. Johannes Schmidt (TU Berlin). Aid in processing and interpreting the XPS data was provided by Prof. Dr. Yvonne Joseph (TU Bergakademie Freiberg) and Dr. Frank Simon (IPF Dresden).

### Liquid-phase NMR

Liquid-phase NMR spectroscopy data were recorded on a Bruker AV-III 600 operating at 600 MHz for  $^1\text{H}$ , 151 MHz for  $^{13}\text{C}$  and 60.8 MHz for  $^{15}\text{N}$  or a Bruker RRX 500 operating at 500 MHz for  $^1\text{H}$  and 126 MHz for  $^{13}\text{C}$ . Chemical shifts  $\delta$  are given in ppm relative to TMS ( $^1\text{H}$  and  $^{13}\text{C}$ ) and  $\text{MeNO}_3$  ( $^{15}\text{N}$ ), respectively. NMR measurements were performed using deuterated organic solvents. Coupling constants  $J$  are given in Hertz, the solvent signals were used as reference ( $^1\text{H}$ :  $\delta_{\text{H}} 2.500$  ppm residual  $\text{DMSO-d}_5$  in  $\text{DMSO-d}_6$ ,  $^{13}\text{C}$ :  $\delta_{\text{C}} 38.56$  ppm). For  $^{15}\text{N}$  universal calibration ( $\Xi_{^{15}\text{N}} = 0.10136767$ ) was used. Coupling constants were determined assuming first-order spin-spin coupling. Carbon and nitrogen chemical shifts were taken from HSQC and HMBC spectra. All liquid phase NMR measurements were conducted by Dr. Tilo Lübken and Anett Rudolph.



### **Solid-state NMR**

For the NHC-CTF, the spectra were recorded on a BRUKER Ascend 800 MHz spectrometer using a commercial 2.5 mm MAS NMR probe and operating at a resonance frequency of 800.2 MHz for  $^1\text{H}$  and 201.2 MHz for  $^{13}\text{C}$ . The MAS frequency was 18 kHz. Adamantane was used as external chemical shift reference.

$^1\text{H}$  NMR spectra were measured with a recycle delay of 3 s. 16 scans were accumulated. For  $^{13}\text{C}$  NMR measurements, ramped  $^1\text{H}$ - $^{13}\text{C}$  cross-polarization (CP, contact time: 4 ms) and SPINAL  $^1\text{H}$ -decoupling during the signal acquisition was applied. The recycle delay was 3 s. 40.000 scans (Monomer) / 25.000 scans (NHC-CFT) were accumulated.  $^1\text{H}$  NMR spectra were analysed by means of the Dmfit software.<sup>159</sup>

For the mechanochemically synthesised CTFs, the experiments were performed on a Bruker Avance 300 spectrometer operating at 75.47 MHz for  $^{13}\text{C}$  using a commercial double resonance 4 mm MAS NMR probe. Ramped  $^1\text{H}$ - $^{13}\text{C}$  cross-polarization (CP, contact time: 4 ms, pulse repetition time: 3 s) and SPINAL  $^1\text{H}$ -decoupling was applied. The MAS frequency was 12 kHz. The  $^{13}\text{C}$  chemical shifts were referenced with adamantane. All solid-state NMR measurements were conducted by Dr. Silvia Paasch (Bioanalytical Chemistry, TU Dresden).

### **Matrix assisted laser desorption ionization time of flight mass spectroscopy**

MALDI-TOF measurements were carried out on a Reflex II TOF spectrometer (Bruker) using a 337 nm nitrogen laser with dithranol and AgTFA as matrix. All MALDI-TOF measurements were conducted by Dr. Valeriya Tkachova (Molecular functional materials, Technische Universität Dresden).

### **Gas chromatography**

All GC measurements were performed using a Shimadzu GC 17 A equipped with a flame ionization detector (FID) and a BPX5 column (30 m length, 0.25 mm in inner diameter, and 0.25 mm film thickness). The following temperature program for GC analysis was used: the samples were firstly heated from 40 to 48 °C with a heating rate of 4 °C/min; then from 48 °C to 270 °C with 20 °C/min and held at 270 °C for 2 min. Inlet and detector temperatures were set constant at 270 °C. Mesitylene was used as an internal standard to calculate reaction yields.

Mass spectra were collected using a Shimadzu GCMS-QP5000, and were referred to database of NIST library.

### **Electrode preparation and electrochemical characterisation**

The CTF composite materials were prepared as free standing electrodes. They were dispersed in ethanol and 5 w% polytetrafluoroethylene (PTFE, granular) as binder was added. By grinding the mixture in a mortar, a dough-like mass was obtained, which was further rolled until the electrodes had a thickness of about 150  $\mu\text{m}$ . The electrodes were dried in a vacuum oven at 120  $^{\circ}\text{C}$  for 24 h and a disc cutter was used to obtain electrodes with a diameter of 10 mm. The measurements were conducted in custom-built cells.<sup>160</sup> A 12 mm diameter Whatmann GF/D was used as a separator.

The electrochemical measurements were performed with a Biologic VMP3 potentiostat/galvanostat. The specific capacitances were calculated following (see Eq. 8) derived from galvanostatic discharge curves at 1  $\text{Ag}^{-1}$ .

$$C_{spec.} = \frac{4Q}{U_{corr} \cdot m} \quad (\text{Equation 8})$$

Q refers to the charging of the discharge cycle;  $U_{corr}$  refers to the iR-drop corrected cell voltage and m refers to the mass of carbon in both electrodes.

Potential limited electrochemical impedance spectroscopy (PEIS) was performed in a frequency range of 100 kHz to 10 mHz with an amplitude of 0.5 V.

Cyclic voltammetry was performed from 0 V to 1 V with different scan rates from 5  $\text{mVs}^{-1}$  to 500  $\text{mVs}^{-1}$ .

The electrochemical characterisation was conducted by Tilo Rensch during his bachelor thesis.

### **Supercritical drying**

For supercritical drying, supernatant solvent of the samples which were dispersed in acetone was changed several times against anhydrous acetone. Consequently, the samples were placed in glass filter frits in the Jumbo Critical Point Dryer 13200J AB (SPI Supplies) which was subsequently filled with liquid  $\text{CO}_2$  (99.995 % purity) at 15  $^{\circ}\text{C}$  and 50 bar. After complete substitution of acetone against  $\text{CO}_2$  (e.g. solvent was changed three times a day for three days), the pressure and temperature was then raised beyond the supercritical point of  $\text{CO}_2$  to 35  $^{\circ}\text{C}$  and

100 bar and kept until the temperature and pressure was constant. The supercritical CO<sub>2</sub> was steadily released over 3 hours and the dry powder was used as received.

### **Ball mill syntheses**

Ball mill syntheses were carried out on a PULVERISETTE 7 premium line planetary ball mill (Fritsch). If not stated differently, the ball mill was operating at a rotation speed of 800 rpm. The syntheses were performed either in a 45 mL tungsten carbide grinding jar with 22 WC balls (10 mm in diameter) or a 45 mL zircon oxide grinding jar with 22 WC balls (10 mm in diameter).

## **4.3 General information**

If not stated differently, all CTF syntheses were performed in quartz ampoules under inert argon atmosphere (in a glovebox). Prior to use them in a glovebox, all ampoules were dried at 150 °C in a heating oven and transferred into the glovebox. After preparing the ampoules, they were closed with a socket/cone adapter piece with valve, evacuated in high vacuum (10<sup>-3</sup> mbar) and flame-sealed using an oxy-hydrogen torch.

Anhydrous zinc chloride was stored in a glove box and used as commercially received.

## **4.4 Syntheses of salt templated CTFs in binary salt mixtures<sup>\*\*\*</sup>**

To generate the binary salt mixtures, lithium chloride, sodium chloride and potassium chloride were dried at 200 °C in high vacuum prior to use the compounds in the glovebox.

**Synthesis of CTF-1\_450 (reference sample):** 1596 mg of anhydrous zinc chloride (11.7 mmol, 5 eq.) and 300 mg of 1,4-dicyanobenzene (2.34 mmol, 1 eq.) were mixed thoroughly by grinding in a mortar and transferred into a quartz ampoule.

**Synthesis of CTF1\_LiCl:** 496 mg LiCl (11.7 mmol, 5 eq.) and 1596 mg of anhydrous zinc chloride (11.7 mmol, 5 eq.) were mixed thoroughly by grinding in a mortar and 300 mg of 1,4-dicyanobenzene (2.34 mmol, 1 eq.) were added and mixed again in the mortar. Finally, the mixture was transferred into a quartz ampoule.

---

<sup>\*\*\*</sup> Parts of this chapter have been adopted verbatim from my publication.<sup>158</sup>

**Synthesis of CTF1\_NaCl:** 293 mg NaCl (5.0 mmol, 2.1 eq.) and 1596 mg of anhydrous zinc chloride (11.7 mmol, 5 eq.) were mixed thoroughly by grinding in a mortar and 300 mg of 1,4-dicyanobenzene (2.34 mmol, 1 eq.) were added and mixed again in the mortar. Finally, the mixture was transferred into a quartz ampoule.

**Synthesis of CTF1\_KCl:** 219 mg KCl (2.9 mmol, 1.25 eq.) and 1596 mg of anhydrous zinc chloride (11.7 mmol, 5 eq.) were mixed thoroughly by grinding in a mortar and 300 mg of 1,4-dicyanobenzene (2.34 mmol, 1 eq.) were added and mixed again in the mortar. Finally, the mixture was transferred into a quartz ampoule.

The sealed ampoules were and heated according to the temperature profile of Figure 1.

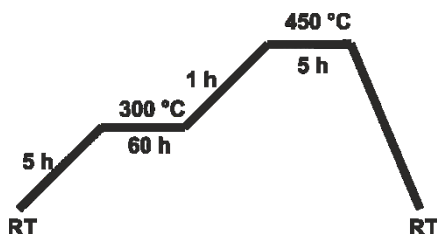


**Figure 1** Temperature protocol for salt templated CTF samples.

**General work-up:** After cooling down to room temperature, the ampoules were opened. No pressure was detected, i.e. the ampoules were still under vacuum. The obtained black monolith was subsequently ground and then stirred in 6 M HCl for 24 h at 60 °C. The samples were washed thoroughly with water (ca. 500 mL), *N,N*-dimethylformamide (ca. 200 mL) and acetone (ca. 150 mL) in order to remove residual salt and organic impurities. After washing, the resulting black powder was dried in high vacuum at 150 °C. **yield:** > 90 %

#### 4.5 Mechanochemical CTF syntheses\*\*\*

All syntheses were performed in a glovebox. Prior to the syntheses, a 45 mL grinding jar with twenty-two 10 mm-diameter grinding balls was introduced into the glovebox. If not stated differently, the all mechanochemical syntheses were conducted at a rotation speed of 800 rpm.

\*\*\* Parts of this chapter have been adopted verbatim from my publication.<sup>104</sup>

**CTF-CBZ**

1.018 g of cyanuric chloride (5.52 mmol, 1 eq.), 3.681 g of aluminium chloride (27.61 mmol, 5 eq.) und 3.916 g of anhydrous zinc chloride (28.73 mmol, 5.2 eq.) were weighed and transferred into a 45 mL tungsten carbide grinding jar. The grinding jar was carefully closed and the educts were milled for 2 min. Consequently, the grinding jar was introduced into the glovebox again and 1.385 g of carbazole (8.28 mmol, 1.5 eq.) was added. The grinding jar was closed carefully to avoid air contact and the mixture was milled for further 60 min. A detailed explanation of the work-up protocol is given at the end of this chapter. **yield: 97 %**

**CTF-AC**

1.009 g of cyanuric chloride (5.47 mmol, 1 eq.), 3.684 g of aluminium chloride (27.36 mmol, 5 eq.) und 3.881 g of anhydrous zinc chloride (28.73 mmol, 5.2 eq.) were weighed and transferred into a 45 mL tungsten carbide grinding jar. The grinding jar was carefully closed and the educts were milled for 2 min. Consequently, the grinding jar was introduced into the glovebox again and 1.463 g of anthracene (8.21 mmol, 1.5 eq.) was added. The grinding jar was closed carefully to avoid air contact and the mixture was milled for further 120 min. **yield: 96 %**

**CTF-TPB**

0.988 g of cyanuric chloride (5.36 mmol, 1 eq.), 3.571 g of aluminium chloride (27.78 mmol, 5 eq.) und 3.799 g of anhydrous zinc chloride (27.87 mmol, 5.2 eq.) were weighed and transferred into a 45 mL tungsten carbide grinding jar. The grinding jar was carefully closed and the educts were milled for 2 min. Consequently, the grinding jar was introduced into the glovebox again and 1.641 g of 1,3,5-triphenylbenzene (5.36 mmol, 1.0 eq.) was added. The grinding jar was closed carefully to avoid air contact and the mixture was milled for further 120 min. **yield: 82 %**

**CTF-BZ**

1.099 g of cyanuric chloride (5.96 mmol, 1 eq.), 3.974 g of aluminium chloride (29.80 mmol, 5 eq.) und 4.228 g of anhydrous zinc chloride (31.02 mmol, 5.2 eq.) were weighed and transferred into a 45 mL tungsten carbide grinding jar. The grinding jar was carefully closed and the educts were milled for 2 min. Consequently, the grinding jar was introduced into the glovebox again and 0.700 g of benzene (8.96 mmol, 1.5 eq.) was added. The grinding jar was closed carefully to avoid air contact and the mixture was milled for further 120 min. **yield: 5 %**

### CTF-NT

1.052 g of cyanuric chloride (5.70 mmol, 1 eq.), 3.804 g of aluminium chloride (28.53 mmol, 5 eq.) und 4.047 g of anhydrous zinc chloride (29.69 mmol, 5.2 eq.) were weighed and transferred into a 45 mL tungsten carbide grinding jar. The grinding jar was carefully closed and the educts were milled for 2 min. Consequently, the grinding jar was introduced into the glovebox again and 1.097 g of naphthalene (8.56 mmol, 1.5 eq.) was added. The grinding jar was closed carefully to avoid air contact and the mixture was milled for further 120 min. **yield:** 2 %

### CTF-TPM

1.024 g of cyanuric chloride (5.55 mmol, 1 eq.), 3.700 g of aluminium chloride (27.75 mmol, 5 eq.) und 3.939 g of anhydrous zinc chloride (28.90 mmol, 5.2 eq.) were weighed and transferred into a 45 mL tungsten carbide grinding jar. The grinding jar was carefully closed and the educts were milled for 2 min. Consequently, the grinding jar was introduced into the glovebox again and 1.335 g of tetraphenylmethane (4.17 mmol, 0.75 eq.) was added. The grinding jar was closed carefully to avoid air contact and the mixture was milled for further 120 min. **yield:** 3 %

### General synthetic procedure for other mechanochemically synthesised CTF samples

In a typical synthesis, cyanuric chloride (1 eq.), aluminium chloride (5 eq.) and the inert bulk-ing material (see Table 5 for equivalents) were transferred into a 45 mL grinding jar with twenty-two 10 mm-diameter grinding balls. The educts were then milled for 2 min. The grinding jar was introduced into the glovebox again and the monomer (see Table 5 for equivalents) was added. The grinding jar was closed carefully to avoid air contact and the mixture was milled for the respective time again.

### General protocol of sample work-up

After the reaction, the grinding jar was opened and the reaction mixture was poured into acidic water (10 mL of 1 M hydrochloric acid in 300 mL of cold water). The crude product was transferred into an extraction thimble and was purified by Soxhlet-Extraction with water and THF, consequently. The samples were dried at 100 °C and stored under ambient conditions. To determine the maximum porosity, the resulting materials were re-dispersed in anhydrous acetone after washing. After precipitation of the polymer, the supernatant solvent was removed and

changed against fresh solvent for at least 6 times. After changing the solvent, the samples were placed in glass filter frits in the Jumbo Critical Point Dryer and supercritically dried with liquid carbon dioxide. After complete substitution of acetone against CO<sub>2</sub> (e.g. solvent was changed three times a day for three days), the supercritical CO<sub>2</sub> was steadily released over 3 hours and the dry powder was directly transferred into a glovebox. To characterise the adsorption properties, the samples were activated in high vacuum at 25 °C prior to the measurement.

**Table 5** Synthetic parameters of different mechanochemically synthesised CTF samples.

sample	cyanuric chloride	monomer	AlCl <sub>3</sub>	bulking agent	jar	time min	yield
	m [g] / n [mmol] / eq.	m [g] / n [mmol] / eq.	m [g] / n [mmol] / eq.	m [g] / n [mmol] / eq.			
CTF-CBZ	1.018 / 5.52 / 1	carbazole 1.385 / 8.28 / 1.5	3.681 / 27.61 / 5	ZnCl <sub>2</sub> 3.916 / 28.73 / 5.2	WC	60	97 %
CTF-CBZ_ZrO <sub>2</sub> _1h	1.018 / 5.52 / 1	carbazole 1.385 / 8.28 / 1.5	3.681 / 27.61 / 5	ZnCl <sub>2</sub> 3.916 / 28.73 / 5.2	ZrO <sub>2</sub>	180	50 %
CTF-CBZ_KCl	1.426 / 7.73 / 1	carbazole 1.939 / 11.60 / 1.5	5.154 / 38.65 / 5	KCl 1.481 / 19.87 / 2.57	WC	60	89 %
CTF-CBZ_NaCl	1.431 / 7.76 / 1	carbazole 1.946 / 11.64 / 1.5	5.173 / 38.80 / 5	NaCl 1.450 / 24.80 / 3.2	WC	60	82 %
CTF-CBZ_IaCl	1.469 / 7.97 / 1	carbazole 1.998 / 11.95 / 1.5	5.311 / 39.83 / 5	IaCl 1.222 / 28.84 / 3.2	WC	60	96 %
CTF-CBZ_AlCl <sub>3</sub>	1.674 / 9.08 / 1	carbazole 2.276 / 13.61 / 1.5	6.050 / 45.38 / 5	-	WC	60	91 %
CTF-FAC	1.009 / 5.47 / 1	anthra-cene 1.463 / 8.21 / 1.5	3.684 / 27.36 / 5	ZnCl <sub>2</sub> 3.881 / 28.48 / 5.2	WC	120	96 %
CTF-TPB	0.988 / 5.36 / 1	triphenyl-benzene 1.641 / 5.36 / 1.0	3.571 / 26.78 / 5	ZnCl <sub>2</sub> 3.799 / 27.87 / 5.2	WC	120	82 %
CTF-BZ	1.099 / 5.96 / 1	benzene 0.700 / 8.96 / 1.5	3.974 / 29.80 / 5	ZnCl <sub>2</sub> 4.228 / 31.02 / 5.2	WC	120	5 %
CTF-NT	1.052 / 5.70 / 1	naphthalene 1.097 / 8.56 / 1.5	3.804 / 28.53 / 5	ZnCl <sub>2</sub> 4.047 / 29.69 / 5.2	WC	120	2 %
CTF-TPM	1.024 / 5.55 / 1	tetra-phenyl-methane 1.335 / 4.17 / 0.75	3.700 / 27.75 / 5	ZnCl <sub>2</sub> 3.939 / 28.90 / 5.2	WC	120	3 %



## 4.6 Synthesis of CTFs containing covalently bound sulfur

### 4.6.1 Synthesis of the parent materials

#### Synthesis of CTF-Mono

In a typical synthesis, 0.50 g of 1,4-dicyanobenzene (3.9 mmol, 1 eq.) and 2.66 g of anhydrous zinc chloride (19.5 mmol, 5 eq.) were mixed by grinding and transferred into quartz ampoules. The ampoules were sealed under vacuum and heated (Figure 2).

#### Synthesis of CTF-Bi

In a typical synthesis, 0.50 g of 4,4'-dicyano-1,1'-biphenyl (2.4 mmol, 1 eq.) and 1.67 g of anhydrous zinc chloride (12.2 mmol, 5 eq.) were mixed by grinding and transferred into quartz ampoules. The ampoules were sealed under vacuum and heated (Figure 2).

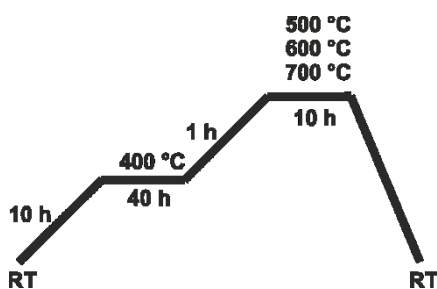


**Figure 2** Temperature protocol for the synthesis of CTF-Mono and CTF-Bi.

#### General protocol of sample work-up

After cooling down to room temperature, the ampoules were opened. The obtained black monolith was subsequently ground with the aid of 2 mL of 1 M hydrochloric acid and consequently stirred in 1 M HCl for 24 h at 60 °C. The samples were washed thoroughly with heated water (ca. 500 mL, ca. 50 °C), *N,N*-dimethylformamide (ca. 200 mL) and acetone (ca. 150 mL) in order to remove residual salt and organic impurities. After washing, the resulting black powder was dried in a heating oven at 150 °C prior to dry the sample in high vacuum at 150 °C.  
**yield:** > 85 %

### 4.6.2 Synthesis of the S@CTF materials

The CTFs (0.3 g) were activated at 150 °C under vacuum and mixed with 4.5g sulfur in a ball mill for 2 minutes. The resulting homogeneous mixture was transferred to a quartz boat which was placed in a horizontal tubular furnace and purged at 60 °C under flowing argon. The tem-

perature was increased to 155 °C (60 K/h heating rate) and maintained there for 3 h. Then the temperature was raised to 350 °C (100 K/h heating rate) and kept for 3 h. After cooling down, the resulting material was separately washed via Soxhlet extraction with toluene and THF for 24 h, respectively. The samples were dried at 70 °C in a heating oven and then at 150 °C in high vacuum.

## 4.7 Synthesis of CTFs based on 3,5-dicyanopyridine

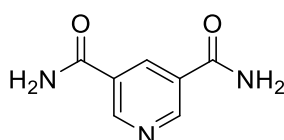
### 4.7.1 Synthesis of 3,5-dicyanopyridine

In general, all organic syntheses were performed under argon atmosphere. The syntheses were conducted using slight modifications of the protocol of Šturala et. al.<sup>161</sup> Some results were taken from the Bachelor thesis of Tilo Rensch I supervised in 2017.<sup>162</sup>

#### Synthesis of Pyridine-3,5-dicarboxamide

Pyridine-3,5-dicarboxylic acid (19.5 g, 0.12 mol, 1 eq.) was suspended in dry dichloromethane (250 mL). Freshly distilled thionyl chloride (60 mL, 0.83 mol, 7 eq.) and dry *N,N*-dimethylformamide (4 mL) were added and the resulting mixture was heated to reflux until the acid was completely dissolved. Then, the reaction mixture was heated overnight. The solvent and the excess of thionyl chloride were removed in vacuo. The resulting acyl chloride was dissolved in benzene (150 mL) and evaporated under reduced pressure. The residual solid was dissolved in dioxane (500 mL) and aqueous ammonia (600 mL) was added. After 60 min, the white precipitate was collected by filtration, washed with water (8 × 100 mL) and dried in vacuo to give a white solid.

#### Pyridine-3,5-dicarboxamide:



yield:	62 % (11.85 g)
molar mass:	165.15 g mol <sup>-1</sup>
formula:	C <sub>7</sub> H <sub>7</sub> N <sub>3</sub> O <sub>2</sub>

<sup>1</sup>H-NMR (600 MHz, DMSO-*d*<sub>6</sub>): δ [ppm]: = 9.12 (d, *J* = 2.16 Hz, 2 x CH<sub>arom</sub>), 8.63 (t, *J* = 2.16 Hz, 1 x CH<sub>arom</sub>), 8.25 (br s, 2 x NH), 7.69 (br s, 2 x NH).

<sup>13</sup>C-NMR (151 MHz, DMSO-*d*<sub>6</sub>): δ [ppm]: = 166 (2 x CONH<sub>2</sub>), 150 (2 x CN<sub>arom</sub>), 134 (2 x C<sub>q,arom</sub>), 129 (1 x CH<sub>arom</sub>).

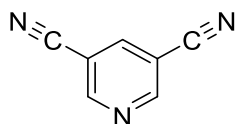
**FT-IR:**  $\nu$  [ $\text{cm}^{-1}$ ] = 3400 ( $\nu_{\text{N-H}}$ ), 3320 ( $\nu_{\text{C-H}}$ ), 3160 ( $\nu_{\text{C-H}}$ ), 3100 ( $\nu_{\text{N-H}}$ ), 1690 (amide I), 1620 (amide II), 1580 ( $\nu_{\text{C=C}}$ ), 1460 ( $\nu_{\text{C=C}}$ ), 1400 ( $\nu_{\text{C=C}}$ ), 1390 ( $\nu_{\text{C-N}}$ ), 1240 (amide III), 1120 ( $\delta_{\text{C=C ip}}$ ), 1100 ( $\delta_{\text{C=C ip}}$ ), 1020 ( $\delta_{\text{C=C ip}}$ ), 800 ( $\delta_{\text{ringbending}}$ ), 730 ( $\delta_{\text{C-H deformation oop}}$ ), 690 ( $\gamma_{\text{C-H}}$ ), 680 ( $\delta_{\text{O=C-NH2 oop}}$ ).

**EA:** calculated: C: 50.91 % H: 4.27 % N: 25.44 % O: 19.38 % C/H: 1.00 C/N: 2.33  
found: C: 49.81 % H: 4.17 % N: 24.14 % C/H: 1.00 C/N: 2.41

### 3,5-dicyanopyridine

Pyridine-3,5-dicarboxamide (10.3 g, 62.4 mmol, 1 eq.) was suspended in dry *N,N*-dimethylformamide (250 mL). Freshly distilled phosphoryl trichloride (34 mL, 0.37 mol, 5.8 eq.) was added dropwise and a clear orange solution was resulting. The mixture was stirred for 3.5 h at room temperature and allowed to stand overnight. The excess of phosphoryl trichloride was quenched and neutralised with aqueous  $\text{NaHCO}_3$ . The mixture was extracted with ethyl acetate ( $5 \times 300$  mL). The organic layers were combined, dried with magnesium sulfate, filtrated and evaporated in vacuo. The crude product was purified by sublimation ( $70^\circ\text{C}$ ,  $10^{-3}$  mbar) over night to give 3,5-dicyanopyridine as a white crystalline solid.

#### 3,5-dicyanopyridine:



yield:	85 % (6.87 g)
molar mass:	129.12 g mol <sup>-1</sup>
formula:	C <sub>7</sub> H <sub>3</sub> N <sub>3</sub>

<sup>1</sup>H-NMR (600 MHz, DMSO-d<sub>6</sub>):  $\delta$  [ppm]: = 9.12 (d, J = 2.07 Hz, 2 x CH<sub>arom</sub>), 8.25 (t, J = 2.07 Hz, 1 x CH<sub>arom</sub>).

<sup>13</sup>C-NMR (151 MHz, DMSO-d<sub>6</sub>):  $\delta$  [ppm]: = 155 (2 x CN<sub>Nitril</sub>), 141 (2 x CN<sub>arom</sub>), 113 (2 x C<sub>q,arom</sub>), 110 (1 x CH<sub>arom</sub>).

**FT-IR:**  $\nu$  [ $\text{cm}^{-1}$ ] = 3040 ( $\nu_{\text{C-H}}$ ), 3020 ( $\nu_{\text{C-H}}$ ), 3000 ( $\nu_{\text{C-H}}$ ), 2900 ( $\nu_{\text{C-H}}$ ), 2240 ( $\nu_{\text{nitrile}}$ ), 1560 ( $\nu_{\text{C=C}}$ ), 1410 ( $\nu_{\text{C=C}}$ ), 1130 ( $\delta_{\text{C=C ip}}$ ), 920 ( $\delta_{\text{ringbending}}$ ), 700 ( $\gamma_{\text{C-H}}$ ).

**EA:** calculated: C: 65.11 % H: 2.34 % N: 32.54 % C/H: 2.33 C/N: 2.33  
found: C: 65.03 % H: 2.18 % N: 32.76 % C/H: 2.49 C/N: 2.32

### 4.7.2 CTF synthesis

In a typical synthesis, 0.50 g 3,5-dicyanopyridine (3.9 mmol, 1 eq.) and 2.64 g  $\text{ZnCl}_2$  (19.5 mmol, 5 eq.) were mixed by grinding and transferred into quartz ampoules. The ampoules were sealed under vacuum and heated (Figure 3).

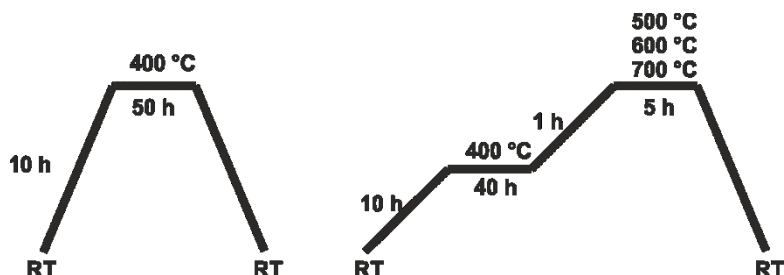


**Figure 3** Temperature protocol for the synthesis of 3,5-dicyanopyridine derived CTF.

The ampoules were cooled down to room temperature and opened. For each ampoule, 250 mg of the CTF/ $\text{ZnCl}_2$  composite were removed from the reaction mixture and processed separately. The remaining reaction product was subsequently ground with the aid of 2 mL of 1 M hydrochloric acid and subsequently stirred in 1 M HCl (ca. 300 mL) for 24 h at 60 °C. The samples were washed thoroughly with heated water (ca. 500 mL, ca. 50 °C), *N,N*-dimethylformamide (ca. 200 mL) and acetone (ca. 150 mL) in order to remove residual salt and organic impurities. After washing, the resulting black powder was dried in a heating oven at 150 °C prior to dry the sample in high vacuum at 150 °C. **yield:** > 90 %

## 4.8 Synthesis of the imidazolium CTF

### 4.8.1 Synthesis of the imidazolium monomer

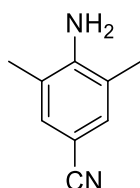
In general, all organic syntheses were performed under argon atmosphere. The syntheses were conducted using slight modifications of the protocol of Nickerl *et al.*<sup>163</sup>

#### 4-Amino-3,5-dimethylbenzonitrile

In a glovebox, 4-bromo-2,6-dimethylaniline (50.0 g, 0.25 mol, 1.00 eq.), sodium cyanide (14.7 g, 0.3 mol, 1.20 eq.), copper(I) iodide (4.8 g, 0.025 mol, 0.10 eq.) and water free potassium iodide (8.0 g, 0.05 mol, 0.2 eq) were added to a flamedried 500 mL Schlenk flask. Subsequently, dry toluene (0.175 L) and *N,N'*-dimethylethane-1,2-diamine (24.8 mL, 0.25 mol, 1.00 eq.) were added. The mixture was stirred in an argon atmosphere at 110 °C for 3 days. Af-

ter cooling down the reaction mixture to room temperature,  $\text{CHCl}_3$  (1.20 L) was added and the mixture was transferred in a separation funnel. The solution was washed with conc.  $\text{NH}_3$ -solution (0.40 L) and the organic phase was separated. The organic phase was subsequently washed with conc.  $\text{NH}_3$ -solution (0.40 L) for a second time, water, dried over  $\text{Na}_2\text{SO}_4$  and the solvents were evaporated under reduced pressure. The aqueous layer was cautiously deactivated by adding  $\text{H}_2\text{O}_2$  in portions. Purification by flash column chromatography on silica gel (pentane: $\text{Et}_2\text{O}$  = 3:1) afforded the analytically pure product as white-yellowish solid.

**4-Amino-3,5-dimethylbenzonitrile:**



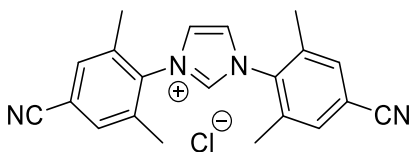
yield:	95 % (30.5 g)
molar mass:	146.19 $\text{g mol}^{-1}$
formula:	$\text{C}_9\text{H}_{10}\text{N}_2$

$^1\text{H-NMR}$  (500 MHz,  $\text{CDCl}_3$ ):  $\delta$  [ppm]: = 7.23 (s, 2 H,  $\text{CH}_{\text{arom}}$ ), 4.33 (br. s, 2 H,  $\text{NH}_2$ ), 2.19 (s, 6 H,  $\text{CH}_3$ ).

**1,3-Bis(4-cyano-2,6-dimethylphenyl)-1H-imidazolium chloride**

Paraformaldehyde (3.55 g, 0.12 mol, 1.00 eq.) was suspended in toluene (220 mL). To the mixture, 4-amino-3,5-dimethylbenzonitrile (34.50 g, 0.24 mol, 2.00 eq.) and aqueous glyoxal-solution (40 w% in  $\text{H}_2\text{O}$ , 17.23 g, 0.12 mol, 1.00 eq.) were added. Hydrochloric acid (37 w% in  $\text{H}_2\text{O}$ , 13.50 mL, 0.12 mol, 1.00 eq.) was added dropwise and a white precipitate was formed. Applying a Dean-Stark apparatus, the mixture was stirred at 130 °C for 3 h until no further formation of  $\text{H}_2\text{O}$  was detected. After cooling down to room temperature, toluene and water were evaporated under reduced pressure. The product was obtained by recrystallizing the crude product in DMF twice. After precipitation, filtration and washing with  $\text{Et}_2\text{O}$ , a white solid was obtained.

**1,3-Bis(4-cyano-2,6-dimethylphenyl)-1H-imidazolium chloride:**



yield:	70 % (30.84 g)
molar mass:	362.86 $\text{g mol}^{-1}$
formula:	$\text{C}_{21}\text{H}_{19}\text{N}_4\text{Cl}$

$^1\text{H-NMR}$  (500 MHz,  $\text{DMSO-d}_6$ ):  $\delta$  [ppm]: = 9.89 (s, 1H,  $\text{CH}_{\text{arom}}$ ), 8.41 (s, 2H,  $\text{CH}_{\text{arom}}$ ), 7.98 (s, 4H,  $\text{CH}_{\text{arom}}$ ), 2.23 (s, 12H, 4  $\times$   $\text{CH}_3$ ).

$^{13}\text{C}$ -NMR (126 MHz, DMSO- $d_6$ ):  $\delta$  [ppm]: = 138.7 (2 x  $C_{q, \text{arom}}$ ), 137.1 ( $C_{\text{aromH}}$ ), 136.6 (4 x  $C_{q, \text{arom}}$ ), 132.6 (4 x  $C_{\text{aromH}}$ ), 124.5 (2 x  $C_{\text{aromH}}$ ), 117.8 (2 x  $C_{q, \text{arom}}$ ), 113.6 (2 x CN), 16.9 (4 x  $\text{CH}_3$ ).

EA: calculated: C: 69.51 % H: 5.28 % N: 15.44 % Cl: 9.77 C/H: 1.10 C/N: 5.25  
found: C: 69.47 % H: 5.34 % N: 15.70 % Cl: 9.26 C/H: 1.08 C/N: 5.16

#### 4.8.2 Synthesis of the imidazolium CTF

In a typical synthesis, 0.50 g of 3-Bis(4-cyano-2,6-dimethylphenyl)-1*H*-imidazolium chloride (1.31 mmol, 1 eq.) and 0.89 g anhydrous zinc chloride (6.53 mmol, 5 eq.) were mixed by grinding and transferred into quartz ampoules. The ampoules were sealed under vacuum and heated (Figure 4).

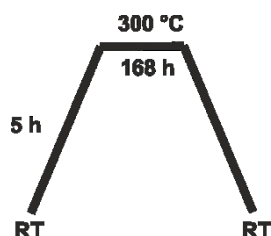


**Figure 4** Temperature protocol for the synthesis of NHC-CTF.

The ampoules were cooled down to room temperature and opened. The crude reaction product was subsequently ground with the aid of 2 mL of 1 M hydrochloric acid and subsequently stirred in 1 M HCl (ca. 300 mL) for 24 h at 60 °C. The samples were washed thoroughly with heated water (ca. 500 mL, ca. 50 °C), *N,N*-dimethylformamide (ca. 200 mL) and acetone (ca. 150 mL) in order to remove residual salt and organic impurities. After washing, the resulting black powder was dried in a heating oven at 150 °C prior to dry the sample in high vacuum at 150 °C. **yield:** 83 %

#### 4.8.3 Catalytic testing of the imidazolium CTF

Catalytic testing was performed by M. Sc. Khoa Dang Nguyen.

In a representative procedure, a mixture of *trans*-cinnamaldehyde (38  $\mu\text{L}$ , 0.3 mmol, 1 eq.), trifluoroacetophenone (82  $\mu\text{L}$ , 0.6 mmol, 2 eq.), DBU (5  $\mu\text{L}$ , 0.2 eq.) and mesitylene (20  $\mu\text{L}$ ) as internal standard in 2 mL acetonitrile were placed into a 10 mL Schlenk tube containing NHC-CTF (0.016 g, 15 mol-%). The resulting mixture was stirred at 70 °C. The resulting samples at defined time intervals were prepared as followed: Aliquots (0.20 mL) were withdrawn

from the reaction mixture, diluted with ethylacetate (1.0 mL), and filtrated over  $\text{Mg}_2\text{SO}_4$ . Consequently, reaction progress was monitored by GC. Yields were calculated by comparing the area of product peak ( $t_{\text{major}} = 12.005$  min and  $t_{\text{minor}} = 12.794$  min) with the area of mesitylene peak ( $t = 5.376$  min). The product, 5-(trifluoromethyl)-dihydro-4,5-diphenylfuran-2(3H)-one, was isolated by column chromatography (silica gel, ethyl acetate/hexane = 1:16) as a clear colorless oil for like form and a white solid for unlike form.

For the recyclability of NHC-CTF, a control experiment was conducted. The NHC-CTF material was collected by centrifugation, washed intensively with dry ethanol and dry ethylacetate to remove any undesired compounds, activated in vacuum at 150 °C for 8 h, and used continuously for a new catalytic run. To ensure the heterogeneity of the catalyst, the catalyst was removed after 2 h from the reaction. The remaining reaction solution was then stirred for further 22 h at 70 °C. Reaction yield was monitored by GC as previously described.

## 5 Results and discussion

### 5.1 Salt templated synthesis of hierarchical covalent triazine frameworks\*\*\*

Many applications such as heterogeneous catalysis<sup>128,164</sup> or the adsorption of large molecules<sup>120</sup> benefit from a porous host material providing both - a high specific surface area as well as mesoporosity. Particularly the existence of mesopores serves to enhance the transport in a secondary pore system and largely increases the total pore volume of the material. For example in lithium sulphur batteries,<sup>###</sup> a high pore volume is necessary to encapsulate large amounts of the electrochemically active sulphur.<sup>165-167</sup> Nitrogen rich materials such as CTFs were recently shown to be promising host materials for this application,<sup>143,145</sup> since they are anticipated to prevent the polysulfide shuttle which is currently one of the major reasons for early cell failure. Therefore, CTF materials with enhanced pore volume and a tailored mesoporosity are desirable for this kind of application (Be aware that chapter 5.4 critically reinvestigates the role of CTFs in lithium sulphur batteries). It was already shown that elevated synthesis temperatures (up to 700 °C) induce formation of mesopores and enlarge the pore volume of CTF-1 (made from 1,4-dicyanobenzene).<sup>91</sup> However, higher reaction temperatures led to a loss of nitrogen and less defined structures of the resulting materials compared to the materials obtained under common reaction conditions, i.e. 40 h at 400 °C. While the triazine framework formation turned out to be reversible at 400 °C, which leads to well defined materials, at higher temperatures additional irreversible reaction pathways like carbonisation and thermal decomposition take place causing defects and nitrogen loss. Thus, this chapter describes the development of an advanced synthetic protocol involving salt templating<sup>168,169</sup> to enable the controlled introduction of mesopores into microporous CTF-1\_400 (Scheme 21) without reducing the nitrogen content drastically.

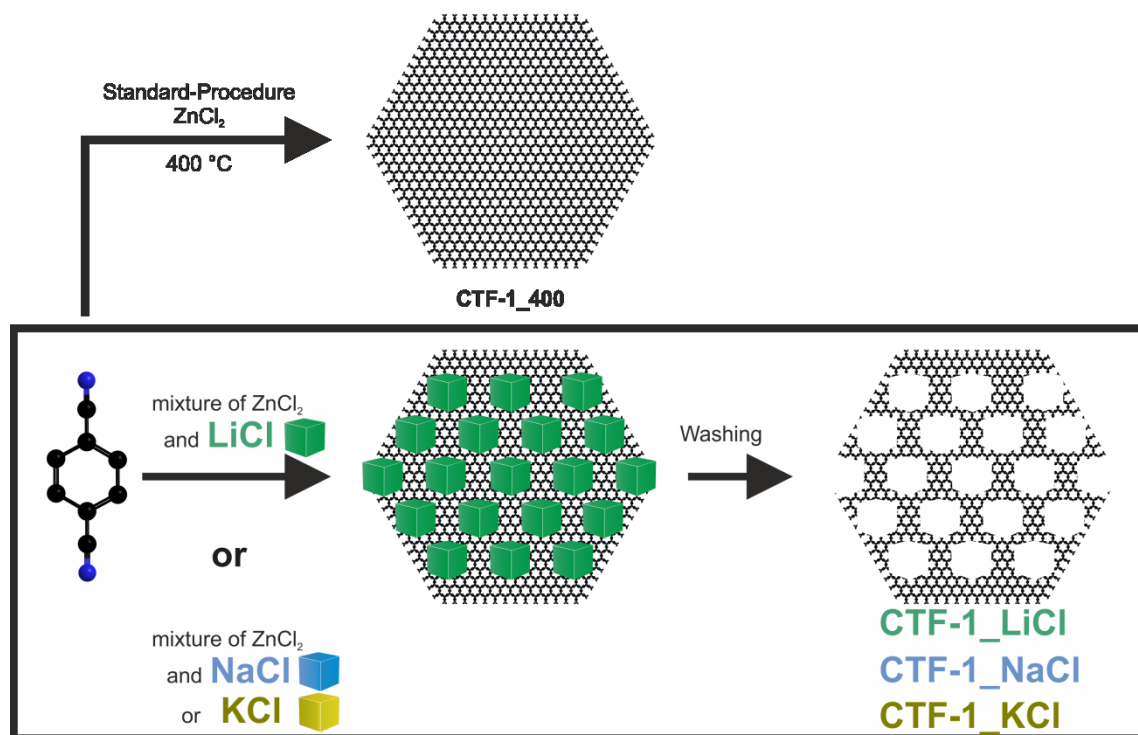
---

\*\*\* Parts of this chapter have been adopted verbatim from my publication.<sup>158</sup>

### In this thesis, a detailed theoretical consideration of the lithium sulphur battery is omitted. In-depth descriptions regarding this topic are provided in the PhD theses of Jan Brückner and Sören Thieme that have been conducted in the group of Prof. Kaskel.<sup>165,166</sup>

---





**Scheme 21** Salt templating procedure for the synthesis of hierarchical CTFs.

In conventional CTF syntheses at  $400\text{ }^\circ\text{C}$  molten  $\text{ZnCl}_2$  acts both as solvent as well as porogen. Instead of using  $\text{ZnCl}_2$  only, binary mixtures of zinc chloride with various alkali chlorides, i.e.  $\text{LiCl}$ ,  $\text{NaCl}$  and  $\text{KCl}$  were used as reaction medium in combination with a modified temperature protocol. In order to maintain mild synthetic conditions the synthesis was performed at  $300\text{ }^\circ\text{C}$  for 60 h to initiate the formation of oligomers (Figure 5a). Subsequently the samples were heated to  $450\text{ }^\circ\text{C}$  for additional 5 h to obtain fully polymerised materials which could be confirmed via infrared spectroscopy by the absence of the intense carbonitrile band at  $2218\text{ cm}^{-1}$  in the spectra (Figure 5b). As a reference a CTF-1 material was synthesised with the same temperature protocol but without additional salt template (CTF-1\_450).

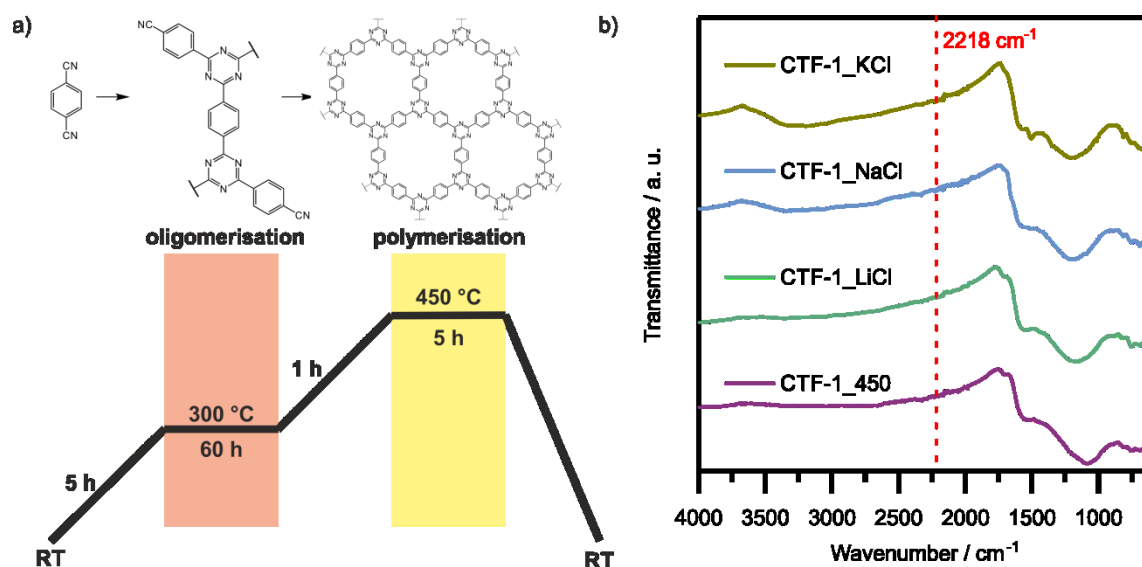


**Figure 5** Temperature protocol applied for the synthesis of salt templated CTFs (a); FT-IR spectra of salt template CTF samples and reference (b).

To figure out the optimal conditions in terms of the porosity several ratios of  $\text{ZnCl}_2$  with employed alkali halides were investigated. Contrary to the findings reported in literature for salt templated carbons,<sup>168</sup> LiCl as well as NaCl and KCl templating creates mesopores with a broad size distribution - showing no impact of the alkali metal cation. For LiCl as a template, an optimal  $\text{ZnCl}_2$ /template molar ratio (with regard to specific surface area and total pore volume) was found to be 1 : 1. For NaCl as template, a  $\text{ZnCl}_2$ /template ratio of 1 : 0.43 and for KCl a  $\text{ZnCl}_2$ /template ratio of 1 : 0.25 led to the best results. Figure 6 exemplarily shows the impact of the NaCl ratio on the porosity properties of the resulting CTF material.

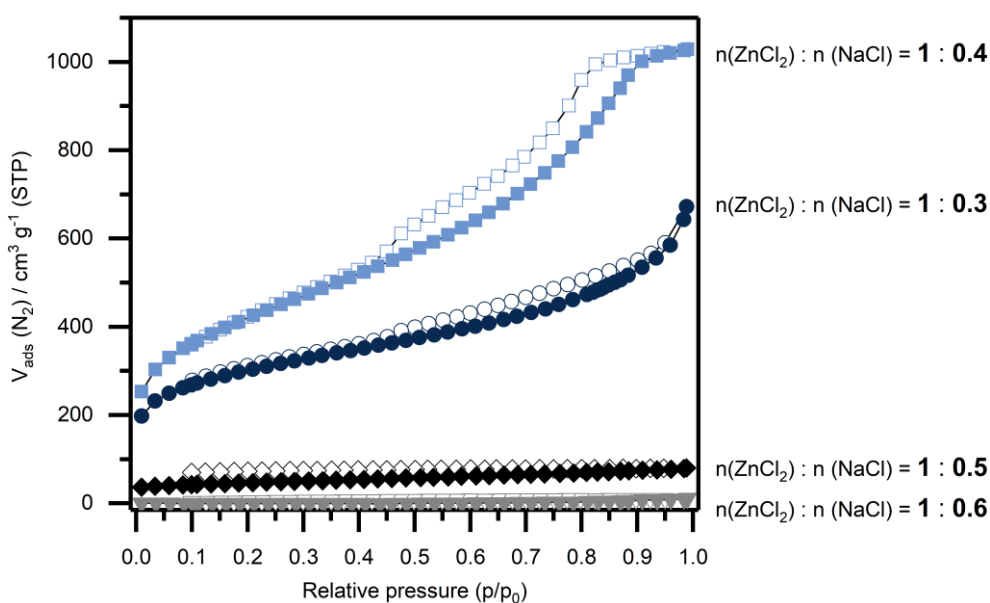


**Figure 6** Influence of different  $\text{ZnCl}_2$  : NaCl ratios on the porosity of the resulting CTF material.

Regarding these findings it is important to consider that the  $\text{ZnCl}_2$ /template ratio strongly influences the melting temperature of the respective binary salt mixture. According to the phase diagrams of the three different  $\text{ZnCl}_2$ /alkali chloride mixtures, at 300 °C the binary mixtures are in the liquid phase for all three empirically determined ratios (see phase diagrams Figure A5–A7).<sup>170,171</sup> The effect of different optimal  $\text{ZnCl}_2$ /template ratios on the porosity may be rationalised by a different solubility of the organic precursors in the corresponding salt melt.<sup>172</sup> A variation of the  $\text{ZnCl}_2$ / template ratio (thus the solution properties of the salt melt) seems to influence the onset of phase demixing during the polymerisation which induces the creation of mesoporosity.<sup>168</sup> Thus, variation of the  $\text{ZnCl}_2$ /alkali chloride ratio may allow for adjusting the solubility of the organic phase (thus of monomers and oligomers) in the molten salt phase.<sup>173</sup> If the optimal ratio in terms of solubility properties is exceeded, a phase demixing is favoured in earlier stages of the polymerisation reaction and a decreased porosity in terms of specific surface area and total pore volume was observed.

To exactly investigate the porosity, argon physisorption measurements were performed at 87 K in addition to nitrogen physisorption at 77 K (Figure 7a). As described earlier in chapter 3.1, argon is more favourable than nitrogen as adsorptive for CTF materials to obtain accurate pore size distributions,<sup>4</sup> because of its indifference with respect to polar surface features of the nitrogen rich CTFs. The physisorption experiments reveal that salt templating leads to an enormous increase of total pore volume as compared to the reference CTF\_450 material synthesised with the same temperature protocol but without additional salt template. While the reference is a predominantly microporous material with a type I(a) isotherm (mean pore width 0.5 nm and 1.0 nm, see Figure 7b), LiCl templated CTF-1 (CTF-1\_LiCl) shows a comparable gas uptake in the low relative pressure range and a continuously increasing gas uptake in the whole pressure range, pointing to the presence of mesopores (from 2 to 16 nm, Figure 7b). Also NaCl templated CTF-1 (CTF-1\_NaCl) and KCl templated CTF-1 (CTF-1\_KCl) show type IV(a) isotherm characteristic for mesoporous materials, but the hysteresis loop for both materials closes at a lower relative pressure of  $p/p_0 = 0.4$ , which can be attributed to differences in pore connection.

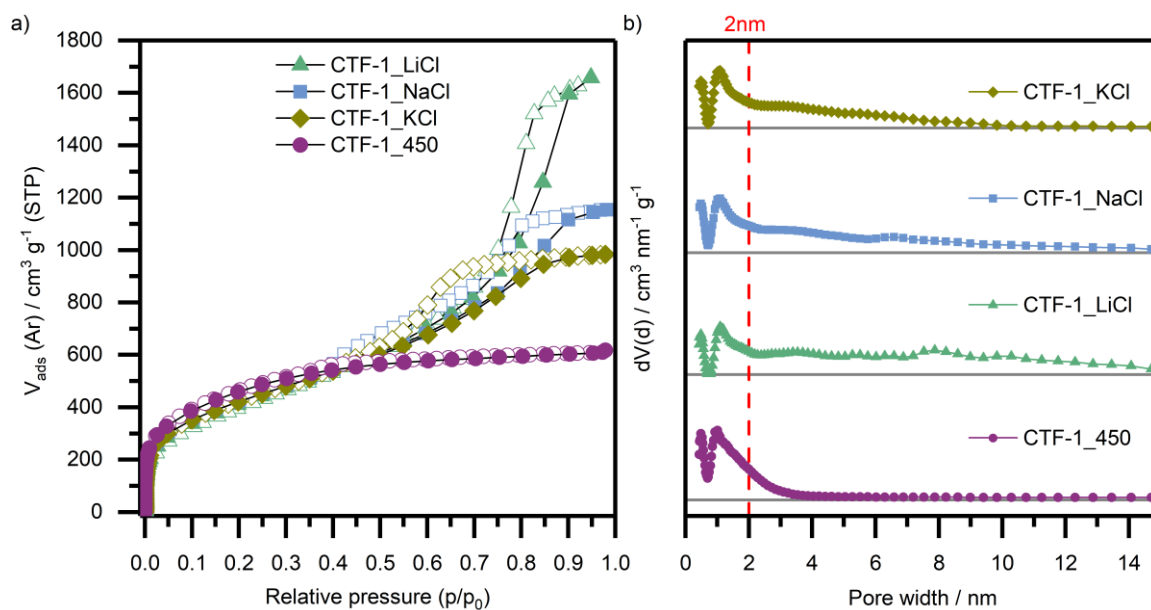


**Figure 7** Argon physisorption isotherm (87 K) of salt templated CTF samples and reference (a); Pore size distribution (QSDFT) of respective samples (b).

To estimate the specific surface area (Table 6) as well as the pore size distribution of the materials, the BET model and the Quenched Solid Density Functional Theory (QSDFT) method developed for carbons (slit pores, equilibrium kernel) were applied. Interestingly, all salt templated samples have comparable specific surface areas of approx.  $1340 \text{ m}^2 \text{ g}^{-1}$  (according to argon isotherms). These values are only slightly lower than that of reference CTF-1\_450 material ( $S_{\text{BET}} = 1450 \text{ m}^2 \text{ g}^{-1}$ , see Table 6) prepared in a  $\text{ZnCl}_2$  melt without additional alkali halides. Nevertheless, the salt templated samples exhibit significantly increased specific surface areas compared to a conventionally synthesised CTF-1\_400 ( $S_{\text{BET}} = 1070 \text{ m}^2 \text{ g}^{-1}$ ). It is also important to mention the overestimation of the specific ultramicropore volume (see Table 6) in these N-doped materials using  $\text{N}_2$  physisorption caused by quadrupole interactions. The latter demonstrates the importance of argon adsorption at 87 K in analysing pore size distributions of the investigated samples within this thesis.<sup>4</sup> More importantly, salt templating leads to a drastic increase of the mesopore volume ( $V_{\text{Meso}}$ ). Both materials, conventionally synthesised CTF-1\_400 ( $V_{\text{Micro}}/V_{\text{Meso}} = 8.60$ ) and the reference CTF-1\_450 ( $V_{\text{Micro}}/V_{\text{Meso}} = 3.47$ ) are predominantly microporous with small mesopore volume of  $0.05 \text{ cm}^3 \text{ g}^{-1}$  and  $0.17 \text{ cm}^3 \text{ g}^{-1}$ , respectively. In contrast, CTF-1\_LiCl has a ten times higher mesopore volume of  $1.72 \text{ cm}^3 \text{ g}^{-1}$ . Also CTF-1\_NaCl and CTF-1\_KCl display a high mesopore volume of  $1.01 \text{ cm}^3 \text{ g}^{-1}$  and  $0.79 \text{ cm}^3 \text{ g}^{-1}$ , respectively. These data prove that salt templating enables the synthesis of

predominantly mesoporous materials ( $V_{\text{Micro}}/V_{\text{Meso}} = 0.21$  for CTF-1\_LiCl, 0.43 for CTF-1\_NaCl, and 0.56 for CTF-1\_KCl, respectively) while still retaining high surface areas.

**Table 6** Porosity data of the investigated CTF samples including their specific surface area, ultramicropore volume, supermicropore volume, mesopore volume, ratio of micropore and mesopore volume and total pore volume (at  $p/p_0 = 0.95$ ).

Sample	Gas	$S_{\text{BET}}$ $\text{m}^2 \text{g}^{-1}$	$V_{\text{Umicro}}$ $\text{cm}^3 \text{g}^{-1}$	$V_{\text{Smicro}}$ $\text{cm}^3 \text{g}^{-1}$	$V_{\text{Meso}}$ $\text{cm}^3 \text{g}^{-1}$	$V_{\text{Micro}}/V_{\text{Meso}}$	$V_{\text{Total}}$ $\text{cm}^3 \text{g}^{-1}$
CTF-1_400	Ar	1070	0.13	0.30	0.05	9.16	0.5
	N <sub>2</sub>	1130	0.17	0.27	0.10	4.24	0.5
CTF-1_450	Ar	1445	0.11	0.48	0.17	3.35	0.8
	N <sub>2</sub>	1520	0.15	0.43	0.17	3.51	0.8
CTF-1_LiCl	Ar	1323	0.06	0.30	1.72	0.21	2.1
	N <sub>2</sub>	1440	0.09	0.31	1.66	0.24	2.1
CTF-1_NaCl	Ar	1345	0.08	0.35	1.01	0.43	1.5
	N <sub>2</sub>	1450	0.12	0.32	0.98	0.45	1.5
CTF-1_KCl	Ar	1340	0.08	0.36	0.79	0.56	1.25
	N <sub>2</sub>	1470	0.11	0.35	0.99	0.47	1.3

PXRD data reveal that all analysed samples are amorphous (Figure A8). In a next step, the sample morphology was investigated by means of scanning electron microscopy. The SEM images represent different textural properties and seem to be affected by the respective salt template. While CTF-1\_450 shows a very smooth surface, all templated samples show a different morphology with varying surface roughness (see Figure 8). Additional transmission electron microscopy (TEM) measurements could not represent the pore structure, which indicates statistically distributed mesopores (Figure A9–A12).

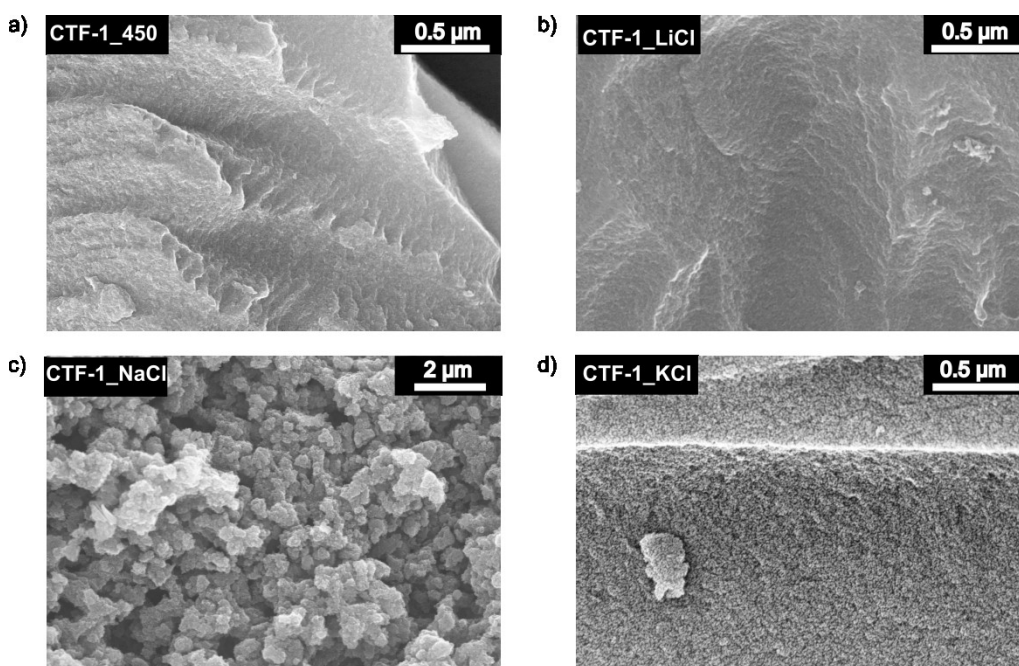


**Figure 8** SEM pictures of CTF-1\_450 (a), CTF-1\_LiCl (b), CTF-1\_NaCl (c) and CTF-1\_KCl (d).

Bulk combustion elemental analysis (Figure 9, Table A1 in appendix) reveals that CTF-1\_KCl shows the lowest C/N ratio ( $C/N = 5.5$ ) of all investigated samples (CTF-1\_400:  $C/N = 5.8$ ; ideal  $C/N$  is 4.0, assuming that no degradation and no carbonisation take place). Also CTF-1\_LiCl and CTF-1\_NaCl show a fairly good C/N value of 6.3 and 5.6, respectively.

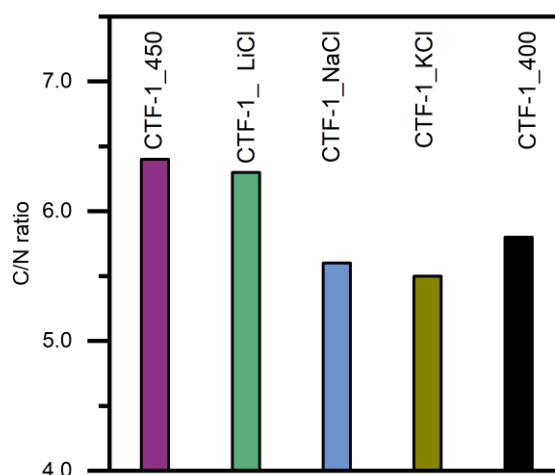


**Figure 9** Carbon to nitrogen ratio derived from elemental analysis of investigated CTF samples.

According to the literature,<sup>81</sup> it is possible to increase the nitrogen content and to obtain ordered materials using an equimolar ratio of monomer to  $ZnCl_2$ . To this end, it was also tried to synthesise ordered CTF-1 materials via the salt templating approach. Indeed, the results from elemental analysis show an increased nitrogen content as illustrated by low C/N values of 5.0 (for CTF-1\_LiCl [1 eq.  $ZnCl_2$ ]),  $C/N = 4.9$  (for NaCl), and  $C/N = 4.8$  (for KCl),

respectively. As expected, all samples show mesoporosity (Figure A13). However, no ordered materials could be obtained as proven by PXRD (Figure A14). Based on these results, the synthetic conditions need to be adjusted precisely in the future to possibly obtain crystalline and mesoporous materials.

In conclusion, salt templating is an effective synthetic tool to simultaneously achieve a high nitrogen content and total pore volume, while established CTF syntheses at elevated temperatures used to enhance the pore volume in general cause nitrogen loss. The method invented within this thesis can also be considered as highly competitive when considering the rare examples of other templating methods to induce additional pores to create porosity.<sup>174</sup> A template approach applying silica nanoparticles yielded less porous CTFs with specific surface areas ranging from 90 – 565 m<sup>2</sup> g<sup>-1</sup> and pore volumes of 0.32 – 0.44 cm<sup>3</sup> g<sup>-1</sup>. However, the method reported allows for the synthesis of CTF materials exhibiting an ordered interconnected pore system. In contrast, the possibility to form hierarchical CTFs by introducing mesopores associated with enhanced total pore volume can be regarded as the main benefit of this work. Exemplarily, NaCl templated CTF-1\_NaCl has a pore volume of 1.5 cm<sup>3</sup> g<sup>-1</sup>, which exceeds the value for microporous CTF-1\_400 of 0.5 cm<sup>3</sup> g<sup>-1</sup> significantly. Moreover, elemental analysis show a low C/N value of 5.6, which is slightly better compared with CTF-1\_400 (C/N = 5.8) synthesised under established conditions.

## 5.2 Mechanochemical synthesis of covalent triazine frameworks<sup>\*\*\*</sup>

The classical synthetic pathway of CTFs includes the ionothermal trimerization of aromatic nitriles in molten  $\text{ZnCl}_2$ .<sup>81</sup> Since this approach requires the synthesis in sealed ampoules at harsh conditions, many possible monomers are excluded due to the simple fact that they decompose at elevated temperatures. To overcome this problem, Cooper and co-workers developed a room temperature synthesis including trifluoromethanesulfonic acid as strong Brønsted acid catalyst to activate nitrile groups and subsequently trigger trimerization.<sup>96</sup> In general, the Brønsted acid catalysed protocol demands inert solvents like chloroform which do not interact with the strong acid. Thus, this method is limited to those monomers well soluble in unreactive solvents and is not scalable very well. Both synthetic pathways are strongly restricted to aromatic nitriles of which just a few are commercially available. More complex compounds, required for tailored applications, involve complex and time-consuming organic synthesis which often contains a cyanation using hazardous inorganic metal cyanides in the last sequence. A very recent approach applies  $\text{AlCl}_3$  mediated Friedel-Crafts alkylation of cyanuric chloride which already bears the triazine core to synthesise CTF materials.<sup>97</sup> A drawback of this route is that the formation of these polymers does not occur reversibly, like in the case of a dynamic trimerization, but significantly broadens the variety of possible monomers since they do not require cyano-functionalization anymore.

However, all classical CTF syntheses are neither economically nor ecologically favourable, hugely suffering from a lack of scalability. To overcome these restrictions and in parallel bypass the need for hazardous solvents, a novel mechanochemical pathway for the synthesis of CTFs has been investigated within this thesis. This chapter describes the findings of this approach that combines the benefits of a scalable synthesis with readily available and inexpensive educts.

Initial tests were performed using the simplest aromatic nitrile (1,4-dicyanobenzene) to mechanochemically trigger the trimerization reaction by the aid of a Lewis acid ( $\text{ZnCl}_2$  or  $\text{AlCl}_3$ ) like in the case of a conventional ampoule synthesis. It became apparent that none of these approaches led to the formation of a polymer, not even oligomerisation was observed (by means of FT-IR spectroscopy, Figure A15). Thus, the synthetic efforts were moved towards another

---

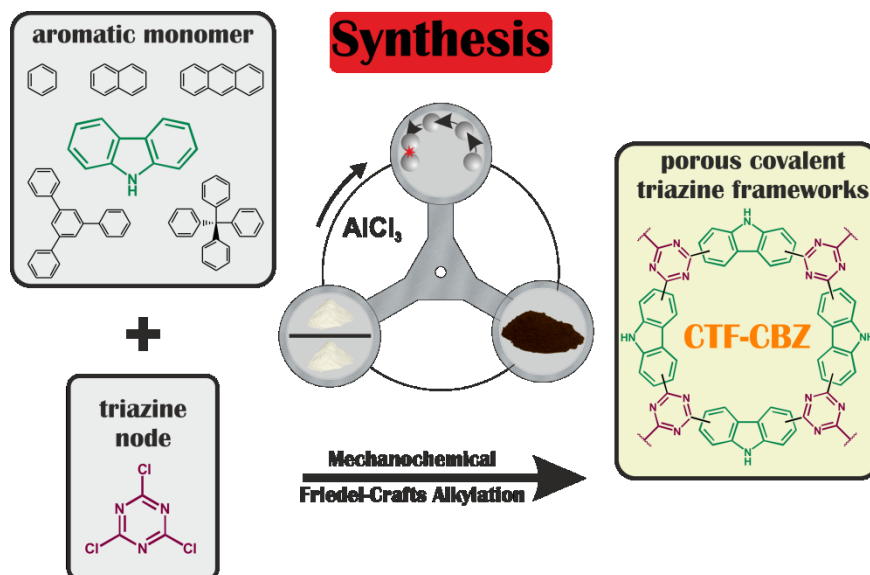
<sup>\*\*\*</sup> Parts of this chapter have been adopted verbatim from my publication.<sup>104</sup>



possibility - the mechanochemical synthesis of CTF materials by Friedel-Crafts alkylation (see Scheme 22).

### 5.2.1 Carbazole-based porous organic polymers

For the initial experiments, carbazole was chosen as a model monomer. Being an electron-rich substrate, carbazole would easily react with electrophilic cyanuric chloride to prove the feasibility of Friedel-Crafts alkylation for mechanochemistry. A decisive factor in mechanochemistry is the milling material, since its density determines the energy impact on the reactants. Exhibiting the highest density, tungsten carbide balls were utilised to perform the polymerisation reaction. Taking 1.5 equivalent of the monomer (carbazole), a stoichiometric amount of the triazine node cyanuric chloride (1.0 equivalents), as well as 5 equivalents of  $\text{AlCl}_3$  as an activating reagent and  $\text{ZnCl}_2$  as a bulking agent (to reach a minimum amount of 10 g in the grinding jar), the educts were converted into an insoluble solid by milling them for 1 h in a planetary ball mill. The samples were purified via Soxhlet extraction with water and THF to obtain a permanently porous CTF ( $S_{\text{BET}} = 380 \text{ m}^2 \text{ g}^{-1}$  according  $\text{N}_2$  adsorption, see Figure 10) with yields surpassing 90 %.



**Scheme 22** Mechanochemical syntheses of porous covalent triazine frameworks by Friedel-Crafts alkylation of different aromatic monomers with cyanuric chloride.\*\*\*

\*\*\* Within this general scheme, the substitution pattern of carbazole is not determined. The exact position of the substitution will be illustrated later in this chapter.

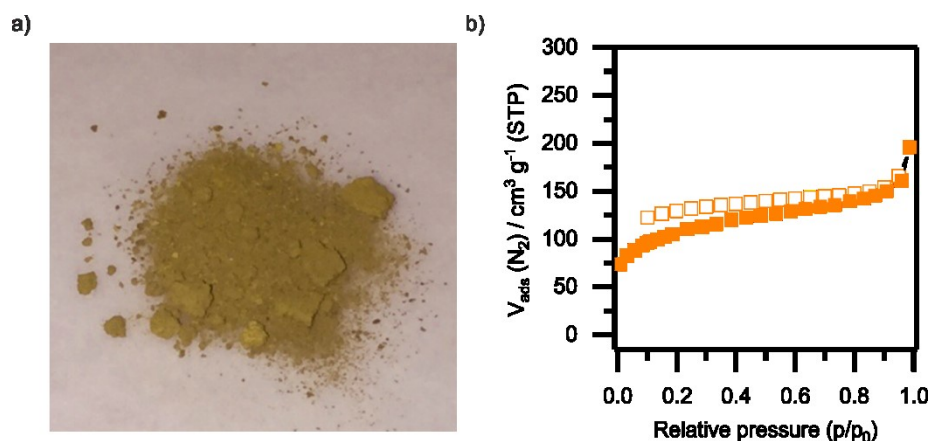


**Figure 10** a) picture of CTF-CBZ, b) nitrogen physisorption isotherm (77 K) of CTF-CBZ.

The successful network formation was initially verified by means of FT-IR spectroscopy. Confirming C-C bond formation which is occurring during the Friedel-Crafts alkylation is difficult for insoluble CTF materials. FT-IR spectroscopy reveals the presence of characteristic N-H vibration (br,  $3300 - 3400 \text{ cm}^{-1}$ ) of the carbazole unit as well as strong C=N vibrations ( $1490 \text{ cm}^{-1}$  and  $1348 \text{ cm}^{-1}$ ) resulting from the triazine core (Figure 11a). In contrast to classical CTF syntheses, the IR spectrum displays discrete vibrations due to a well-defined material showing no carbonisation. To support this structural information  $^{13}\text{C}$  CP/MAS NMR spectroscopy (Figure 11b) was performed, comparing the monomer carbazole and the resulting carbazole-CTF (CTF-CBZ). The presence of a signal in the expected range of the triazine ring carbons (171 ppm) supports the successful network formation. Also all other major peaks corresponding to the aromatic carbons of the carbazole unit (105 ppm – 145 ppm) are present in the spectrum. All signals show a small shift which represents the electron withdrawing character of the triazine moieties and thus a changed electronic environment of the carbazole unit in the CTF-CBZ.

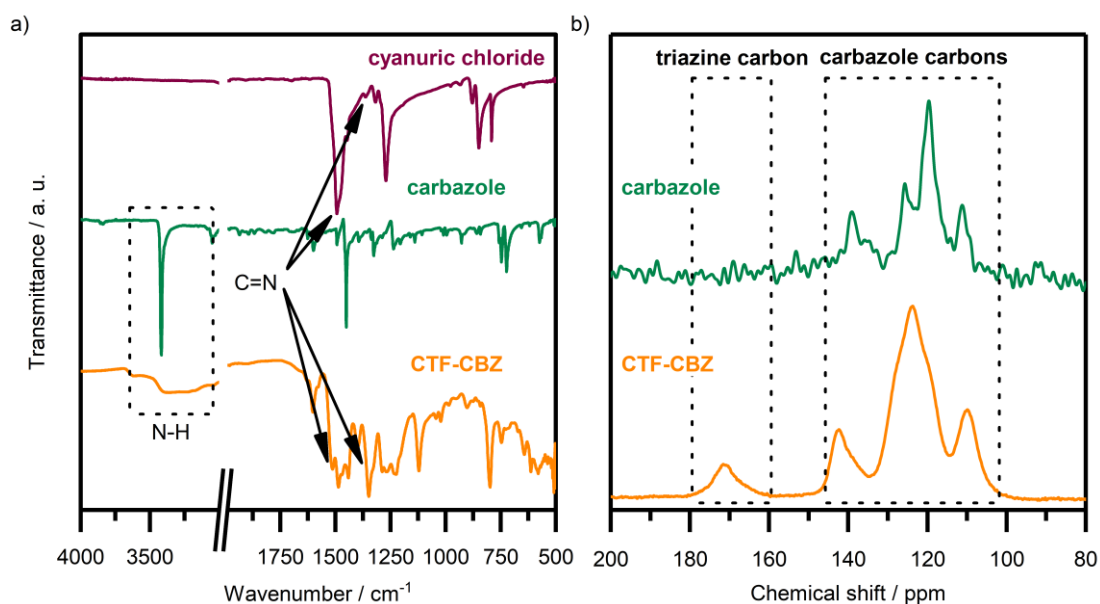


**Figure 11** a) FT-IR spectra of carbazole-CTF (CTF-CBZ), carbazole and cyanuric chloride, b) <sup>13</sup>C CP/MAS NMR spectra of CTF-CBZ and carbazole.

To gain insight into the local chemical environment in the material, X-ray photoelectron spectroscopy (XPS) measurements were conducted. The C 1s spectrum of CTF-CBZ reveals three major peaks (Figure 12a), which can be attributed to sp<sup>2</sup> carbon atoms of the carbazole moiety (284.7 eV), the carbon atoms in the triazine node (285.5 eV) and to phenolic C-OH groups (286.6 eV), which may occur due to hydrolysis of unsaturated C-Cl groups of the triazine node during workup. The high resolution N 1s spectrum (Figure 12b) shows two major nitrogen species. The first signal observed at around 398.7 eV can be assigned to nitrogen atoms within the triazine units (C-N=C). The peak at 400.2 eV arises from pyrrolic nitrogen of the carbazole moiety, which proves the intact structure of the resulting CTF material. Furthermore at a binding energy of 401.3 eV a minor contribution of quaternary nitrogen species becomes apparent which also may occur upon hydrolysis under acidic conditions.

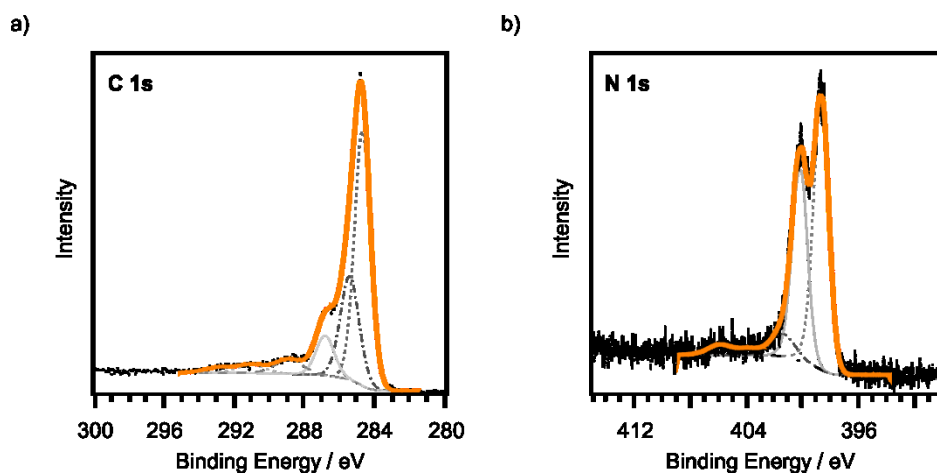


**Figure 12** C 1s XPS spectrum of CTF-CBZ (c), N 1s XPS spectrum of CTF-CBZ (d).

Elemental analysis (EA) of CTF-CBZ showed a C/N ratio ( $C/N = 4.8$ ) close to the theoretical one assuming a perfect structure ( $C/N = 4.7$ ) (see Table A2 for all investigated samples). As expected, the material synthesised in the ball mill showed no carbonisation (indicated by a higher C/N ratio) in contrast to CTF materials synthesised in ampoules.<sup>81</sup>

In order to determine the maximum porosity of the flexible polymer, the resulting yellowish sample was re-dispersed in anhydrous acetone which was exchanged by liquid CO<sub>2</sub> and subsequently supercritically dried. Consequently, argon physisorption measurements were performed at 87 K (Figure 13a). The isotherm reveals a steep increase in argon uptake in the low relative pressure range, indicating microporosity. A continuous increase of gas uptake in the whole pressure range points to adsorption on the outer surface of small particles, mesopores with a very broad size distribution or swelling. The increase at a relative pressure above 0.9 could be attributed to the condensation of argon in interparticular voids.<sup>70</sup> The hysteresis loop does not close throughout the whole pressure range, displaying the flexible framework structure. This effect was described several times before, especially for disordered porous polymers. It is attributed to a dynamic behaviour of the materials by swelling of the frameworks through elastic deformations in course of the gas adsorption.<sup>53</sup> The physisorption experiments reveal a specific surface area of  $570 \text{ m}^2 \text{ g}^{-1}$  ( $S_{\text{BET}}$ ) and a narrow pore size distribution (QSDFT, Figure 13b) showing two types of micropores with a size of 0.5 nm and 1.0 nm, respectively. However, pore size distributions of soft, organic microporous materials need to be regarded with care, since effects like swelling render these methods prone to errors.<sup>153</sup>

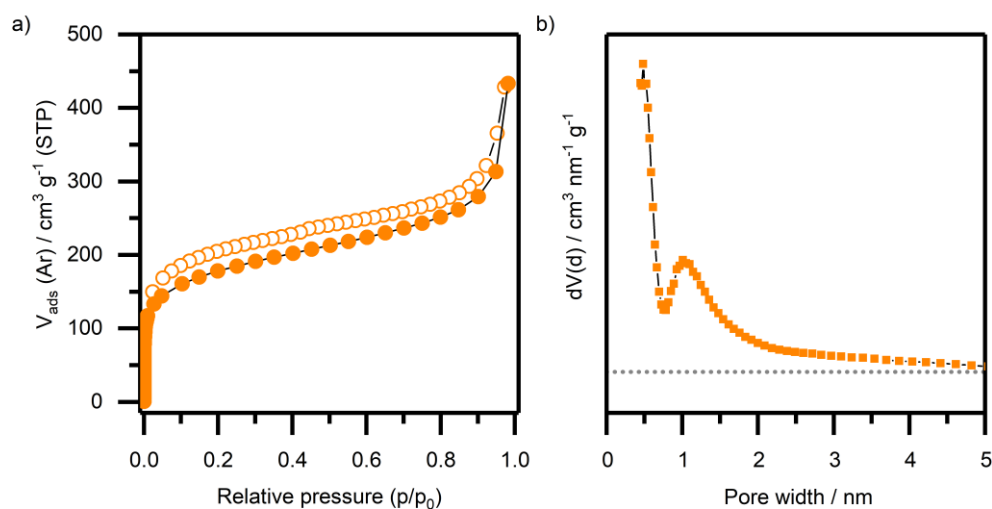


**Figure 13** Argon physisorption isotherm (87 K) of CTF-CBZ (a), Pore size distributed (QSDTF) (b).

As expected, the carbazole CTF is amorphous as determined by powder X-ray diffraction (Figure 14a). The diffractogram shows no reflections of an ordered CTF structure but reveals the presence of tungsten carbide which is caused by abrasion during the milling process. To quantify the amount of residual milling material, thermogravimetric analysis (TGA) in air was performed (Figure 14b). TGA shows a low residual mass of 1.5 %, reflecting an acceptable degree of impurity that can be hardly suppressed by mechanochemistry. Furthermore, it can be observed that decomposition of the material starts at 480 °C in air and 620 °C in argon, respectively (Figure A16). Scanning electron microscopy (SEM) reveals agglomeration of particles with a rough surface, showing no uniform shape (Figure A17).

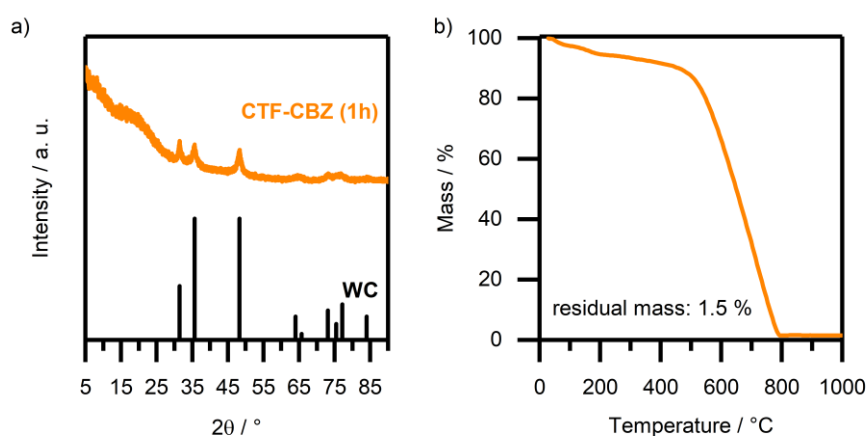


**Figure 14** PXRD data of CTF-CBZ revealing traces of tungsten carbide (a); Thermogravimetric analysis of CTF-CBZ under synthetic air (b).

After having characterised the resulting material in detail, the influence of a different milling material was studied, choosing  $\text{ZrO}_2$  which should be not affected by the corrosive environment during the reaction (instead of other alternatives such as steel). As a consequence, the yields of the reaction dropped down drastically, yielding only 17 % after a reaction time of 1 h and 50 % after 3 h, respectively. The porosity of these carbazole-based polymers remained comparable to those materials, synthesised with WC balls ( $650 \text{ m}^2 \text{ g}^{-1}$  with  $\text{ZrO}_2$  and  $740 \text{ m}^2 \text{ g}^{-1}$  with WC). Also the bulking material was varied, which role can be interpreted as an inert additive enabling control of the reaction scale (a total mass loading of 10 g in the milling jar was applied for all experiments). By applying inert alkali halides instead of  $\text{ZnCl}_2$ , as expected no pronounced difference could be detected (Figure A18). Thus, all further investigations were performed on the initial system, using WC balls and  $\text{ZnCl}_2$  as bulking agent.

To gain insight into the mechanisms of the ongoing network formation, kinetic studies on the polymerisation reaction were performed. Therefore samples after 5, 10, 15, 30, 45 and 60 minutes were examined to study the evolution of porosity and yield during the reaction (Figure 15a). After 15 min already, a porous material in a yield of 32 % was obtained. While the porosity remained constant from this point on ( $S_{\text{BET}} = 740 \text{ m}^2 \text{ g}^{-1}$  due to  $\text{N}_2$  physisorption; Figure A20), the yield is increasing to reach a complete conversion with a yield of 98 % after 60 min. The reaction kinetics was investigated applying an advanced milling setup allowing the *in situ* monitoring of pressure and temperature developments inside the milling chamber (Figure 15b). In order to consider the heating induced by the milling progress, the data of a blank sample (only  $\text{AlCl}_3$ ) was subtracted to correct the obtained data. An induction period of 10 min could be observed for the polymerisation reaction. Starting after 10 min already, a steep increase of the pressure in the milling chamber associated with a temperature rise takes place, indicating the beginning of an exothermic reaction.

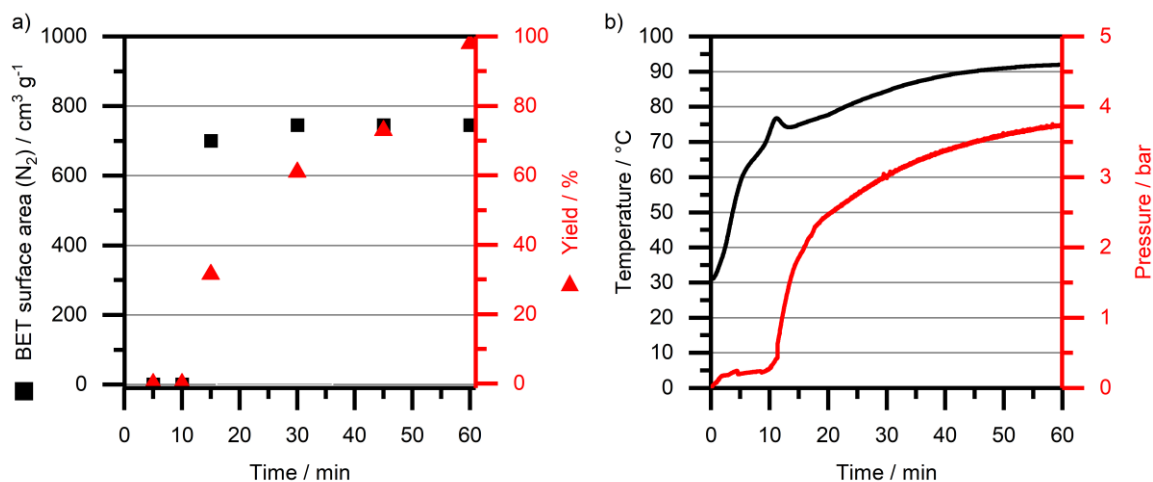


**Figure 15** a) Evolution of porosity and yield of the polymerisation reaction for the synthesis of CTF-CBZ, b) *in situ* analysis of temperature and pressure in the milling jar.

To study the mechanisms of polymerisation, the reaction mixture was analysed by means of liquid-state <sup>1</sup>H (Figure 17a) and <sup>13</sup>C NMR spectroscopy (Figure 17b) after 5 min and 10 min, respectively (Figure 17b). Following an aqueous work-up of the crude reaction mixture, solely unreacted starting material could be observed (pure carbazole) after 5 min. After 10 min additional peaks in the region of the triazine unit can be observed, suggesting soluble adducts of carbazole and cyanuric chloride. Two-dimensional liquid-state <sup>1</sup>H/<sup>13</sup>C-HMBC NMR spectroscopy of the reaction product after 10 min could provide proof that carbazole shows a substitution in position 3, as would have been expected from liquid-phase reactions (Figure 17). Thus, these spectra verify the formation of intermediate carbazole/cyanuric chloride adducts during the polymerisation reaction, supporting the assumed structure of CTF-CBZ.

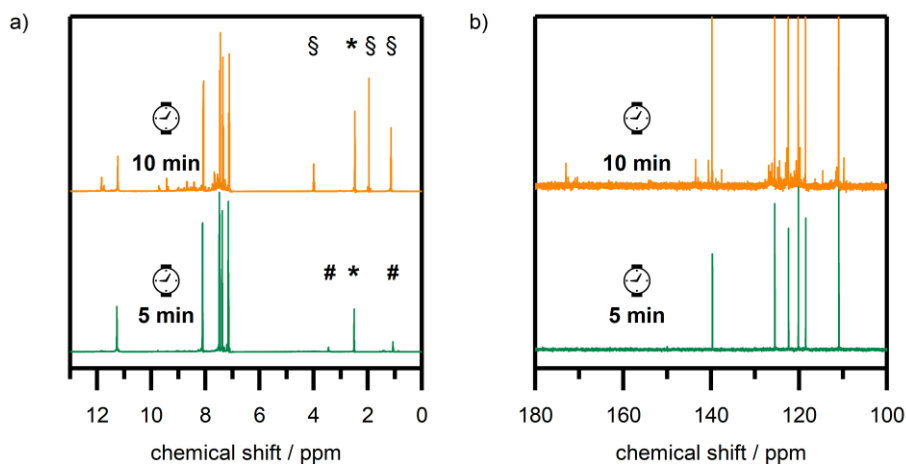


**Figure 16** (a) <sup>1</sup>H NMR spectra of samples taken after 5 minutes and 10 minutes. § EtOAc, \* DMSO, # EtOH; (b) <sup>13</sup>C NMR spectra of samples taken after 5 minutes and 10 minutes. Deuterated solvent: DMSO-d<sub>6</sub>.

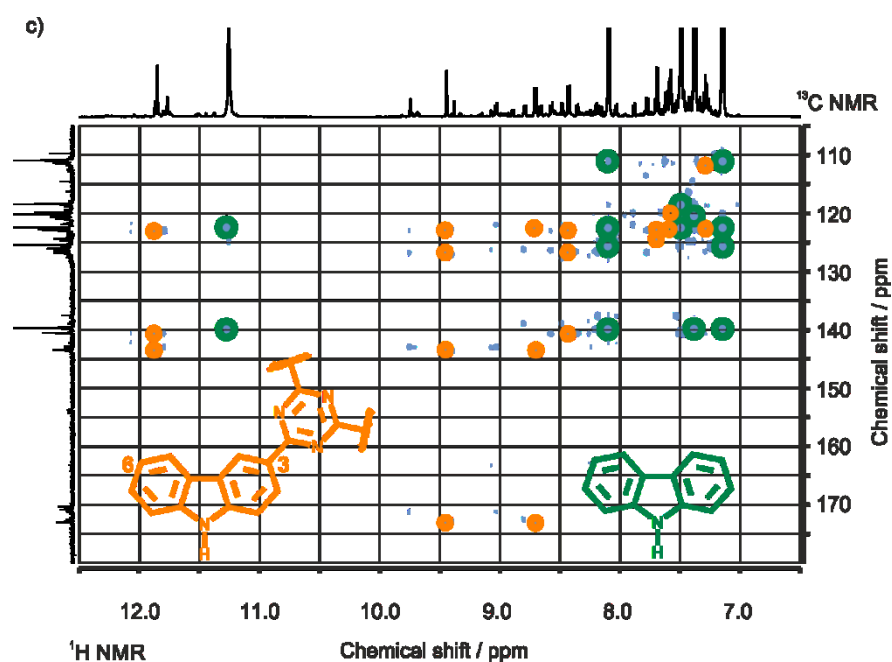


**Figure 17**  $^1\text{H}/^{13}\text{C}$ -HMBC spectrum of CTF-CBZ reaction mixture after 10 min reaction time. Main component is unreacted carbazole. Peaks corresponding to the main product (3-substituted carbazole) are marked.

Furthermore the existence of an oligomeric fraction can also be observed in the MALDI-TOF spectrum of the 10 minute sample (Figure 18).

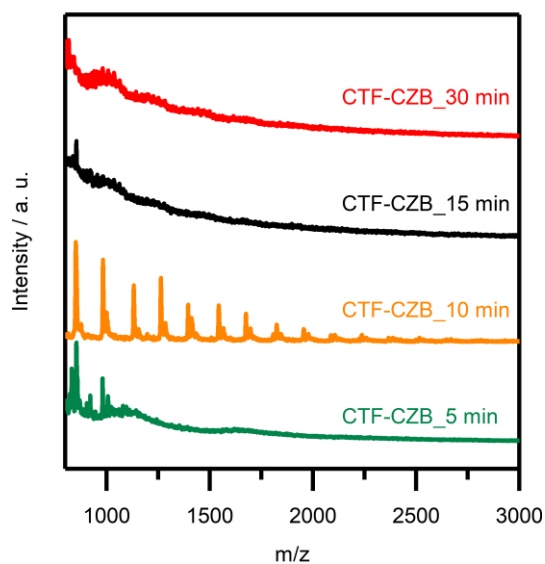


**Figure 18** MALDI-TOF spectra of CTF-CBZ samples taken at different times from the polymerisation reaction.



### 5.2.2 Porous organic polymers from other aromatic monomers

To demonstrate a general applicability of this approach, other monomers with different geometry and different size were also investigated (see Scheme 22). As a general trend, all those monomers which bear a large conjugated  $\pi$ -system led to a high yield in the Friedel-Crafts alkylation. Thus, anthracene and 1,3,5-triphenylbenzene could be converted into porous CTFs (CTF-AC and CTF-TPB) with a high yield of 96 % and 82 %, respectively (see Table 7).

**Table 7** Porous CTFs of different monomers and their specific surface area (argon), total pore volume (at  $p/p_0 = 0.95$ ) and yield (reaction time).

Sample	Monomer	$S_{\text{BET}}$ $\text{m}^2 \text{g}^{-1}$	$V_{\text{Total}}$ $\text{cm}^3 \text{g}^{-1}$	Yield / (time)
CTF-CBZ	carbazole	570	0.40	98 % (1 h)
CTF-AC	anthracene	470	0.34	96 % (1 h)
CTF-TPB	triphenylbenzene	590	0.39	82 % (1 h)
CTF-BZ	benzene	170	0.20	5 % (2 h)
CTF-NT	naphthalene	110	0.17	2 % (2 h)
CTF-TPM	tetraphenylmethane	390	0.43	3 % (2 h)

To prove the successful network formation,  $^{13}\text{C}$  CP/MAS NMR, FT-IR and XPS were performed, showing clearly that C-C bond formation occurred to build up the porous polymer (Figure A21 – A25).\*\*\* Argon physisorption reveals that all investigated monomers yield porous polymers. The most porous CTFs can be obtained from anthracene (CTF-AC, with a surface area of  $470 \text{ m}^2 \text{ g}^{-1}$ ) and triphenylbenzene (CTF-TPB,  $S_{\text{BET}} = 590 \text{ m}^2 \text{ g}^{-1}$ ), respectively (Figure 19). Since the porosity of these polymers is presumably a result of ineffective packing of the polymer chains, different porosities were obtained for different monomers. It can be assumed that larger monomers such as carbazole, triphenylbenzene and anthracene cause sterically more hindered and contorted polymeric units which may potentially be a reason for higher

\*\*\* From these experiments, it was not possible to determine the position of triazine substitution. However, from liquid phase reactions the preferred positions of electrophilic substitution of those aromatic compounds investigated here are well understood (1,3 for benzene, 1,5 for naphthalene, 9,10 for anthracene, *para* isomer for triphenylbenzene, *para* isomer for tetraphenylmethane).<sup>175</sup>

surface areas. Also the different connectivity of the tectons should be taken into account. While the triazine node is an A3 type building block, the applied monomers are A2 type (carbazole, benzene, naphthalene and anthracene), A3 type (triphenylbenzene) or A4 type (tetraphenylmethane) monomers. From these geometric restrictions, different structures will result which also explains differences in the porosity of the respective polymers.

Elemental analysis display C/N-values of 8.5 for CTF-AC (ideal 8.0) and 11.5 for CTF-TPB (ideal 9.0) which strengthen the hypothesis of network formation, since the monomers contain no nitrogen (Table A2). Interestingly, also those monomers assumed to be unreactive such as benzene, naphthalene and tetraphenylmethane yielded small amounts of porous polymers (Table 7). Moreover, FT-IR spectroscopy and elemental analysis verified the formation of all assumed products.

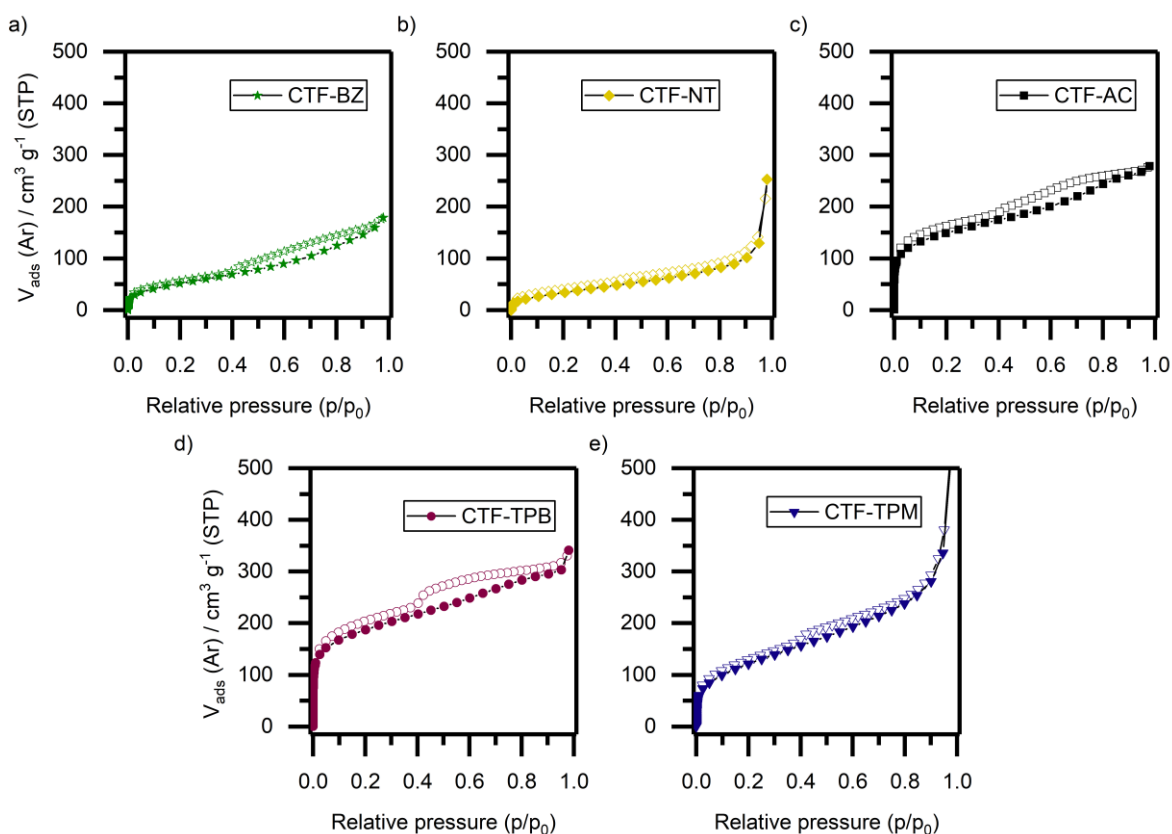


**Figure 19** Argon physisorption isotherm (87 K) of mechanochemically synthesised CTFs from benzene (a), naphthalene (b), anthracene (c), triphenylbenzene (d) and tetraphenylmethane (e).

The presented results show that the general rules of reactivity/nucleophilicity are still valid but mechanochemistry enables the reaction with monomers, which were seen to be completely unreactive in liquid-phase chemistry. In Table 8, a comparison of the surface areas regarding different monomers and the derived CTFs using classical ampoule syntheses, Brønsted acid

catalysed and the mechanochemically synthesised CTFs is given. Considering these results, it is evident that some CTFs are not accessible by the existing methods. While the method presented within the thesis at hand yields porous materials for each monomer, other approaches have limitations.

**Table 8** Comparison of BET surface areas regarding different monomers and the derived CTFs using classical ampoule syntheses ( $\text{N}_2$  BET surface area), Brønsted acid catalysed ( $\text{N}_2$  BET surface area) and the mechanochemically synthesised CTFs (Argon BET surface area).

Monomer	Ampoule synthesis	Synthesis via Brønsted acid	Ball mill synthesis
1,4-dicyanobenzene benzene	800 -1000 $\text{m}^2 \text{g}^{-1}$ ( $\text{N}_2$ ) <sup>81</sup>	2 $\text{m}^2 \text{g}^{-1}$ ( $\text{N}_2$ ) <sup>96</sup>	170 $\text{m}^2 \text{g}^{-1}$ ( <b>Argon</b> )
2,6-naphthalenedicarbonitrile naphthalene	90 $\text{m}^2 \text{g}^{-1}$ ( $\text{N}_2$ ) <sup>86</sup>	-	110 $\text{m}^2 \text{g}^{-1}$ ( <b>Argon</b> )
anthracene	-	-	470 $\text{m}^2 \text{g}^{-1}$ ( <b>Argon</b> )
3,6-dicyanocarbazole carbazole	1187 $\text{m}^2 \text{g}^{-1}$ ( $\text{N}_2$ ) <sup>92</sup>	-	570 $\text{m}^2 \text{g}^{-1}$ ( <b>Argon</b> )
1,3,5-tris(4- cyanophenyl)benzene triphenylbenzene	975 $\text{m}^2 \text{g}^{-1}$ ( $\text{N}_2$ ) <sup>81</sup>	867 $\text{m}^2 \text{g}^{-1}$ ( $\text{N}_2$ ) <sup>96</sup>	590 $\text{m}^2 \text{g}^{-1}$ ( <b>Argon</b> )
4,4',4'',4'''- methanetetrayltetrabenzonitrile tetraphenylmethane	-	1152 $\text{m}^2 \text{g}^{-1}$ ( $\text{N}_2$ ) <sup>96</sup>	390 $\text{m}^2 \text{g}^{-1}$ ( <b>Argon</b> )

In the field of porous materials, some applications require very high BET surface areas like gas separation or electrochemical energy storage. However, there are other applications, for instance in photocatalysis, where a moderately high BET surface area is fully sufficient and it may become even more important to precisely gain control over the structure of the material - a requirement that can be provided by this method. This request can be ensured by moderate reaction temperatures, thus disadvantageous carbonisation and consequently a loss of structural integrity can be avoided as indicated by almost ideal C/N and C/H ratios of the reaction products. Furthermore, this approach profits from readily available monomers and renders this synthetic protocol as a large toolbox for the generation of new CTFs.

### 5.3 Synthesis of pyridine-based CTFs for direct supercapacitor integration\*\*\*

Supercapacitors based on porous carbon materials emerged from a myriad of potential systems to face the challenges of electrochemical energy storage.<sup>140</sup> Unfortunately, the synthesis of electrode materials for supercapacitors is often inextricably linked with the generation of waste.<sup>176</sup> Moreover, porous carbon materials do not display adjustable properties on a molecular basis as it is known for materials such as porous organic polymers.<sup>7</sup> In order to overcome these limitations, this chapter showcases the synthesis of novel and tailored 3,5-dicyanopyridine derived covalent triazine framework materials which are subsequently applied to demonstrate a straightforward *in situ* electrolyte concept that utilises the addition of water to the non-purified reaction product. Thereby, two main features are presented within the thesis at hand: 1) an electrode material providing control over the materials' properties as well as 2) a smart methodology to bypass extensive washing of the CTF materials that avoids the accumulation of waste.

Covalent triazine frameworks have been designed from various monomeric building blocks including also heterocyclic poly-carbonitriles.<sup>104</sup> Such monomers like pyridine-,<sup>131</sup> carbazole-, or furane-derivatives<sup>92</sup> enable the valuable introduction of exposed heteroatoms in order to precisely adjust the adsorption properties or to establish coordination sites. A drawback of covalent triazine frameworks is, however, a lack of conductivity, since they are known to be semiconducting as obtained at standard reaction temperature, that is, 400 °C. To overcome this particular issue, higher reaction temperatures are required in order to induce conductivity.<sup>177</sup> Elevated reaction temperatures are further known to be accompanied by a huge increase of porosity.<sup>91,178</sup> In parallel, the well-defined porous polymer is partially decomposed due to carbonisation processes leading to a N-doped carbon rather than a polymer.

---

\*\*\* I supervised the bachelor thesis of Tilo Rensch in 2017. In this work, he reproduced the material synthesis and characterisation of the DCP-CTF materials that I invented before. Physisorption, elemental analysis, TGA as well as electrochemical data are taken from his thesis.<sup>162</sup>

---

The here applied 3,5-dicyanopyridine (DCP) monomer was synthesised by a two-step synthesis (see Figure 20). Starting from abundant pyridine-3,5-dicarboxylic acid, thionyl chloride was used to generate the respective sulfonyl halide, which was converted into pyridine-3,5-dicarboxamide by treatment with aqueous ammonia. In the next step, the aromatic dicarboxamide was dehydrated using phosphoryl chloride. By applying sublimation, an ultra-pure 3,5-dicyanopyridine could be obtained in a large scale with a yield of 53 % in the whole sequence.

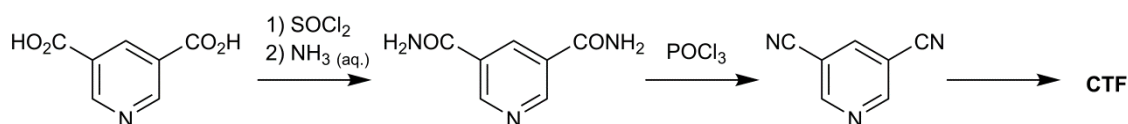


**Figure 20** Synthesis of 3-5-dicyanopyridine and derived covalent triazine frameworks.

In principal, the 3,5-dicyanopyridine monomer exhibits a high degree of pyridinic nitrogen and the ability to generate highly porous frameworks. A striking difference is displayed by the reduced steric hindrance of the 3,5-substituted monomer in contrast to the literature known 2,6-dicyanopyridine (2,6-DCP).<sup>93</sup> Thus, the formation of highly porous open frameworks bearing exposed pyridinic nitrogen was anticipated to be favoured in contrast to 2,6-DCP, which is known to provoke dense  $\text{ZnCl}_2$ -monomer assemblies, leading to networks with moderate porosity.<sup>93</sup>

The 3,5-dicyanopyridine CTF (DCP-CTF) was synthesised under ionothermal conditions in molten  $\text{ZnCl}_2$ . Four different materials were obtained applying syntheses temperatures of 400 °C, 500 °C, 600 °C, and 700 °C. In consequence, a large impact on the porosity was anticipated due to a thermally induced structural evolution. Prior to the analysis of structural properties, the samples were purified in order to remove residual  $\text{ZnCl}_2$  (henceforth referred to as DCP-CTF-X; while X stands for the synthesis temperature).

The porosity of these nitrogen-rich porous polymers was investigated using argon physisorption at 87 K. All isotherms reveal a steep increase in the low pressure region, indicating pronounced microporosity (Figure 21). Furthermore, the isotherms can be classified as type I(a) for the samples obtained at 400 °C (DCP-CTF-400) and 500 °C (DCP-CTF-500) and type I(b) for the samples generated at elevated temperatures. The samples DCP-CTF-600 and DCP-CTF-700 have a continuous uptake of argon until a relative pressure of ca.  $p/p_0 = 0.4$ , which can be interpreted by the presence of smaller mesopores. Based on the adsorption exper-

iments, BET surface areas covering a broad range from  $680 \text{ m}^2 \text{ g}^{-1}$  (for DCP-CTF-400) up to  $3120 \text{ m}^2 \text{ g}^{-1}$  (for DCP-CTF-700) could be achieved (Table 9 for all physisorption data). Thus, thermal treatment yielded highly porous nitrogen-rich samples (see elemental analysis later in this chapter) which should lose their polymeric character with increasing temperature. All materials show a narrow pore size distribution. As mentioned above, DCP-CTF-400 is a purely microporous material – as confirmed by ultramicropores with a diameter of 0.5 nm. All samples obtained at higher reaction temperatures further display supermicropores with a size of 0.8 nm and an enhanced degree of smaller mesopores with a maximum diameter of 3 nm (at  $600^\circ\text{C}$  and  $700^\circ\text{C}$ ).

Water vapour adsorption experiments were carried out to estimate the affinity towards water which might be enhanced due to a high degree of nitrogen-doping. For DCP-CTF-600 and DCP-CTF-700 that are assumed to be the most hydrophobic samples in this series, type V isotherms could be observed (see Figure 22). Thus, weak adsorbent-adsorbate interactions are indicated by a low uptake at low relative pressures between  $p/p_0 = 0.0 - 0.4$ . In contrast, DCP-CTF-400 and DCP-CTF-500 do not exhibit a pronounced uptake at higher relative pressures which might be due to the absence of mesoporosity and/or a more hydrophilic character of these samples.

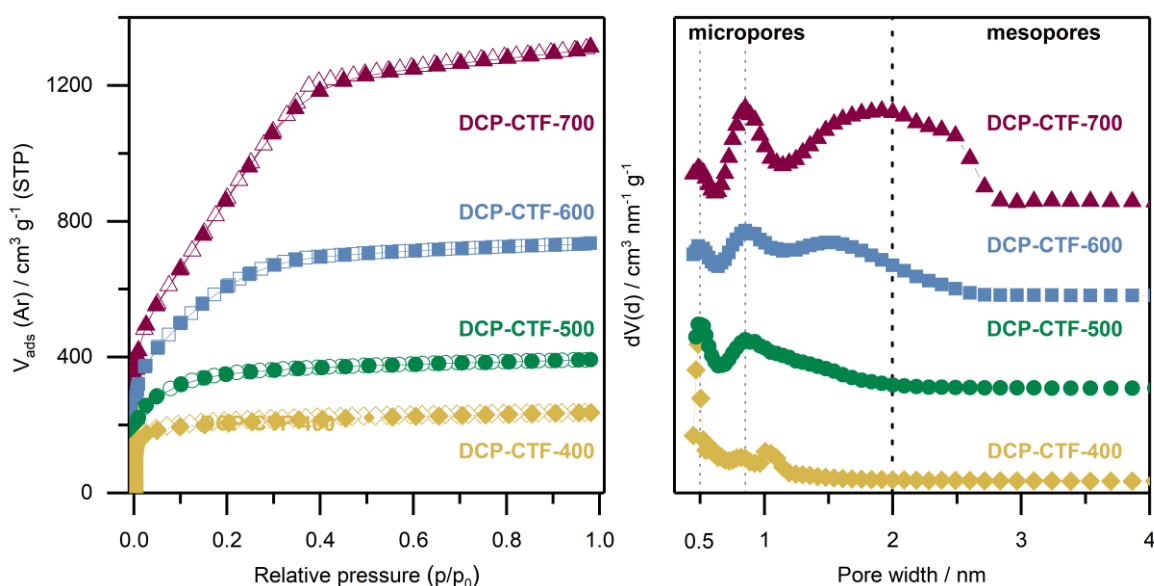


**Figure 21** (a) Argon physisorption (87 K) isotherms revealing a temperature induced evolution of porosity. b) Pore size distribution (QSDFT).

**Table 9** Porosity data of the investigated CTF samples including their specific surface area (argon), micropore volume, mesopore volume, ratio of micropore and mesopore volume and total pore volume (at  $p/p_0 = 0.95$ ).

Sample	Gas	$S_{\text{BET}}$ $\text{m}^2 \text{g}^{-1}$	$V_{\text{Micro}}$ $\text{cm}^3 \text{g}^{-1}$	$V_{\text{Meso}}$ $\text{cm}^3 \text{g}^{-1}$	$V_{\text{Micro}}/V_{\text{Meso}}$	$V_{\text{Total}}$ $\text{cm}^3 \text{g}^{-1}$
DCP-CTF-400	Ar	680	0.26	0.03	8.7	0.30
DCP-CTF-500	Ar	1120	0.45	0.03	15.0	0.50
DCP-CTF-600	Ar	1940	0.80	0.11	7.3	0.93
DCP-CTF-700	Ar	3120	1.08	0.54	2	1.66

As a general trend, the adsorbed amount of water at full saturation ( $p/p_0 = 0.98$ ) increases with the reaction temperature to reach a huge capacity of  $1650 \text{ cm}^3 \text{ g}^{-1}$  for DCP-CTF-700. This trend clearly follows the findings of argon physisorption experiments and can be attributed to growing pore volumes within this series of samples.

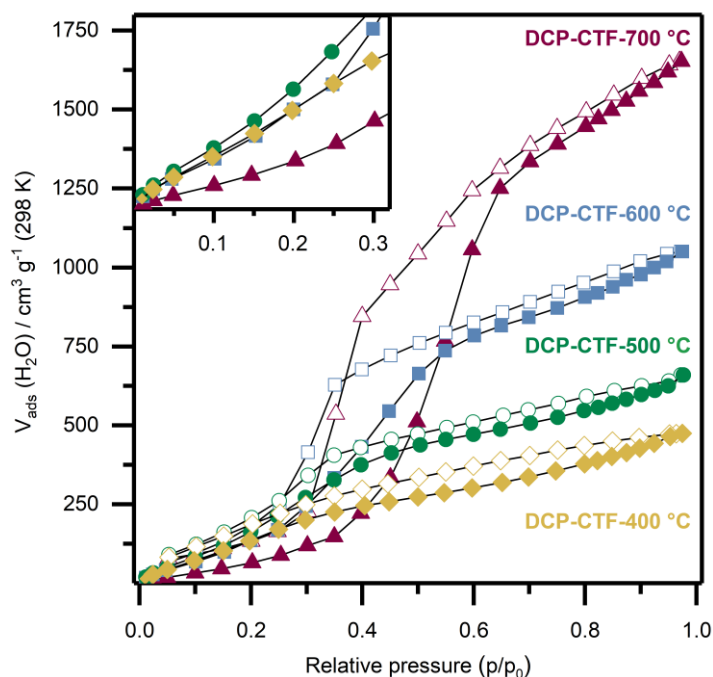


**Figure 22** Water vapour adsorption isotherms measured at 298 K.

To estimate the differing nitrogen contents within this set of samples, elemental analysis was conducted. Due to the presence of adsorbed water at ambient conditions, careful activation at  $230^\circ\text{C}$  was necessary prior to elemental analysis. Close to ideal values for C/H ( $C/H_{\text{ideal}} = 2.3$ ) and C/N ( $C/N_{\text{ideal}} = 2.3$ ) ratios, which are well suited to evaluate the degree of carbonisation, were determined for DCP-CTF-400 ( $C/H = 2.0$ ;  $C/N = 2.5$ ). As expected, at elevated reaction temperatures, an increase of the C/H as well as the C/N ratio is detected (see Table 10). Ex-

emplarily, CTF-DCP-700 shows a C/H ratio of 8.5 and a C/N ratio of 6.9. Based on these findings, the expected trends of a growing degree of carbonisation, accompanied by a loss of nitrogen, could be confirmed.

**Table 10** Elemental analysis of 3,5-dicyanopyridine derived CTF materials.

Sample	found (%)					calculated (%)				
	C	H	N	C/H	C/N	C	H	N	C/H	C/N
ideal values						65.1	2.3	32.5	2.3	2.3
DCP-CTF-400	61.6	2.6	28	2.0	2.6	65.1	2.3	32.5	2.3	2.3
DCP-CTF-500	57.4	1.5	23.5	3.2	2.9	65.1	2.3	32.5	2.3	2.3
DCP-CTF-600	48.9	1.0	15.8	4.1	3.6	65.1	2.3	32.5	2.3	2.3
DCP-CTF-700	75.32	0.7	12.7	8.5	6.9	65.1	2.3	32.5	2.3	2.3

Since a structural rearrangement as a result of elevated reaction temperatures is expected, X-Ray photoelectron spectroscopy was applied to monitor the transition. Due to the broad range of N 1s binding energies, XPS is a powerful tool for the characterisation of CTFs and to distinguish between different nitrogen species. Considering an ideal polymerisation, the material should exclusively contain pyridinic (or triazinic) aromatic nitrogen with a binding energy (BE) of  $\approx 398.0$  eV.<sup>179</sup> Deconvolution of the DCP-CTF-400 high resolution N 1s XPS spectrum shows a broader peak at 398.0 eV which is representing a well retained structure (see Figure 23a). A shoulder of the peak at higher binding energies (BE of  $\approx 399.5$  eV) may be induced from pyrrolic nitrogen species. Also metal coordination should be considered but is less probable as no Zn is detected in the survey XPS spectrum of DCP-CTF-400 (see Figure 24).<sup>179</sup> This observation can be rationalised by a structural reorganisation of the scaffold, either caused by irreversible C-C or C-N bond formation under Lewis-acidic conditions (e.g. cycloaddition reactions) or carbonisation of the material. For the samples obtained at higher reaction temperatures, the second peak (“decomposition peak”) at higher binding energies becomes even more pronounced. Moreover, deconvolution of the N 1s XPS spectra for DCP-CTF-500, DCP-CTF-600 and DCP-CTF-700 reveals a third peak with a higher binding energy of BE  $\approx 400.7$  eV which can be assigned to quaternary nitrogen.<sup>180</sup> Since an ongoing



carbonization is expected, the formation of graphitic layers and in consequence, the introduction of quaternary nitrogen species into these layers takes place. This effect is reflected in a growing peak area of the quaternary nitrogen species up to a temperature of 700 °C (DCP-CTF-700), thus strongly supporting the impact of the reaction temperature on the structure. A structural change is also indicated by the high resolution C 1s spectra (see Figure 23b). As expected, for DCP-CTF-400 exclusively C-C sp<sup>2</sup> carbon (BE of  $\approx 284.2$  eV), C=N (BE of  $\approx 285.5$  eV, carbons in the triazine core) and oxidized carbon species (C-O, BE  $\approx 286.3$  eV and BE  $\approx 288.2$  eV) can be detected.<sup>181</sup> In contrast, also C-C sp<sup>3</sup> carbon (BE of  $\approx 284.7 \pm 0.3$  eV) is observed for the high temperature samples. Interestingly, for DCP-CTF-600, the peak area for sp<sup>3</sup> carbon (and also the ratio of sp<sup>3</sup> : sp<sup>2</sup>) reaches a maximum of 40% and decreases again for DCP-CTF-700 (peak area = 28%) (see detailed XPS data, Table A3). Thus, DCP-CTF-600 can be considered as a structural transition between the polymer and a graphitised structure.

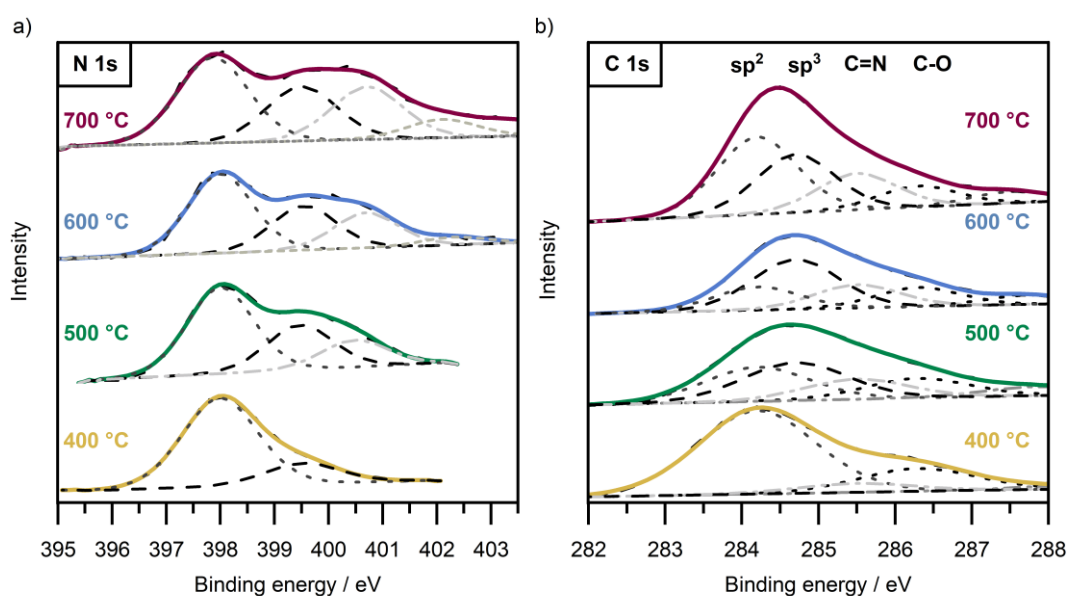


**Figure 23** High resolution N 1s XPS spectra of 3,5-dicyanopyridine derived CTF materials (a); High resolution C 1s XPS spectra of 3,5-dicyanopyridine derived CTF materials (b).

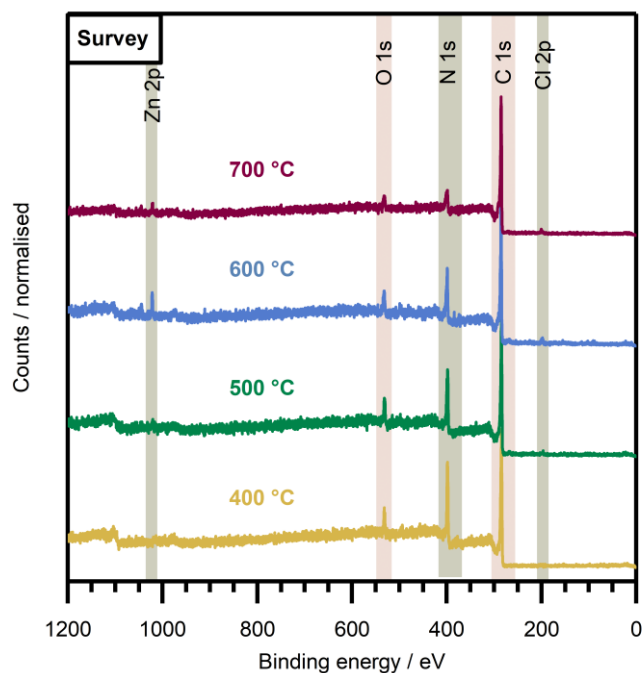


**Figure 24** Survey XPS spectra of 3,5-dicyanopyridine derived CTF materials.

Raman spectroscopy was conducted in order to further evaluate structural differences of the polymeric system upon thermal treatment (see Figure 25). As expected, for porous carbon materials, the typical appearance of a D-Band at  $\sim 1350\text{ cm}^{-1}$  and a G-band at  $\sim 1600\text{ cm}^{-1}$  is observed. The D-Band is caused by the breathing mode of  $\text{sp}^2$  carbon in aromatic rings and becomes active in the presence of defects.

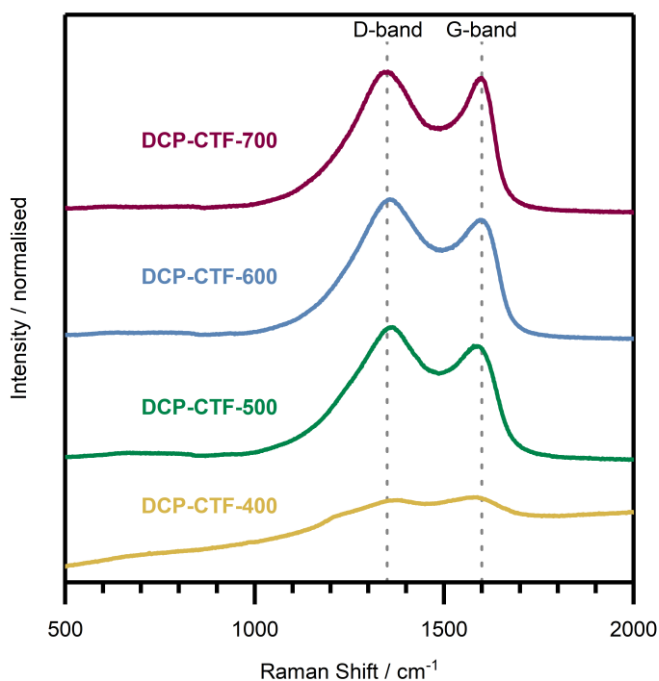


**Figure 25** Raman spectra of the investigated 3,5-dicyanopyridine derived CTF materials.

In contrast, the G-band includes the in-plane-bond-stretching motion of  $sp^2$  carbon atoms in graphitic carbon parts and does not require the presence of aromatic rings.<sup>182,183</sup> For DCP-CTF-400 almost no intensity of the aforementioned vibrations is detectable. This observation might be due to the polymeric character of the sample. Thus, strong background fluorescence is present for this sample and no pronounced vibrations are visible.<sup>184</sup> Contrary to these findings, for all samples obtained at elevated reaction temperatures, an evolution of Raman activity and in consequence, the presence of D- and G-band, is determined. Regarding the peak intensity ratio  $I(D)/I(G)$  of full-width at half maximum, a drop of the value with higher reaction temperature (500 °C:  $I(D)/I(G) = 3.88$  to 700 °C:  $I(D)/I(G) = 2.60$ ) is determined (see Table 11). This trend might be caused by different effects in parallel. With increasing temperature, a growing degree of disorder is anticipated. Simultaneously, as a consequence of reorganisation of the polymeric scaffold towards a carbonaceous material, polymeric ring structures will break and the number of carbon atoms contributing to the intensity of the G-band will increase. Both concomitant effects can be interpreted as a significant reorganisation within the initially polymeric system towards a carbon-like material.

**Table 11** Raman fitting data of DCP-CTF-500, DCP-CTF-600 and DCP-CTF-700.

Sample	Peak height		Area		All area	
DCP-CTF-500	$I(D1)/I(G1)$	1.80	$I(D1)/I(G1)$	5.54	$I(D)/I(G)$	3.88
	$I(D2)/I(G2)$	0.23	$I(D2)/I(G2)$	2.31		
	$I(G2)/I(G1)$	0.78	$I(G2)/I(G1)$	1.06		
DCP-CTF-600	$I(D1)/I(G1)$	1.89	$I(D1)/I(G1)$	6.48	$I(D)/I(G)$	2.68
	$I(D2)/I(G2)$	0.19	$I(D2)/I(G2)$	0.36		
	$I(G2)/I(G1)$	0.88	$I(G2)/I(G1)$	1.63		
DCP-CTF-700	$I(D1)/I(G1)$	1.74	$I(D1)/I(G1)$	6.76	$I(D)/I(G)$	2.60
	$I(D2)/I(G2)$	0.22	$I(D2)/I(G2)$	0.40		
	$I(G2)/I(G1)$	0.87	$I(G2)/I(G1)$	1.89		

According to powder X-ray diffraction (PXRD) experiments, all samples are amorphous (Figure A26). A certain degree of long range order, however, is a just rarely observed feature for CTFs.<sup>81,86,88</sup> Thermogravimetric analysis (TGA) under synthetic air revealed a high thermal stability up to 400 °C. Similar trends for the stability can be found for TGA experiments performed under argon (Figure A27/A28). Scanning electron microscopy (SEM) measurements revealed a rough surface texture with residual small crystallites of the reaction medium  $ZnCl_2$ .

When comparing an unwashed sample with the washed analogue, a clear difference can be observed (see Figure 26). Prior to washing,  $\text{ZnCl}_2$  is covering the rough surface homogeneously. After washing, the surface texture has changed significantly and appears to be uneven.

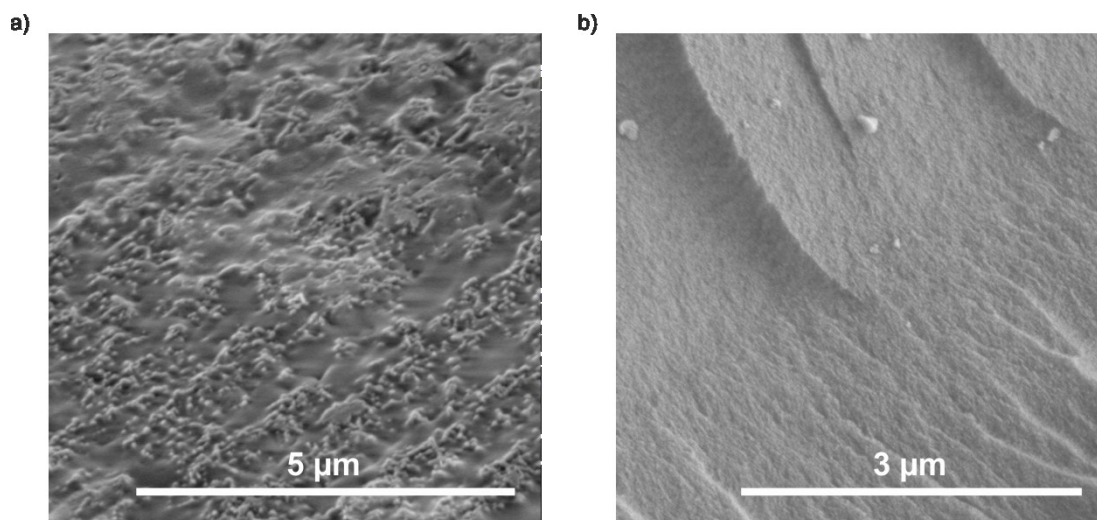


**Figure 26** SEM pictures of DCP-CTF-700 comparing an unwashed (left) and washed sample (right).

After a conventional CTF synthesis, which is usually performed in an ampoule, the pristine material is obtained but still contains large amount of  $\text{ZnCl}_2$ , which is finely dispersed throughout the whole sample. Hence, an extensive washing procedure is required in order to obtain the CTF material, which can be consequently applied as electrode material in a supercapacitor. Ironically, an electrolyte, consisting of a dissolved salt, must be added prior to the evaluation of the electrochemical performance. Bypassing multiple washing steps would drastically facilitate the efforts towards the final application and would save huge amounts of solvents.  $\text{ZnCl}_2$  has not been widely investigated as electrolyte system in supercapacitors yet. However, it certainly fulfils the prerequisites of an aqueous electrolyte like ionic conductivity and good solubility such as conventional  $\text{Li}_2\text{SO}_4$ - or  $\text{H}_2\text{SO}_4$ -based electrolytes.<sup>140</sup> Moreover, in course of the synthesis,  $\text{ZnCl}_2$  is located within the pores of the CTF material. Hence, the addition of water should *in situ* generate an aqueous  $\text{ZnCl}_2$  electrolyte and simultaneously unblock the porosity of the CTF.

For the electrochemical characterisation, the CTF/ZnCl<sub>2</sub> composites were characterised as symmetric electrical-double layer capacitor applying the “*in situ* electrolyte” concept.<sup>\*\*\*</sup> Therefore, the materials were directly processed to electrodes after ionothermal synthesis without any further washing (henceforth referred to as CTF/ZnCl<sub>2</sub>-X; while X stands for the synthesis temperature). Based on the amount of starting material, the electrode contains an excess of ZnCl<sub>2</sub> (84 w%). By adding water, the “*in situ* electrolyte” is generated in the porous framework (16 w%). Purified water (0.1 mL) was added to an electrode mass of 48 mg, which leads to an electrolyte concentration of 403 g L<sup>-1</sup> of salt in water. Assuming that the electrolyte salt purely consists of residual ZnCl<sub>2</sub> the molar concentration is calculated to be 2.96 mol L<sup>-1</sup>.

Regarding the Nyquist plot (Figure 27a) the capacitive behaviour depends on the synthesis temperature. From 400 °C to 500 °C the energy storage mechanism becomes more capacitive as reflected by a sharper increase at lower frequencies. Raising the temperature to 600 °C leads to a dramatic resistance increase of the system. This trend can be confirmed by the large equivalent distributed resistance (EDR). The polymeric framework is anticipated to be partially converted into a carbonaceous material at higher temperatures resulting in a higher resistance and an inferior capacitive performance. It is assumed that the material synthesised at 600 °C can be interpreted as a transition state between a semiconductor and a conductor. This observation might be explained by a stepwise change of the mechanisms responsible for conductivity. Whereas the CTF material at 400 °C exhibits conductivity based on its conjugated  $\pi$ -system and potential charge transfer processes stemming from nitrogen functionalities, the material obtained at temperatures above 600 °C shows graphitic domains (Figure 25). These domains provoke an enhanced conductivity as present in carbon materials, which induces the EDR drop of sample CTF/ZnCl<sub>2</sub>-700. The conductivity loss of CTF/ZnCl<sub>2</sub>-600 is correlated with the transition between these two conductivity mechanisms. This hypothesis of carbonisation/decomposition is strongly supported by the results of both the X-ray photoelectron spectroscopy and elemental analysis. Moreover, the cyclic voltammograms and the galvanostatic charge-discharge curves demonstrate the transition from non-capacitive to capacitive energy storage (Figure 27b and Figure 27c). Sample CTF/ZnCl<sub>2</sub>-400 and CTF/ZnCl<sub>2</sub>-500 do not show any capacitance (Table 12). These findings are attributed to a lack of conductivity and the polymeric character of the

---

<sup>\*\*\*</sup> The “*in situ* electrolyte” concept of Desirée Leistenschneider (Inorganic Chemistry, TU Dresden) has not been published at the time of writing.

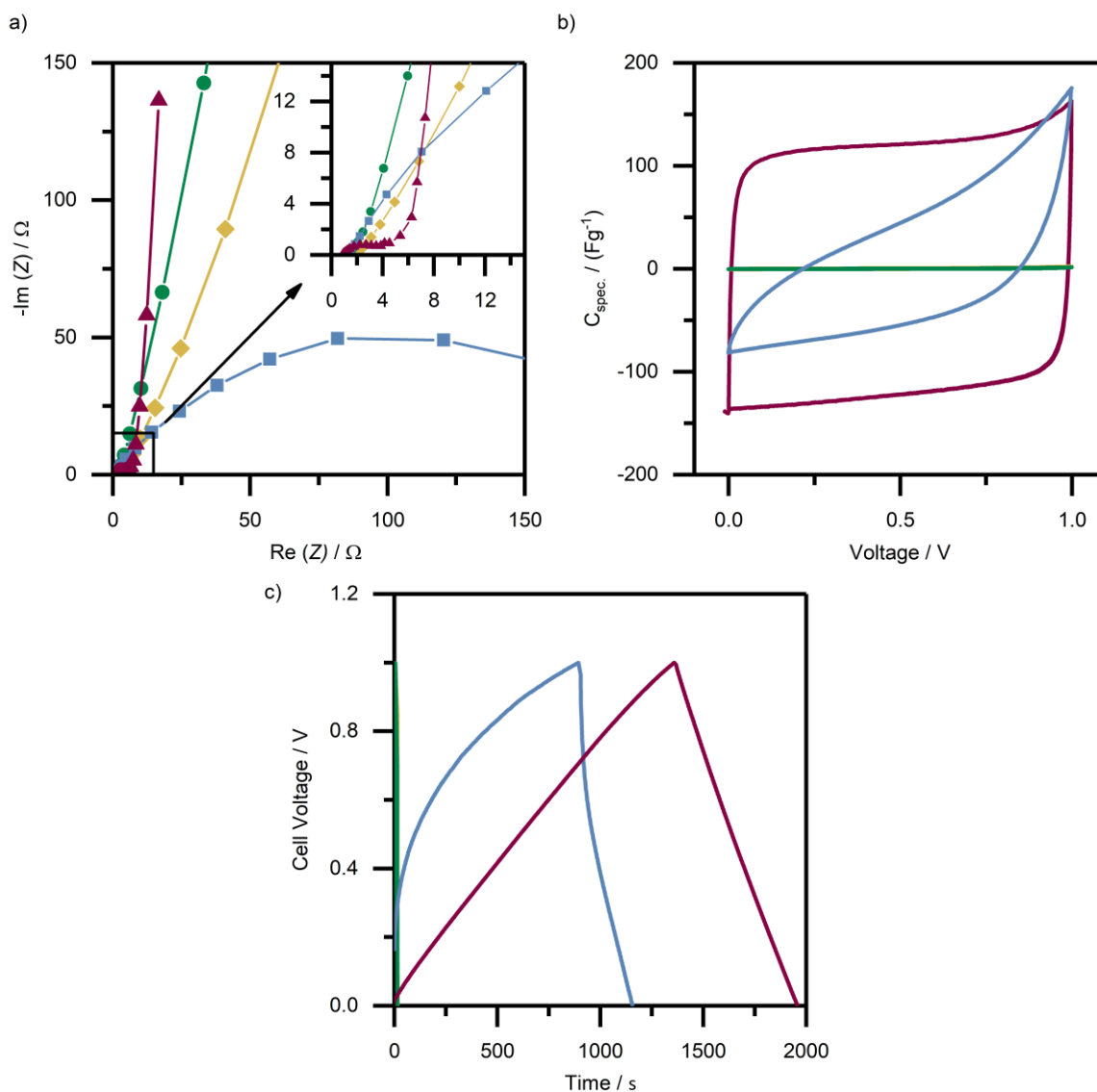


**Figure 27** a) Nyquist plot; b) Cyclic voltammograms at  $10 \text{ mVs}^{-1}$ ; c) Galvanostatic charge- and discharge cycles at  $1 \text{ A g}^{-1}$ .  
 Sample code: *in situ*: CTF/ZnCl<sub>2</sub>-400 (yellow); CTF/ZnCl<sub>2</sub>-500 (green); CTF/ZnCl<sub>2</sub>-600 (blue); CTF/ZnCl<sub>2</sub>-700 (violet).

electrodes which leads to stronger interactions between the electrode surface and the electrolyte ions in contrast to a pure electrosorption. Therefore, the materials CTF/ZnCl<sub>2</sub>-400 and -500 are not acting as an electric double-layer capacitor and a capacitance cannot be developed. A structural change at  $600^\circ\text{C}$  is indicated by a nonrectangular CV shape and a curved discharge graph. This finding implies a transitional state between a polymeric and a carbonaceous scaffold. Hence, for CTF/ZnCl<sub>2</sub>-600 a specific capacitance of  $60 \text{ F g}^{-1}$  was calculated from the discharge cycle. In contrast, the specific capacitance of the supercapacitor derived from unwashed CTF/ZnCl<sub>2</sub>-700 (Table 12) is  $141 \text{ F g}^{-1}$ . Moreover, CTF/ZnCl<sub>2</sub>-700 shows a typical rectangular shaped CV as expected for a porous supercapacitor material that electrosorbs electrolyte

ions on its surface. This further supports the assumption that the CTF material obtained at 700 °C (DCP-CTF-700) can be considered as a pure carbon-like porous network. The electrochemical performance of all unwashed CTF materials fits very well to the structural insights gained from *ex situ* textural characterisation (physisorption, XPS, Raman). Without purifying the material in advance, this method allows for estimating the materials' properties based on the behaviour as supercapacitor. Thus, by using ZnCl<sub>2</sub> as an inexpensive electrolyte precursor, the drawback of purification can be turned into a benefit for CTF materials.

**Table 12** Electrochemical data of 3,5-dicyanopyridine derived CTF materials determined by galvanostatic charge- and discharge cycles at 1 A g<sup>-1</sup>.

Sample	Electrolyte <sup>a</sup>	C <sub>Spec</sub> <sup>b</sup> F g <sup>-1</sup>	Specific energy <sup>c</sup> Wh kg <sup>-1</sup>	Energy efficiency <sup>d</sup> %
CTF/ZnCl <sub>2</sub> -400	<i>in situ</i>	0	0	0
CTF/ZnCl <sub>2</sub> -500	<i>in situ</i>	0	0	0
CTF/ZnCl <sub>2</sub> -600	<i>in situ</i>	60	2.45	59
CTF/ZnCl <sub>2</sub> -700	<i>in situ</i>	141	3.79	69

**a** a volume of 0.1 mL H<sub>2</sub>O was added to an electrode mass of 48 mg. Based on the applied stoichiometry the molar concentration of ZnCl<sub>2</sub> in H<sub>2</sub>O was calculated to be 2.96 mol L<sup>-1</sup>.

**b** calculated with discharge at 1 A g<sup>-1</sup>, normalized to the carbon mass in one electrode.

**c** calculated with discharge at 1 A g<sup>-1</sup>.

**d** calculated as quotient of the specific energy obtained from discharge and charge at 1 A g<sup>-1</sup>.

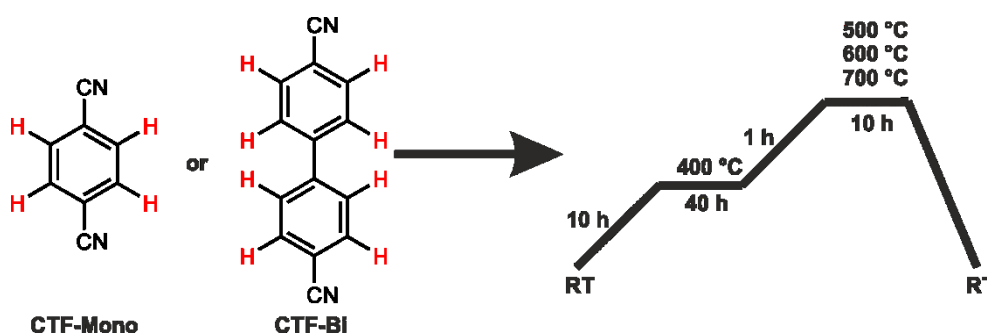
## 5.4 Covalent triazine frameworks containing covalently bound sulfur and their evaluation as cathodes in the lithium sulfur battery

A major problem of current battery research in the area of lithium sulfur batteries is the polysulfide shuttle, which is preventing the application of carbonate electrolytes.<sup>185</sup> Although carbonate electrolytes suffer from their reactivity with polysulfide intermediates, these electrolytes promise a longer cycle life, since they allow the use of graphite as anode material instead of lithium.<sup>186</sup> To overcome the issue of electrolyte degradation, one approach is to encapsulate sulfur into narrow and well defined micropores of a porous carbon given that the overlapping of the Lennard-Jones potentials in these small pores lead to a strong interaction between polysulfides and pore walls.<sup>187,188</sup> In consequence, the polysulfides are hindered to leave the micropores, thus avoiding an irreversible reaction with the carbonate electrolyte which consequently prevents irreversible decomposition of the electrolyte. Another innovative approach is applying covalent bonding of sulfur to a conductive poly(acrylonitrile) (PAN) polymer.<sup>189</sup> The resulting sulfur rich polymer (SPAN) contains up to 41 w% of covalently bound sulfur after washing and shows an almost complete sulfur utilisation and stable cycling performance in a carbonate electrolyte, thus proving the absence of intermediate polysulfide species. Also covalent triazine frameworks have been discussed as a possible cathode material to prevent the polysulfide shuttle since they combine extended microporosity and polar surfaces.<sup>190,191</sup> CTFs obtained from 1,4-dicyanobenzene (CTF-1) were discussed in a contribution of Coskun and co-workers.<sup>143</sup> They elucidated CTF-1 with a high amount of embedded sulfur which was obtained by adding sulfur prior to the synthesis. The resulting material contained sulfur within the micropores of the CTF as well as covalent sulfur, which is bound to the polymeric backbone via C-H cleavage, thus replacing hydrogen against short chained sulfur. In course of the synthetic procedure, no washing step was carried out, thus the resulting material still contained large amounts of unreacted elemental sulfur at the outer surface. The CTF synthesis was conducted at 400 °C; therefore no intrinsically conductive material could be obtained (see also further investigations towards the conductivity of CTFs later in this chapter). In consequence, large amounts of conductive additive were required to utilise the insulating sulfur and realise the evaluation of the electrochemical performance in a sulfur cathode.

Hence, this chapter describes a systematic synthetic approach towards the generation of intrinsically conductive model CTFs, which shall exclusively contain covalently attached sulfur.



To apply covalent triazine frameworks as cathode materials for Li/S battery applications, a certain conductivity is required which cannot be provided by CTFs synthesised at 400 °C which are known to be semiconducting.<sup>192</sup> Within the thesis at hand, two different model CTFs made from 1,4-dicyanobenzene (CTF-Mono) and 4,4'-dicyano-1,1'-biphenyl (CTF-Bi) were synthesised (Scheme 23). Due to the twofold amount of potential sulfur anchor sites in the CTF-Bi system regarding one linker unit, an enhanced amount of potential sites for covalent sulfur bonding compared to CTF-Mono was intended.



**Scheme 23** Synthesis of CTF-Mono (derived from 1,4-dicyanobenzene) and CTF-Bi (4,4'-dicyano-1,1'-biphenyl) and corresponding temperature protocol for the CTF synthesis.

To obtain conductive materials, the syntheses were conducted at 400 °C in combination with an additional heating step at 500 °C, 600 °C and 700 °C.<sup>177</sup> Thus, a partial carbonisation of the networks to different degrees was anticipated. For CTF-Mono, as expected, higher reaction temperatures of the polymers are accompanied by a huge increase of porosity as determined by nitrogen physisorption measurements at 77 K (Figure 28a).

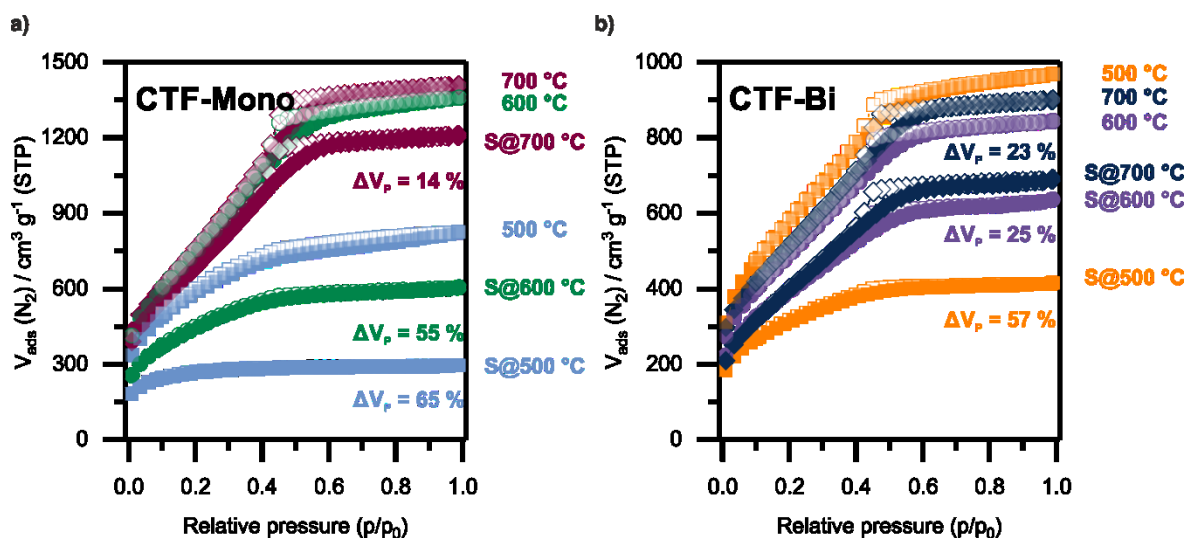


**Figure 28** Nitrogen physisorption isotherms (77 K) of CTF materials synthesised at different temperatures and derived materials containing covalently bound sulfur obtained from a) 1,4-dicyanobenzene (CTF-Mono) and b) 4,4'-dicyano-1,1'-biphenyl (CTF-Bi).  $\Delta V_p$  represents the percental decrease of the total pore volume after sulfur attachment.

All of the three materials synthesised at different temperatures show a high gas uptake in the low relative pressure range, reflecting a high micropore volume. Thus, high specific surface areas of  $2120 \text{ m}^2 \text{ g}^{-1}$  (CTF-Mono\_500),  $2730 \text{ m}^2 \text{ g}^{-1}$  (CTF-Mono\_600) and  $2780 \text{ m}^2 \text{ g}^{-1}$  (CTF-Mono\_700) were determined (see Table 13 for porosity data). In addition, enhanced mesoporosity was observed for the materials synthesised at 600 °C and 700 °C, respectively. As a consequence, CTF-Mono\_600 and CTF-Mono\_700 show total pore volumes of  $2.1 \text{ cm}^3 \text{ g}^{-1}$  and  $2.2 \text{ cm}^3 \text{ g}^{-1}$ , which largely exceed the pore volume of CTF-Mono\_500 ( $1.3 \text{ cm}^3 \text{ g}^{-1}$ ). In contrast, there is no pronounced impact of the reaction temperature on the porosity of the CTF-Bi materials. Interestingly, CTF-Bi\_500 exhibits the highest BET surface area ( $2130 \text{ m}^2 \text{ g}^{-1}$ ) of all three samples. This effect might potentially be attributed to a reorganisation of the polymeric scaffold in course of graphitisation processes leading to a competing reduction in porosity as an effect of elevated reaction temperatures.<sup>178</sup> Moreover, at these temperatures enhanced carbonisation reactions and even cycloaddition reactions of the biphenyl can occur. In consequence, mesopores are created at the cost of micropores, thus causing a decreased micropore contribution (Figure A30 – A33 for pore size distributions and for pore volumes). However, also CTF-Bi\_600 and CTF-Bi\_700 show high specific surface areas of  $1800 \text{ m}^2 \text{ g}^{-1}$  and  $1870 \text{ m}^2 \text{ g}^{-1}$ , respectively (see Table 13).

**Table 13** Porosity data of all CTF samples and their sulfur treated analogues (from Nitrogen adsorption at 77 K).

Sample	$S_{BET}$ $m^2 g^{-1}$	$V_{Micro}$ $cm^3 g^{-1}$	$V_{Meso}$ $cm^3 g^{-1}$	$V_{Total}$ $cm^3 g^{-1}$	Sample	$S_{BET}$ $m^2 g^{-1}$	$V_{Micro}$ $cm^3 g^{-1}$	$V_{Meso}$ $cm^3 g^{-1}$	$V_{Total}$ $cm^3 g^{-1}$
CTF-Mono_500	2120	0.76	0.51	1.28	CTF-Bi_500	2130	0.65	0.85	1.50
S@CTF-Mono_500	970	0.39	0.06	0.45	S@CTF-Bi_500	1130	0.41	0.23	0.64
CTF-Mono_600	2730	0.76	1.34	2.10	CTF-Bi_600	1800	0.53	0.77	1.30
S@CTF-Mono_600	1620	0.58	0.35	0.93	S@CTF-Bi_600	1430	0.45	0.53	0.98
CTF-Mono_700	2780	0.75	1.43	2.18	CTF-Bi_700	1870	0.55	0.84	1.39
S@CTF-Mono_700	2700	0.72	1.15	1.87	S@CTF-Bi_700	1475	0.43	0.6	1.07

After the synthesis of a variety of different samples in terms of carbonisation degree and conductivity (see conductivity measurements later in this chapter), in a next step, sulfur was covalently bound onto the CTF materials. Therefore, the activated samples were thoroughly mixed with an excess of sulfur (15 mass eq.) in a ball mill and transferred into an argon purged tubular furnace. In order to impregnate the samples with sulfur, the samples were kept at 155 °C given the fact that sulfur has its lowest viscosity at that temperature. To reach covalent bonding, the temperature was consequently raised to 350 °C to induce C-H cleavage, thus replacing hydrogen against sulfur, which can be nicely followed by the evolution of H<sub>2</sub>S. Due to residual sulfur that still remains within the materials after the synthesis, the samples were carefully washed by means of Soxhlet extraction. Successively, toluene as well as THF were applied in order to remove excessive sulfur completely. To investigate how sulfur bonding affects the porosity, the nitrogen physisorption data isotherms of the parent material and the sulfur loaded CTFs were compared. The isotherms of all sulfur loaded CTF samples (S@CTF-Mono and S@CTF-Bi) reveal a global decrease of specific surface area and total pore volume (Figure 28 and Table 13). This trend proves that sulfur within the pore system strongly influences the porosity. In order to exclude a loss of porosity due to mechanical stress caused by ball milling, CTF-Bi\_500 was mixed with sulfur as a reference sample. After Soxhlet washing with toluene, no loss of porosity could be detected, thus indicating an intact pore system (Figure 29).

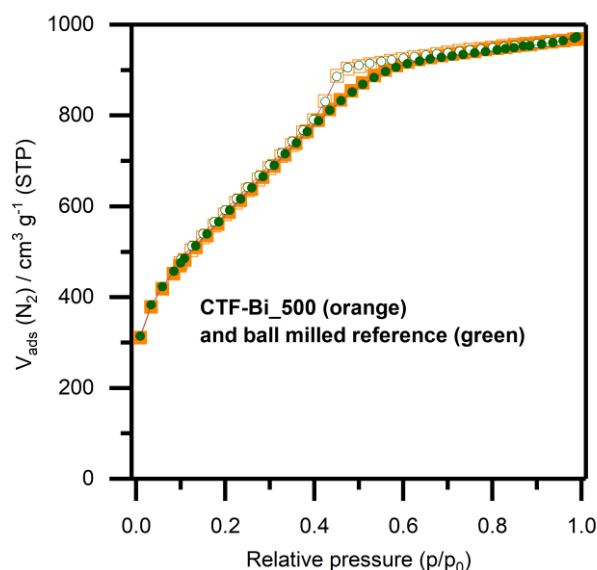


**Figure 29** Nitrogen physisorption isotherm (77 K) of CTF-Bi\_500 and a ball milled reference sample. After ball milling, no loss of porosity is observed. Therefore, the isotherms can be considered as identical.

To gain further insight QSDFT was employed to analyse if the sulfur is preferentially bound in the micro- or mesopores of the parent materials. Comparing the respective micropore- ( $V_{\text{Micro}}$ ) and mesopore volumes ( $V_{\text{Meso}}$ ) prior to and following sulfur treatment verifies that both pore types are filled - in all cases the micropore as well as the mesopore volume of the S@CTF samples show a decrease. Exemplarily, CTF-Mono\_500 has a micropore volume of  $V_{\text{Micro}} = 0.76 \text{ cm}^3 \text{ g}^{-1}$  and mesopore volume of  $V_{\text{Meso}} = 0.51 \text{ cm}^3 \text{ g}^{-1}$ , respectively. For the sulfur treated sample S@CTF-Mono\_500, the values drop down to  $V_{\text{Micro}} = 0.39 \text{ cm}^3 \text{ g}^{-1}$  and  $V_{\text{Meso}} = 0.06 \text{ cm}^3 \text{ g}^{-1}$ . Moreover, the percental deviation of the respective micropore and mesopore volume after sulfur treatment was investigated for the samples synthesised from the same monomer but at different temperatures. To showcase this effect, the respective values of S@CTF-Mono samples are applied. For CTF-Mono\_500 a drop of the micropore volume of  $\Delta V_{\text{Micro}} = 49 \%$  and for the respective mesopore volume of  $\Delta V_{\text{Meso}} = 88 \%$  was found. Considering the samples S@CTF-Mono\_600 and S@CTF-Mono\_700, the data show that the percental deviation decreases with higher temperatures. At 600 °C, a drop of  $\Delta V_{\text{Micro}} = 24 \%$  and  $\Delta V_{\text{Meso}} = 73 \%$  is observed. Even lower values of  $\Delta V_{\text{Micro}} = 5 \%$  and  $\Delta V_{\text{Meso}} = 19 \%$  were determined for the S@CTF-Mono\_700 sample. In accordance with these values, also the S@CTF-Bi samples show comparable trends. Based on these findings, a slight preference of sulfur bonding for mesopores was observed.

Elemental analysis was conducted to further investigate the amount of covalently bound sulfur within the CTF materials (Figure 30). Since higher synthesis temperatures induce more carbonisation of the CTF materials, increased carbon/hydrogen and carbon/nitrogen ratios are expected for samples synthesised at 600 °C and 700 °C. The latter should result in less covalently bound sulfur, since the number of C-H binding sites will be reduced. In agreement with this hypothesis, decreasing amounts regarding lower to higher synthesis temperatures were found. S@CTF-Mono\_500 shows a total sulfur content of ca. 29 w%, whereas S@CTF-Mono\_600 and S@CTF-Mono\_700 show values of ca. 12 w% and 9 w%, respectively. Also for the S@CTF-Bi samples, the values decrease with higher temperatures from 33.5 w% to 17 w% and 11 w%.

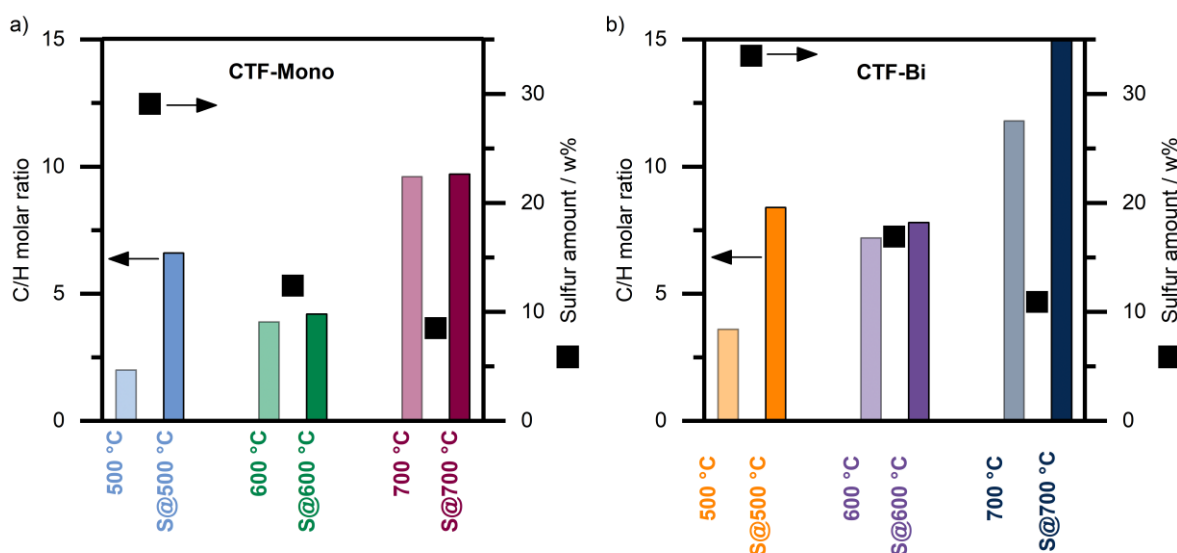


**Figure 30** Elemental analyses and the respective C/H molar ratios of CTF-Mono samples (a) and CTF-Bi samples (b) obtained at different temperatures. Sulfur content with respect to the synthesis temperature for S@CTF-Mono (a) and S@CTF-Bi (b) samples.

Powder X-ray diffraction revealed no additional reflections caused by elemental sulfur within the sulfur treated samples (Figure 31). All samples remained amorphous after sulfur bonding (see Figure A34/A35 for PXRD data of parent materials). Thus, two potential conclusions can be drawn from these findings. Either no elemental sulfur is present within the samples as a separate crystalline phase or sulfur is finely dispersed at the nanometer scale or in a polymeric form. Both of which would preclude detection via the PXRD technique.

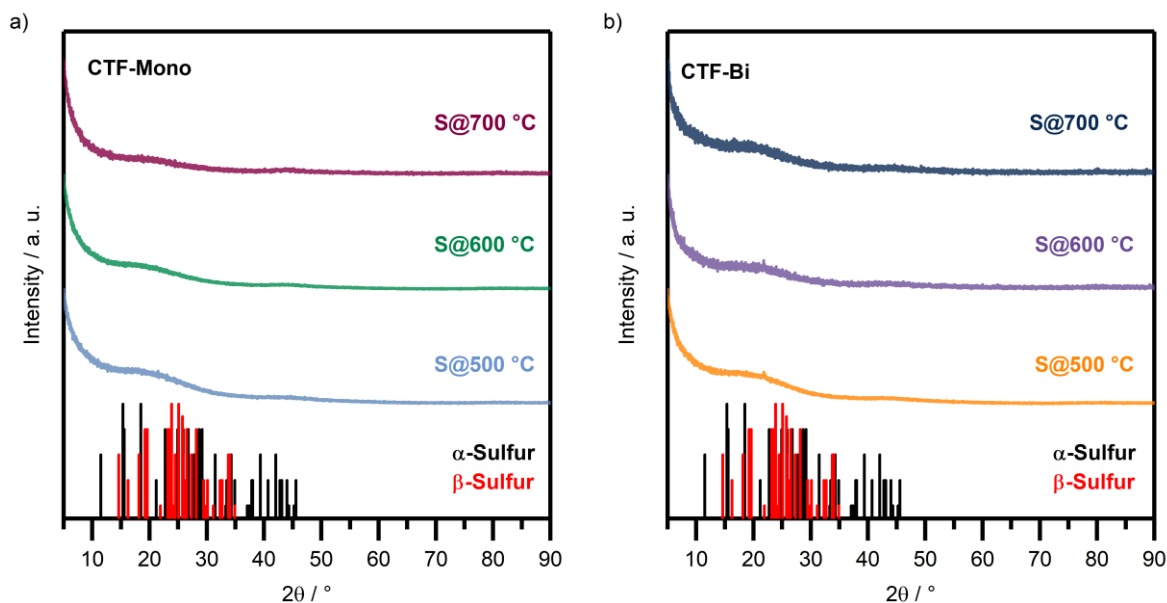


**Figure 31** Powder X-ray diffraction data of a) S@CTF-Mono and b) S@CTF-Bi.

To further probe the bonding situation of sulfur within the CTFs, X-ray photoelectron spectroscopy was conducted (Figure 32). Survey XPS spectra comparing the parent material and its sulfur treated counterpart reveal a distinct difference, since sulfur can be detected in all S@CTF samples. When comparing the samples obtained at different temperatures, a decreased absolute intensity of the sulfur peaks with increasing temperatures can be observed. This finding is in agreement with the results from elemental analysis, since the sulfur amount decreases with higher synthesis temperatures. Interestingly, the peak for oxygen (O 1s: 531 eV) is much more pronounced in all sulfur containing samples. This observation can be attributed to a potential oxidation of terminal sulfur atoms towards SO<sub>x</sub> end groups which could take place upon washing. In addition, carbon, nitrogen, residual zinc (Zn 2p: 1022 eV), and chlorine (Cl 2p: 199 eV) can be observed.<sup>193</sup>

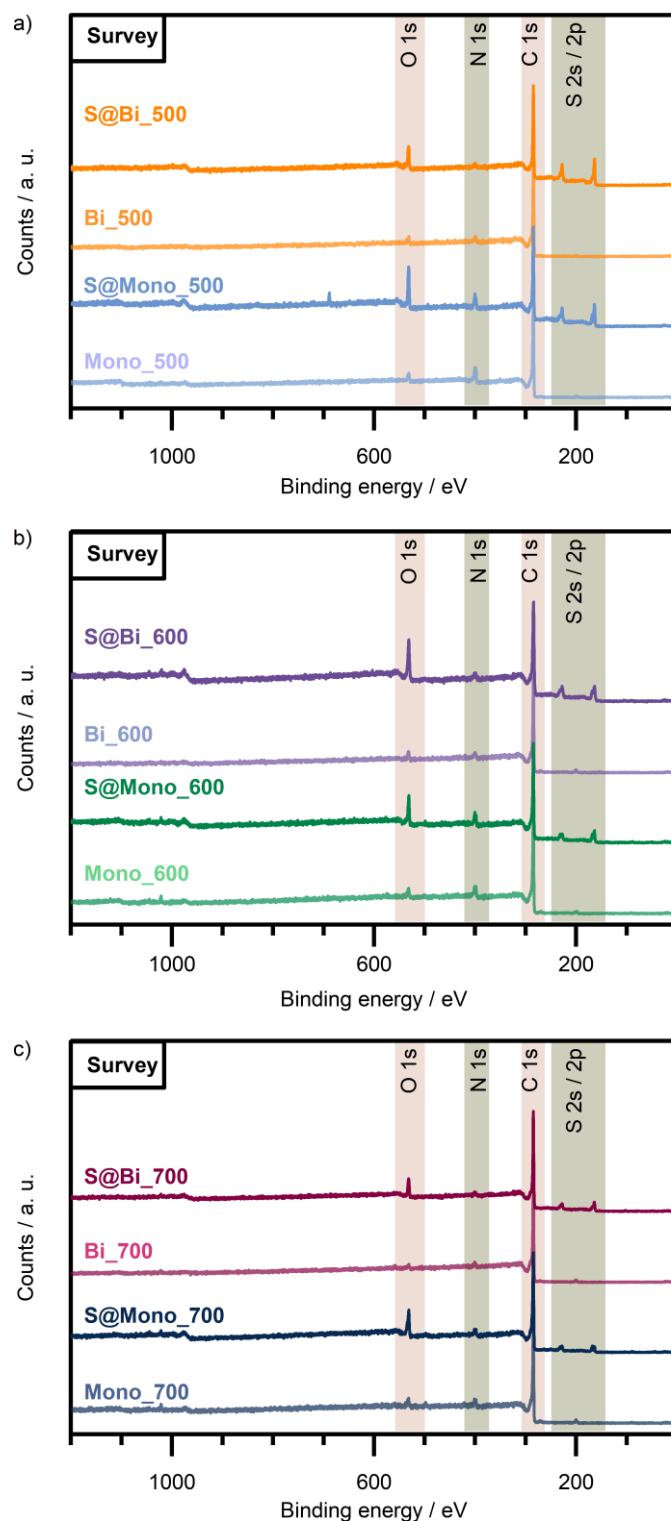


**Figure 32** Survey XPS spectra of CTF-Mono and CTF-Bi samples.

High resolution S 2p spectra disclose that there are various bonding situations of sulfur within the samples. For better understanding, all trends are discussed with regard to the CTF-Mono\_600 and CTF-Bi\_600 samples and their sulfur treated analogues (see Figure A36/A37 for other samples). Sulfur 2p peaks always contain a contribution of  $p_{1/2}$  and  $p_{3/2}$  which have a difference of binding energy of 1.18 eV. For the sake of simplification, the resulting peaks were

always obtained by adding  $p_{1/2}$  and  $p_{3/2}$  component fit and subtracting the background. The main peak with a binding energy of  $163.3\pm 0.1$  eV ( $2p_{3/2}$ ) and a shoulder at a binding energy of  $164.3\pm 0.1$  eV ( $2p_{1/2}$ ) can be referred to a C-S or S-S bonding motif.<sup>194,195</sup> Since the XPS data do not allow for a distinction of these species, the results need to be considered in combination with the findings gained from other methods. The PXRD data reveal no elemental sulfur, thus strengthening the hypothesis of covalently bound sulfur.<sup>193</sup> Other peaks were observed at binding energies of  $165.0\pm 0.1$  eV ( $2p_{3/2}$ ; sulphoxides),  $167.2\pm 0.1$  eV ( $2p_{3/2}$ ; sulphones) and  $168.3\pm 0.1$  eV ( $2p_{3/2}$ ; sulphates) which gives rise to the existence of oxidised (terminal) sulfur atoms.<sup>194,195</sup>

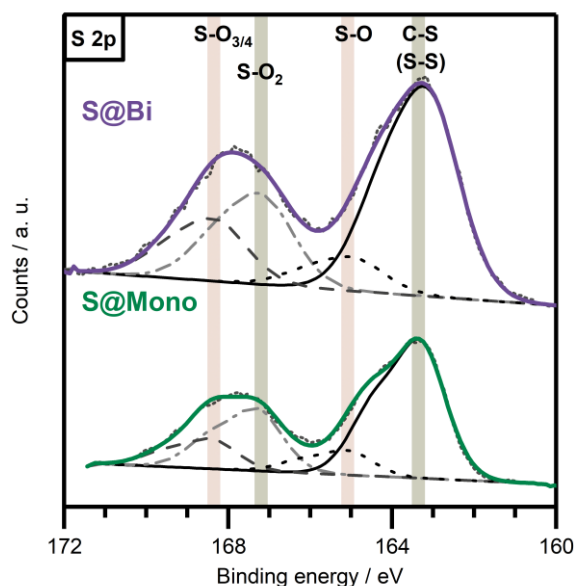


**Figure 33** High resolution S 2p XPS spectra of S@CTF-Mono\_600 and S@CTF-Bi\_600. Resulting peaks were obtained by adding  $p_{1/2}$  and  $p_{3/2}$  component fit and subtracting the background.

When taking also into account the C 1s XPS data (Figure 34a) of CTF-Mono\_600 and S@CTF-Mono\_600, which have been chosen exemplarily, a slight increase of the peak area of the C=N or C-S peak (BE =  $285.7\pm 0.3$  eV) for S@CTF-Mono\_600 (21.03% in contrast to 20.90%, see Table A4/Table A5 for detailed XPS peak table) becomes apparent. Although these values do not display huge differences, this trend was found for every sample. Moreover, when considering the high resolution N 1s spectra of the CTF-Mono\_600 in contrast to the S@CTF-Mono\_600 (Figure 34b), no pronounced difference of the shape and also the peak areas before and after sulfur treatment can be determined. Also these trends could be confirmed for all other samples (see Figure A38 – A49 and Table A4/Table A5). Thus, it is assumable that nitrogen species within the samples did not undergo any reaction or change upon sulfur treat-



ment. The combination of these findings suggests the generation of C-S species in the sulfur treated materials. Thus, the existence of short sulfur chains which most likely bear differently oxidised terminal atoms can be assumed.

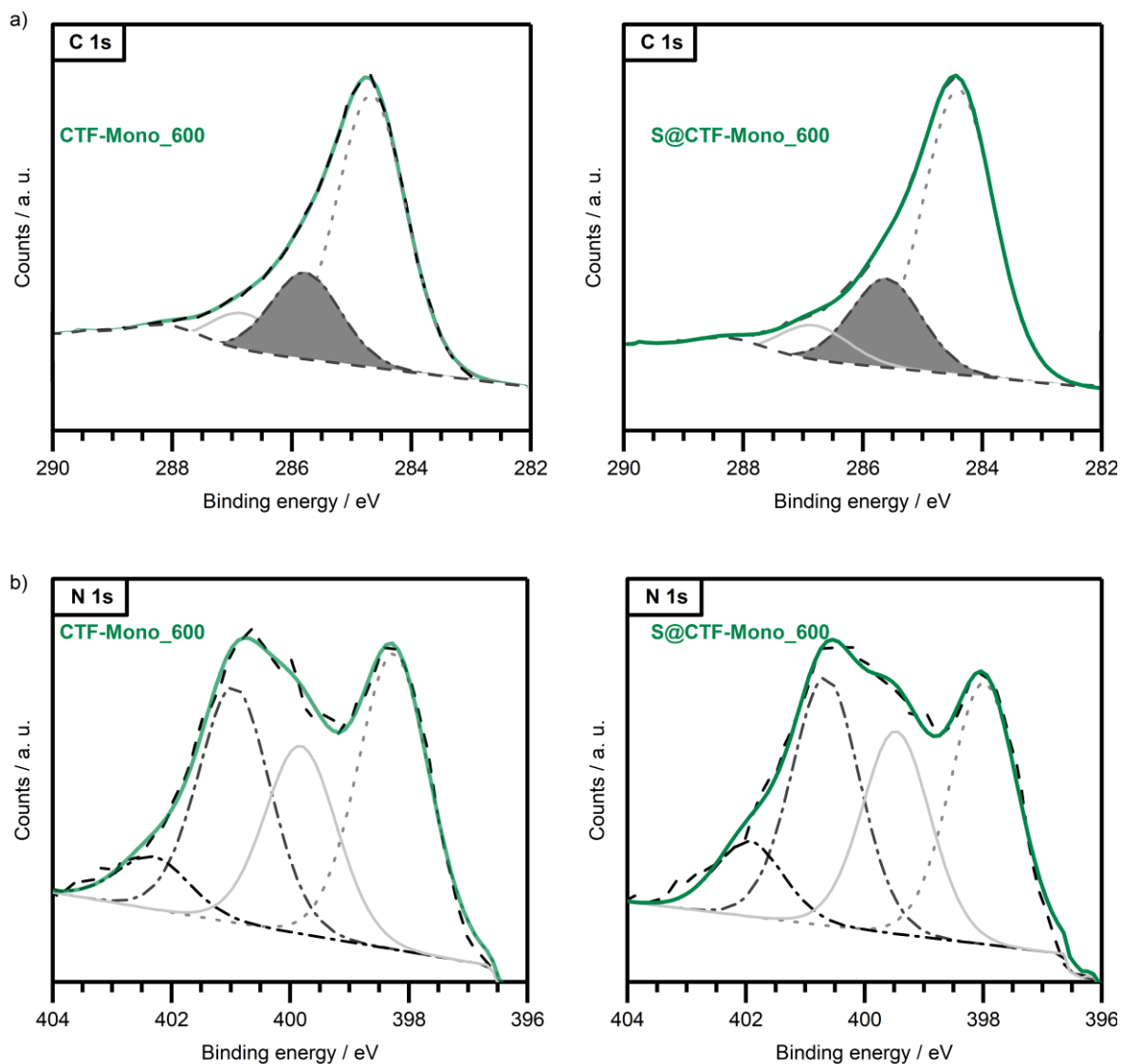


**Figure 34** a) High resolution C 1s XPS spectra of CTF-Mono\_600 and S@ CTF-Mono\_600, b) High resolution N 1s spectra of the same samples.

Fourier transform infrared spectroscopy displays a high degree of carbonisation for all samples, which is reflected by very broad and undefined peaks. In spite of that, an additional broad vibration at approximately  $1060\text{ cm}^{-1}$  (dotted line) is observed for all sulfur treated samples, which can be assigned to C=S stretching modes (see Figure A50 – A53 for all spectra).<sup>194</sup> In line with these findings, the intensity of the new vibration decreases when comparing the samples synthesised at lower reaction temperatures (thus, containing more sulfur) and the high temperature samples (containing less sulfur). Scanning electron microscopy (SEM) revealed a rough

surface, showing no distinct difference between the parent materials and their sulfur treated analogues (Figure A54 – A59).

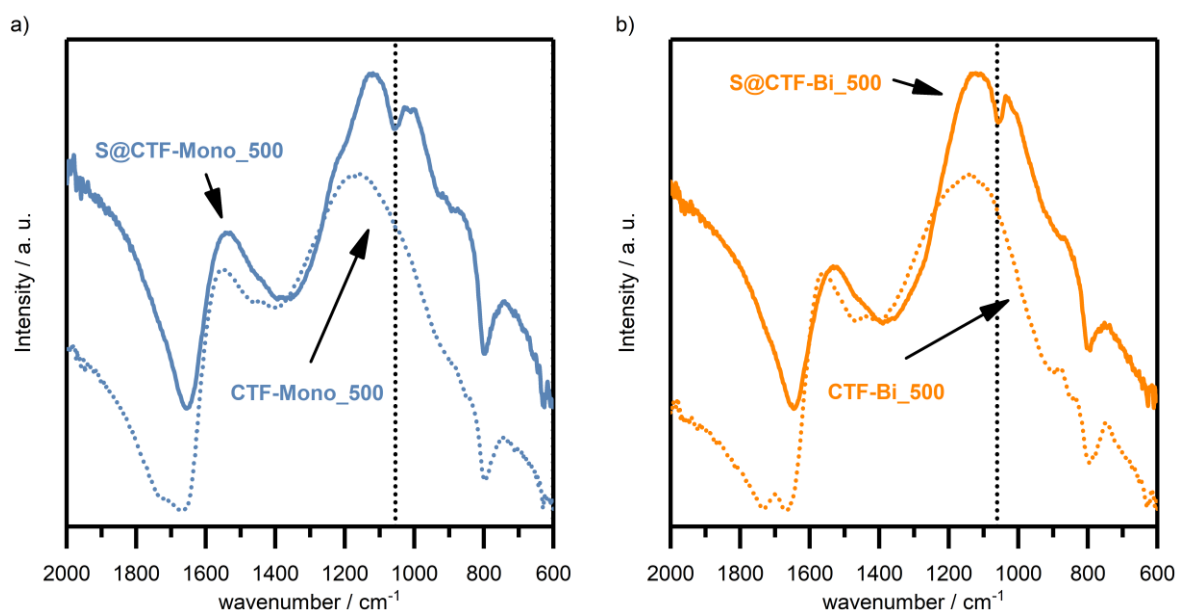


**Figure 35** FT-IR spectra of CTF-Mono/CTF-Bi\_500 and the sulfur treated analogues revealing an additional C=S stretching mode. The spectra shown here are normalised and an offset was applied for better visibility.

As it was mentioned earlier, the conductivity of the CTF materials plays a decisive role when considering CTFs as potential cathode materials. Especially when discussing the literature,<sup>143–145</sup> it is obvious that a huge amount of conductive additive (> 30 w%) is added in most cases prior to the electrode preparation. Hence, a reliable assessment of CTFs is actually not possible. Therefore, the gravimetric powder resistivity of all sulfur treated samples was determined in order to evaluate the suitability of CTFs as potential cathode materials. To this end, ca. 100 mg of the CTF were pressed (contact pressure 2 ton) in a cell with a diameter of 1 cm and the gravimetric powder resistivity was measured.<sup>\*\*\*</sup> Also conventionally synthesised CTF-1 (synthesised at 400 °C) was additionally investigated. The results reveal that the gravimetric powder resistivity of CTF-1 exceeds the values of the S@CTF samples by 6 orders of magnitude (M $\Omega$  vs.  $\Omega$ ; Figure 36). Thus, the application of CTF-1 as cathode material in a lithium sulfur battery remains at least unclear, since the required conductivity is not provided at all by the material itself. In contrast, all S@CTF samples which were obtained in a temperature range of 500 –

<sup>\*\*\*</sup> Instead of the specific resistivity, the gravimetric powder resistivity was determined, since an exact measurement of the filling height in this setup was error-prone. Thus, in order to compare the obtained values among each other, the mass of powder was used as an indirect correction factor for the filling height.

700°C display low gravimetric powder resistivities of 15 – 0.3  $\Omega \text{ mm}^2 \text{ mg}^{-1}$  (Table 14). Moreover, a decrease of the value is observed for samples obtained at higher temperatures, thus matching the expectations.

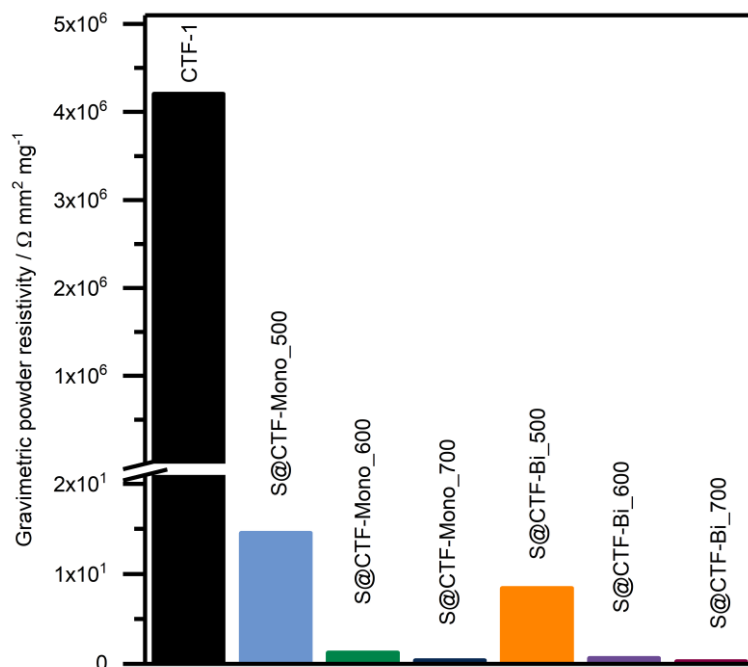


**Figure 36** Gravimetric powder resistivities of investigated sulfur treated CTF samples and CTF-1.

**Table 14** Gravimetric powder resistivities of investigated sulfur treated CTF samples and CTF-1.

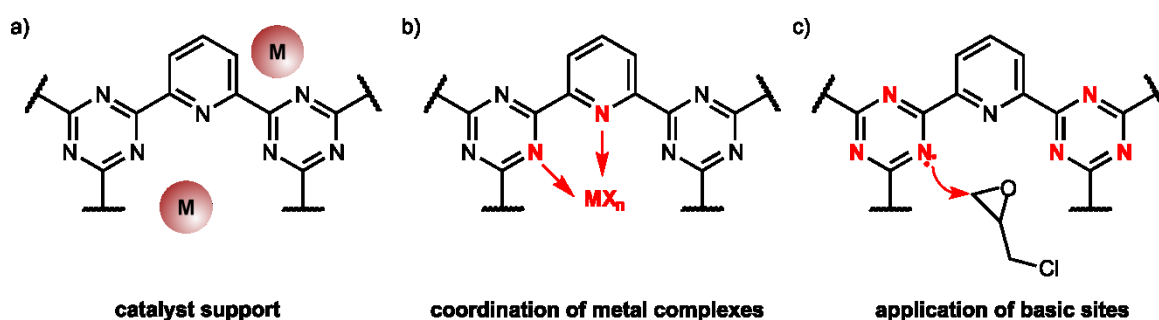
Sample	CTF-1	S@Mono_500	S@Mono_600	S@Mono_700	S@Bi_500	S@ Bi_600	S@ Bi_700
Gravimetric powder resistivity $\Omega \text{ mm}^2 \text{ g}^{-1}$	4.2 x 10 <sup>6</sup>	14.5	1.2	0.4	8.4	0.6	0.3

Within the thesis at hand, it was shown that the synthesis of conductive CTF materials containing covalently bound sulfur was successful. In a next step, the electrochemical evaluation of the discussed materials was conducted by M. Sc. Christian Kensy (Fraunhofer IWS, Dresden). Briefly, the targeted application of carbonate electrolytes was not possible, since a drastic loss of capacity was observed after a few cycles already which is most likely caused by a loss of active material. This leads to the hypothesis that covalently bound sulfur is just applicable under defined circumstances.<sup>196</sup> Thus, an ultramicroporous material is necessary that leads to a confinement of the sulfur species after the first discharge cycle. For this very reason, the hierarchical CTFs investigated here did not lead to a positive result in carbonate electrolytes, since the poly-

sulfides were not efficiently trapped within a very narrow ultramicroporous system. It is assumed that covalent sulfur is exclusively present prior to the first discharge cycle. After charging, it remains at least unclear if covalent bonding is obtained again. Certainly, covalent bonding is less important than an efficient trapping by the aid of an ultramicroporous material as already presented for carbons with a pore size of 0.5 nm.<sup>187,197</sup>

## 5.5 Integration of an N-heterocyclic carbene precursor into a covalent triazine framework for organocatalysis<sup>\*\*\*</sup>

To utilise CTFs as heterogeneous catalysts, three different pathways have been pursued lately (Scheme 24). The most facile approach is applying CTF materials as robust heterogeneous and porous catalyst support for catalytically active metal nanoparticles as demonstrated for palladium<sup>124,199</sup> and nickel.<sup>127</sup> However, these approaches do not take any advantage of particular structural benefits like open coordination sites of the CTF material itself.



**Scheme 24** Possible application of CTF materials as heterogeneous catalyst including: a) CTF as catalyst support for deposited metal nanoparticles (M), b) coordination of catalytically active metal complexes, c) application of basic properties of triazinic nitrogen atoms.

A more developed method makes use of pyridinic nitrogen atoms in the framework which enable coordination of different metal complexes. For example, Palkovits *et al.* demonstrated coordination of platinum(II) to a CTF based on a 2,6-dicyanopyridine to convert methane into methanol.<sup>128</sup> An alternative metal-free approach, presented by Roeser *et al.*, applies the basic nitrogen sites of CTFs to perform a ring-opening reaction to generate cyclic carbonates.<sup>123</sup> However, none of the aforementioned examples can be considered as a purely CTF-based organocatalyst that benefits from a monomer bearing a catalytically active functionality. Thus, this chapter describes the incorporation of a thermally fragile imidazolium functionality into a covalent triazine framework which results in a heterogeneous organocatalyst active in carbene-catalysed Umpolung reaction (Figure 37).

<sup>\*\*\*</sup> Parts of this chapter have been adopted verbatim from my publication.<sup>198</sup>

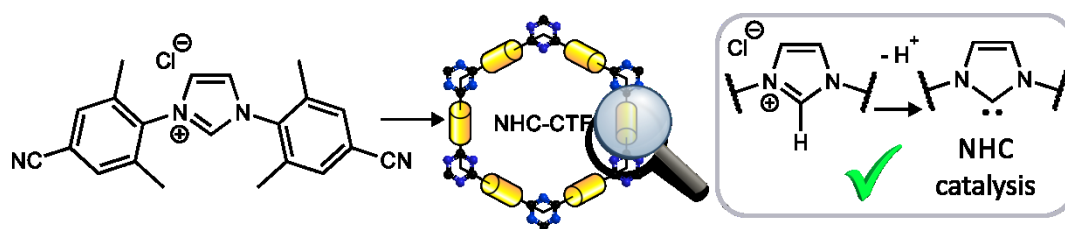


**Figure 37** Integration of an *N*-heterocyclic carbene precursor into a covalent triazine framework and its application as heterogeneous organocatalyst for carbene-catalysed Umpolung reaction (see Scheme 25).

The successful integration of an imidazolium monomer as a NHC-precursor into a CTF leads to a robust and functional catalyst but is just rarely described. In contrast to syntheses of MOFs<sup>200–202</sup> or EOFs,<sup>203</sup> an ionothermal trimerization of nitriles requires temperatures of up to 400 °C. Therefore, chemically fragile monomers bearing a NHC-precursor do not withstand these harsh conditions and well-defined functionalities simply decompose. This issue was reinvestigated carefully within the thesis at hand, especially when discussing the few examples of CTFs with embedded cationic imidazolium moieties (NHC-CTF).<sup>204–206</sup> In these publications, thermogravimetric analysis indicate a substantial decomposition of the respective imidazolium monomers starting at 300 °C already. Thus, a complete structural integrity of these materials remains unclear. Moreover, the presented applications (CO<sub>2</sub> capture and its hydrogenation to formate) gave at least indirect evidence of an intact structure. To overcome the delicate balance between decomposition of the imidazolium functionality and its transformation into a CTF, a finely adjusted synthetic protocol was developed.

Owing to the assumed thermal lability of the imidazolium-based monomer, thermogravimetric analysis (TGA) in argon was performed in order to estimate the optimal synthetic conditions for the new NHC-CTF. These experiments revealed a substantial mass loss of 75 w% between 350 °C and 400 °C (Figure 38).

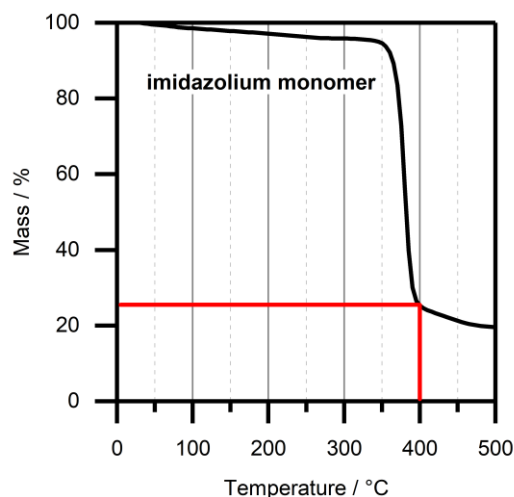


**Figure 38** Thermogravimetric analysis of imidazolium monomer in argon. The red horizontal line indicates the mass loss at 400 °C.

With respect to these findings, it was necessary to apply a significantly reduced reaction temperature of only 300 °C. To compensate the reduced reaction temperature and to achieve a high degree polymerisation, the reaction time was increased to 168 h (at 400 °C: 40 h). To this end, a mixture of the imidazolium monomer and  $\text{ZnCl}_2$  (5 eq.) was transferred into a quartz ampoule and subsequently sealed under vacuum. The ampoule was heated to 300 °C and opened. After grinding of the resulting black monolith, the crude product was washed with aqueous HCl, water and DMF in order to remove residual salt and organic impurities.

A structural confirmation of CTF materials is challenging in many cases, since the reaction products are usually black and insoluble solids thus limiting the use of potential characterisation techniques. For example, solid-state NMR techniques are better suited, if the materials provide any order which usually disappears at higher reaction temperatures ( $> 400^\circ\text{C}$ ). In those cases, only very broad signals are observable which do not provide insightful structural information.

Due to the reduced reaction temperature of the novel synthetic protocol, it was possible to record  $^1\text{H}$  MAS NMR spectra of the monomer and the resulting NHC-CTF. Comparing the solid state  $^1\text{H}$  MAS NMR spectra of the monomer and the resulting NHC-CTF confirms – despite differences in the line width due to a more disordered structure in the polymer – that the imidazolium moiety within the covalent triazine framework remains mostly intact (Figure 39a). The spectra show the presence of methyl groups (1 – 4 ppm) as well as of the protons in the aromatic regime (7 – 10 ppm) and most importantly the signal of the acidic imidazolium proton at a higher chemical shift of 12.2 ppm. Abstraction of this proton would lead to a free carbene

which acts as catalytically active species for the targeted application.<sup>207</sup> However, thermal treatment of imidazolium compounds is often associated by dimerization and/or elimination reactions of the imidazolium proton.<sup>208</sup> Regarding the signal areas of the methyl groups and the aromatic protons in the solid state  $^1\text{H}$  MAS NMR spectrum, no distinct decrease in the resulting polymer is evident. The signal intensity of the imidazolium proton in the NHC-CTF appears to be reduced slightly, which might stem from broadened signals caused by a less ordered polymer structure and/or a limited degree of decomposition.

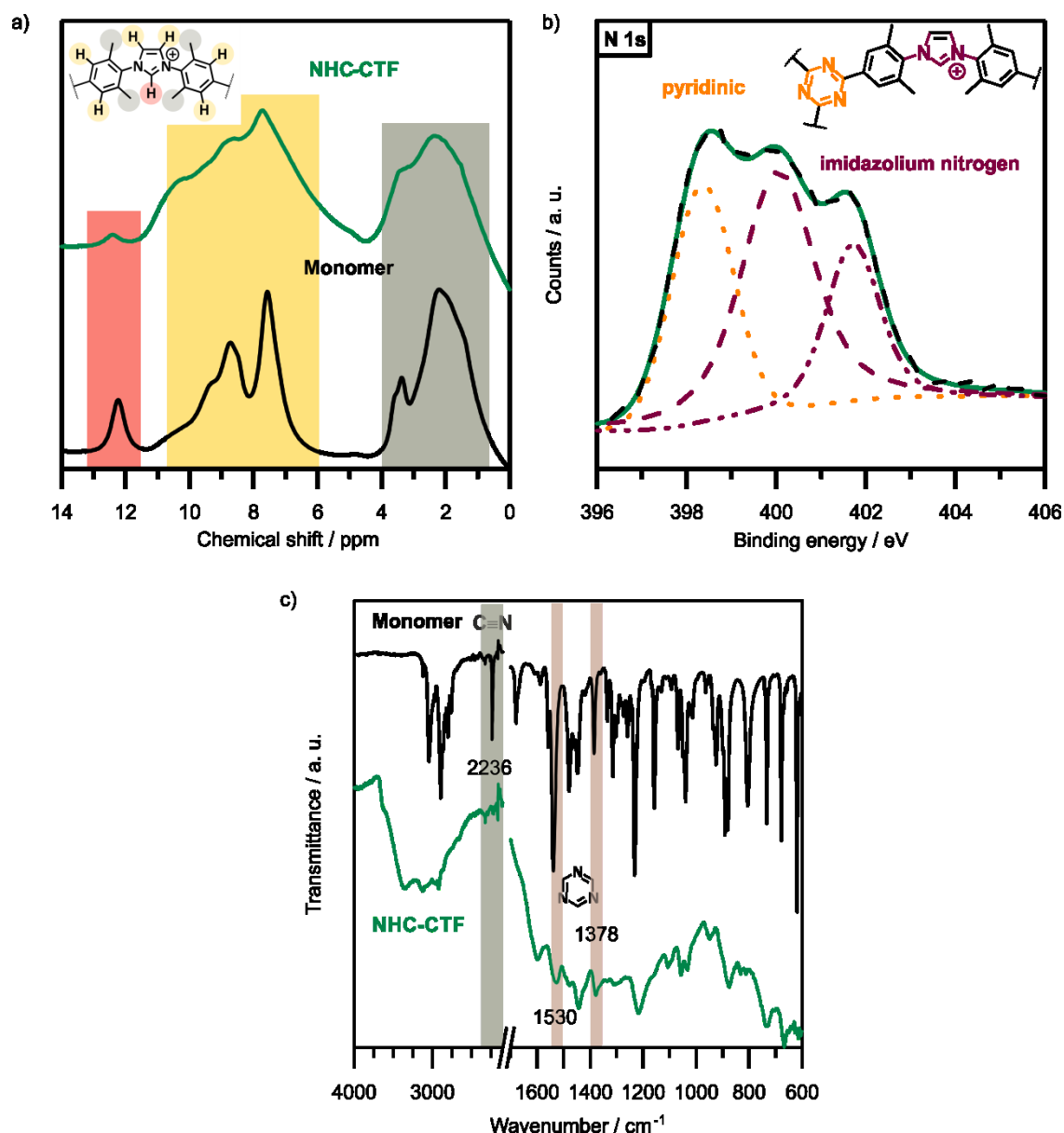


**Figure 39** a)  $^1\text{H}$  solid-state MAS NMR spectra of imidazolium-monomer and corresponding NHC-CTF; b) Deconvoluted N 1s XPS spectrum of NHC-CTF; and c) FT-IR spectra of imidazolium-monomer and corresponding NHC-CTF.



High resolution XPS nitrogen N 1s spectra were recorded to distinguish between several nitrogen species which should be present within the NHC-CTF (Figure 39b). Deconvolution of the N 1s spectra reveals the existence of pyridinic nitrogen with a binding energy (BE) of  $\approx 398.4$  eV which reflects nitrogen atoms from the triazine cores of the polymeric network.<sup>179</sup> More importantly, the presence of imidazolium nitrogen atoms (BE of  $\approx 400.0$  eV, 401.7 eV) provided clear evidence of an intact structure bearing cationic imidazolium moieties.<sup>179</sup>

Due to the reduced reaction temperature (and thus, a low degree of carbonisation), a well-defined material is obtained as reflected by discrete vibrations in the FT-IR spectrum (Figure 39c). The absence of the strong  $\text{C}\equiv\text{N}$  vibration ( $2236\text{ cm}^{-1}$ ) in the polymer points on a complete conversion of the monomer, since new vibrations at  $1530\text{ cm}^{-1}$  and  $1378\text{ cm}^{-1}$  suggest the formation of the triazine core.<sup>81</sup> Further verification of an intact structure is also implied by elemental analysis. For the NHC-CTF, a C/N ratio of 6.7 (ideal C/N: 5.3) and a C/H ratio of 1.2 (ideal C/H: 1.1) was determined. In contrast to these almost ideal values, thermal decomposition would be accompanied by increased C/N and C/H ratios. Powder X-ray diffraction shows interlayer (001) stacking (interlayer distance of 0.2 nm) as displayed by a broad reflection at  $22.1^\circ$  (Figure 40). According to TGA in air, a residual mass as low as 2.2 w% could be detected after combustion, which can be ascribed to residual  $\text{ZnCl}_2$  within the sample (Figure A60). Furthermore, the material is thermally stable under argon up to  $300^\circ\text{C}$  which matches the range of expectation based on the monomer stability (Figure A61). Scanning electron microscopy (SEM) pictures reveal a rough and lamellar surface of the particles (Figure A62).

**Table 15** Elemental analyses of NHC-CTF and samples obtained at  $320^\circ\text{C}$  and  $330^\circ\text{C}$ .

Sample	found (%)					calculated (%)				
	C	H	N	C/H	C/N	C	H	N	C/H	C/N
ideal values						69.5	5.3	15.4	1.1	5.3
NHC-CTF	71.1	5.1	12.5	1.2	6.7	69.5	5.3	15.4	1.1	5.3
NHC-CTF_320	70.1	4.7	9.4	1.2	8.7	69.5	5.3	15.4	1.1	5.3
NHC-CTF_330	73.0	4.0	8.3	1.5	10.2	69.5	5.3	15.4	1.1	5.3

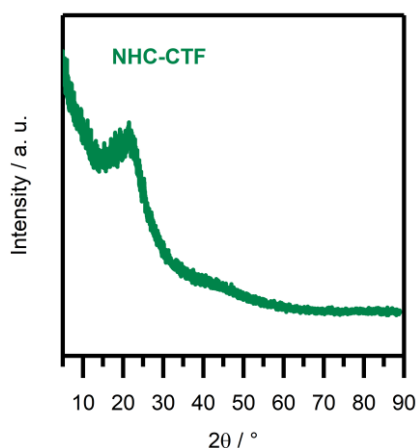


**Figure 40** PXRD data of NHC-CTF reflecting interlayer stacking.

To determine the porosity of the NHC-CTF, nitrogen physisorption measurements at 77 K were performed initially. The material is nonporous against nitrogen (Figure 41a). This might be a result of the low reaction temperature, thus inducing no chemical activation of  $\text{ZnCl}_2$ , which triggers both the trimerization reaction but also serves as a porogen at higher temperatures. Limitations in using nitrogen physisorption, as a result of a denser state after desolvation and cooling to 77 K, may arise for ultramicroporous materials or highly flexible frameworks.<sup>4</sup> In consequence,  $\text{CO}_2$  adsorption at 273 K was performed in order to enhance the mobility of the adsorptive and to unveil potential microporosity.<sup>4</sup> The resulting isotherm reveals an uptake of  $2.05 \text{ mmol g}^{-1}$  at 1 bar (Figure 41b). Moreover, the desorption branch shows a hysteresis loop in the whole pressure range, indicating a flexible character of the polymeric framework.<sup>104</sup> The high affinity of  $\text{CO}_2$  towards the charged network originates from quadrupole interactions. However, these findings do not allow for an exact pore size analysis, since strong interactions and dynamics lead to erroneous correlations of pore filling pressure and the corresponding pore size.<sup>4</sup> However,  $\text{CO}_2$  adsorption reveals the presence of small but accessible ultramicropores, which would not be ideally suited for a catalytic application in the liquid phase.

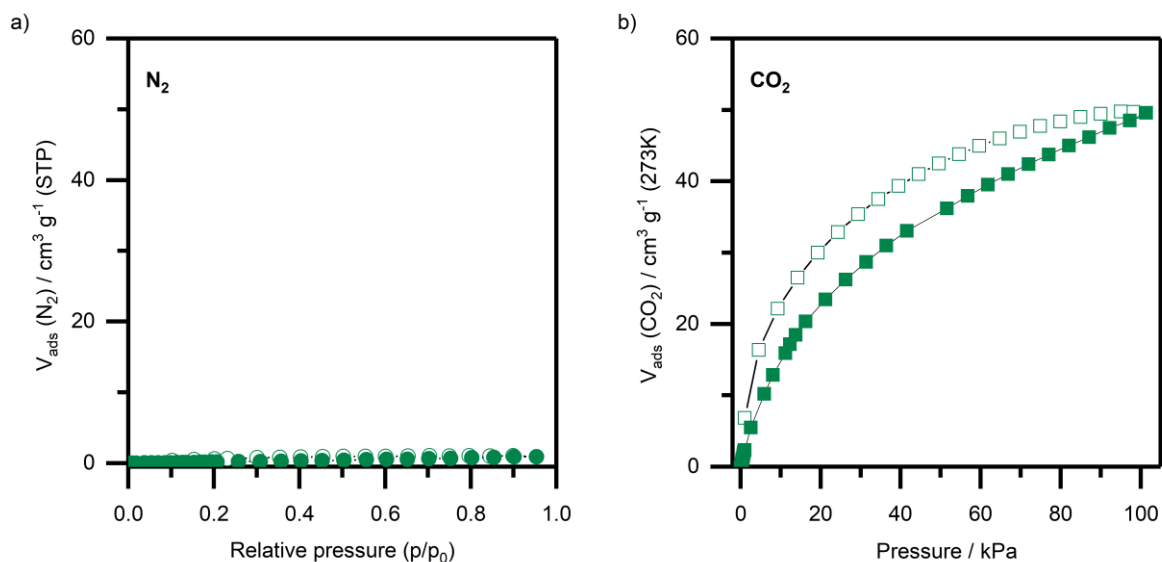


**Figure 41** a) Nitrogen physisorption isotherm (77 K) of NHC-CTF; b) Carbon dioxide physisorption isotherm (273 K) of NHC-CTF.

Vapour adsorption experiments at 298 K (Figure 42) were performed to further evaluate interactions with different solvents, since a significant swelling of the NHC-CTF was anticipated due to its flexible character. For MeCN and EtOH as adsorptives, thus very polar and small molecules, a continuous uptake over the whole pressure range at 298 K was observed, suggesting a constant swelling of the framework upon adsorption. This effect arises from strong interactions of the charged and nitrogen-rich polymer with these polar solvents. Especially interactions with MeCN (bearing nitrile groups) induce efficient swelling of the NHC-CTF which contains analogue structural motifs. In contrast, vapour adsorption applying toluene displays very weak interactions as reflected in a negligible uptake at  $p/p_0 = 1$  and almost zero uptake in the low pressure regime ( $< p/p_0 = 0.2$ ).

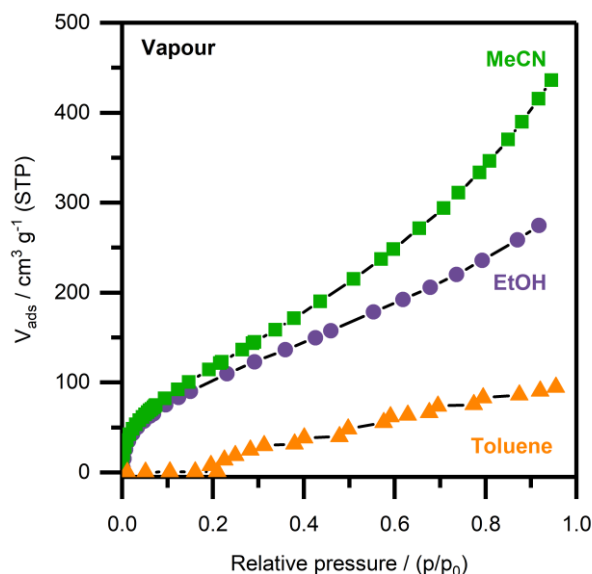
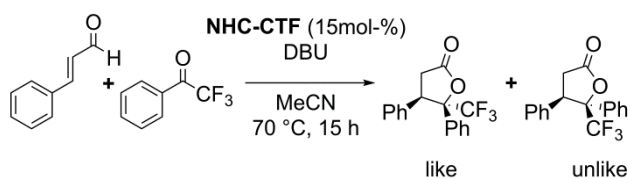


**Figure 42** Vapour adsorption isotherms (MeCN, EtOH, toluene) of NHC-CTF.

After verifying the structural integrity and the adsorption properties of the NHC-CTF, the catalytic activity of the material was evaluated choosing conjugated Umpolung as a prototypical test reaction.<sup>207</sup> This reaction takes advantage of an *in situ* generated free carbene species which catalyses the reaction of an  $\alpha,\beta$ -unsaturated cinnamaldehyde with trifluoroacetophenone (Scheme 25).<sup>209</sup>



**Scheme 25** Application of NHC-CTF as heterogeneous catalyst in carbene-catalysed conjugated Umpolung reaction.

To explore the feasibility of the NHC-CTF for this reaction, and thus to prove the existence of accessible carbene sites, several solvents (with high yields in the homogeneous reaction)<sup>210</sup> were tested for the reaction (Figure 43a). These experiments confirm the results obtained from vapour adsorption. For the reactions in MeCN and EtOH, thus polar and small solvents, yields of 81 % and 63 % after 24 h were obtained. In contrast, for *tert*-BuOH (polar, but bulky) and aromatic solvents like toluene and *ortho*-dichlorobenzene just very low yields of less than 10 % were found. Based on these results, MeCN was chosen for the follow-up experiments. Next, the heterogeneity of the reaction was confirmed by filtering the catalyst off before reaching complete conversion (Figure 43b). Indeed, no significant product formation could be observed,

thus excluding a leaching of the catalyst. A key feature of heterogeneous catalyst is easy recyclability; therefore the heterogeneous NHC-CTF catalyst was investigated over several runs. The yields did not vary significantly over 5 cycles, ranging from 75% – 81% (Figure 44 and Table 16). Hence, no structural collapse or pore blocking causing an activity loss can be determined. Control experiments were conducted, applying catalyst samples prepared at higher temperatures of 320 °C and 330 °C, respectively (henceforth referred to as NHC-CTF\_320 and NHC-CTF\_330). Given the fact that the imidazolium moiety should decompose upon thermal treatment, these samples should provide drastically reduced catalytic activity. These assumptions are strongly supported by poor yields of 8% (NHC-CTF\_320) and 0.7% (NHC-CTF\_330). Synthesising NHC-CTFs at temperatures of 330 °C or above results essentially in negligible catalytic activity, which confirms the proposed thermal decomposition characteristics and sensitivity of the imidazolium moiety.

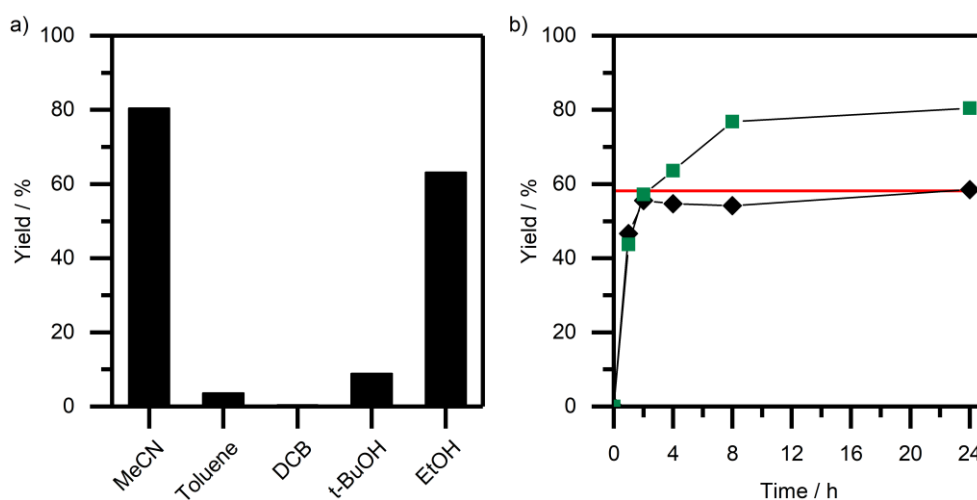


**Figure 43** a) Comparison of obtained yields using different solvents in heterogeneous catalysis; b) Kinetic data and heterogeneity testing of NHC-CTF. Red horizontal line illustrates no further product formation after removal of the catalyst. Reaction conditions:  $T = 70\text{ }^{\circ}\text{C}$ , 15 mol% of catalyst with respect to *trans*-cinnamaldehyde.

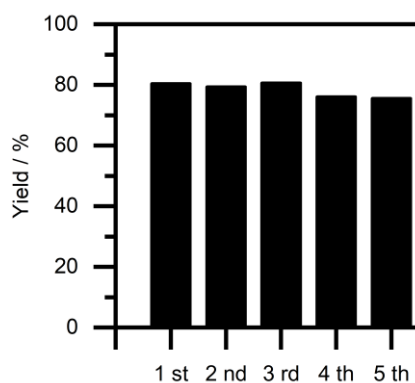


**Figure 44** Recyclability of NHC-CTF investigated over five runs in MeCN. Reaction conditions: T = 70 °C, 15 mol% of catalyst with respect to *trans*-cinnamaldehyde.

These results disconfirm recent findings in literature,<sup>204–206</sup> proposing the existence of an intact imidazolium motif in CTF materials produced at 400 °C. Finally, the heterogeneous system was compared with its homogeneous counterparts. As expected, the reaction kinetics (Figure A63) as well as the overall yield were slightly higher applying two different imidazolium salts (monomer, IMesxHCl bearing methyl groups instead of nitrile groups) (Table 16). However, the heterogeneous catalysis using solid NHC-CTF as catalyst provides significant benefits, in particular recyclability and stability.

**Table 16** Results of catalytic testing and comparison of NHC-CTF with samples synthesised at higher temperature and homogeneous analogues.

Catalyst	Cycle	Yield (GC) <sup>a</sup>	dr (like : unlike) <sup>b</sup>
NHC-CTF	1	81	1.1:1
	2	79	1.2:1
	3	81	1.2:1
	4	76	1.2:1
	5	76	1.2:1
NHC-CTF_320	1	7.9	1.3:1
NHC-CTF_330	1	0.7	1.3:1
Monomer	1	100	1.4:1
IMesxHCl	1	100	1.3:1

**a** determined by GC.

**b** determined by GC and confirmed by <sup>1</sup>H-NMR.

## 6 Summary, Conclusion and Outlook

The aim of this thesis was to advance the emerging field of covalent triazine frameworks from a synthetic point of view as well as to extend the scope of their potential applications. At the time of writing, the research area of covalent triazine frameworks is still small with approximately 220 publications. Despite this fact, several synthetic concepts have been published and intensively presented in chapter 2.5. However, none of these allows for a targeted introduction of mesoporosity into CTFs without a significant carbonisation of the material as a result of elevated reaction temperatures. To overcome this issue, a salt templating method was developed that applies binary salt mixtures of  $\text{ZnCl}_2$  (the conventional reaction medium) in combination with alkali halides at moderate temperatures. By varying the composition of the molten salt phase (the ratio of  $\text{ZnCl}_2$  to alkali halide) and thus its properties, a strong impact on the porosity of the resulting materials was observed. In contrast to a conventional synthetic method in pure molten  $\text{ZnCl}_2$ , the total pore volume of the salt templated materials was increased four-fold ( $2.1 \text{ cm}^3 \text{ g}^{-1}$  for CTF-1\_LiCl vs.  $0.5 \text{ cm}^3 \text{ g}^{-1}$  conventional CTF-1) under almost complete retention of the specific surface area ( $1320 \text{ m}^2 \text{ g}^{-1}$  vs.  $1440 \text{ m}^2 \text{ g}^{-1}$ ). In the future, this new method to access mesoporous CTFs could be expanded by utilising other metal salts to study their impact on the porosity of the materials. Further, it would be fascinating to track the ongoing processes in the molten salt phase via *in situ* Raman spectroscopy. The evolution of porosity within CTF materials strongly depends on the phase mixing/demixing of the organic phase and the molten salt phase. By means of *in situ* investigations, further insights into the origin of porosity in CTF materials could be gained by identifying the actual species in the molten salt phase.

Another aspect of this thesis covered a novel approach to synthesise CTF materials in a solvent-free, time-efficient and scalable manner. To this end, a mechanochemical synthesis route was developed that benefits from Friedel-Crafts alkylation to generate CTF materials from cyanuric chloride serving as triazine node and electron-rich aromatic compounds as linker molecules. By this method, permanently porous materials (up to  $570 \text{ m}^2 \text{ g}^{-1}$ ) could be synthesised from various monomers with different length and geometry. The syntheses can be conducted within two hours and on a gram scale, thus significantly exceeding known methods in terms of time-efficiency and scalability. It also became evident that the newly presented method gave access to

materials such as an anthracene-based CTF that could not be synthesised by any other existing method. Most importantly, this synthetic route is not suffering from incipient carbonisation in course of the synthesis. In consequence, it gives access to materials with potential photocatalytic activity. Hence, further investigation towards different applications such as the photocatalytic hydrogen evolution reaction should be considered. Also hydrogen storage could be an auspicious research area and in particular carbazole could be a promising platform molecule since it can easily be hydrogenated. The immobilisation of structurally intact carbazole moieties in CTFs (by means of a Friedel-Crafts alkylation) and the hydrogenation of those may be studied by solid-state NMR or FT-IR spectroscopy.

It has been outlined that elevated reaction temperatures (up to 700 °C) lead to the generation of mesoporosity in CTFs, but cause significant carbonisation. The structural changes upon thermal treatment have not been satisfactorily investigated except for some pioneering publications.<sup>179,211</sup> Within the thesis at hand, a novel CTF based on 3,5-dicyanopyridine could be established. By variation of the reaction temperature ranging from 400 – 700 °C, a set of (partially carbonised) samples was created and their structural changes were intensively investigated by XPS and physisorption measurements as a function of temperature. It turned out that higher temperatures lead to a significant increase of pyrrolic and quaternary nitrogen (at 400 °C, almost exclusively pyridinic nitrogen is present), pointing to a substantial degree of graphitisation. In a next step, these *ex situ* measurements were correlated with electrochemical data. Therefore, a new concept was introduced into the field of CTF research. The non-purified CTFs – still containing large amounts of ZnCl<sub>2</sub> – were directly processed into supercapacitor electrodes. Thereby, ZnCl<sub>2</sub> is serving two purposes: it acts as a porogen during the CTF synthesis (surface areas up to 3100 m<sup>2</sup> g<sup>-1</sup> were obtained) and is a precursor for an *in situ* generated aqueous electrolyte. It was demonstrated that this methodology bypasses extensive washing and more importantly, the findings gained from the electrochemical characterisation matched the structural indications from the XPS experiments. It could be proven that the material synthesised at 400 °C (DCP-CTF-400) exhibits inferior conductivity due to exclusive charge transfer in its conjugated  $\pi$ -system. In course of the temperature increase and thus a progressing degree of carbonisation, the formerly polymeric character of the CTF changes into an N-doped carbon rather than a polymer. Thus, a superior conductivity for DCP-CTF-700 is reflected by a pronounced capacitive behaviour and a rectangular cyclic voltammogram. The electrochemical



characterisation was ideally suited to display the structural changes upon thermal treatment and also illuminates the quest of conductivity in CTF materials which is decisive for potential electrochemical applications.

It was an initial goal of this thesis to evaluate the application of CTF materials as cathode materials in lithium sulphur batteries. The background of these investigations is a conductive poly(acrylonitrile) (PAN) polymer that contains large amounts of covalently bound sulfur (SPAN) and showed excellent and stable cycling performance in a carbonate based electrolyte system.<sup>189</sup> In analogy, CTFs were anticipated as promising platform materials in order to covalently attach sulfur. To this end, model CTFs based on 1,4-dicyanobenzene (CTF-Mono) and 4,4'-dicyano-1,1'-biphenyl (CTF-Bi) were synthesised at three different temperatures to induce different degrees of carbonisation. Consequently, a postsynthetic thermal treatment followed by severe purification steps leads to CTF materials containing covalently bound sulfur. The amounts of sulfur that could be integrated were determined by elemental analysis and followed the expected trends. Hence, for the samples obtained at the lowest temperature (500 °C), the highest amounts of sulfur (up to 33 w%) were detected. With higher temperatures the values decreased, reaching a minimum amount of 9 w%. These findings could be explained by the mechanism of sulfur attachment, since sulfur is exchanged against hydrogen atoms whose number is significantly reduced for the high temperature samples (due to carbonisation). In a next step, the impact of sulfur attachment on the porosity of the resulting S@CTF materials was investigated and two main trends were extracted. The porosity for each material decreased after the sulfur attachment and the largest percental drop of the total pore volume comparing the sulfur containing and its parent materials was found for the samples synthesised at 500 °C, thus for those samples containing the highest amount of sulfur. Interestingly, QSDFT analyses revealed a slight preference of sulfur bonding for mesopores. XPS experiments suggested the presence of C-S species in the sulfur treated materials and supported the formation of covalently bound sulfur. Briefly, the electrochemical characterisation underlined that CTFs (or more correct) hierarchical materials are not ideally suited to pursue the concept of covalent sulfur attaching. For all materials, a dramatic capacity loss was observed after only a few cycles, most probably due to a loss of active material (sulfur). It is highly probable that the key to succeed in this area is confinement of sulfur in ultramicropores which is also assumed in the case of SPAN. If polysulfides are not efficiently trapped in ultramicropores, they will irreversibly react with

carbonate based electrolytes and cause degradation. In the light of these results, a way to apply CTFs anyway could be a high temperature synthesis in the absence of  $\text{ZnCl}_2$  (the porogen). The formation of sheet-like, non-porous and carbonaceous CTF materials will occur and sulfur could be introduced by (vapour/melt) impregnation. It may be possible that sulfur accesses the interlayer voids and potentially, a suitable cathode material based on a CTF precursor can be generated.

The last chapter described the successful immobilisation of a charged cationic imidazolium moiety into a microporous covalent triazine framework. In this regard, the imidazolium motif can be considered as a protected N-heterocyclic carbene species within a CTF (NHC-CTF) that can be *in situ* generated and serves as an immobilised organocatalyst. Thereby, a rare example (except for the utilisation of basic nitrogen sites) of a CTF-based organocatalyst that intrinsically comprises a catalytically active functionality was generated. Within this thesis, it was demonstrated that conventional synthetic pathways did not lead to the desired NHC-CTF. Therefore, a finely adjusted synthetic protocol was developed that enabled the structural retention of the thermally labile imidazolium motif. The successful integration of the imidazolium moiety was proven by an in-depth structural characterisation, applying solid-state  $^1\text{H}$  MAS NMR, XPS and FT-IR spectroscopy and verifies the effective synthetic strategy. The resulting material is non-porous against nitrogen (due to stacking effects within the charged network) but has a high affinity towards carbon dioxide. More importantly, vapour adsorption experiments revealed a substantial swelling of the material with respect to different adsorptives. It turned out that small and polar solvents (MeCN und EtOH) led to a significant swelling and were therefore applied in consecutive catalytic studies. If applied as heterogeneous organocatalyst, the NHC-CTF is active in the carbene-catalysed Umpolung reaction. In consequence, catalytic testing of the NHC-CTF provided clear evidence of an intact structure, since the catalytically active carbene species is generated by proton abstraction from the imidazolium moiety. In parallel, the results obtained within the thesis at hand also contradict recent literature findings<sup>204–206</sup> that emphasise the existence of intact imidazolium motifs in CTF materials synthesised at 400 °C. In the future, the processes during  $\text{CO}_2$  adsorption should be monitored via *in situ* FT-IR or NMR investigations. These experiments may provide valuable insights inside the respective adsorption mechanisms, e.g. a potential chemical bonding of the

CO<sub>2</sub> molecules at the carbene sites. In analogy, different metal complexes could also be introduced and applied to expand the set of reactions that can be catalysed by the NHC-CTF.

The thesis at hand could provide significant contributions to the emerging field of covalent triazine frameworks. It was a main concern of this thesis to evaluate and compare the findings obtained in context with results of the recent literature. A key challenge in the future is the synthesis of truly crystalline materials that mostly depends on synthetic conditions allowing for an enhanced reversibility of the triazine formation. Although (highly) ordered materials are not necessary for certain applications such as gas storage or catalysis, crystalline CTFs could be a valuable platform in order to enable diffractometric investigations and to gain insights into the relation of structure and property. In analogy to COF chemistry, highly ordered CTF materials could be considered as 2D stacked materials and would allow for accessing optoelectronic applications where an efficient charge photogeneration is crucial and stacking faults due to disorder represent a serious issue. Also the combination of other methods, e.g. adsorption, with diffractometry will enable powerful characterisation and could thereby overcome a drawback of amorphous materials whose structure is sometimes considered as a black-box. In addition, transmission electron microscopy, X-ray absorption near edge structure (XANES) and extended X-ray absorption fine structure (EXAFS) could be applied for ordered CTF materials and would extend the scope of potential characterisation techniques. Without regard to the latter, a key question is the final application beyond extensive characterisation. As such, for example electrocatalysis may be of particular interest, since this application would strongly benefit from an enhanced intrinsic conductivity in  $\pi$ -conjugated 2D sheets of the respective CTF material.

## References

- (1) Davis, B. H.; Sing, K. S. W. Historical Aspects. In *Handbook of Porous Solids*; Wiley-VCH Verlag GmbH: Weinheim, Germany, **2002**; pp 1–23.
- (2) Schüth, F. Poröse Materialien Im Überblick. *Chemie Ing. Tech.* **2010**, *82* (6), 769–777.
- (3) Rouquerol, F.; Rouquerol, J.; Sing, K. S. W.; Llewellyn, P.; Maurin, G. Introduction. In *Adsorption by Powders and Porous Solids*; Elsevier Ltd.: Amsterdam, Netherlands, **2014**; pp 1–24.
- (4) Thommes, M.; Kaneko, K.; Neimark, A. V.; Olivier, J. P.; Rodriguez-Reinoso, F.; Rouquerol, J.; Sing, K. S. W. Physisorption of Gases, with Special Reference to the Evaluation of Surface Area and Pore Size Distribution (IUPAC Technical Report). *Pure Appl. Chem.* **2015**, *87* (9–10), 1051–1069.
- (5) Thomas, A. Functional Materials: From Hard to Soft Porous Frameworks. *Angew. Chem., Int. Ed.* **2010**, *49* (45), 8328–8344.
- (6) Dawson, R.; Cooper, A. I.; Adams, D. J. Nanoporous Organic Polymer Networks. *Prog. Polym. Sci.* **2012**, *37* (4), 530–563.
- (7) Chaoui, N.; Trunk, M.; Dawson, R.; Schmidt, J.; Thomas, A. Trends and Challenges for Microporous Polymers. *Chem. Soc. Rev.* **2017**, *46* (11), 3302–3321.
- (8) Zhang, H.; Cooper, A. I. Synthesis and Applications of Emulsion-Templated Porous Materials. *Soft Matter* **2005**, *1* (2), 107–113.
- (9) McKeown, N. B.; Makhseed, S.; Budd, P. M. Phthalocyanine-Based Nanoporous Network Polymers. *Chem. Commun.* **2002**, *0* (23), 2780–2781.
- (10) Budd, P. M.; Ghanem, B. S.; Makhseed, S.; McKeown, N. B.; Msayib, K. J.; Tattershall, C. E. Polymers of Intrinsic Microporosity (PIMs): Robust, Solution-Processable, Organic Nanoporous Materials. *Chem. Commun.* **2004**, *0* (2), 230–231.
- (11) Davankov, V. A.; Rogoshin, S. V.; Tsyurupa, M. P. Macroreticular Isoporous Gels through Crosslinking of Dissolved Polystyrene. *J. Polym. Sci. Polym. Symp.* **1974**, *47* (1), 95–101.
- (12) Germain, J.; Fréchet, J. M. J.; Svec, F. Hypercrosslinked Polyanilines with Nanoporous Structure and High Surface Area: Potential Adsorbents for Hydrogen Storage. *J. Mater. Chem.* **2007**, *17* (47), 4989–4997.
- (13) Kaskel, S. Poren per Baukasten. *Nachrichten aus der Chemie* **2005**, *53* (4), 394–399.
- (14) Li, H.; Eddaoudi, M.; O’Keeffe, M.; Yaghi, O. M. Design and Synthesis of an Exceptionally Stable and Highly Porous Metal-Organic Framework. *Nature* **1999**, *402* (6759), 276–279.
- (15) McKeown, N. B.; Budd, P. M. Polymers of Intrinsic Microporosity (PIMs): Organic Materials for Membrane Separations, Heterogeneous Catalysis and Hydrogen Storage. *Chem. Soc. Rev.* **2006**, *35* (8), 675–683.
- (16) Waller, P. J.; Gándara, F.; Yaghi, O. M. Chemistry of Covalent Organic Frameworks. *Acc. Chem. Res.* **2015**, *48* (12), 3053–3063.
- (17) Xu, Y.; Jin, S.; Xu, H.; Nagai, A.; Jiang, D. Conjugated Microporous Polymers: Design, Synthesis and Application. *Chem. Soc. Rev.* **2013**, *42* (20), 8012–8031.
- (18) Huang, J.; Turner, S. R. Hypercrosslinked Polymers: A Review. *Polym. Rev.* **2018**, *58* (1), 1–41.
- (19) Xu, L.; Li, Y. Responsive Guest Encapsulation of Dynamic Conjugated Microporous Polymers. *Sci. Rep.* **2016**, *6* (1), 28784.

- 
- (20) Yu, S.-Y.; Mahmood, J.; Noh, H.-J.; Seo, J.-M.; Jung, S.-M.; Shin, S.-H.; Im, Y.-K.; Jeon, I.-Y.; Baek, J.-B. Direct Synthesis of Covalent Triazine-Based Framework from Aromatic Amides. *Angew. Chem., Int. Ed.* **2018**, *57* (28), 8438–8442.
- (21) Ben, T.; Qiu, S. Porous Aromatic Frameworks: Synthesis, Structure and Functions. *CrystEngComm* **2013**, *15* (1), 17–26.
- (22) Ritter, N.; Antonietti, M.; Thomas, A.; Senkowska, I.; Kaskel, S.; Weber, J. Binaphthalene-Based, Soluble Polyimides: The Limits of Intrinsic Microporosity. *Macromolecules* **2009**, *42* (21), 8017–8020.
- (23) Ritter, N.; Senkowska, I.; Kaskel, S.; Weber, J. Intrinsically Microporous Poly(Imide)s: Structure–Porosity Relationship Studied by Gas Sorption and X-Ray Scattering. *Macromolecules* **2011**, *44* (7), 2025–2033.
- (24) Ritter, N.; Senkowska, I.; Kaskel, S.; Weber, J. Towards Chiral Microporous Soluble Polymers-Binaphthalene-Based Polyimides. *Macromol. Rapid Commun.* **2011**, *32* (5), 438–443.
- (25) Budd, P. M.; McKeown, N. B.; Fritsch, D. Free Volume and Intrinsic Microporosity in Polymers. *J. Mater. Chem.* **2005**, *15* (20), 1977–1986.
- (26) Ghanem, B. S.; Msayib, K. J.; McKeown, N. B.; Harris, K. D. M.; Pan, Z.; Budd, P. M.; Butler, A.; Selbie, J.; Book, D.; Walton, A. A Triptycene-Based Polymer of Intrinsic Microporosity That Displays Enhanced Surface Area and Hydrogen Adsorption. *Chem. Commun.* **2007**, *0* (1), 67–69.
- (27) Ghanem, B. S.; Hashem, M.; Harris, K. D. M.; Msayib, K. J.; Xu, M.; Budd, P. M.; Chaukura, N.; Book, D.; Tedds, S.; Walton, A.; et al. Triptycene-Based Polymers of Intrinsic Microporosity: Organic Materials That Can Be Tailored for Gas Adsorption. *Macromolecules* **2010**, *43* (12), 5287–5294.
- (28) Côté, A. P.; Benin, A. I.; Ockwig, N. W.; O’Keeffe, M.; Matzger, A. J.; Yaghi, O. M. Porous, Crystalline, Covalent Organic Frameworks. *Science* **2005**, *310* (5751), 1166–1170.
- (29) Diercks, C. S.; Yaghi, O. M. The Atom, the Molecule, and the Covalent Organic Framework. *Science* **2017**, *355* (6328).
- (30) El-Kaderi, H. M.; Hunt, J. R.; Mendoza-Cortés, J. L.; Côté, A. P.; Taylor, R. E.; O’Keeffe, M.; Yaghi, O. M. Designed Synthesis of 3D Covalent Organic Frameworks. *Science* **2007**, *316* (5822), 268–272.
- (31) Hunt, J. R.; Doonan, C. J.; LeVangie, J. D.; Côté, A. P.; Yaghi, O. M. Reticular Synthesis of Covalent Organic Borosilicate Frameworks. *J. Am. Chem. Soc.* **2008**, *130* (36), 11872–11873.
- (32) Du, Y.; Yang, H.; Whiteley, J. M.; Wan, S.; Jin, Y.; Lee, S.-H.; Zhang, W. Ionic Covalent Organic Frameworks with Spiroborate Linkage. *Angew. Chem., Int. Ed.* **2016**, *55* (5), 1737–1741.
- (33) Uribe-Romo, F. J.; Hunt, J. R.; Furukawa, H.; Klöck, C.; O’Keeffe, M.; Yaghi, O. M. A Crystalline Imine-Linked 3-D Porous Covalent Organic Framework. *J. Am. Chem. Soc.* **2009**, *131* (13), 4570–4571.
- (34) Uribe-Romo, F. J.; Doonan, C. J.; Furukawa, H.; Oisaki, K.; Yaghi, O. M. Crystalline Covalent Organic Frameworks with Hydrazone Linkages. *J. Am. Chem. Soc.* **2011**, *133* (30), 11478–11481.
- (35) Nagai, A.; Chen, X.; Feng, X.; Ding, X.; Guo, Z.; Jiang, D. A Squaraine-Linked Mesoporous Covalent Organic Framework. *Angew. Chem., Int. Ed.* **2013**, *52* (13), 3770–3774.
-

- (36) DeBlase, C. R.; Silberstein, K. E.; Truong, T.-T.; Abruña, H. D.; Dichtel, W. R.  $\beta$ -Ketoenamine-Linked Covalent Organic Frameworks Capable of Pseudocapacitive Energy Storage. *J. Am. Chem. Soc.* **2013**, *135* (45), 16821–16824.
- (37) Fang, Q.; Zhuang, Z.; Gu, S.; Kaspar, R. B.; Zheng, J.; Wang, J.; Qiu, S.; Yan, Y. Designed Synthesis of Large-Pore Crystalline Polyimide Covalent Organic Frameworks. *Nat. Commun.* **2014**, *5*, 4503.
- (38) Waller, P. J.; Lyle, S. J.; Osborn Popp, T. M.; Diercks, C. S.; Reimer, J. A.; Yaghi, O. M. Chemical Conversion of Linkages in Covalent Organic Frameworks. *J. Am. Chem. Soc.* **2016**, *138* (48), 15519–15522.
- (39) Beaudoin, D.; Maris, T.; Wuest, J. D. Constructing Monocrystalline Covalent Organic Networks by Polymerization. *Nat. Chem.* **2013**, *5* (10), 830–834.
- (40) Fang, Q.; Gu, S.; Zheng, J.; Zhuang, Z.; Qiu, S.; Yan, Y. 3D Microporous Base-Functionalized Covalent Organic Frameworks for Size-Selective Catalysis. *Angew. Chem., Int. Ed.* **2014**, *53* (11), 2878–2882.
- (41) Medina, D. D.; Sick, T.; Bein, T. Photoactive and Conducting Covalent Organic Frameworks. *Adv. Energy Mater.* **2017**, *7* (16), 1700387.
- (42) Sick, T.; Hufnagel, A. G.; Kampmann, J.; Kondofersky, I.; Calik, M.; Rotter, J. M.; Evans, A.; Döblinger, M.; Herbert, S.; Peters, K.; et al. Oriented Films of Conjugated 2D Covalent Organic Frameworks as Photocathodes for Water Splitting. *J. Am. Chem. Soc.* **2018**, *140* (6), 2085–2092.
- (43) Ascherl, L.; Sick, T.; Margraf, J. T.; Lapidus, S. H.; Calik, M.; Hettstedt, C.; Karaghiosoff, K.; Döblinger, M.; Clark, T.; Chapman, K. W.; et al. Molecular Docking Sites Designed for the Generation of Highly Crystalline Covalent Organic Frameworks. *Nat. Chem.* **2016**, *8* (4), 310–316.
- (44) Auras, F.; Ascherl, L.; Hakimiooun, A. H.; Margraf, J. T.; Hanusch, F. C.; Reuter, S.; Bessinger, D.; Döblinger, M.; Hettstedt, C.; Karaghiosoff, K.; et al. Synchronized Offset Stacking: A Concept for Growing Large-Domain and Highly Crystalline 2D Covalent Organic Frameworks. *J. Am. Chem. Soc.* **2016**, *138* (51), 16703–16710.
- (45) Reich, T. E.; Jackson, K. T.; Li, S.; Jena, P.; El-Kaderi, H. M. Synthesis and Characterization of Highly Porous Borazine-Linked Polymers and Their Performance in Hydrogen Storage Application. *J. Mater. Chem.* **2011**, *21* (29), 10629–10632.
- (46) Jackson, K. T.; Reich, T. E.; El-Kaderi, H. M. Targeted Synthesis of a Porous Borazine-Linked Covalent Organic Framework. *Chem. Commun.* **2012**, *48* (70), 8823–8825.
- (47) Rose, M.; Klein, N.; Senkovska, I.; Schrage, C.; Wollmann, P.; Böhlmann, W.; Böhringer, B.; Fichtner, S.; Kaskel, S. A New Route to Porous Monolithic Organic Frameworks via Cyclotrimerization. *J. Mater. Chem.* **2011**, *21* (3), 711–716.
- (48) Wisser, F. M.; Eckhardt, K.; Wisser, D.; Böhlmann, W.; Grothe, J.; Brunner, E.; Kaskel, S. Tailoring Pore Structure and Properties of Functionalized Porous Polymers by Cyclotrimerization. *Macromolecules* **2014**, *47* (13), 4210–4216.
- (49) Wisser, F. M.; Grothe, J.; Kaskel, S. Nanoporous Polymers as Highly Sensitive Functional Material in Chemiresistive Gas Sensors. *Sensors Actuators B Chem.* **2016**, *223*, 166–171.
- (50) Kou, Y.; Xu, Y.; Guo, Z.; Jiang, D. Supercapacitive Energy Storage and Electric Power Supply Using an Aza-Fused  $\pi$ -Conjugated Microporous Framework. *Angew. Chem.* **2011**, *123* (37), 8912–8916.
- (51) Jiang, J.-X.; Su, F.; Trewin, A.; Wood, C. D.; Campbell, N. L.; Niu, H.; Dickinson, C.; Ganin, A. Y.; Rosseinsky, M. J.; Khimiyak, Y. Z.; et al. Conjugated Microporous

- Poly(Aryleneethynylene) Networks. *Angew. Chem., Int. Ed.* **2007**, *46* (45), 8574–8578.
- (52) Trunk, M.; Herrmann, A.; Bildirir, H.; Yassin, A.; Schmidt, J.; Thomas, A. Copper-Free Sonogashira Coupling for High-Surface-Area Conjugated Microporous Poly(Aryleneethynylene) Networks. *Chem. - A Eur. J.* **2016**, *22* (21), 7179–7183.
- (53) Weber, J.; Thomas, A. Toward Stable Interfaces in Conjugated Polymers: Microporous Poly(*p*-Phenylene) and Poly(Phenyleneethynylene) Based on a Spirobifluorene Building Block. *J. Am. Chem. Soc.* **2008**, *130* (20), 6334–6335.
- (54) Trunk, M.; Teichert, J. F.; Thomas, A. Room-Temperature Activation of Hydrogen by Semi-Immobilized Frustrated Lewis Pairs in Microporous Polymer Networks. *J. Am. Chem. Soc.* **2017**, *139* (10), 3615–3618.
- (55) Liao, Y.; Weber, J.; Faul, C. F. J. Conjugated Microporous Polytriphenylamine Networks. *Chem. Commun.* **2014**, *50* (59), 8002–8005.
- (56) Lu, W.; Wei, Z.; Yuan, D.; Tian, J.; Fordham, S.; Zhou, H.-C. Rational Design and Synthesis of Porous Polymer Networks: Toward High Surface Area. *Chem. Mater.* **2014**, *26* (15), 4589–4597.
- (57) Sun, L.; Liang, Z.; Yu, J.; Xu, R. Luminescent Microporous Organic Polymers Containing the 1,3,5-Tri(4-Ethenylphenyl)Benzene Unit Constructed by Heck Coupling Reaction. *Polym. Chem.* **2013**, *4* (6), 1932–1938.
- (58) Chaikittisilp, W.; Kubo, M.; Moteki, T.; Sugawara-Narutaki, A.; Shimojima, A.; Okubo, T. Porous Siloxane–Organic Hybrid with Ultrahigh Surface Area through Simultaneous Polymerization–Destruction of Functionalized Cubic Siloxane Cages. *J. Am. Chem. Soc.* **2011**, *133* (35), 13832–13835.
- (59) Chen, L.; Honsho, Y.; Seki, S.; Jiang, D. Light-Harvesting Conjugated Microporous Polymers: Rapid and Highly Efficient Flow of Light Energy with a Porous Polyphenylene Framework as Antenna. *J. Am. Chem. Soc.* **2010**, *132* (19), 6742–6748.
- (60) Jiang, J.-X.; Su, F.; Trewin, A.; Wood, C. D.; Niu, H.; Jones, J. T. A.; Khimyak, Y. Z.; Cooper, A. I. Synthetic Control of the Pore Dimension and Surface Area in Conjugated Microporous Polymer and Copolymer Networks. *J. Am. Chem. Soc.* **2008**, *130* (24), 7710–7720.
- (61) Yuan, D.; Lu, W.; Zhao, D.; Zhou, H.-C. Highly Stable Porous Polymer Networks with Exceptionally High Gas-Uptake Capacities. *Adv. Mater.* **2011**, *23* (32), 3723–3725.
- (62) Schmidt, J.; Weber, J.; Epping, J. D.; Antonietti, M.; Thomas, A. Microporous Conjugated Poly(Thienylene Arylene) Networks. *Adv. Mater.* **2009**, *21* (6), 702–705.
- (63) Ahn, J.-H.; Jang, J.-E.; Oh, C.-G.; Ihm, S.-K.; Cortez, J.; Sherrington, D. C. Rapid Generation and Control of Microporosity, Bimodal Pore Size Distribution, and Surface Area in Davankov-Type Hyper-Cross-Linked Resins. *Macromolecules* **2005**, *39* (2), 627–632.
- (64) Schwab, M. G.; Senkovska, I.; Rose, M.; Klein, N.; Koch, M.; Pahnke, J.; Jonschker, G.; Schmitz, B.; Hirscher, M.; Kaskel, S. High Surface Area PolyHIPEs with Hierarchical Pore System. *Soft Matter* **2009**, *5* (5), 1055–1059.
- (65) Schwab, M. G.; Lennert, A.; Pahnke, J.; Jonschker, G.; Koch, M.; Senkovska, I.; Rehahn, M.; Kaskel, S. Nanoporous Copolymer Networks through Multiple Friedel-Crafts-Alkylation–studies on Hydrogen and Methane Storage. *J. Mater. Chem.* **2011**, *21* (7), 2131–2135.
- (66) Rose, M. Nanoporous Polymers: Bridging the Gap between Molecular and Solid Catalysts? *ChemCatChem* **2014**, *6* (5), 1166–1182.
- (67) Eddaoudi, M.; Kim, J.; Rosi, N.; Vodak, D.; Wachter, J.; O’Keeffe, M.; Yaghi, O. M.

- Systematic Design of Pore Size and Functionality in Isoreticular MOFs and Their Application in Methane Storage. *Science* **2002**, *295* (5554), 469–472.
- (68) Schmidt, J.; Werner, M.; Thomas, A. Conjugated Microporous Polymer Networks via Yamamoto Polymerization. *Macromolecules* **2009**, *42* (13), 4426–4429.
- (69) Cheng, G.; Hasell, T.; Trewin, A.; Adams, D. J.; Cooper, A. I. Soluble Conjugated Microporous Polymers. *Angew. Chem., Int. Ed.* **2012**, *51*, 12727–12731.
- (70) Rose, M.; Klein, N.; Böhlmann, W.; Böhringer, B.; Fichtner, S.; Kaskel, S. New Element Organic Frameworks Via Suzuki Coupling with High Adsorption Capacity for Hydrophobic Molecules. *Soft Matter* **2010**, *6* (16), 3918–3923.
- (71) Zhao, W.; Zhuang, X.; Wu, D.; Zhang, F.; Gehrig, D.; Laquai, F.; Feng, X. Boron- $\pi$ -Nitrogen-Based Conjugated Porous Polymers with Multi-Functions. *J. Mater. Chem. A* **2013**, *1* (44), 13878–13884.
- (72) Fischer, S.; Schimanowitz, A.; Dawson, R.; Senkovska, I.; Kaskel, S.; Thomas, A. Cationic Microporous Polymer Networks by Polymerisation of Weakly Coordinating Cations with CO<sub>2</sub>-Storage Ability. *J. Mater. Chem. A* **2014**, *2* (30), 11825–11829.
- (73) Ben, T.; Ren, H.; Ma, S.; Cao, D.; Lan, J.; Jing, X.; Wang, W.; Xu, J.; Deng, F.; Simmons, J. M.; et al. Targeted Synthesis of a Porous Aromatic Framework with High Stability and Exceptionally High Surface Area. *Angew. Chem.* **2009**, *121* (50), 9621–9624.
- (74) Trewin, A.; Cooper, A. I. Porous Organic Polymers: Distinction from Disorder? *Angew. Chem., Int. Ed.* **2010**, *49* (9), 1533–1535.
- (75) Fayon, P.; Trewin, A. Formation Mechanism of Ultra Porous Framework Materials. *Phys. Chem. Chem. Phys.* **2016**, *18* (25), 16840–16847.
- (76) Farha, O. K.; Eryazici, I.; Jeong, N. C.; Hauser, B. G.; Wilmer, C. E.; Sarjeant, A. A.; Snurr, R. Q.; Nguyen, S. T.; Yazaydin, A. Ö.; Hupp, J. T. Metal–Organic Framework Materials with Ultrahigh Surface Areas: Is the Sky the Limit? *J. Am. Chem. Soc.* **2012**, *134* (36), 15016–15021.
- (77) Fritsch, J.; Drache, F.; Nickerl, G.; Böhlmann, W.; Kaskel, S. Porous Phosphorus-Based Element Organic Frameworks: A New Platform for Transition Metal Catalysts Immobilization. *Microporous Mesoporous Mater.* **2013**, *172*, 167–173.
- (78) Rose, M.; Böhlmann, W.; Sabo, M.; Kaskel, S. Element–organic Frameworks with High Permanent Porosity. *Chem. Commun.* **2008**, 2462–2464.
- (79) Fritsch, J.; Rose, M.; Wollmann, P.; Böhlmann, W.; Kaskel, S. New Element Organic Frameworks Based on Sn, Sb, and Bi, with Permanent Porosity and High Catalytic Activity. *Materials* **2010**, *3* (4), 2447–2462.
- (80) Yuan, S.; Dorney, B.; White, D.; Kirklín, S.; Zapol, P.; Yu, L.; Liu, D.-J. Microporous Polyphenylenes with Tunable Pore Size for Hydrogen Storage. *Chem. Commun.* **2010**, *46* (25), 4547–4549.
- (81) Kuhn, P.; Antonietti, M.; Thomas, A. Porous, Covalent Triazine-Based Frameworks Prepared by Ionothermal Synthesis. *Angew. Chem., Int. Ed.* **2008**, *47* (18), 3450–3453.
- (82) Toland, W. G. (California Research Corporation, San Francisco, California). US3060179, **1962**.
- (83) Miller, G. H. (Texaco Inc., New York, N.Y.). US3775380, **1973**.
- (84) Caturla, F.; Molina-Sabio, M.; Rodríguez-Reinoso, F. Preparation of Activated Carbon by Chemical Activation with ZnCl<sub>2</sub>. *Carbon* **1991**, *29* (7), 999–1007.
- (85) Katekomol, P.; Roeser, J.; Bojdys, M.; Weber, J.; Thomas, A. Covalent Triazine Frameworks Prepared from 1,3,5-Tricyanobenzene. *Chem. Mater.* **2013**, *25* (9), 1542–1548.



- (86) Bojdys, M. J.; Jeromenok, J.; Thomas, A.; Antonietti, M. Rational Extension of the Family of Layered, Covalent, Triazine-Based Frameworks with Regular Porosity. *Adv Mater* **2010**, *22* (19), 2202–2205.
- (87) Zhao, Y.; Yao, K. X.; Teng, B.; Zhang, T.; Han, Y. A Perfluorinated Covalent Triazine-Based Framework for Highly Selective and Water-tolerant CO<sub>2</sub> Capture. *Energy Environ. Sci.* **2013**, *6* (12), 3684–3692.
- (88) Kuecken, S.; Schmidt, J.; Zhi, L.; Thomas, A. Conversion of Amorphous Polymer Networks to Covalent Organic Frameworks under Ionothermal Conditions: A Facile Synthesis Route for Covalent Triazine Frameworks. *J. Mater. Chem. A* **2015**, *3*, 24422–24427.
- (89) Li, Z.; Han, Y.; Guo, Y.; Xu, S.; Chen, F.; Ye, L.; Luo, Z.; Liu, X.; Zhou, H.; Zhao, T. Evolution of the Formation of a Covalent Triazine-Based Framework Catalyzed by *p*-Toluenesulfonic Acid Monohydrate. *RSC Adv.* **2017**, *7* (72), 45818–45823.
- (90) Artz, J. Covalent Triazine-Based Frameworks - Tailor-Made Catalysts and Catalyst Supports for Molecular and Nanoparticulate Species. *ChemCatChem* **2018**, *10* (8), 1753–1771.
- (91) Kuhn, P.; Forget, A.; Su, D.; Thomas, A.; Antonietti, M. From Microporous Regular Frameworks to Mesoporous Materials with Ultrahigh Surface Area: Dynamic Reorganization of Porous Polymer Networks. *J. Am. Chem. Soc.* **2008**, *130* (40), 13333–13337.
- (92) Wu, S.; Liu, Y.; Yu, G.; Guan, J.; Pan, C.; Du, Y.; Xiong, X.; Wang, Z. Facile Preparation of Dibenzoheterocycle-Functional Nanoporous Polymeric Networks with High Gas Uptake Capacities. *Macromolecules* **2014**, *47* (9), 2875–2882.
- (93) Kuhn, P.; Thomas, A.; Antonietti, M. Toward Tailorable Porous Organic Polymer Networks: A High-Temperature Dynamic Polymerization Scheme Based on Aromatic Nitriles. *Macromolecules* **2009**, *42* (1), 319–326.
- (94) Puthiaraj, P.; Lee, Y.-R.; Zhang, S.; Ahn, W.-S. Triazine-Based Covalent Organic Polymers: Design, Synthesis and Applications in Heterogeneous Catalysis. *J. Mater. Chem. A* **2016**, *4* (42), 16288–16311.
- (95) Zhang, W.; Li, C.; Yuan, Y.-P.; Qiu, L.-G.; Xie, A.-J.; Shen, Y.-H.; Zhu, J.-F.; Mastalerz, M.; Maly, K. E.; Germain, J.; et al. Highly Energy- and Time-Efficient Synthesis of Porous Triazine-Based Framework: Microwave-Enhanced Ionothermal Polymerization and Hydrogen Uptake. *J. Mater. Chem.* **2010**, *20* (31), 6413–6415.
- (96) Ren, S.; Bojdys, M. J.; Dawson, R.; Laybourn, A.; Khimyak, Y. Z.; Adams, D. J.; Cooper, A. I. Porous, Fluorescent, Covalent Triazine-Based Frameworks via Room-Temperature and Microwave-Assisted Synthesis. *Adv Mater* **2012**, *24* (17), 2357–2361.
- (97) Dey, S.; Bhunia, A.; Dolores Esquivel, M.; Janiak, C. Covalent Triazine-Based Frameworks (CTFs) from Triptycene and Fluorene Motif for CO<sub>2</sub> Adsorption. *J. Mater. Chem. A* **2016**, *4*, 6259–6263.
- (98) Xiang, Z.; Cao, D. Synthesis of Luminescent Covalent-Organic Polymers for Detecting Nitroaromatic Explosives and Small Organic Molecules. *Macromol. Rapid Commun.* **2012**, *33* (14), 1184–1190.
- (99) Ren, S.; Dawson, R.; Laybourn, A.; Jiang, J.; Khimyak, Y.; Adams, D. J.; Cooper, A. I. Functional Conjugated Microporous Polymers: From 1,3,5-Benzene to 1,3,5-Triazine. *Polym. Chem.* **2012**, *3* (4), 928–934.
- (100) Kuecken, S.; Acharjya, A.; Zhi, L.; Schwarze, M.; Schomäcker, R.; Thomas, A. Fast Tuning of Covalent Triazine Frameworks for Photocatalytic Hydrogen Evolution. *Chem.*

- Commun.* **2017**, *53* (43), 5854–5857.
- (101) Schwinghammer, K.; Hug, S.; Mesch, M. B.; Senker, J.; Lotsch, B. V. Phenyl-Triazine Oligomers for Light-Driven Hydrogen Evolution. *Energy Environ. Sci.* **2015**, *8* (11), 3345–3353.
- (102) Bhunia, A.; Boldog, I.; Moller, A.; Janiak, C. Highly Stable Nanoporous Covalent Triazine-Based Frameworks with an Adamantane Core for Carbon Dioxide Sorption and Separation. *J. Mater. Chem. A* **2013**, *1* (47), 14990–14999.
- (103) Bhunia, A.; Esquivel, D.; Dey, S.; Fernández-Terán, R.; Goto, Y.; Inagaki, S.; Van Der Voort, P.; Janiak, C. A Photoluminescent Covalent Triazine Framework: CO<sub>2</sub> Adsorption, Light-Driven Hydrogen Evolution and Sensing of Nitroaromatics. *J. Mater. Chem. A* **2016**, *4* (35), 13450–13457.
- (104) Troschke, E.; Grätz, S.; Lübken, T.; Borchardt, L. Mechanochemical Friedel-Crafts Alkylation-A Sustainable Pathway Towards Porous Organic Polymers. *Angew. Chem., Int. Ed.* **2017**, *56* (24), 6859–6863.
- (105) Lim, H.; Cha, M. C.; Chang, J. Y. Preparation of Microporous Polymers Based on 1,3,5-Triazine Units Showing High CO<sub>2</sub> Adsorption Capacity. *Macromol. Chem. Phys.* **2012**, *213* (13), 1385–1390.
- (106) Puthiaraj, P.; Cho, S.-M.; Lee, Y.-R.; Ahn, W.-S. Microporous Covalent Triazine Polymers: Efficient Friedel-Crafts Synthesis and Adsorption/Storage of CO<sub>2</sub> and CH<sub>4</sub>. *J. Mater. Chem. A* **2015**, *3* (13), 6792–6797.
- (107) Puthiaraj, P.; Kim, S.-S.; Ahn, W.-S. Covalent Triazine Polymers Using a Cyanuric Chloride Precursor via Friedel-Crafts Reaction for CO<sub>2</sub> Adsorption/Separation. *Chem. Eng. J.* **2016**, *283*, 184–192.
- (108) Wang, K.; Yang, L.; Wang, X.; Guo, L.; Cheng, G.; Zhang, C.; Jin, S.; Tan, B.; Cooper, A. Covalent Triazine Frameworks via a Low Temperature Polycondensation Approach. *Angew. Chem., Int. Ed.* **2017**, *56* (45), 14149–14153.
- (109) Buyukcakir, O.; Je, S. H.; Talapaneni, S. N.; Kim, D.; Coskun, A. Charged Covalent Triazine Frameworks for CO<sub>2</sub> Capture and Conversion. *ACS Appl. Mater. Interfaces* **2017**, *9* (8), 7209–7216.
- (110) Zhu, X.; Tian, C.; Veith, G. M.; Abney, C. W.; Dehaudt, J.; Dai, S. In Situ Doping Strategy for the Preparation of Conjugated Triazine Frameworks Displaying Efficient CO<sub>2</sub> Capture Performance. *J. Am. Chem. Soc.* **2016**, *138* (36), 11497–11500.
- (111) Wang, K.; Huang, H.; Liu, D.; Wang, C.; Li, J.; Zhong, C. Covalent Triazine-Based Frameworks with Ultramicropores and High Nitrogen Contents for Highly Selective CO<sub>2</sub> Capture. *Environ. Sci. Technol.* **2016**, *50* (9), 4869–4876.
- (112) Hug, S.; Stegbauer, L.; Oh, H.; Hirscher, M.; Lotsch, B. V. Nitrogen-Rich Covalent Triazine Frameworks as High-Performance Platforms for Selective Carbon Capture and Storage. *Chem. Mater.* **2015**, *27* (23), 8001–8010.
- (113) Hug, S.; Mesch, M. B.; Oh, H.; Popp, N.; Hirscher, M.; Senker, J.; Lotsch, B. V. A Fluorene Based Covalent Triazine Framework with High CO<sub>2</sub> and H<sub>2</sub> Capture and Storage Capacities. *J. Mater. Chem. A* **2014**, *2* (16), 5928–5936.
- (114) Bhunia, A.; Vasylyeva, V.; Janiak, C. From a Supramolecular Tetranitrile to a Porous Covalent Triazine-Based Framework with High Gas Uptake Capacities. *Chem. Commun.* **2013**, *49* (38), 3961–3963.
- (115) Yao, C.; Li, G.; Wang, J.; Xu, Y.; Chang, L. Template-Free Synthesis of Porous Carbon from Triazine Based Polymers and Their Use in Iodine Adsorption and CO<sub>2</sub> Capture. *Sci. Rep.* **2018**, *8* (1), 1867.

- (116) Zeng, Y.; Zou, R.; Zhao, Y. Covalent Organic Frameworks for CO<sub>2</sub> Capture. *Adv. Mater.* **2016**, *28* (15), 2855–2873.
- (117) Tuci, G.; Pilaski, M.; Ba, H.; Rossin, A.; Luconi, L.; Caporali, S.; Pham-Huu, C.; Palkovits, R.; Giambastiani, G. Unraveling Surface Basicity and Bulk Morphology Relationship on Covalent Triazine Frameworks with Unique Catalytic and Gas Adsorption Properties. *Adv. Funct. Mater.* **2017**, 1605672.
- (118) Dey, S.; Bhunia, A.; Boldog, I.; Janiak, C. A Mixed-Linker Approach towards Improving Covalent Triazine-Based Frameworks for CO<sub>2</sub> Capture and Separation. *Microporous Mesoporous Mater.* **2017**, *241*, 303–315.
- (119) Zhang, W.; Liang, F.; Li, C.; Qiu, L.-G.; Yuan, Y.-P.; Peng, F.-M.; Jiang, X.; Xie, A.-J.; Shen, Y.-H.; Zhu, J.-F. Microwave-Enhanced Synthesis of Magnetic Porous Covalent Triazine-Based Framework Composites for Fast Separation of Organic Dye from Aqueous Solution. *J. Hazard. Mater.* **2011**, *186* (2–3), 984–990.
- (120) Wang, T.; Kailasam, K.; Xiao, P.; Chen, G.; Chen, L.; Wang, L.; Li, J.; Zhu, J. Adsorption Removal of Organic Dyes on Covalent Triazine Framework (CTF). *Microporous Mesoporous Mater.* **2014**, *187*, 63–70.
- (121) Liu, J.; Zong, E.; Fu, H.; Zheng, S.; Xu, Z.; Zhu, D. Adsorption of Aromatic Compounds on Porous Covalent Triazine-Based Framework. *J. Colloid Interface Sci.* **2012**, *372* (1), 99–107.
- (122) Bhunia, A.; Dey, S.; Bous, M.; Zhang, C.; von Rybinski, W.; Janiak, C. High Adsorptive Properties of Covalent Triazine-Based Frameworks (CTFs) for Surfactants from Aqueous Solution. *Chem. Commun.* **2015**, *51* (3), 484–486.
- (123) Roeser, J.; Kailasam, K.; Thomas, A. Covalent Triazine Frameworks as Heterogeneous Catalysts for the Synthesis of Cyclic and Linear Carbonates from Carbon Dioxide and Epoxides. *ChemSusChem* **2012**, *5* (9), 1793–1799.
- (124) Chan-Thaw, C. E.; Villa, A.; Katekomol, P.; Su, D.; Thomas, A.; Prati, L. Covalent Triazine Framework as Catalytic Support for Liquid Phase Reaction. *Nano Lett.* **2010**, *10* (2), 537–541.
- (125) Chan-Thaw, C. E.; Villa, A.; Prati, L.; Thomas, A. Triazine-Based Polymers as Nanostructured Supports for the Liquid-Phase Oxidation of Alcohols. *Chem. - A Eur. J.* **2011**, *17* (3), 1052–1057.
- (126) Chan-Thaw, C. E.; Villa, A.; Wang, D.; Santo, V. D.; Orbelli Biroli, A.; Veith, G. M.; Thomas, A.; Prati, L. PdH<sub>x</sub> Entrapped in a Covalent Triazine Framework Modulates Selectivity in Glycerol Oxidation. *ChemCatChem* **2015**, *7* (14), 2149–2154.
- (127) Li, Z.; He, T.; Liu, L.; Chen, W.; Zhang, M.; Wu, G.; Chen, P. Covalent Triazine Framework Supported Non-Noble Metal Nanoparticles with Superior Activity for Catalytic Hydrolysis of Ammonia Borane: From Mechanistic Study to Catalyst Design. *Chem. Sci.* **2017**, *8* (1), 781–788.
- (128) Palkovits, R.; Antonietti, M.; Kuhn, P.; Thomas, A.; Schüth, F. Solid Catalysts for the Selective Low-Temperature Oxidation of Methane to Methanol. *Angew. Chem., Int. Ed.* **2009**, *48* (37), 6909–6912.
- (129) Periana; Taube; Gamble; Taube; Satoh; Fujii. Platinum Catalysts for the High-Yield Oxidation of Methane to a Methanol Derivative. *Science* **1998**, *280* (5363), 560–564.
- (130) Hug, S.; Tauchert, M. E.; Li, S.; Pachmayr, U. E.; Lotsch, B. V. A Functional Triazine Framework Based on *N*-Heterocyclic Building Blocks. *J. Mater. Chem.* **2012**, *22* (28), 13956–13964.
- (131) Bavykina, A. V.; Goesten, M. G.; Kapteijn, F.; Makkee, M.; Gascon, J. Efficient

- Production of Hydrogen from Formic Acid Using a Covalent Triazine Framework Supported Molecular Catalyst. *ChemSusChem* **2015**, *8* (5), 809–812.
- (132) Bavykina, A. V.; Olivos Suarez, A. I.; Osadchii, D.; Valecha, R.; Franz, R.; Makkee, M.; Kapteijn, F.; Gascon, J. A Facile Method for the Preparation of Covalent Triazine Framework Coated Monoliths as Catalyst Support - Applications in C1 Catalysis. *ACS Appl. Mater. Interfaces* **2017**, *9* (31), 26060–26065.
- (133) Li, L.; Fang, W.; Zhang, P.; Bi, J.; He, Y.; Wang, J.-Y. J.; Su, W. Sulfur-Doped Covalent Triazine-Based Frameworks for Enhanced Photocatalytic Hydrogen Evolution from Water under Visible Light. *J. Mater. Chem. A* **2016**, *4* (32), 12402–12406.
- (134) Meier, C. B.; Sprick, R. S.; Monti, A.; Guiglion, P.; Lee, J.-S. M.; Zwiijnenburg, M. A.; Cooper, A. I. Structure-Property Relationships for Covalent Triazine-Based Frameworks: The Effect of Spacer Length on Photocatalytic Hydrogen Evolution from Water. *Polymer* **2017**, *126*, 283–290.
- (135) Jiang, Q.; Sun, L.; Bi, J.; Liang, S.; Li, L.; Yu, Y.; Wu, L. MoS<sub>2</sub> Quantum Dots Modified Covalent Triazine-Based Frameworks for Enhanced Photocatalytic Hydrogen Evolution. *ChemSusChem* **2018**, *11* (6), 1108–1113.
- (136) Kamiya, K.; Kamai, R.; Hashimoto, K.; Nakanishi, S. Platinum-Modified Covalent Triazine Frameworks Hybridized with Carbon Nanoparticles as Methanol-Tolerant Oxygen Reduction Electrocatalysts. *Nat. Commun.* **2014**, *5*, 5040.
- (137) Iwase, K.; Yoshioka, T.; Nakanishi, S.; Hashimoto, K.; Kamiya, K. Copper-Modified Covalent Triazine Frameworks as Non-Noble-Metal Electrocatalysts for Oxygen Reduction. *Angew. Chem., Int. Ed.* **2015**, *54* (38), 11068–11072.
- (138) Kamai, R.; Kamiya, K.; Hashimoto, K.; Nakanishi, S. Oxygen-Tolerant Electrodes with Platinum-Loaded Covalent Triazine Frameworks for the Hydrogen Oxidation Reaction. *Angew. Chem., Int. Ed.* **2016**, *55* (42), 13184–13188.
- (139) Yamaguchi, S.; Kamiya, K.; Hashimoto, K.; Nakanishi, S. Ru Atom-Modified Covalent Triazine Framework as a Robust Electrocatalyst for Selective Alcohol Oxidation in Aqueous Electrolytes. *Chem. Commun.* **2017**, *53*, 10437–10440.
- (140) Béguin, F.; Presser, V.; Balducci, A.; Frackowiak, E. Carbons and Electrolytes for Advanced Supercapacitors. *Adv. Mater.* **2014**, *26* (14), 2219–2251.
- (141) Zhu, J.; Zhuang, X.; Yang, J.; Feng, X.; Hirano, S.-I. Graphene-Coupled Nitrogen-Enriched Porous Carbon Nanosheets for Energy Storage. *J. Mater. Chem. A* **2017**, *5*, 16732–16739.
- (142) Li, Y.; Zheng, S.; Liu, X.; Li, P.; Sun, L.; Yang, R.; Wang, S.; Wu, Z.; Bao, X.; Deng, W. Conductive Microporous Covalent Triazine-Based Framework for High-Performance Electrochemical Capacitive Energy Storage. *Angew. Chem., Int. Ed.* **2017**, *57* (27), 7992–7996.
- (143) Talapaneni, S. N.; Hwang, T. H.; Je, S. H.; Buyukcakir, O.; Choi, J. W.; Coskun, A. Elemental-Sulfur-Mediated Facile Synthesis of a Covalent Triazine Framework for High-Performance Lithium-Sulfur Batteries. *Angew. Chem., Int. Ed.* **2016**, *55* (9), 3106–3111.
- (144) Je, S. H.; Kim, H. J.; Kim, J.; Choi, J. W.; Coskun, A. Perfluoroaryl-Elemental Sulfur S<sub>N</sub>Ar Chemistry in Covalent Triazine Frameworks with High Sulfur Contents for Lithium-Sulfur Batteries. *Adv. Funct. Mater.* **2017**, 1703947.
- (145) Xu, F.; Yang, S.; Jiang, G.; Ye, Q.; Wei, B.; Wang, H. Fluorinated, Sulfur-Rich, Covalent Triazine Frameworks for Enhanced Confinement of Polysulfides in Lithium-Sulfur Batteries. *ACS Appl. Mater. Interfaces* **2017**, *9* (43), 37731–37738.
- (146) Thommes, M.; Cychosz, K. A. Physical Adsorption Characterization of Nanoporous

- Materials: Progress and Challenges. *Adsorption* **2014**, *20* (2–3), 233–250.
- (147) Lennard-Jones, J. Cohesion. *Proc. Phys. Soc* **1931**, *43* (240), 461–482.
- (148) Langmuir, I. The Constitution and Fundamental Properties of Solids and Liquids. *J. Am. Chem. Soc.* **2016**, *38*, 2221–2295.
- (149) Brunauer, S.; Emmett, P. H.; Teller, E. Adsorption of Gases in Multimolecular Layers. *J. Am. Chem. Soc.* **1938**, *60* (2), 309–319.
- (150) Rouquerol, J.; Llewellyn, P.; Rouquerol, F. Is the BET Equation Applicable to Microporous Adsorbents? In *Studies in Surface Science and Catalysis*; Elsevier Ltd.: Amsterdam, Netherlands, **2007**; Vol. 160, pp 49–56.
- (151) Monson, P. A. Understanding Adsorption/Desorption Hysteresis for Fluids in Mesoporous Materials Using Simple Molecular Models and Classical Density Functional Theory. *Microporous Mesoporous Mater.* **2012**, *160*, 47–66.
- (152) Landers, J.; Yu Gor, G.; Neimark, A. V. Density Functional Theory Methods for Characterization of Porous Materials. *Aspects* **2013**, *437*, 3–32.
- (153) Weber, J.; Antonietti, M.; Thomas, A. Microporous Networks of High-Performance Polymers: Elastic Deformations and Gas Sorption Properties. *Macromolecules* **2008**, *41* (8), 2880–2885.
- (154) Weber, J.; Schmidt, J.; Thomas, A.; Böhlmann, W. Micropore Analysis of Polymer Networks by Gas Sorption and  $^{129}\text{Xe}$  NMR Spectroscopy: Toward a Better Understanding of Intrinsic Microporosity. *Langmuir* **2010**, *26* (19), 15650–15656.
- (155) Ratner, B. D.; Castner, D. G. Electron Spectroscopy for Chemical Analysis. In *Surface Analysis– The Principal Techniques*; John Wiley & Sons, Ltd: Chichester, UK, **2009**; pp 47–112.
- (156) Shirley, D. A. High-Resolution X-Ray Photoemission Spectrum of the Valence Bands of Gold. *Phys. Rev. B* **1972**, *5* (12), 4709–4714.
- (157) Végh, J. The Shirley Background Revised. *J. Electron Spectros. Relat. Phenomena* **2006**, *151* (3), 159–164.
- (158) Troschke, E.; Grätz, S.; Borchardt, L.; Haubold, D.; Senkovska, I.; Eychmueller, A.; Kaskel, S. Salt Templated Synthesis of Hierarchical Covalent Triazine Frameworks. *Microporous Mesoporous Mater.* **2017**, *239*, 190–194.
- (159) Massiot, D.; Fayon, F.; Capron, M.; King, I.; Le Calvé, S.; Alonso, B.; Durand, J.-O.; Bujoli, B.; Gan, Z.; Hoatson, G. Modelling One- and Two-Dimensional Solid-State NMR Spectra. *Magn. Reson. Chem.* **2002**, *40* (1), 70–76.
- (160) Weingarth, D.; Zeiger, M.; Jäckel, N.; Aslan, M.; Feng, G.; Presser, V. Graphitization as a Universal Tool to Tailor the Potential-Dependent Capacitance of Carbon Supercapacitors. *Adv. Energy Mater.* **2014**, *4* (13), 1400316.
- (161) Šturala, J.; Boháčová, S.; Chudoba, J.; Metelková, R.; Cibulka, R. Electron-Deficient Heteroarenium Salts: An Organocatalytic Tool for Activation of Hydrogen Peroxide in Oxidations. *J. Org. Chem.* **2015**, *80* (5), 2676–2699.
- (162) Rensch, T. Bachelor Thesis, TU Dresden, **2017**.
- (163) Nickerl, G.; Notzon, A.; Heitbaum, M.; Senkovska, I.; Glorius, F.; Kaskel, S. Selective Adsorption Properties of Cationic Metal–Organic Frameworks Based on Imidazolic Linker. *Cryst. Growth Des.* **2012**, *13* (1), 198–203.
- (164) Artz, J.; Mallmann, S.; Palkovits, R. Selective Aerobic Oxidation of HMF to 2,5-Diformylfuran on Covalent Triazine Frameworks-Supported Ru Catalysts. *ChemSusChem* **2015**, *8* (4), 672–679.
- (165) Brückner, J. Alternative Anodenmaterialien Für Die Lithium-Schwefel-Batterie, PhD

- Thesis, TU Dresden, 2015.
- (166) Thieme, S. Kathoden- Und Elektrolytkonzepte Für Die Lithium-Schwefel-Batterie, PhD Thesis, TU Dresden, 2016.
- (167) Borchardt, L.; Oschatz, M.; Kaskel, S. Carbon Materials for Lithium Sulfur Batteries - 10 Critical Questions. *Chem. – A Eur. J.* **2016**, *22*, 2–30.
- (168) Fechler, N.; Fellingner, T.-P.; Antonietti, M. “Salt Templating”: A Simple and Sustainable Pathway toward Highly Porous Functional Carbons from Ionic Liquids. *Adv Mater* **2013**, *25* (1), 75–79.
- (169) Ma, Z.; Zhang, H.; Yang, Z.; Zhang, Y.; Yu, B.; Liu, Z. Highly Mesoporous Carbons Derived from Biomass Feedstocks Templated with Eutectic Salt ZnCl<sub>2</sub>/KCl. *J. Mater. Chem. A* **2014**, *2* (45), 19324–19329.
- (170) MacDonald, L. G.; Perry, G. S.; Smith, J. R.; Wilcox, S. D. LiCl-ZnCl<sub>2</sub> Phase Diagram. *Thermochim. Acta* **1986**, *97*, 29–35.
- (171) FTsalt - FACT Salt Phase Diagrams [http://www.crct.polymtl.ca/fact../documentation/FTsalt/FTsalt\\_Figs.htm](http://www.crct.polymtl.ca/fact../documentation/FTsalt/FTsalt_Figs.htm) (accessed Mar 22, 2018).
- (172) Liu, X.; Fechler, N.; Antonietti, M. Salt Melt Synthesis of Ceramics, Semiconductors and Carbon Nanostructures. *Chem. Soc. Rev.* **2013**, *42* (21), 8237–8265.
- (173) Liu, X.; Giordano, C.; Antonietti, M. A Facile Molten-Salt Route to Graphene Synthesis. *Small* **2014**, *10* (1), 193–200.
- (174) Huang, W.; Wang, Z. J.; Ma, B. C.; Ghasimi, S.; Gehrig, D.; Laquai, F.; Landfester, K.; Zhang, K. A. I. Hollow Nanoporous Covalent Triazine Frameworks via Acid Vapor-Assisted Solid Phase Synthesis for Enhanced Visible Light Photoactivity. *J. Mater. Chem. A* **2016**, *4* (20), 7555–7559.
- (175) Vollhardt, K. P. C.; Schore, N. E. In *Organic Chemistry: Structure and Function*; W.H. Freeman & Co. Ltd: New York, USA, 2015.
- (176) Hao, G.-P.; Zhang, Q.; Sin, M.; Hippauf, F.; Borchardt, L.; Brunner, E.; Kaskel, S. Design of Hierarchically Porous Carbons with Interlinked Hydrophilic and Hydrophobic Surface and Their Capacitive Behavior. *Chem. Mater.* **2016**, *28* (23), 8715–8725.
- (177) See, K. A.; Hug, S.; Schwinghammer, K.; Lumley, M. A.; Zheng, Y.; Nolt, J. M.; Stucky, G. D.; Wudl, F.; Lotsch, B. V.; Seshadri, R. Lithium Charge Storage Mechanisms of Cross-Linked Triazine Networks and Their Porous Carbon Derivatives. *Chem. Mater.* **2015**, *27* (11), 3821–3829.
- (178) Kuhn, P.; Forget, A.; Hartmann, J.; Thomas, A.; Antonietti, M. Template-Free Tuning of Nanopores in Carbonaceous Polymers through Ionothermal Synthesis. *Adv. Mater.* **2009**, *21* (8), 897–901.
- (179) Osadchii, D. Y.; Olivos Suarez, A. I.; Bavykina, A. V.; Gascon, J. Revisiting Nitrogen Species in Covalent Triazine Frameworks. *Langmuir* **2017**, *33* (50), 14278–14285.
- (180) Qiang, Z.; Xia, Y.; Xia, X.; Vogt, B. D. Generalized Synthesis of a Family of Highly Heteroatom-Doped Ordered Mesoporous Carbons. *Chem. Mater.* **2017**, *29* (23), 10178–10186.
- (181) Khomenko, V.; Dittrich, R.; Joseph, Y. Graphene Based Chemiresistive Vapor Sensors. *Procedia Eng.* **2015**, *120*, 777–780.
- (182) Oschatz, M.; Pré, P.; Dörfler, S.; Nickel, W.; Beaunier, P.; Rouzaud, J.-N.; Fischer, C.; Brunner, E.; Kaskel, S. Nanostructure Characterization of Carbide-Derived Carbons by Morphological Analysis of Transmission Electron Microscopy Images Combined with

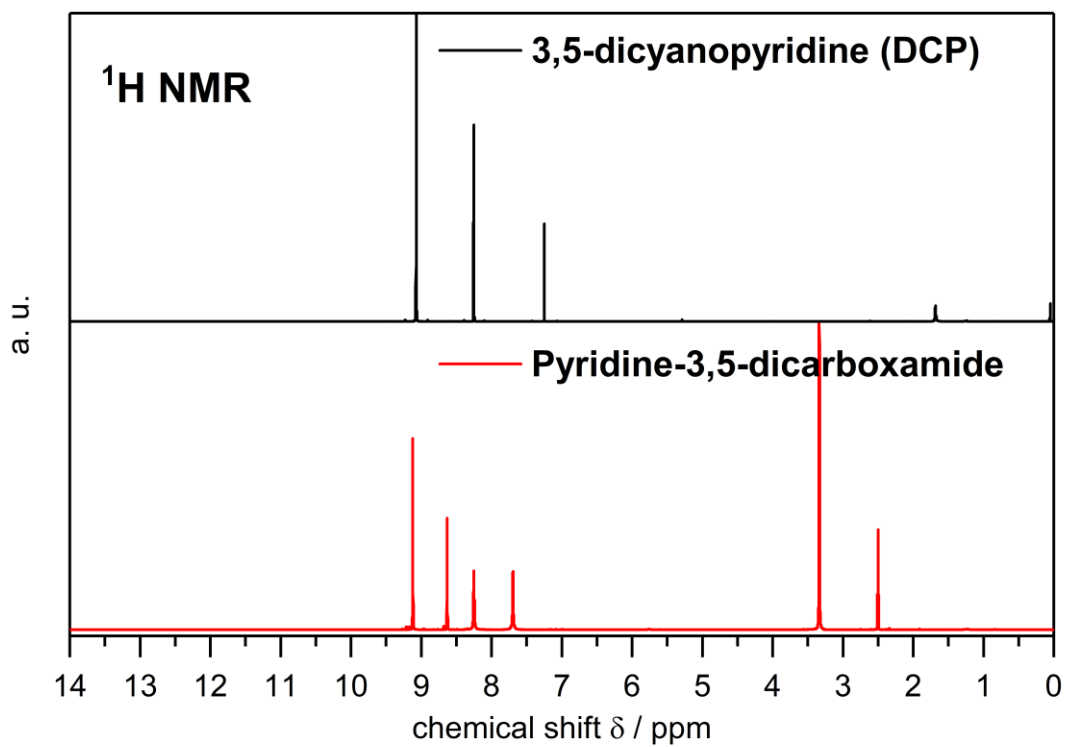
- Physisorption and Raman Spectroscopy. *Carbon* **2016**, *105*, 314–322.
- (183) Ferrari, A. C.; Robertson, J. Interpretation of Raman Spectra of Disordered and Amorphous Carbon. *Phys. Rev. B* **2000**, *61* (20), 14095–14107.
- (184) Everall, N.; Jackson, R. W.; Howard, J.; Hutchinson, K. Fluorescence Rejection in Raman Spectroscopy Using a Gated Intensified Diode Array Detector. *J. Raman Spectrosc.* **1986**, *17* (5), 415–423.
- (185) Ji, X.; Lee, K. T.; Nazar, L. F. A Highly Ordered Nanostructured Carbon-Sulphur Cathode for Lithium-Sulphur Batteries. *Nat. Mater.* **2009**, *8* (6), 500–506.
- (186) Thieme, S.; Brückner, J.; Meier, A.; Bauer, I.; Gruber, K.; Kaspar, J.; Helmer, A.; Althues, H.; Schmuck, M.; Kaskel, S. A Lithium-sulfur Full Cell with Ultralong Cycle Life: Influence of Cathode Structure and Polysulfide Additive. *J. Mater. Chem. A* **2015**, *3* (7), 3808–3820.
- (187) Xin, S.; Gu, L.; Zhao, N.-H.; Yin, Y.-X.; Zhou, L.-J.; Guo, Y.-G.; Wan, L.-J. Smaller Sulfur Molecules Promise Better Lithium-Sulfur Batteries. *J. Am. Chem. Soc.* **2012**, *134* (45), 18510–18513.
- (188) Li, Z.; Yuan, L.; Yi, Z.; Sun, Y.; Liu, Y.; Jiang, Y.; Shen, Y.; Xin, Y.; Zhang, Z.; Huang, Y. Insight into the Electrode Mechanism in Lithium-Sulfur Batteries with Ordered Microporous Carbon Confined Sulfur as the Cathode. *Adv. Energy Mater.* **2014**, *4* (7), 130147373.
- (189) Fanous, J.; Wegner, M.; Grimminger, J.; Andresen, Ä.; Buchmeiser, M. R. Structure-Related Electrochemistry of Sulfur-Poly(Acrylonitrile) Composite Cathode Materials for Rechargeable Lithium Batteries. *Chem. Mater.* **2011**, *23* (22), 5024–5028.
- (190) Liao, H.; Ding, H.; Li, B.; Ai, X.; Wang, C. Covalent-Organic Frameworks: Potential Host Materials for Sulfur Impregnation in Lithium-Sulfur Batteries. *J. Mater. Chem. A* **2014**, *2* (23), 8854–8858.
- (191) Hippauf, F.; Nickel, W.; Hao, G.-P.; Schwedtmann, K.; Giebeler, L.; Oswald, S.; Borchardt, L.; Doerfler, S.; Weigand, J. J.; Kaskel, S. The Importance of Pore Size and Surface Polarity for Polysulfide Adsorption in Lithium Sulfur Batteries. *Adv. Mater. Interfaces* **2016**, *3* (18), 1600508.
- (192) Jiang, X.; Wang, P.; Zhao, J. 2D Covalent Triazine Framework: A New Class of Organic Photocatalyst for Water Splitting. *J. Mater. Chem. A* **2015**, *3* (15), 7750–7758.
- (193) Moulder, J. F.; Chastain, J. *Handbook of X-Ray Photoelectron Spectroscopy: A Reference Book of Standard Spectra for Identification and Interpretation of XPS Data*; Physical Electronics Division, Perkin-Elmer Corp, **1992**.
- (194) Chang, C. H. Preparation and Characterization of Carbon-Sulfur Surface Compounds. *Carbon* **1981**, *19* (3), 175–186.
- (195) Grzybek, T.; Pietrzak, R.; Wachowska, H. X-Ray Photoelectron Spectroscopy Study of Oxidized Coals with Different Sulphur Content. *Fuel Process. Technol.* **2002**, *77–78*, 1–7.
- (196) Li, G.; Wang, S.; Zhang, Y.; Li, M.; Chen, Z.; Lu, J. Revisiting the Role of Polysulfides in Lithium-Sulfur Batteries. *Adv. Mater.* **2018**, 1705590.
- (197) Dominko, R.; Vizintin, A.; Aquilanti, G.; Stievano, L.; Helen, M. J.; Munnangi, A. R.; Fichtner, M.; Arcon, I. Polysulfides Formation in Different Electrolytes from the Perspective of X-Ray Absorption Spectroscopy. *J. Electrochem. Soc.* **2018**, *165* (1), A5014–A5019.
- (198) Troschke, E.; Nguyen, K. D.; Paasch, S.; Schmidt, J.; Nickerl, G.; Senkovska, I.; Brunner, E.; Kaskel, S. Integration of an N-heterocyclic carbene precursor into a covalent triazine framework for organocatalysis. *Chem. Eur. J.* **2018**.

- (199) Wang, Z.; Liu, C.; Huang, Y.; Hu, Y.; Zhang, B. Covalent Triazine Framework-Supported Palladium as a Ligand-Free Catalyst for the Selective Double Carbonylation of Aryl Iodides under Ambient Pressure of CO. *Chem. Commun.* **2016**, 52 (14), 2960–2963.
- (200) Oisaki, K.; Li, Q.; Furukawa, H.; Czaja, A. U.; Yaghi, O. M. A Metal–Organic Framework with Covalently Bound Organometallic Complexes. *J. Am. Chem. Soc.* **2010**, 132 (27), 9262–9264.
- (201) Lalonde, M. B.; Farha, O. K.; Scheidt, K. A.; Hupp, J. T. N-Heterocyclic Carbene-Like Catalysis by a Metal–Organic Framework Material. *ACS Catal.* **2012**, 2 (8), 1550–1554.
- (202) Kong, G.-Q.; Xu, X.; Zou, C.; Wu, C.-D. Two Metal–Organic Frameworks Based on a Double Azolium Derivative: Post-Modification and Catalytic Activity. *Chem. Commun.* **2011**, 47 (39), 11005–11007.
- (203) Rose, M.; Notzon, A.; Heitbaum, M.; Nickerl, G.; Paasch, S.; Brunner, E.; Glorius, F.; Kaskel, S. N-Heterocyclic Carbene Containing Element Organic Frameworks as Heterogeneous Organocatalysts. *Chem. Commun.* **2011**, 47 (16), 4814–4816.
- (204) Park, K.; Lee, K.; Kim, H.; Ganesan, V.; Cho, K.; Jeong, S. K.; Yoon, S. Preparation of Covalent Triazine Framework with the Imidazolium Cation Embedded in Basic Sites and Its Application for CO<sub>2</sub> Capture. *J. Mater. Chem. A* **2017**, 5, 8576–8582.
- (205) Gunasekar, G. H.; Park, K.; Ganesan, V.; Lee, K.; Kim, N.-K.; Jung, K.-D.; Yoon, S. A Covalent Triazine Framework, Functionalized with Ir/N-Heterocyclic Carbene Sites, for the Efficient Hydrogenation of CO<sub>2</sub> to Formate. *Chem. Mater.* **2017**, 29, 6740–6748.
- (206) Liu, T.-T.; Xu, R.; Yi, J.-D.; Liang, J.; Wang, X.-S.; Shi, P.-C.; Huang, Y.-B.; Cao, R. Imidazolium-Based Cationic Covalent Triazine Frameworks for Highly Efficient Cycloaddition of Carbon Dioxide. *ChemCatChem* **2018**, 10 (9), 2036–2040.
- (207) Burstein, C.; Glorius, F. Organocatalyzed Conjugate Umpolung of  $\alpha,\beta$ -Unsaturated Aldehydes for the Synthesis of  $\gamma$ -Butyrolactones. *Angew. Chem., Int. Ed.* **2004**, 43 (45), 6205–6208.
- (208) Hahn, F. E.; Jahnke, M. C. Heterocyclische Carbene – Synthese Und Koordinationschemie. *Angew. Chem.* **2008**, 120 (17), 3166–3216.
- (209) Schrader, W.; Handayani, P. P.; Burstein, C.; Glorius, F. Investigating Organocatalytic Reactions: Mass Spectrometric Studies of a Conjugate Umpolung Reaction. *Chem. Commun.* **2007**, 716–718.
- (210) Hirano, K.; Piel, I.; Glorius, F. Diastereoselective Synthesis of Trifluoromethylated  $\gamma$ -Butyrolactones via N-Heterocyclic Carbene-Catalyzed Conjugated Umpolung of  $\alpha,\beta$ -Unsaturated Aldehydes. *Adv. Synth. Catal.* **2008**, 350 (7–8), 984–988.
- (211) Hao, L.; Ning, J.; Luo, B.; Wang, B.; Zhang, Y.; Tang, Z.; Yang, J.; Thomas, A.; Zhi, L. Structural Evolution of 2D Microporous Covalent Triazine-Based Framework toward the Study of High-Performance Supercapacitors. *J. Am. Chem. Soc.* **2015**, 137 (1), 219–225.

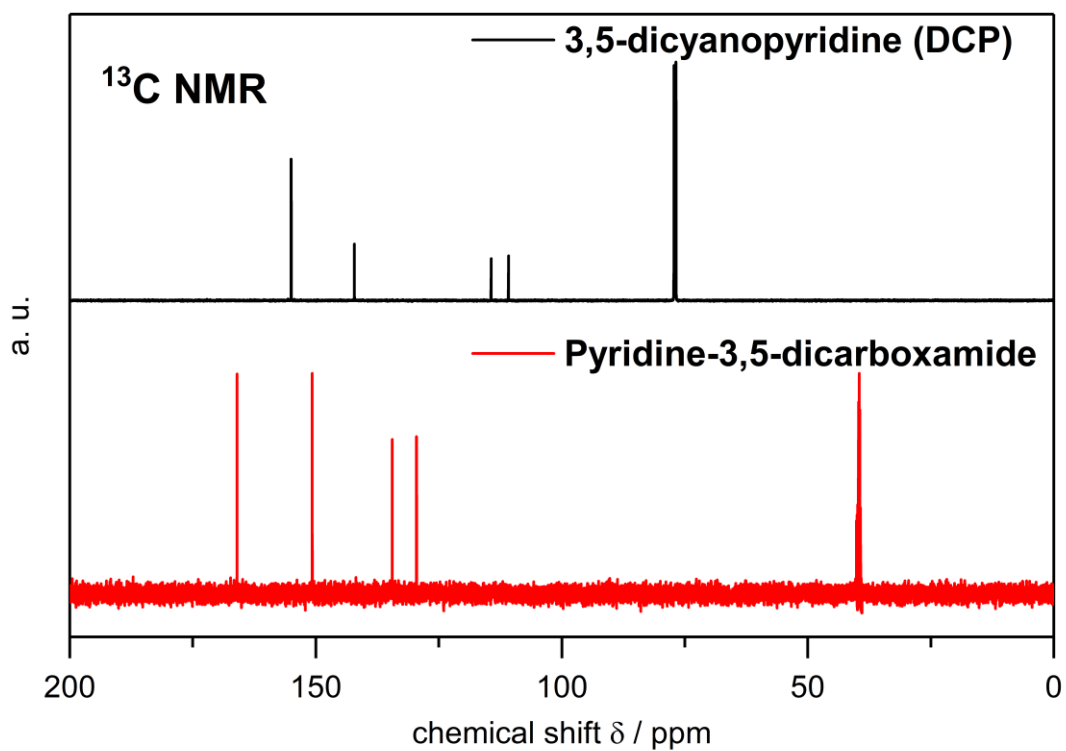


## Appendix

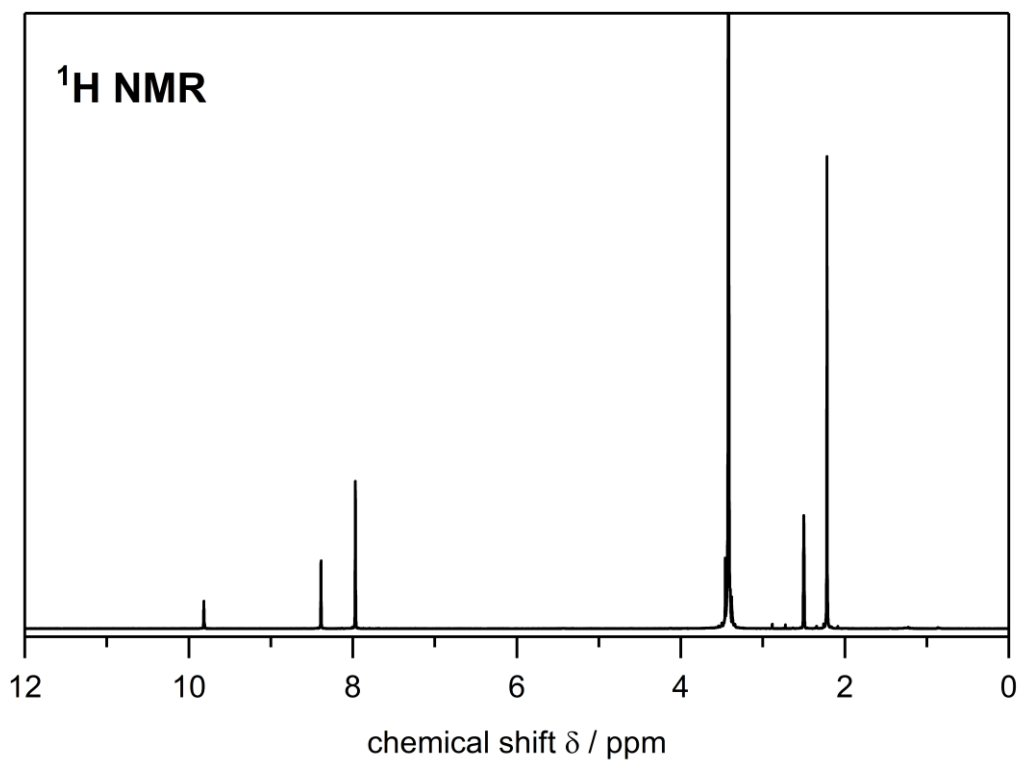
### NMR spectra of the monomers applied within the thesis at hand



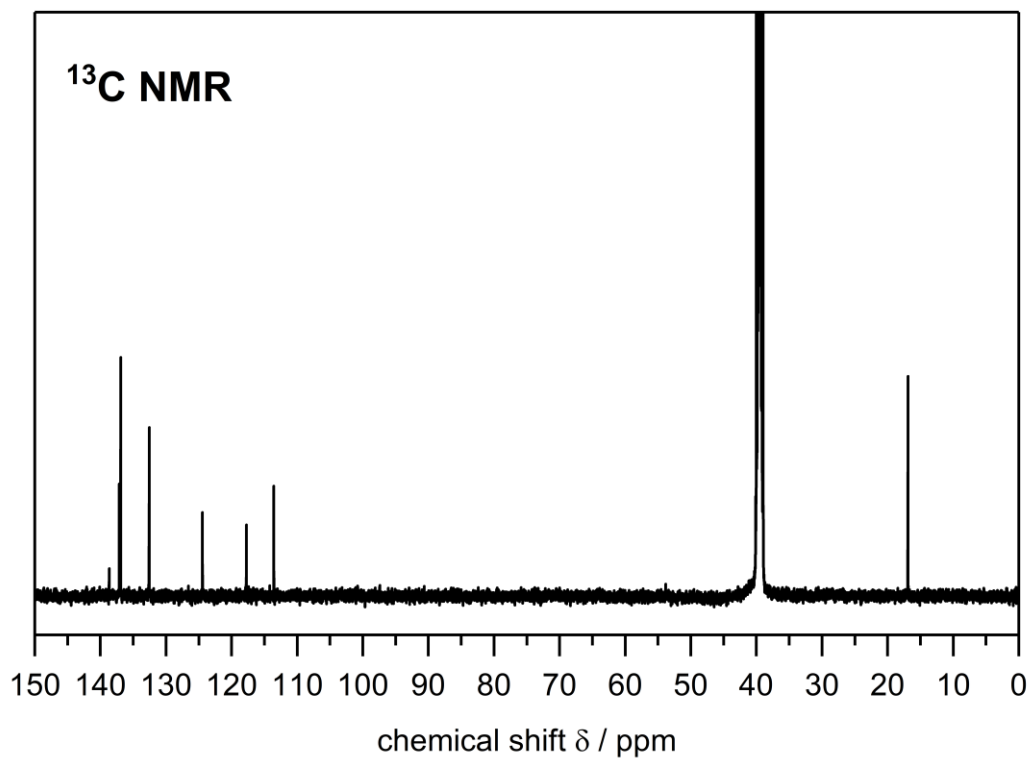
**Figure A1** <sup>1</sup>H NMR spectra of Pyridine-3,5-dicarboxamide and 3,5-dicyanopyridine. Deuterated solvents: CDCl<sub>3</sub>-d<sub>1</sub> (top), DMSO-d<sub>6</sub> (bottom).



**Figure A2**  $^{13}\text{C}$  NMR spectra of Pyridine-3,5-dicarboxamide and 3,5-dicyanopyridine. Deuterated solvents:  $\text{CDCl}_3\text{-d}_1$  (top),  $\text{DMSO-d}_6$  (bottom).

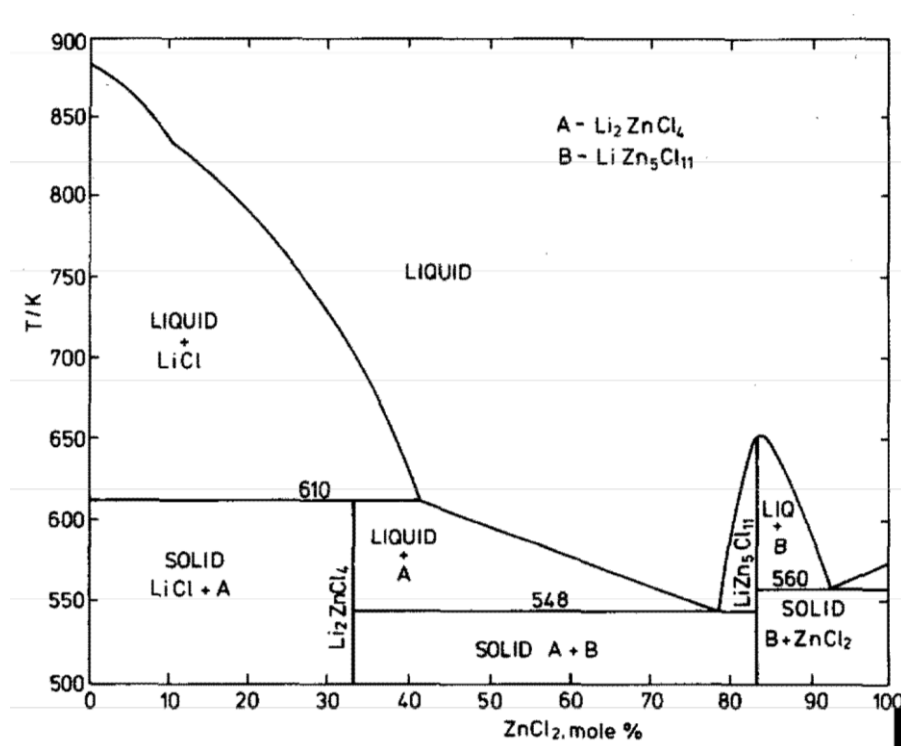
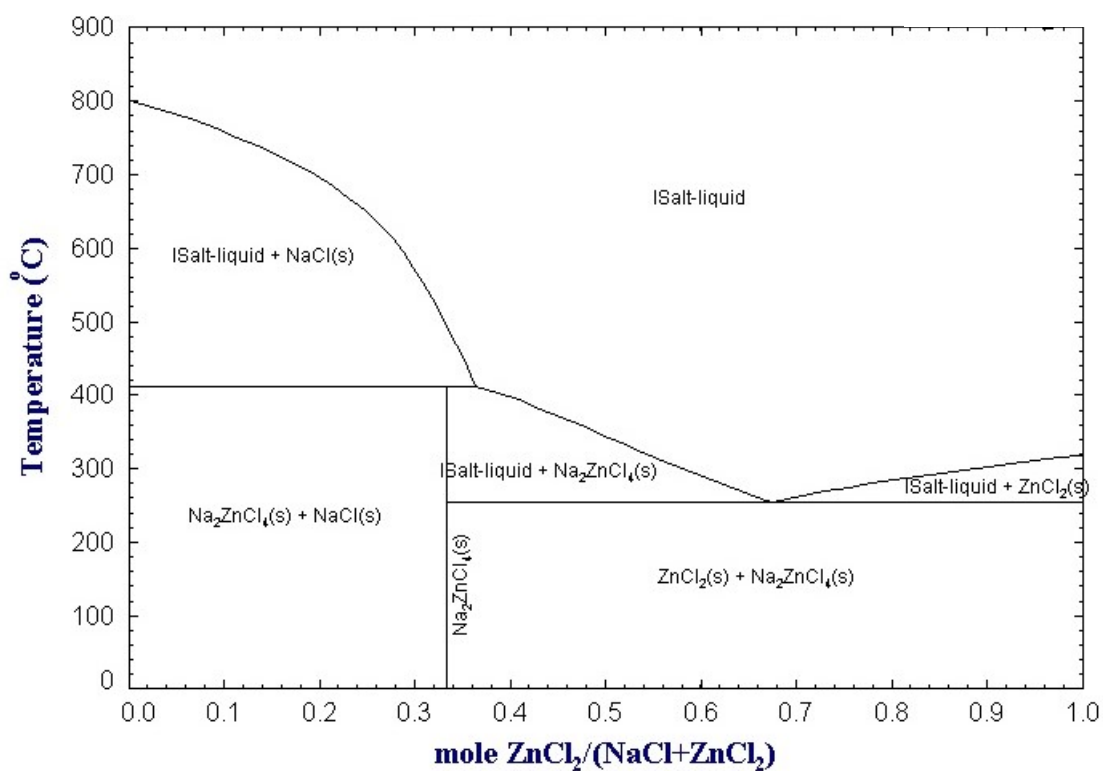


**Figure A3**  $^1\text{H}$  NMR spectrum of the imidazolium monomer. Deuterated solvent:  $\text{DMSO-d}_6$ .



**Figure A4**  $^{13}\text{C}$  NMR spectrum of the imidazolium monomer. Deuterated solvent: DMSO- $d_6$ .

## Salt Templating

Figure A5 Phase diagram of binary salt mixture LiCl/ZnCl<sub>2</sub>.<sup>170</sup>Figure A6 Phase diagram of binary salt mixture NaCl/ZnCl<sub>2</sub>.<sup>171</sup>

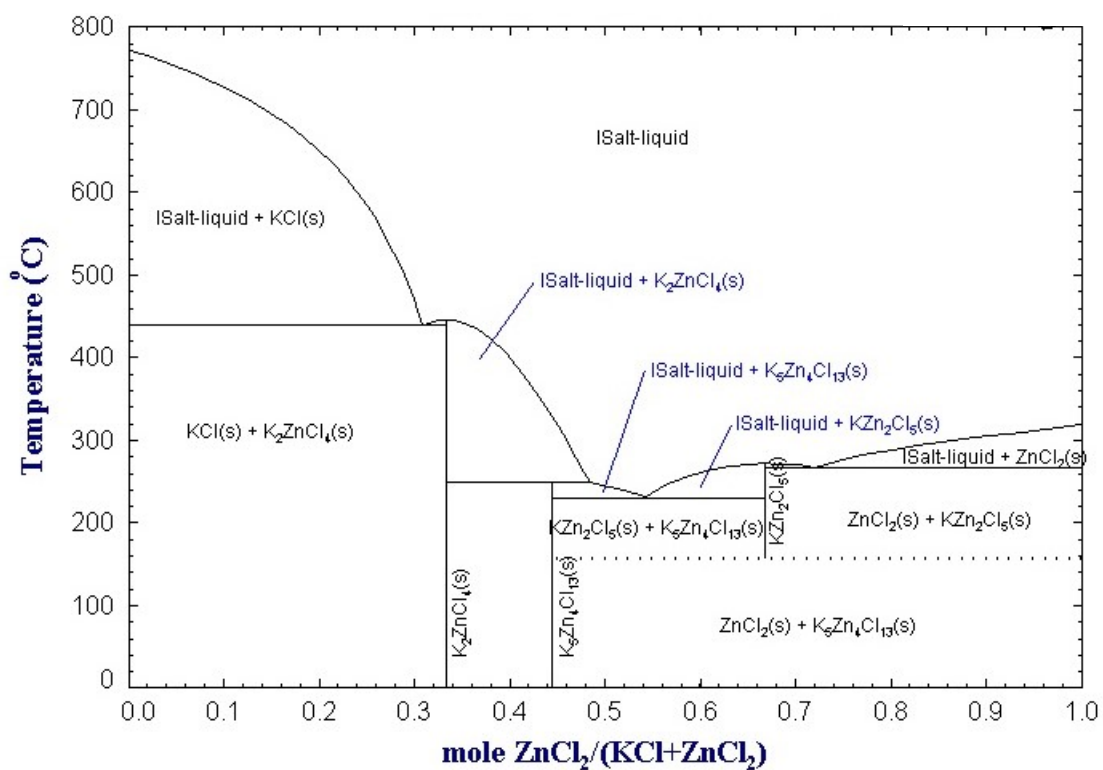


Figure A7 Phase diagram of binary salt mixture KCl/ZnCl<sub>2</sub>.<sup>171</sup>

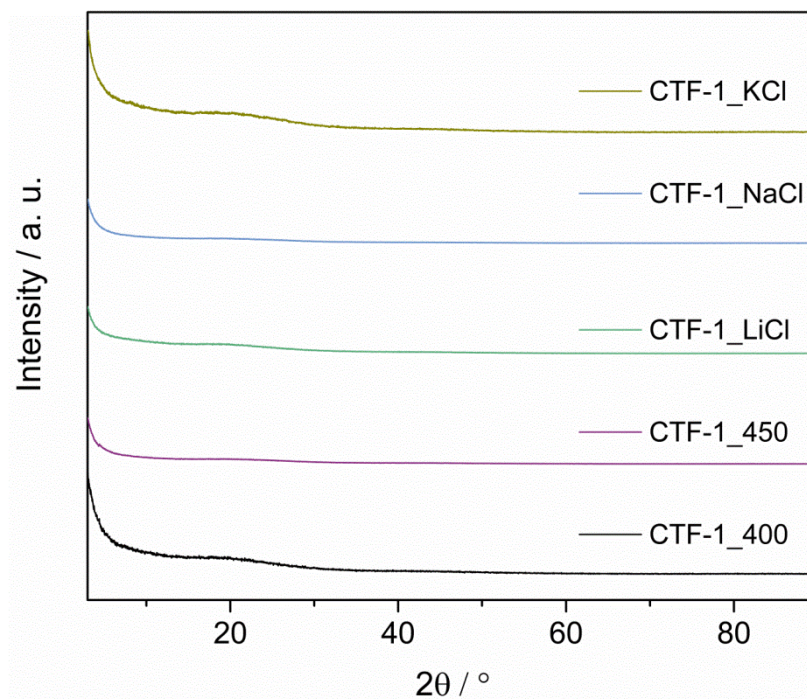
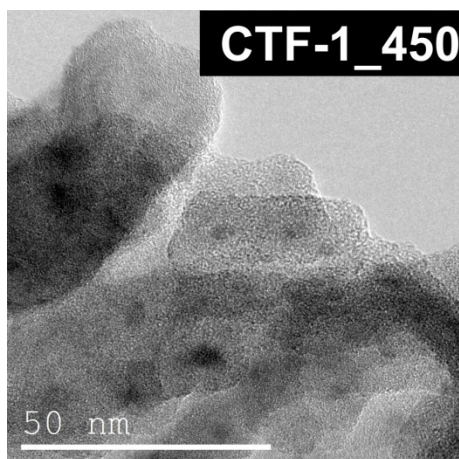
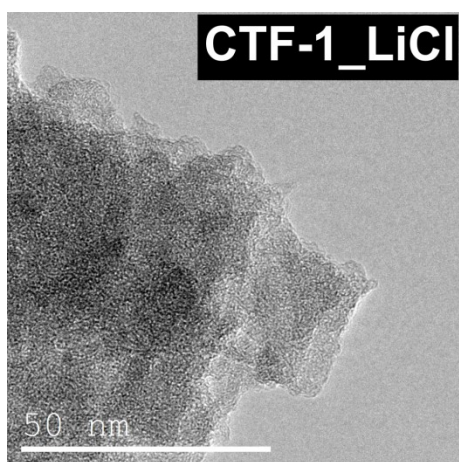


Figure A8 Powder XRD patterns of CTF-1\_KCl (yellow), CTF-1\_NaCl (blue), CTF-1\_LiCl (green), CTF-1\_450 (magenta) and CTF-1 (black).



**Figure A9** TEM image of CTF-1\_450.



**Figure A10** TEM image of CTF-1\_LiCl.

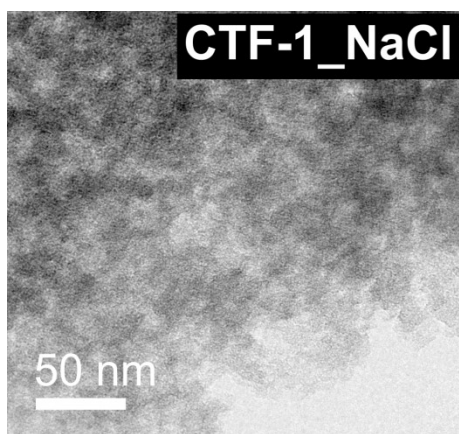


**Figure A11** TEM image of CTF 1\_NaCl.

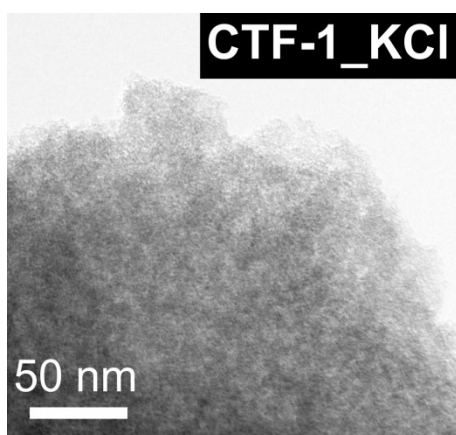
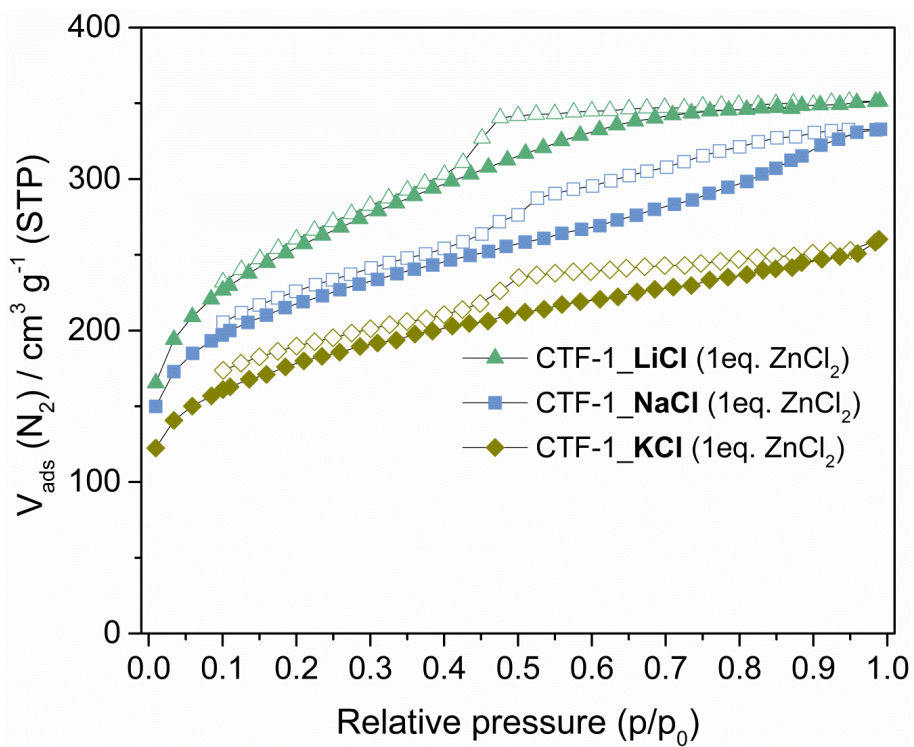


**Figure A12** TEM image of CTF 1\_KCl.

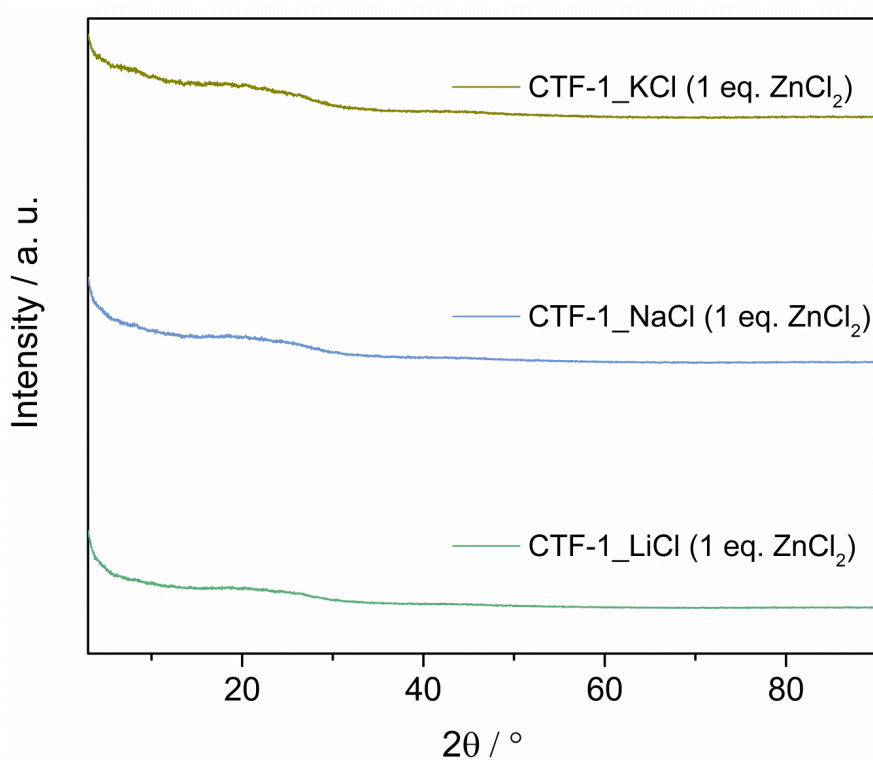
**Table A1** Elemental analysis of investigated salt templated and reference CTF materials.

Sample	Found (%)					Calculated (%)				
	C	H	N	C/H	C/N	C	H	N	C/H	C/N
CTF-1_400	67.4	2.1	13.5	2.7	5.8	75.0	3.2	21.9	2.0	4.0
CTF-1_450	69.8	2.8	12.8	2.1	6.4	75.0	3.2	21.9	2.0	4.0
CTF-1_LiCl	69.5	3.4	12.8	1.7	6.3	75.0	3.2	21.9	2.0	4.0
CTF-1_NaCl	63.2	3.6	13.1	1.5	5.6	75.0	3.2	21.9	2.0	4.0
CTF-1_KCl	58.5	3.2	12.4	1.5	5.5	75.0	3.2	21.9	2.0	4.0
CTF-1_LiCl (1 eq. ZnCl <sub>2</sub> )	64.2	4.0	15.0	1.3	5.0	75.0	3.2	21.9	2.0	4.0
CTF-1_NaCl (1 eq. ZnCl <sub>2</sub> )	64.7	4.0	15.5	1.5	4.9	75.0	3.2	21.9	2.0	4.0
CTF-1_KCl (1 eq. ZnCl <sub>2</sub> )	66.6	4.0	16.3	1.4	4.8	75.0	3.2	21.9	2.0	4.0



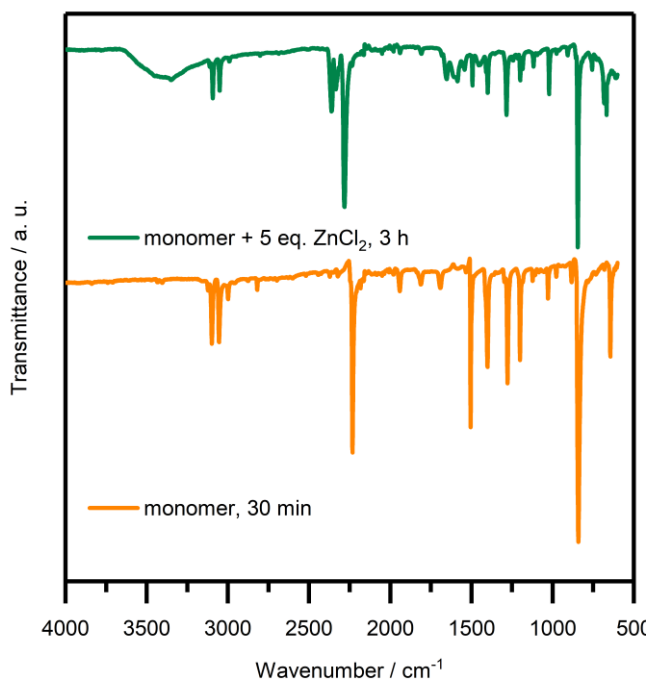


**Figure A13** Nitrogen physisorption isotherms (at 77 K) of CTF-1\_LiCl (1eq.  $\text{ZnCl}_2$ ), CTF-1\_NaCl (1eq.  $\text{ZnCl}_2$ ) and CTF-1\_KCl (1eq.  $\text{ZnCl}_2$ ).



**Figure A14** Powder XRD patterns of CTF-1\_KCl (1eq.  $\text{ZnCl}_2$ ) (yellow), CTF-1\_NaCl (1eq.  $\text{ZnCl}_2$ ) (blue), CTF-1\_LiCl (1eq.  $\text{ZnCl}_2$ ) (green).



Mechanochemical synthesised CTF

**Figure A15** FT-IR spectra of 1,4-dicyanobenzene (milled for 30 min) and the same compound milled with 5 eq.  $\text{ZnCl}_2$  for 3 h.

**Table A2** Elemental analysis of all mechanochemically synthesised CTF materials.

Sample	Found (%)					Calculated (%)				
	C	H	N	C/H	C/N	C	H	N	C/H	C/N
CTF-CBZ	70.98	3.51	17.11	1.69	4.84	77.41	3.25	19.34	1.98	4.67
CTF-CBZ_15min	69.87	3.37	17.52	1.73	4.65	77.41	3.25	19.34	1.98	4.67
CTF-CBZ_30min	70.23	3.40	17.32	1.72	4.73	77.41	3.25	19.34	1.98	4.67
CTF-CBZ_45min	70.23	3.46	17.21	1.69	4.76	77.41	3.25	19.34	1.98	4.67
CTF-CBZ_ ZrO <sub>2</sub> _1h	68.93	3.24	17.67	1.78	4.55	77.41	3.25	19.34	1.98	4.67
CTF-CBZ_ ZrO <sub>2</sub> _3h	69.53	3.19	17.82	1.82	4.55	77.41	3.25	19.34	1.98	4.67
CTF-CBZ_KCl	70.63	3.66	16.85	1.61	4.89	77.41	3.25	19.34	1.98	4.67
CTF-CBZ_NaCl	69.84	3.48	16.76	1.67	4.86	77.41	3.25	19.34	1.98	4.67
CTF-CBZ_LiCl	71.27	3.43	17.39	1.73	4.78	77.41	3.25	19.34	1.98	4.67
CTF-CBZ_AlCl <sub>3</sub>	68.61	3.32	17.13	1.72	4.67	77.41	3.25	19.34	1.98	4.67
CTF-AC	71.05	3.66	9.71	1.62	8.54	84.19	3.53	12.27	1.99	8.01
CTF-TPB	74.93	3.84	7.56	1.62	11.56	85.26	4.09	10.65	1.74	9.34
CTF-BZ	35.81	1.63	6.45	1.84	6.48	74.99	3.15	21.86	1.98	4.00
CTF-NT	24.28	1.11	2.83	1.82	10.01	80.88	3.39	15.72	1.99	6.00
CTF-TPM	49.76	2.89	7.65	1.44	7.59	82.84	3.84	13.32	1.80	7.26

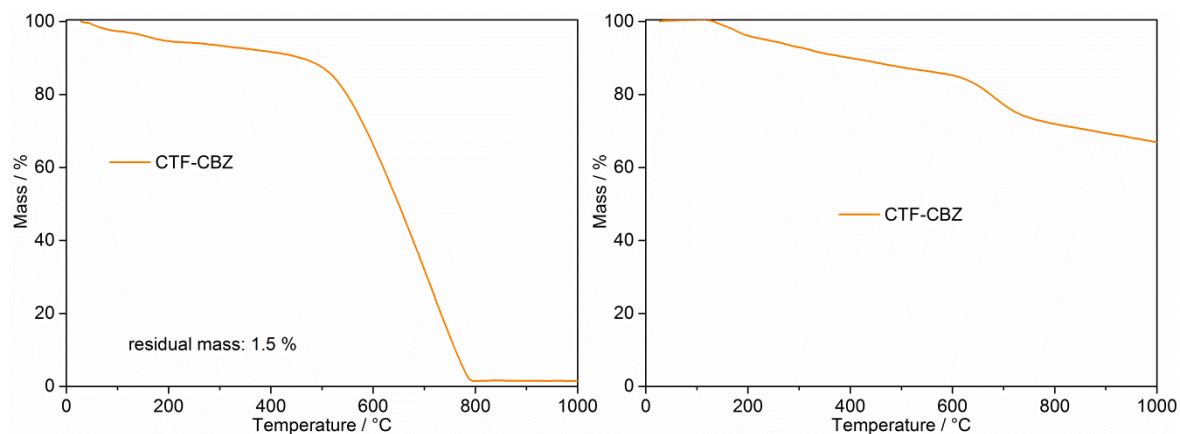


Figure A16 TGA of CTF-CBZ in air (left) and argon (right).

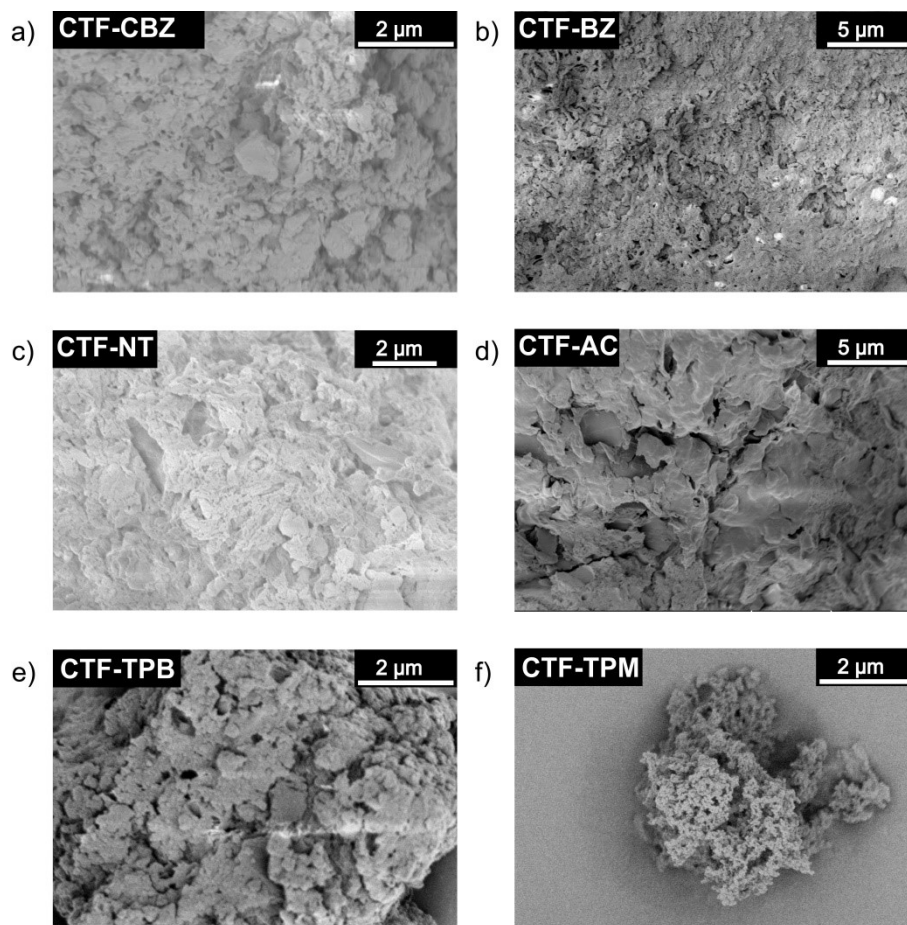
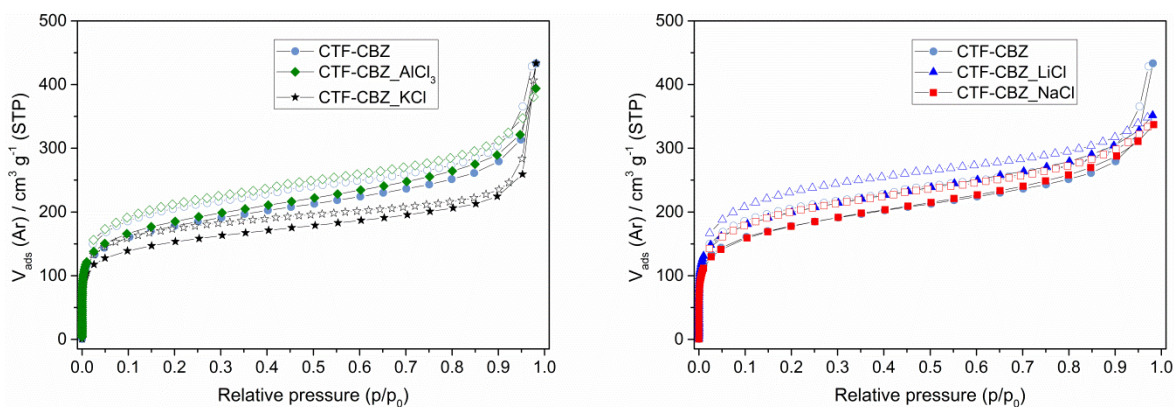
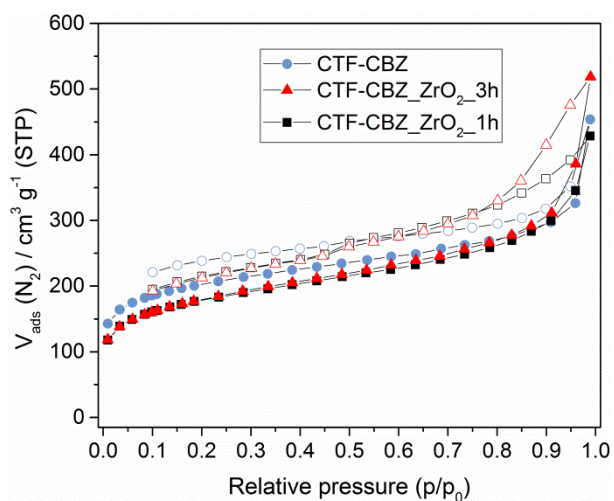


Figure A17 a) SEM picture of CTF-CBZ b) SEM picture of CTF-BZ c) SEM picture of CTF-NT d) SEM picture of CTF-AC e) SEM picture of CTF-TPB f) SEM picture of CTF-TPM.



**Figure A18** left) Argon physisorption isotherm (at 87 K) of CTF-CBZ (circles), CTF-CBZ\_ $\text{AlCl}_3$  (diamonds), and CTF-CBZ\_ $\text{KCl}$  (stars) right) Argon physisorption isotherm (at 87 K) of CTF-CBZ (circles), CTF-CBZ\_ $\text{LiCl}$  (triangles), and CTF-CBZ\_ $\text{NaCl}$  (cubes).



**Figure A19** Nitrogen physisorption isotherm (at 77 K) of CTF-CBZ (circles), CTF-CBZ\_ $\text{ZrO}_2$ \_3h (triangles) and CTF-CBZ\_ $\text{ZrO}_2$ \_1h (cubes).

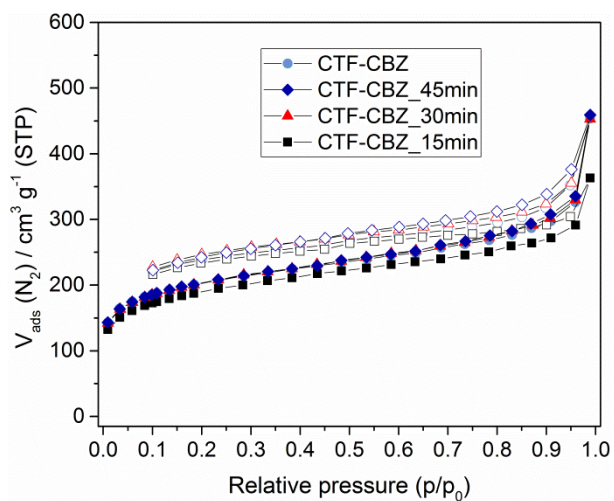


**Figure A20** Nitrogen physisorption isotherm (at 77 K) of CTF-CBZ (circles), CTF-CBZ\_45min (diamonds), CTF-CBZ\_30min (triangles) and CTF-CBZ\_15min (cubes).

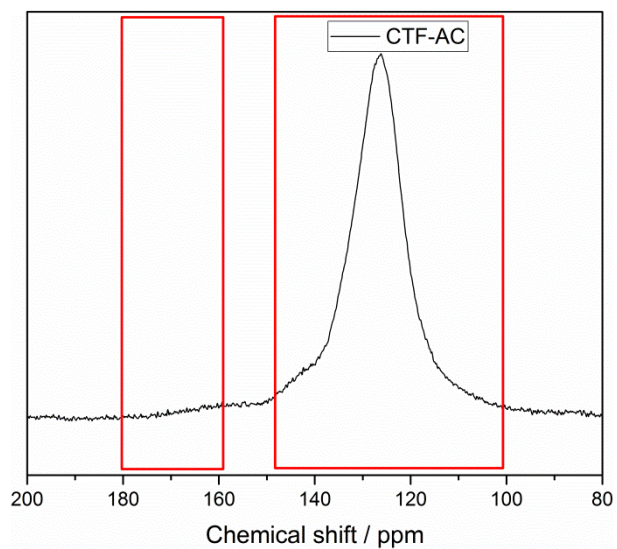


**Figure A21**  $^{13}\text{C}$  CP/MAS NMR spectrum of CTF-AC.

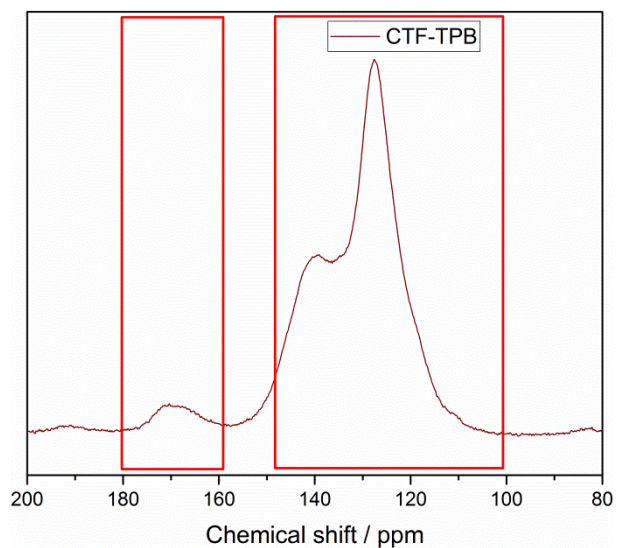


**Figure A22**  $^{13}\text{C}$  CP/MAS NMR spectrum of CTF-TPB.

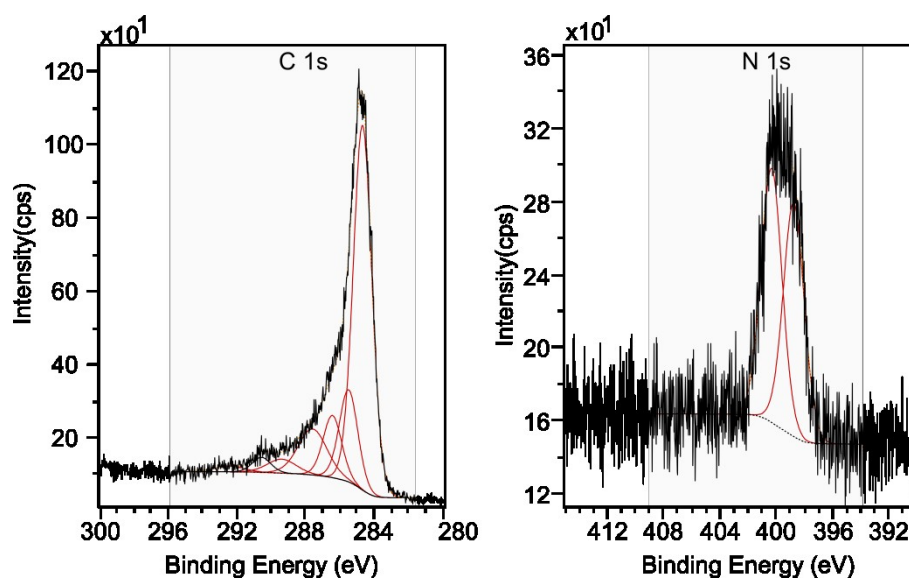


**Figure A23** High resolution XPS C 1s and N 1s spectra of CTF-AC.



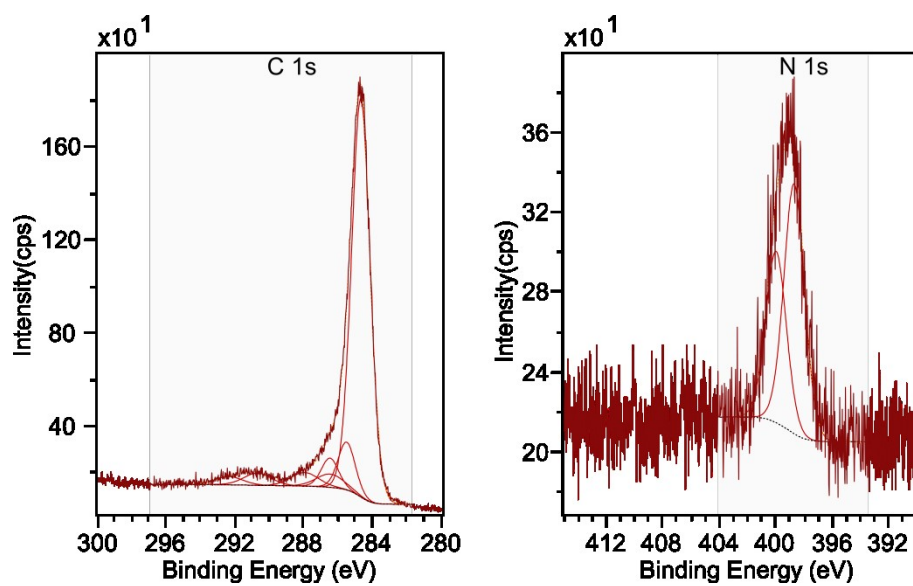


**Figure A24** High resolution XPS C 1s and N 1s spectra of CTF-TPB.

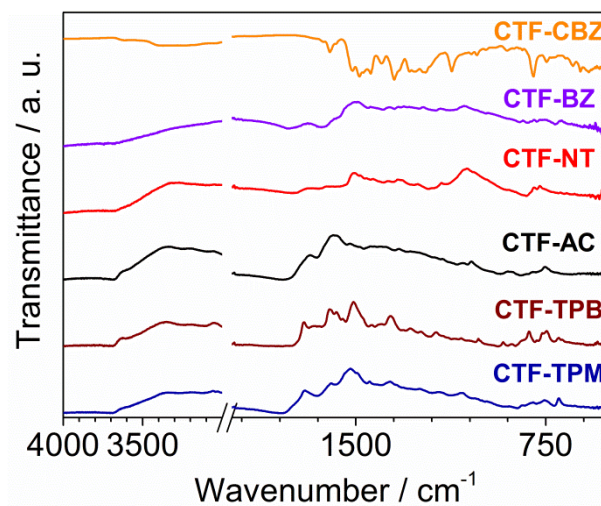


**Figure A25** FT-IR spectra of CTF-CBZ, CTF-BZ, CTF-NT, CTF-AC, CTF-TPB and CTF-TPM.

Pyridine-derived CTFs**Table A3** Position, FWHM, peak area and percental peak area derived from C 1s and N 1s deconvolution.

Sample	C 1s				N 1s			
	Posit. / ev	FWHM / ev	Area	Area / %	Posit. / ev	FWHM / ev	Area	Area / %
<b>DCP-CTF-400</b>	284.20	1.80	2498.36	70.73				
	286.30	1.80	685.17	19.39				
	288.20	1.80	84.09	2.38	398.00	1.64	1485.20	80.96
	285.50	1.80	265.20	7.51	399.53	1.64	349.34	19.04
	284.70	1.80	0.00	0.00				
<b>DCP-CTF-500</b>	284.20	1.62	921.85	28.31				
	286.30	1.62	530.03	16.27	398.00	1.45	883.98	54.59
	287.83	1.62	238.30	7.31	399.47	1.45	459.80	28.38
	285.50	1.62	543.28	16.68	400.48	1.45	275.99	17.03
	284.40	1.62	1023.91	31.44				
<b>DCP-CTF-600</b>	284.20	1.32	507.71	18.54				
	286.30	1.32	420.04	15.33	398.00	1.42	566.70	47.54
	287.72	1.32	199.24	7.27	399.54	1.42	317.67	26.64
	285.50	1.32	508.82	18.58	400.69	1.42	252.49	21.17
	285.03	1.33	1102.83	40.27	402.33	1.42	55.61	4.66
<b>DCP-CTF-700</b>					397.86	1.56	455.51	36.44
	284.20	1.23	1581.54	37.96	399.50	1.56	289.69	23.17
	286.30	1.23	430.02	10.31	400.71	1.56	280.51	22.43
	287.49	1.23	233.49	5.60	402.10	1.56	97.83	7.82
	285.50	1.23	746.11	17.90	403.42	1.56	71.50	5.71
	285.14	1.22	1176.69	28.23	405.02	1.56	55.49	4.43

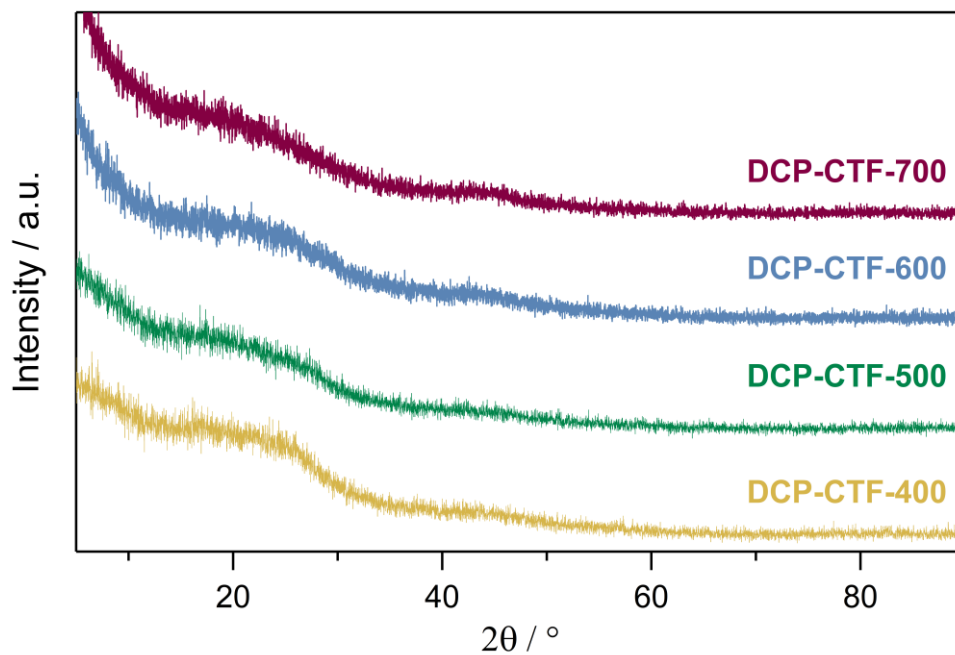


**Figure A26** PXRD data of DCP-CTF-400, DCP-CTF-500, DCP-CTF-600 and DCP-CTF-700.

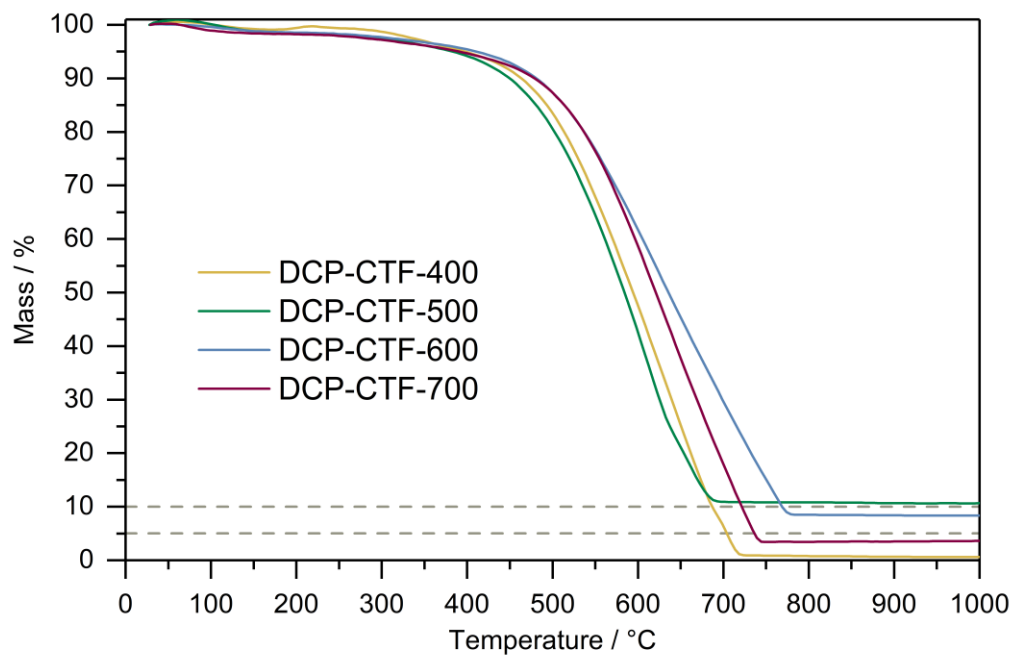


**Figure A27** TGA data (air) of DCP-CTF-400, DCP-CTF-500, DCP-CTF-600 and DCP-CTF-700.



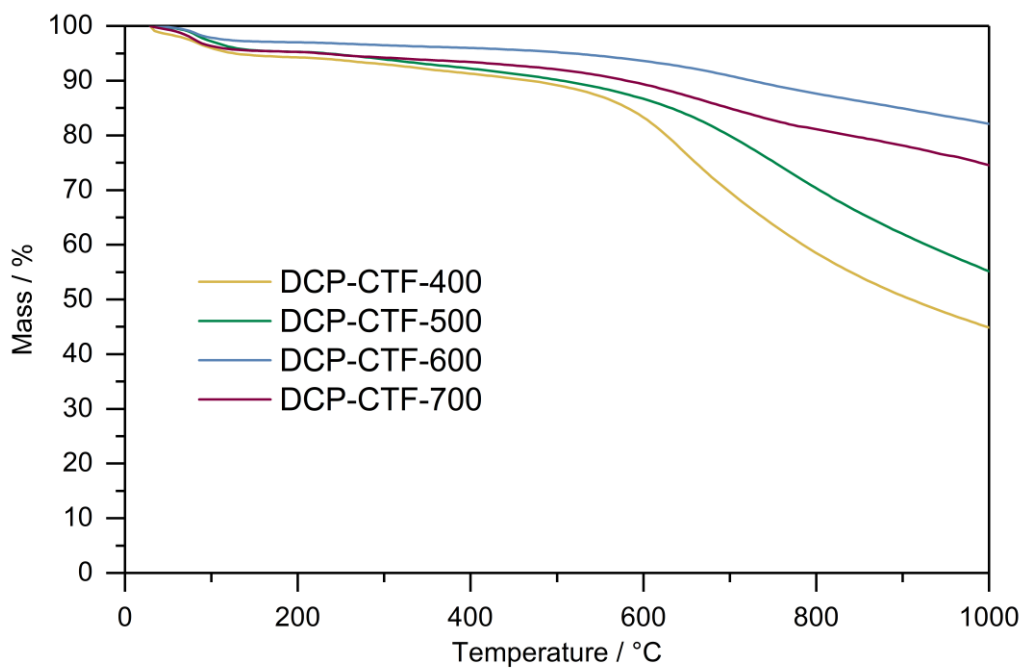


Figure A28 TGA data (argon) of DCP-CTF-400, DCP-CTF-500, DCP-CTF-600 and DCP-CTF-700.

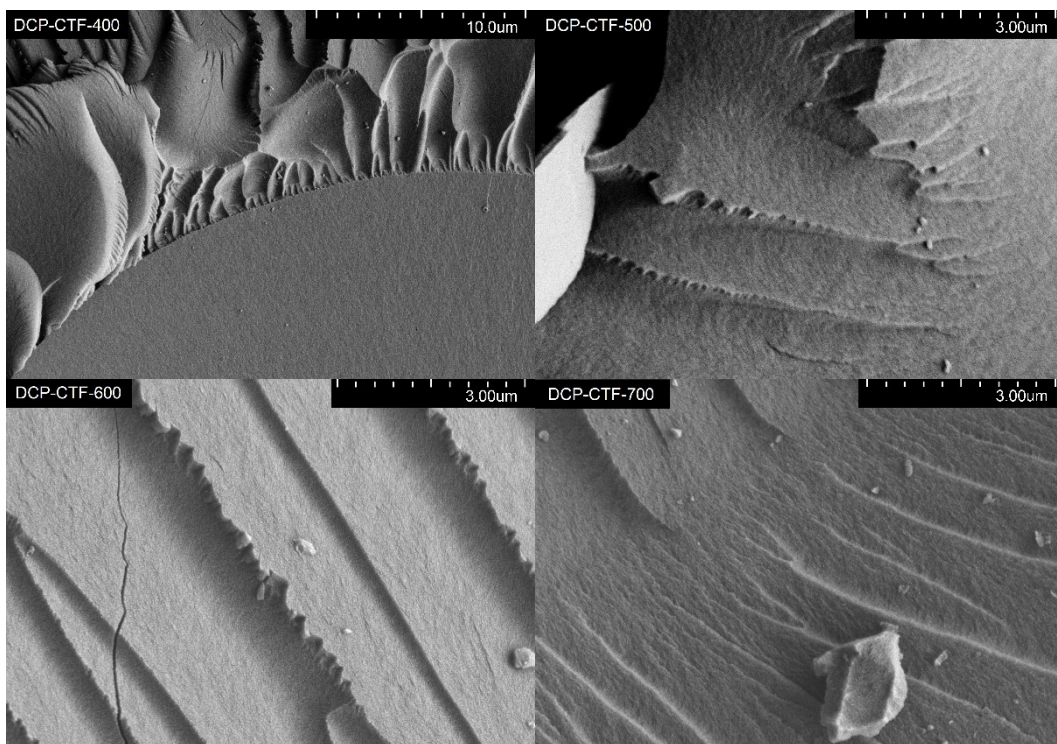
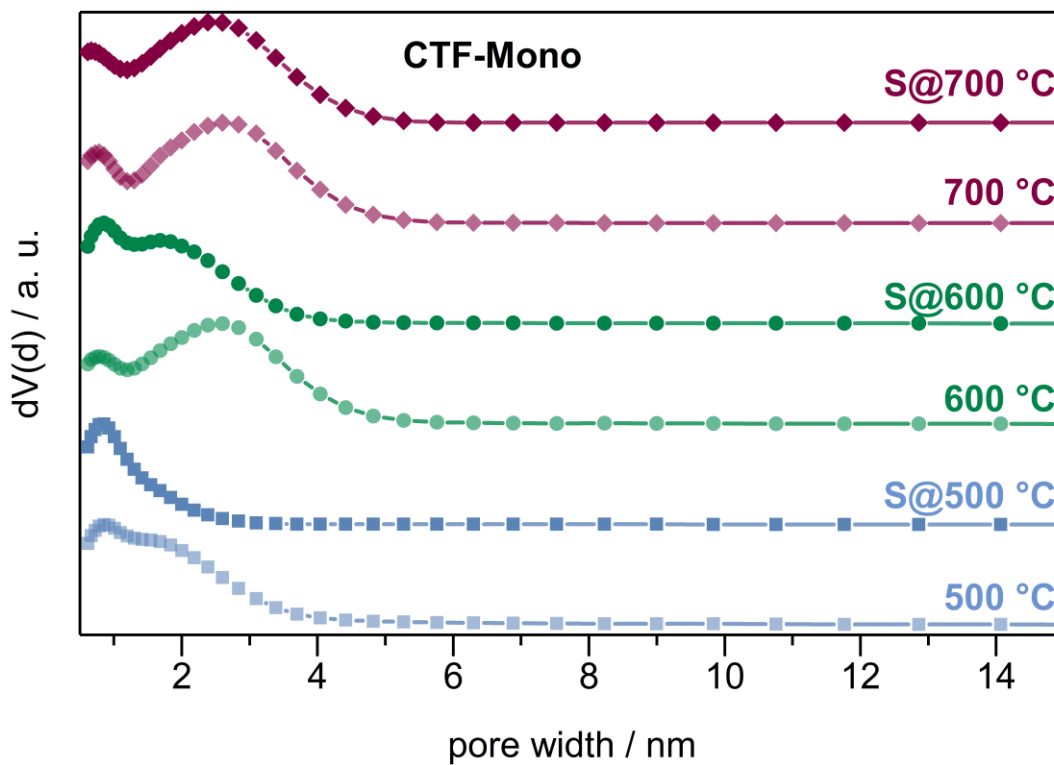
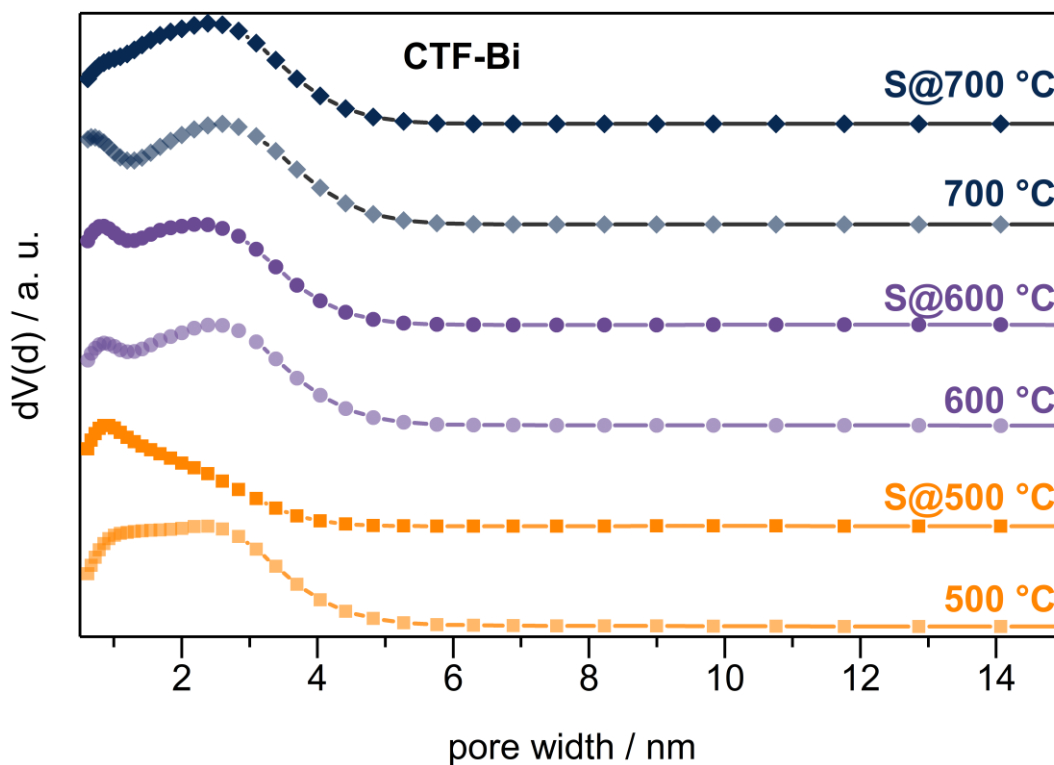


Figure A29 SEM images of DCP-CTF-400, DCP-CTF-500, DCP-CTF-600 and DCP-CTF-700.

Synthesis of sulfur bearing covalent triazine frameworks

**Figure A30** Pore size distribution of all CTF-Mono and S@CTF-Mono samples derived from Nitrogen physisorption (77 K).



**Figure A31** Pore size distribution of all CTF-Bi and S@CTF-Bi samples derived from Nitrogen physisorption (77 K).

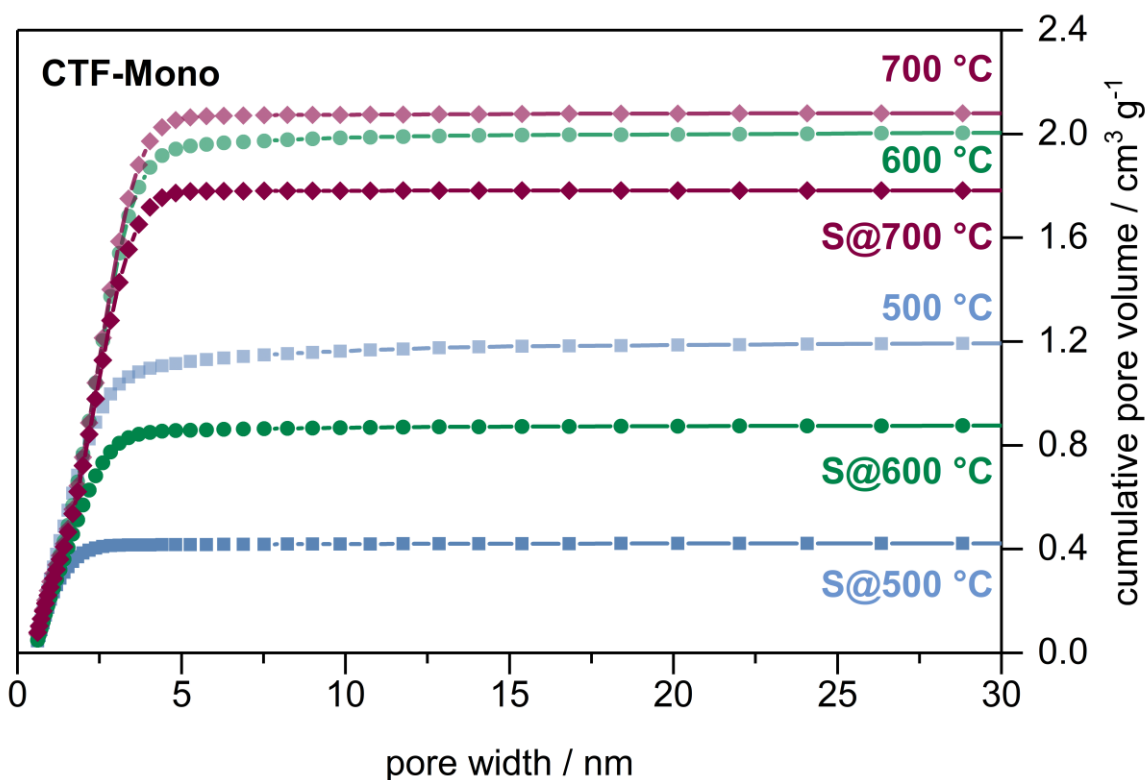


Figure A32 Cumulative total pore volumes of all CTF-Mono and S@CTF-Mono samples derived from nitrogen physisorption (77 K).

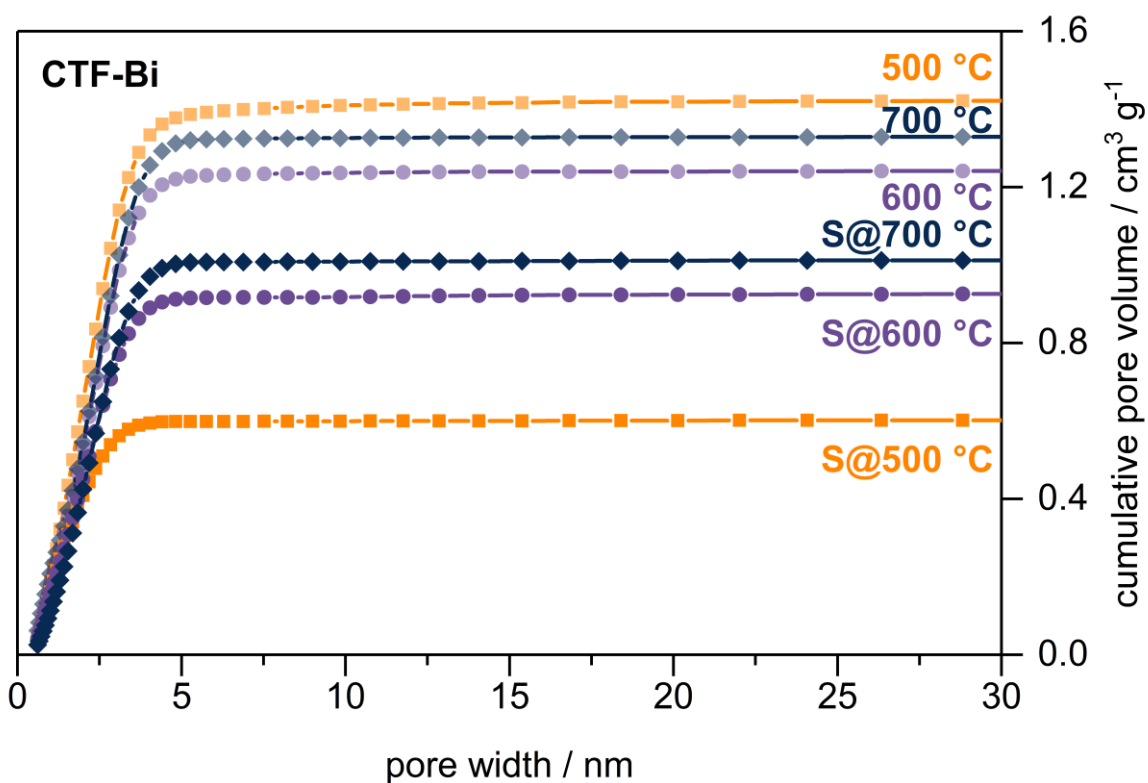


Figure A33 Cumulative total pore volumes of all CTF-Bi and S@CTF-Bi samples derived from nitrogen physisorption (77 K).

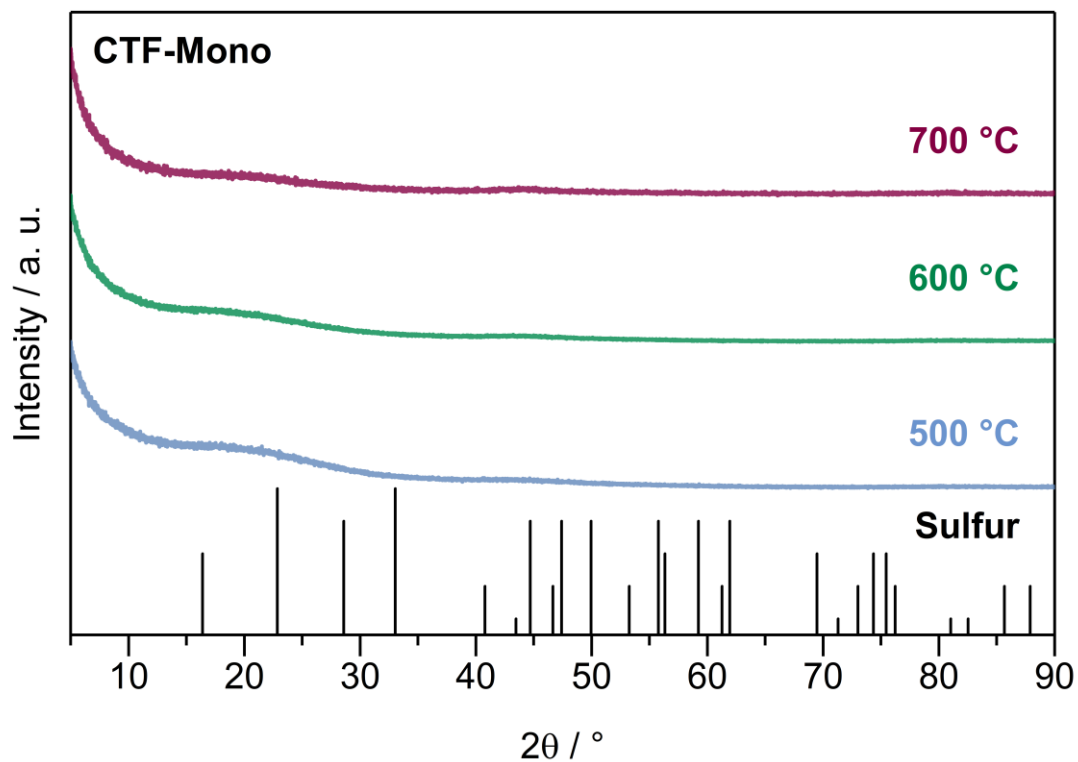


Figure A34 PXRD data of CTF-Mono samples.

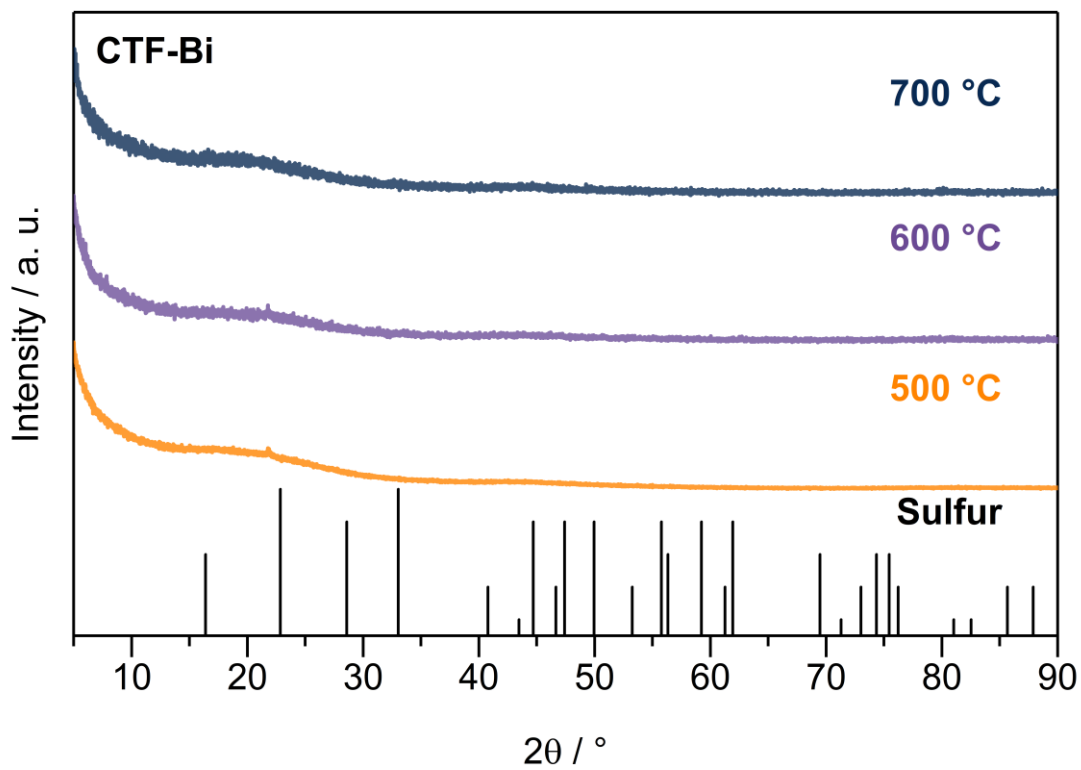
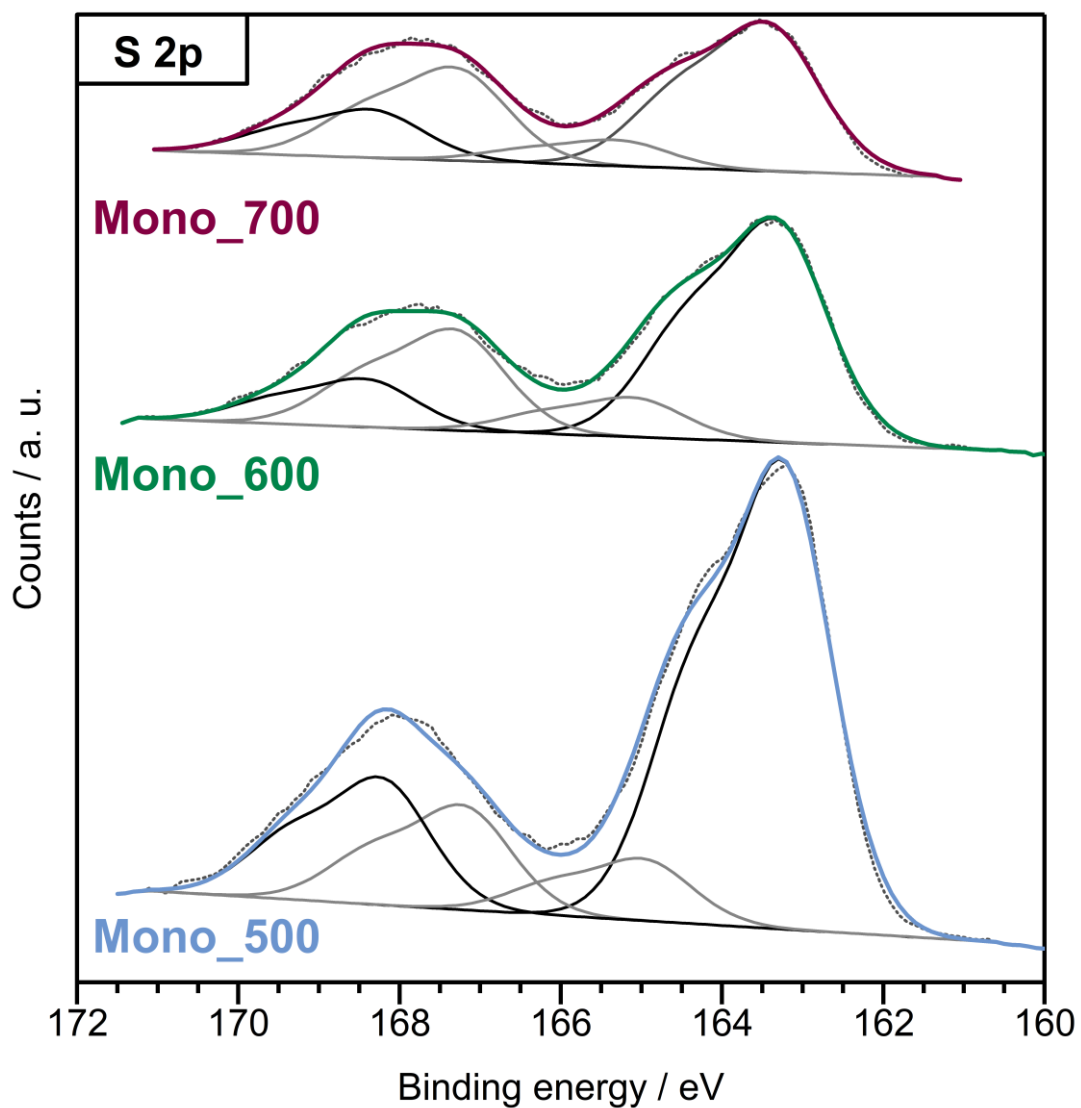
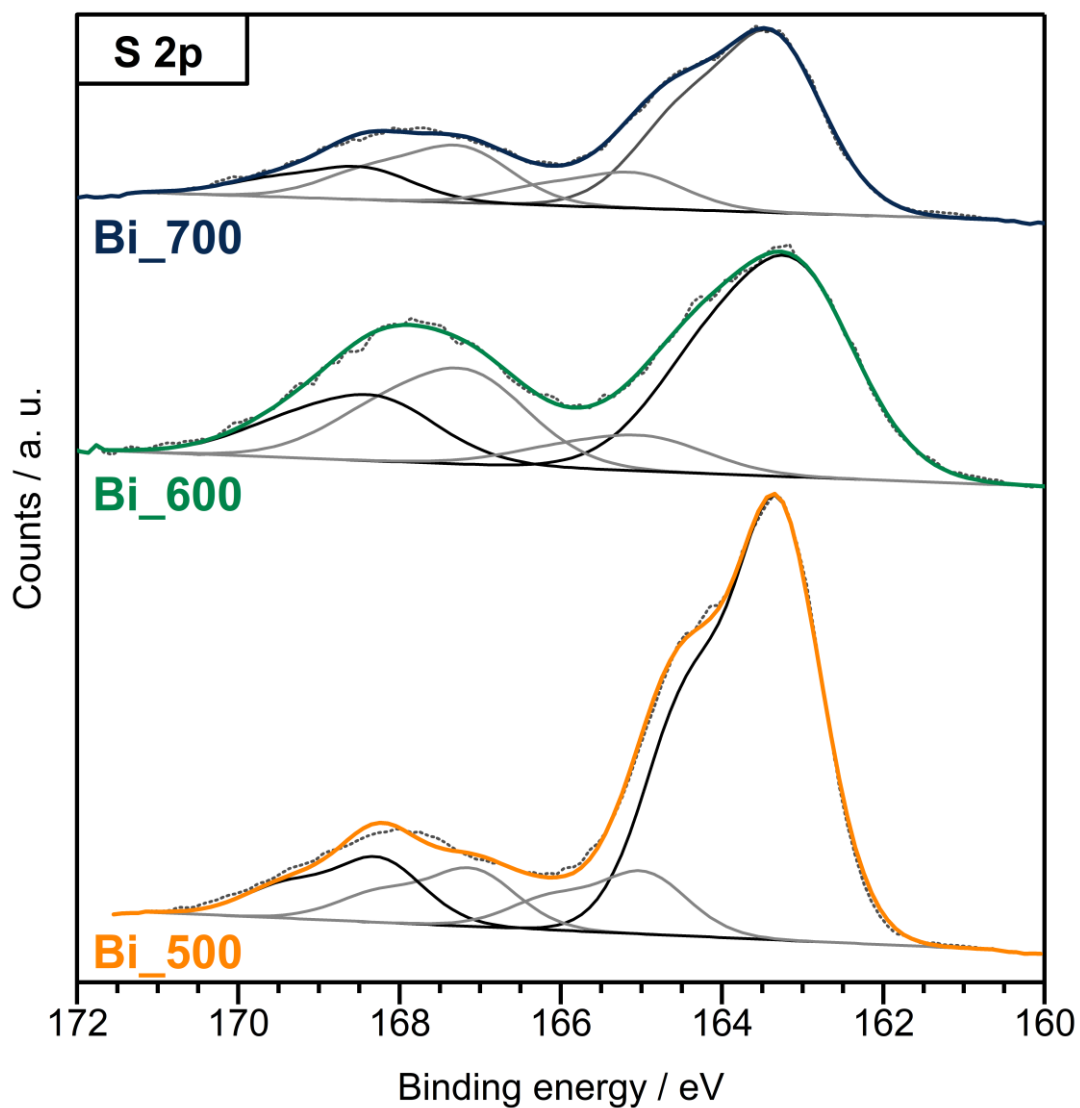


Figure A35 PXRD data of CTF-Bi samples.



**Figure A36** High resolution S 2p XPS spectra of S@CTF-Mono\_500, S@CTF-Mono\_600 and S@CTF-Mono\_700. Corresponding S 2p<sub>3/2</sub> and S 2p<sub>1/2</sub> peaks were added and the background was subtracted to give a resulting S 2p peak.



**Figure A37** High resolution S 2p XPS spectra of S@CTF-Bi\_500, S@CTF-Bi\_600 and S@CTF-Bi\_700. Corresponding S 2p<sub>3/2</sub> and S 2p<sub>1/2</sub> peaks were added and the background was subtracted to give a resulting S 2p peak.

**Table A4** Position, FWHM, peak area and percental peak area derived from C 1s and N 1s deconvolution.

Sample	C 1s				N 1s			
	Posit. / ev	FWHM / ev	Area	Area / %	Posit. / ev	FWHM / ev	Area	Area / %
<b>CTF- Mono_500</b>	284.65	1.46	9757.84	67.66	398.26	1.45	1378.89	43.69
	285.93	1.46	2879.61	19.96	400.86	1.45	825.62	26.14
	287.33	1.46	1153.27	7.99	402.31	1.45	168.29	5.33
	288.90	1.46	634.77	4.40	399.85	1.45	784.12	24.84
<b>S@CTF- Mono_500</b>	284.42	1.40	5874.50	68.74	398.02	1.36	670.48	35.26
	285.65	1.40	1728.60	20.22	400.71	1.36	542.18	28.49
	286.94	1.40	673.73	7.88	402.12	1.36	129.47	6.80
	288.29	1.40	270.60	3.16	399.61	1.36	560.30	29.45
<b>CTF- Mono_600</b>	284.67	1.36	5441.64	65.77	398.25	1.43	533.68	38.27
	286.83	1.36	763.55	9.22	400.94	1.43	426.78	30.58
	285.77	1.36	1731.70	20.92	402.31	1.43	95.26	6.82
	288.07	1.36	338.41	4.09	399.82	1.43	339.46	24.33
<b>S@CTF- Mono_600</b>	284.40	1.39	6344.96	67.33	397.98	1.35	522.18	33.22
	285.60	1.39	1982.64	21.03	400.65	1.35	496.11	31.54
	286.83	1.39	782.69	8.30	401.94	1.35	150.00	9.53
	288.24	1.39	315.04	3.34	399.47	1.35	404.05	25.70
<b>CTF- Mono_700</b>	284.65	1.28	4494.41	72.14	398.14	1.39	276.05	36.15
	286.71	1.28	496.17	7.96	400.95	1.39	240.63	31.49
	285.74	1.28	1239.37	19.89	402.14	1.39	74.58	9.76
	279.86	1.28	0.00	0.02	399.67	1.39	172.77	22.61
<b>S@CTF- Mono_700</b>	284.48	1.26	7178.13	66.89	398.02	1.40	337.73	31.19
	285.71	1.26	2245.05	20.91	400.86	1.40	368.66	34.02
	286.99	1.26	856.15	7.97	402.10	1.40	118.83	10.96
	288.65	1.26	454.15	4.23	399.55	1.40	258.06	23.82
<b>CTF-Bi_500</b>	284.55	1.39	7579.61	74.47	398.27	1.54	316.68	45.30
	286.02	1.39	1411.73	13.86	400.75	1.54	250.27	35.78
	287.53	1.39	702.16	6.89	402.48	1.54	45.19	6.46
	289.28	1.39	486.18	4.77	399.86	1.54	87.21	12.47

Sample	C 1s				N 1s			
	Posit. / ev	FWHM / ev	Area	Area / %	Posit. / ev	FWHM / ev	Area	Area / %
<b>S@ CTF-Bi_500</b>	284.34	1.35	7278.36	74.59	398.01	1.38	243.99	32.30
	285.62	1.35	1538.62	15.76	400.66	1.38	238.10	31.50
	286.97	1.35	636.84	6.52	401.93	1.38	83.10	10.99
	288.52	1.35	305.35	3.13	399.64	1.38	190.50	25.21
<b>CTF-Bi_600</b>	284.58	1.37	6986.79	71.83	398.15	1.39	260.86	37.11
	286.05	1.37	1598.47	16.43	400.80	1.39	229.95	32.69
	287.67	1.37	740.73	7.61	402.08	1.39	68.90	9.79
	289.42	1.37	403.09	4.14	399.61	1.39	143.59	20.42
<b>S@ CTF-Bi_600</b>	284.08	1.67	8817.94	71.45	403.49	1.95	79.02	6.93
	285.46	1.67	2121.16	17.18	397.90	1.95	320.25	28.11
	287.02	1.67	885.57	7.17	401.20	1.95	329.96	28.93
	288.83	1.67	519.35	4.20	399.93	1.95	410.77	36.03
<b>CTF-Bi_700</b>	284.65	1.31	8299.56	69.52	398.18	1.45	225.42	34.55
	285.99	1.31	2115.00	17.71	400.84	1.45	212.72	32.58
	287.36	1.31	969.77	8.12	402.04	1.45	93.42	14.30
	289.16	1.31	556.39	4.65	399.50	1.45	121.18	18.57
<b>S@ CTF-Bi_700</b>	284.35	1.28	9442.30	70.96	398.00	1.42	239.76	32.51
	285.59	1.28	2317.25	17.41	400.91	1.42	241.31	32.70
	286.83	1.28	1020.29	7.66	402.11	1.42	75.56	10.24
	288.33	1.28	529.42	3.97	399.65	1.42	181.09	24.55



**Table A5** Position, FWHM, peak area and percental peak area derived from S 2p deconvolution.

Sample	S 2p			
	Posit. / ev	FWHM / ev	Area	Area / %
<b>S@CTF- Mono_500</b>	163.20	1.36	1262.50	40.98
	164.38	1.36	631.25	20.48
	167.17	1.36	282.04	9.14
	168.35	1.36	141.02	4.57
	168.19	1.36	343.52	11.13
	169.37	1.36	171.76	5.57
	164.94	1.36	167.10	5.42
	166.12	1.36	83.55	2.71
<b>S@CTF- Mono_600</b>	163.28	1.42	617.86	36.14
	164.46	1.42	308.93	18.06
	167.27	1.42	280.04	16.36
	168.45	1.42	140.02	8.18
	168.37	1.42	133.55	7.80
	169.55	1.42	66.77	3.90
	165.05	1.42	109.12	6.38
	166.23	1.42	54.56	3.19
<b>S@CTF- Mono_700</b>	163.38	1.45	416.77	31.34
	164.56	1.45	208.38	15.66
	167.26	1.45	261.78	19.66
	168.44	1.45	130.89	9.83
	168.29	1.45	135.61	10.18
	169.47	1.45	67.81	5.09
	165.24	1.45	73.02	5.49
	166.42	1.45	36.51	2.74
<b>S@CTF- Bi_500</b>	163.29	1.27	1732.08	46.92
	164.47	1.27	866.04	23.45
	167.09	1.27	228.30	6.18
	168.27	1.27	114.15	3.09
	168.25	1.27	255.62	6.92
	169.43	1.27	127.81	3.46
	164.96	1.27	245.96	6.66
	166.14	1.27	122.98	3.33

Sample	S 2p			
	Posit. / eV	FWHM / eV	Area	Area / %
<b>S@CTF- Bi_600</b>	163.05	1.75	1070.93	35.21
	164.23	1.75	535.46	17.60
	167.09	1.75	464.91	15.27
	168.27	1.75	232.46	7.63
	168.22	1.75	319.90	10.50
	169.40	1.75	159.95	5.25
	164.87	1.75	173.06	5.69
	166.05	1.75	86.53	2.84
<b>S@CTF- Bi_700</b>	163.35	1.46	784.21	39.45
	164.53	1.46	392.11	19.72
	167.22	1.46	246.41	12.38
	168.40	1.46	123.20	6.19
	168.43	1.46	141.66	7.12
	169.61	1.46	70.83	3.56
	165.06	1.46	153.72	7.73
	166.24	1.46	76.86	3.86

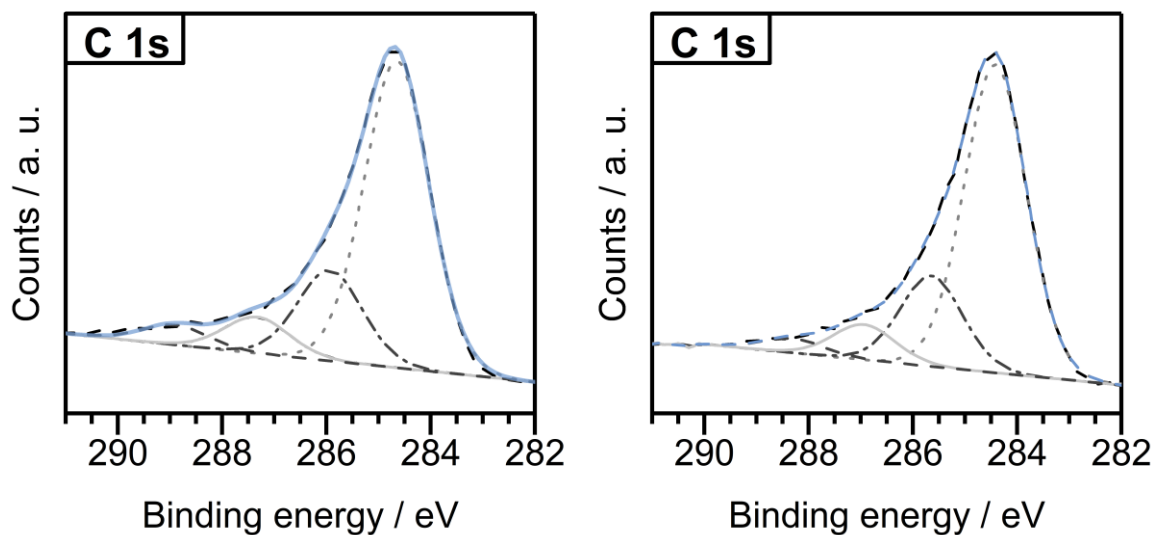


Figure A38 High resolution C 1s XPS spectra of CTF-Mono\_500 (left) and S@CTF-Mono\_500 (right).

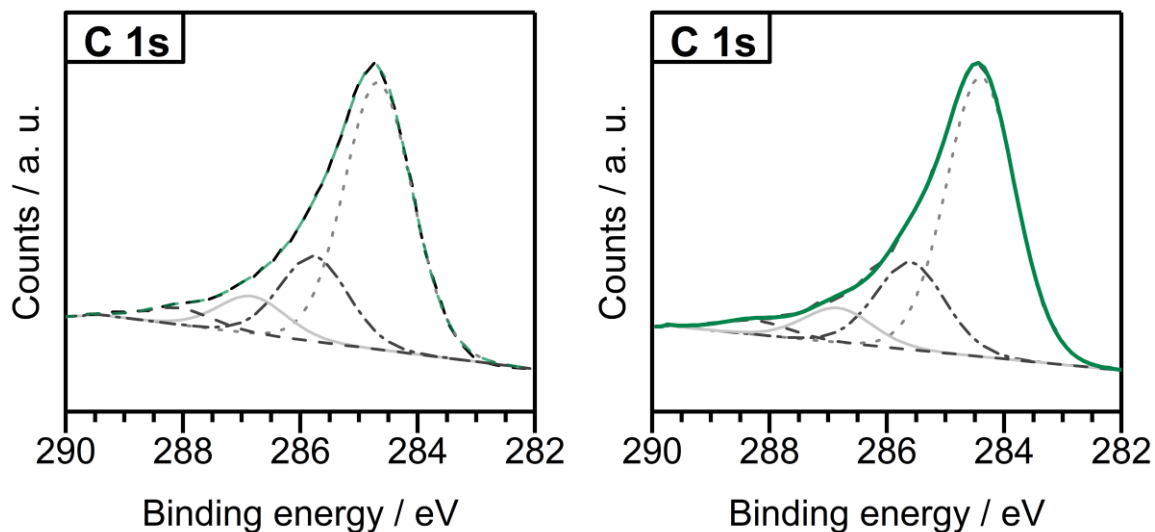


Figure A39 High resolution C 1s XPS spectra of CTF-Mono\_600 (left) and S@CTF-Mono\_600 (right).

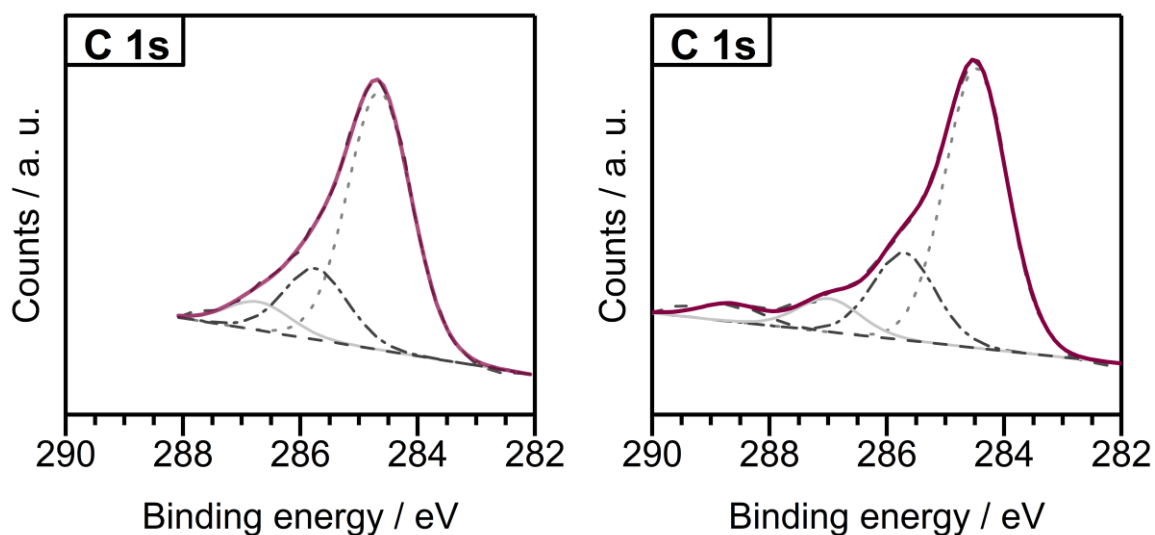


Figure A40 High resolution C 1s XPS spectra of CTF-Mono\_700 (left) and S@CTF-Mono\_700 (right).

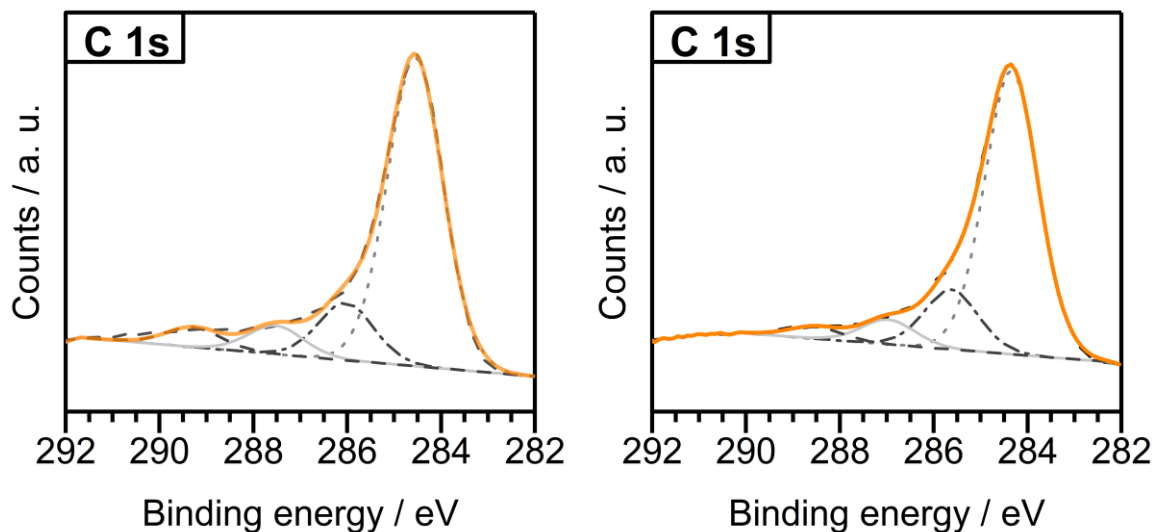


Figure A41 High resolution C 1s XPS spectra of CTF-Bi<sub>500</sub> (left) and S@CTF-Bi<sub>500</sub> (right).

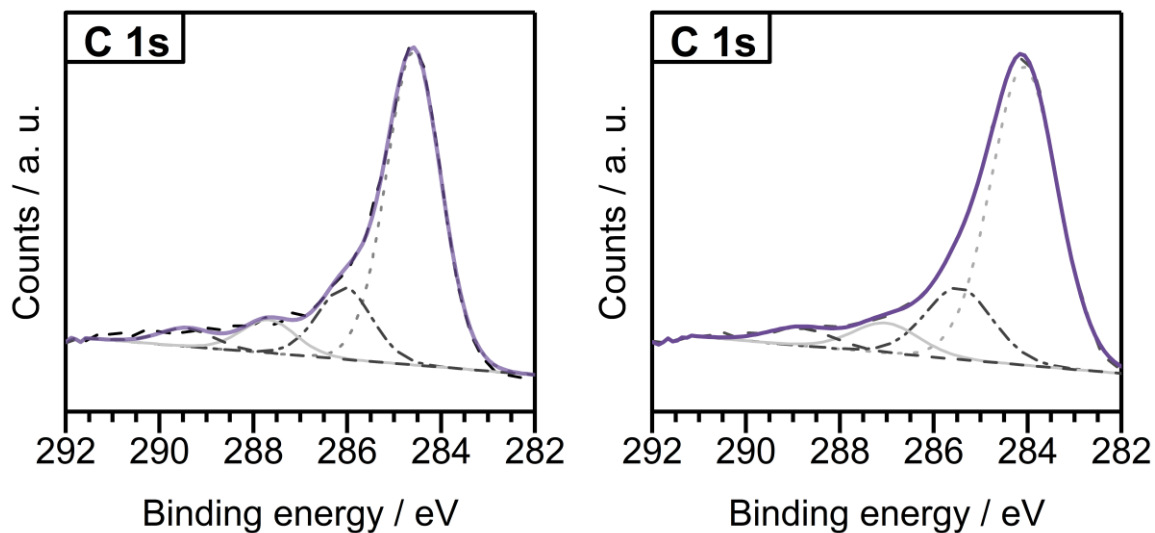


Figure A42 High resolution C 1s XPS spectra of CTF-Bi<sub>600</sub> (left) and S@CTF-Bi<sub>600</sub> (right).

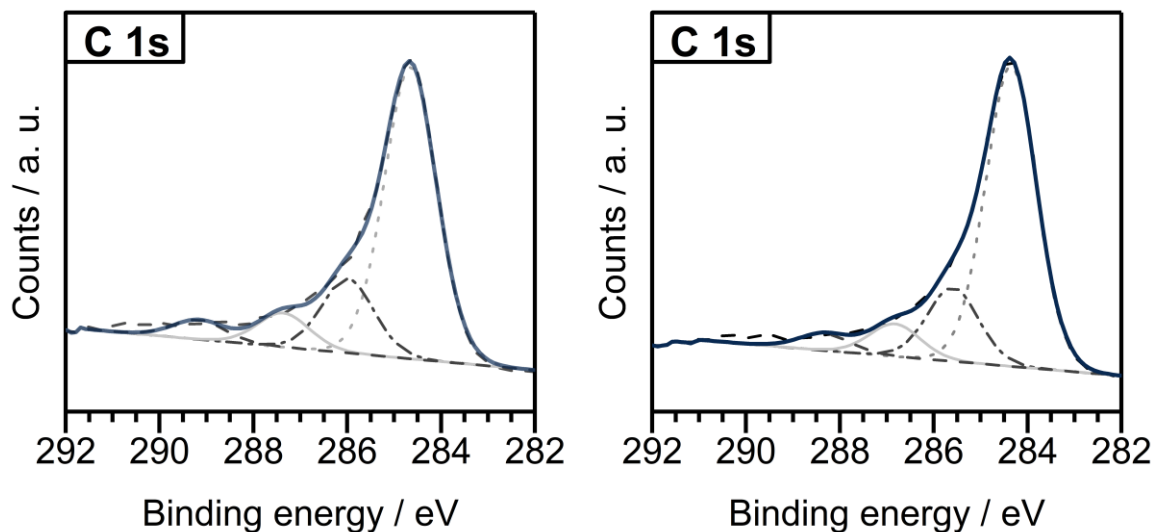


Figure A43 High resolution C 1s XPS spectra of CTF-Bi<sub>700</sub> (left) and S@CTF-Bi<sub>700</sub> (right).

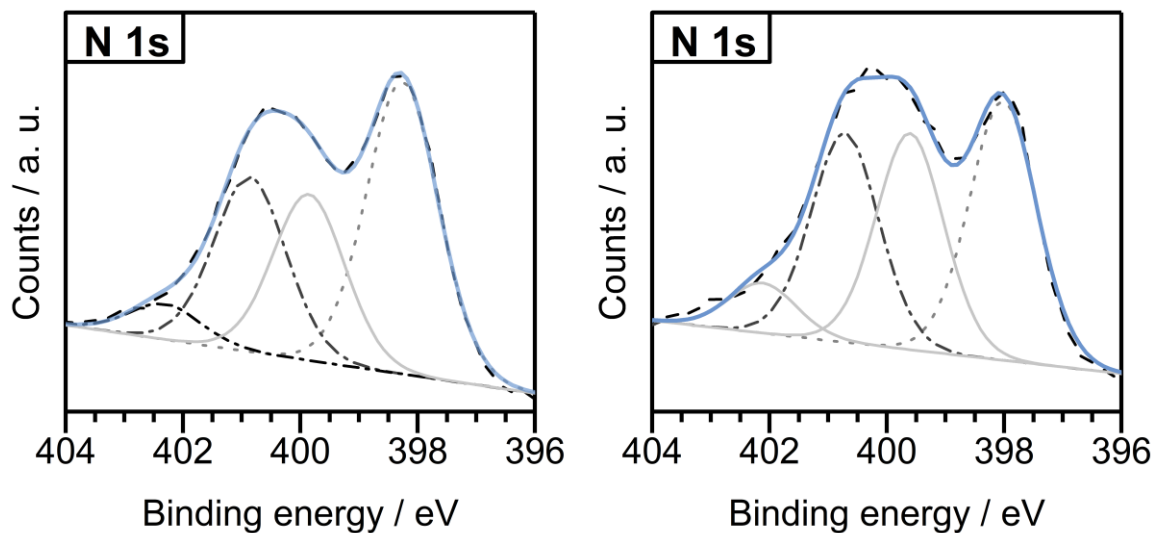


Figure A44 High resolution N 1s XPS spectra of CTF-Mono<sub>500</sub> (left) and S@CTF-Mono<sub>500</sub> (right).

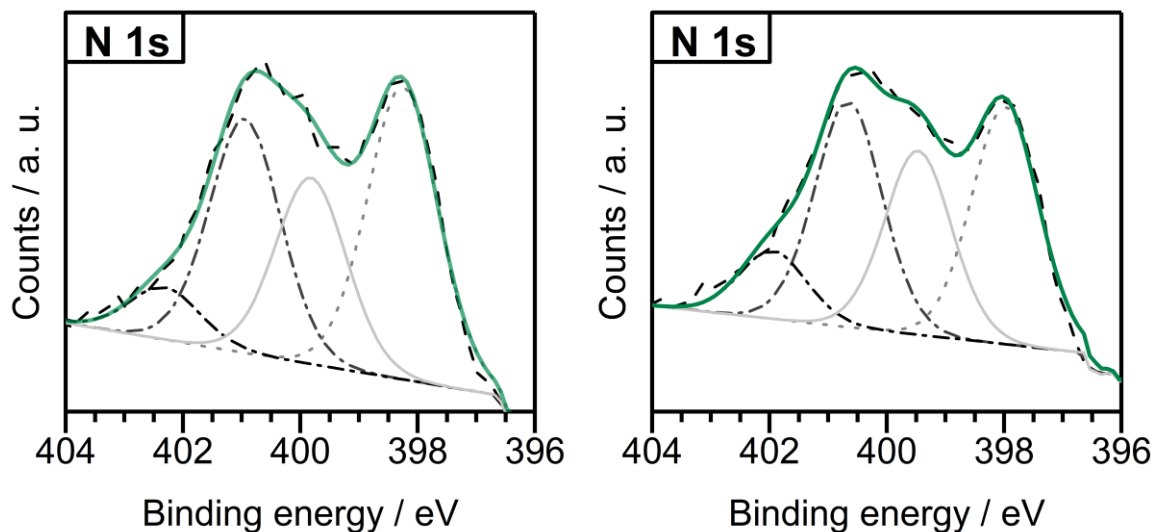


Figure A45 High resolution N 1s XPS spectra of CTF-Mono\_600 (left) and S@CTF-Mono\_600 (right).

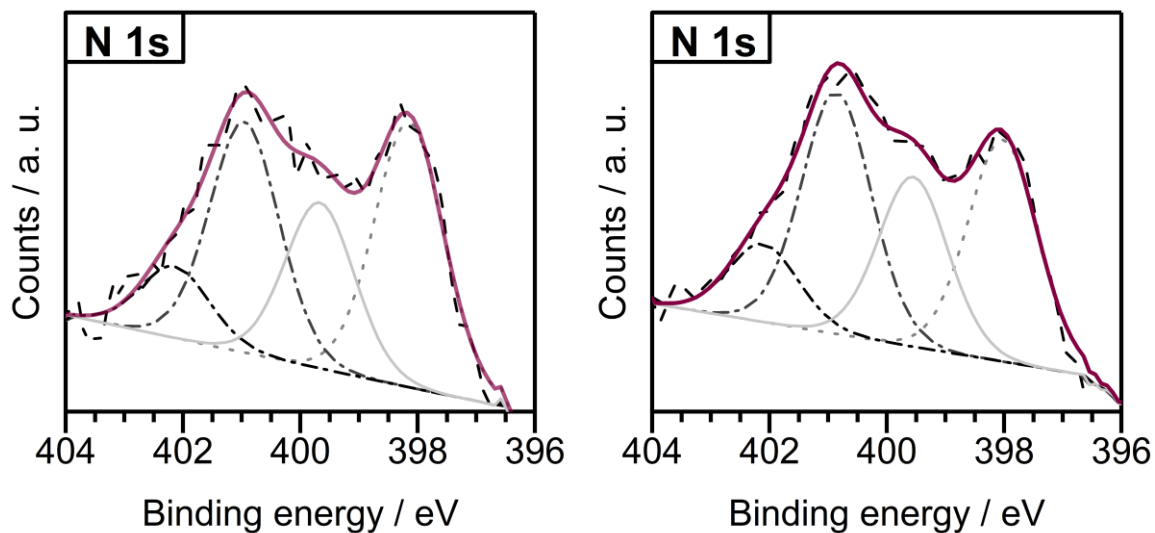


Figure A46 High resolution N 1s XPS spectra of CTF-Mono\_700 (left) and S@CTF-Mono\_700 (right).

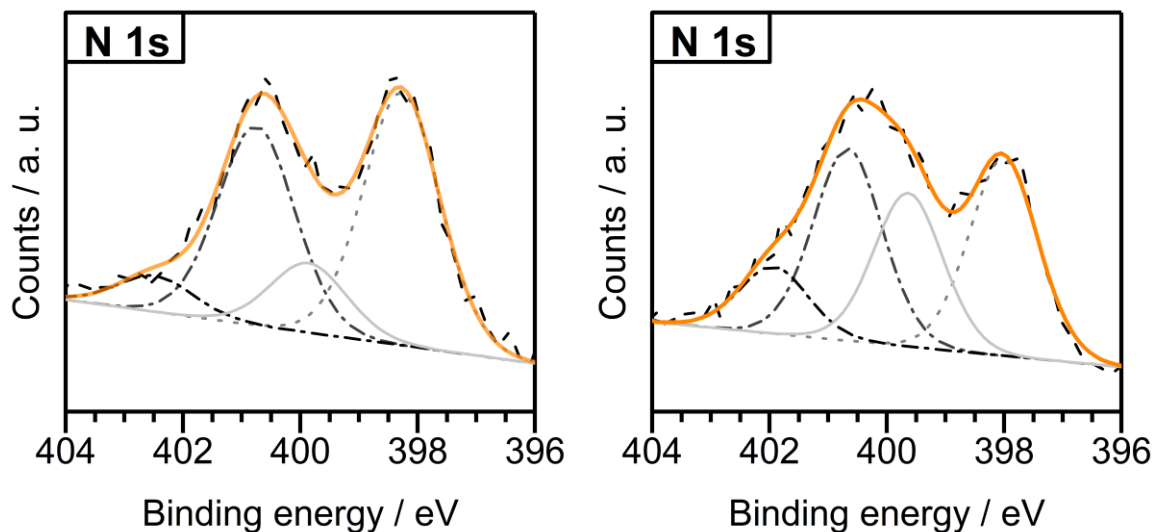


Figure A47 High resolution N 1s XPS spectra of CTF-Bi<sub>500</sub> (left) and S@CTF-Bi<sub>500</sub> (right).

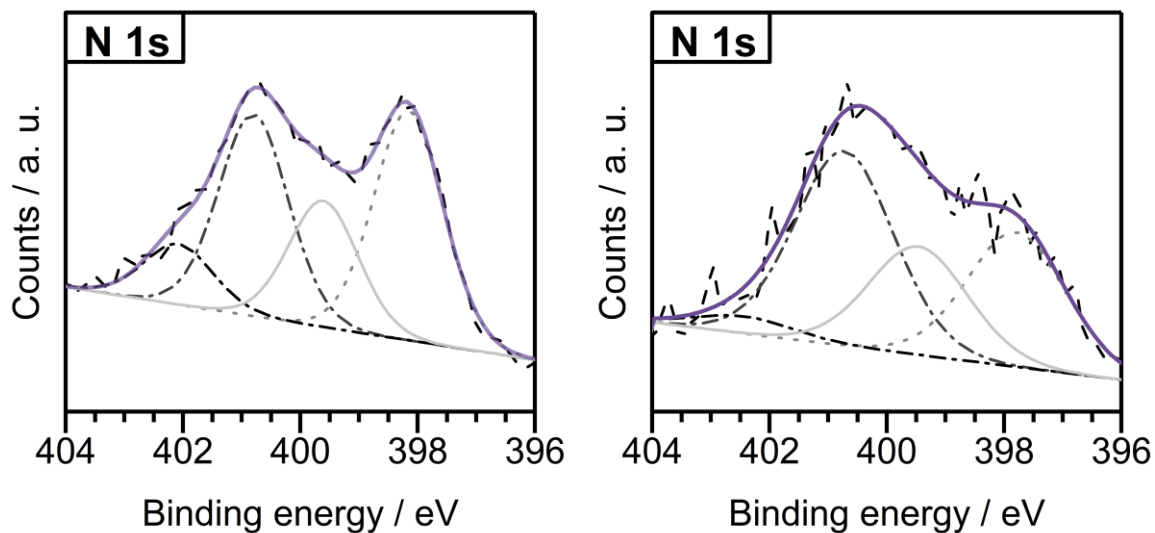


Figure A48 High resolution N 1s XPS spectra of CTF-Bi<sub>600</sub> (left) and S@CTF-Bi<sub>600</sub> (right).

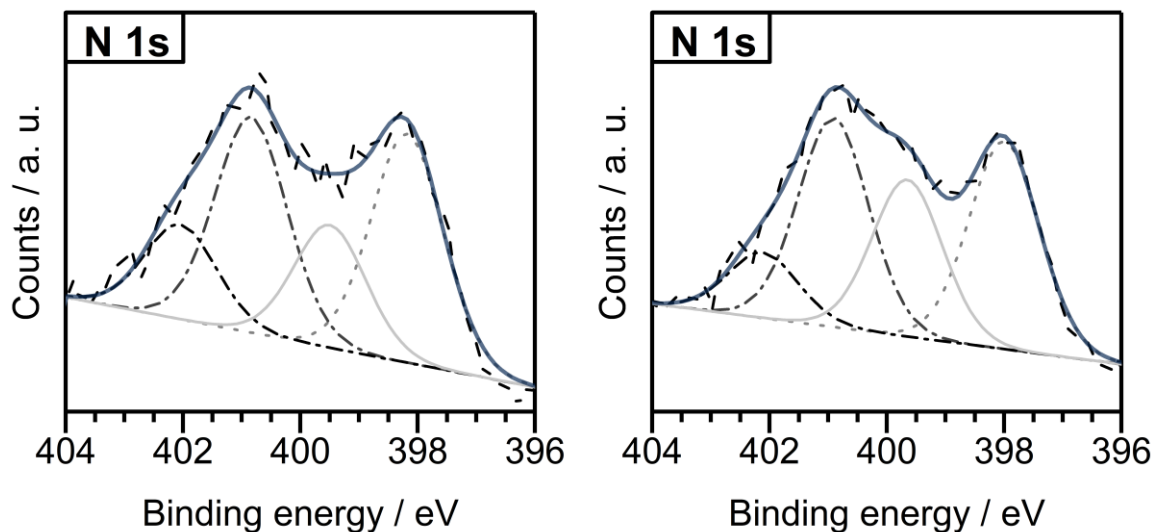


Figure A49 High resolution N 1s XPS spectra of CTF-Bi<sub>700</sub> (left) and S@CTF-Bi<sub>700</sub> (right).

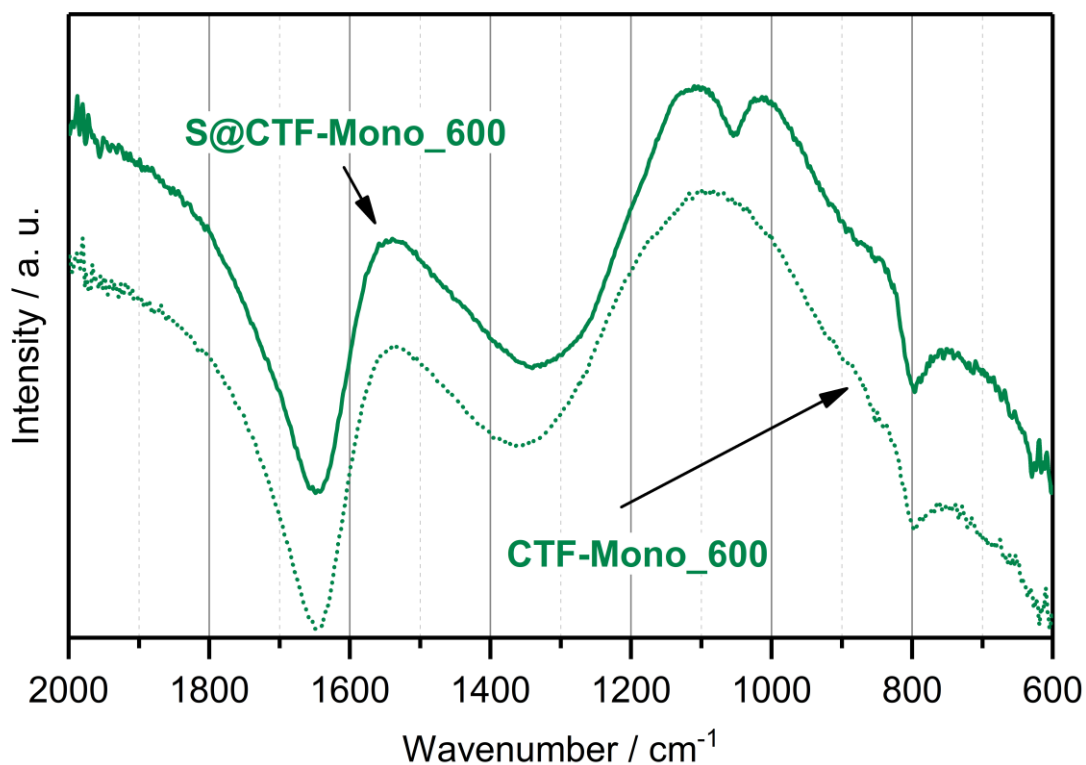
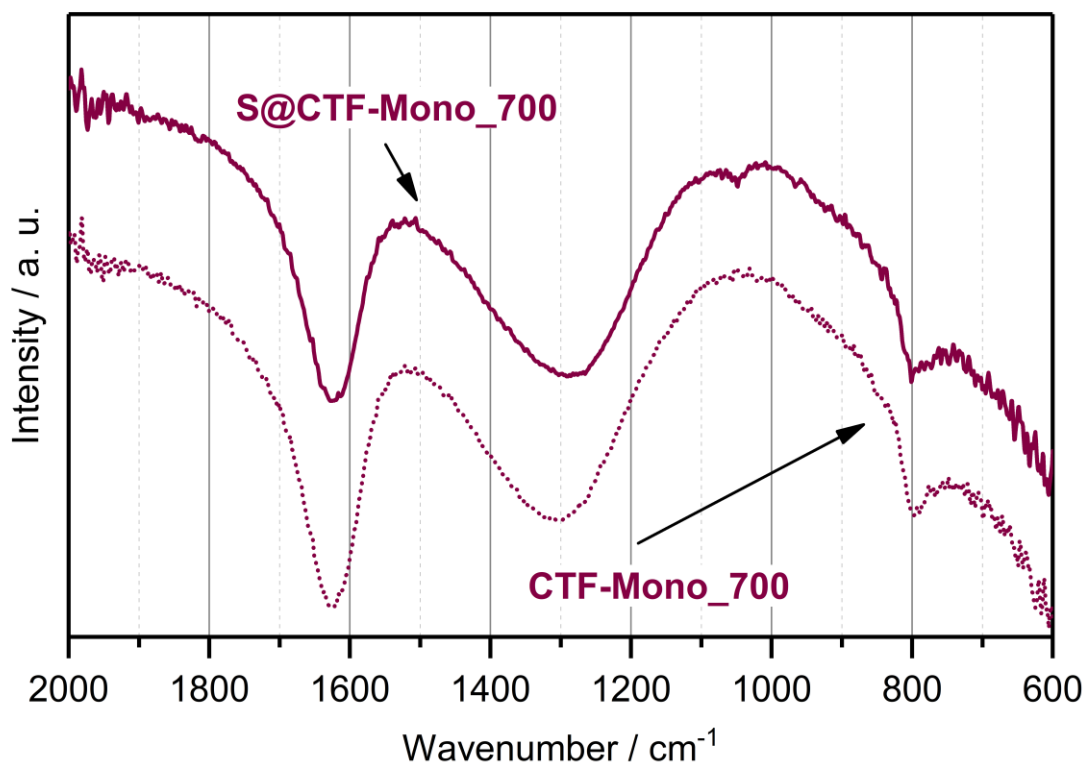
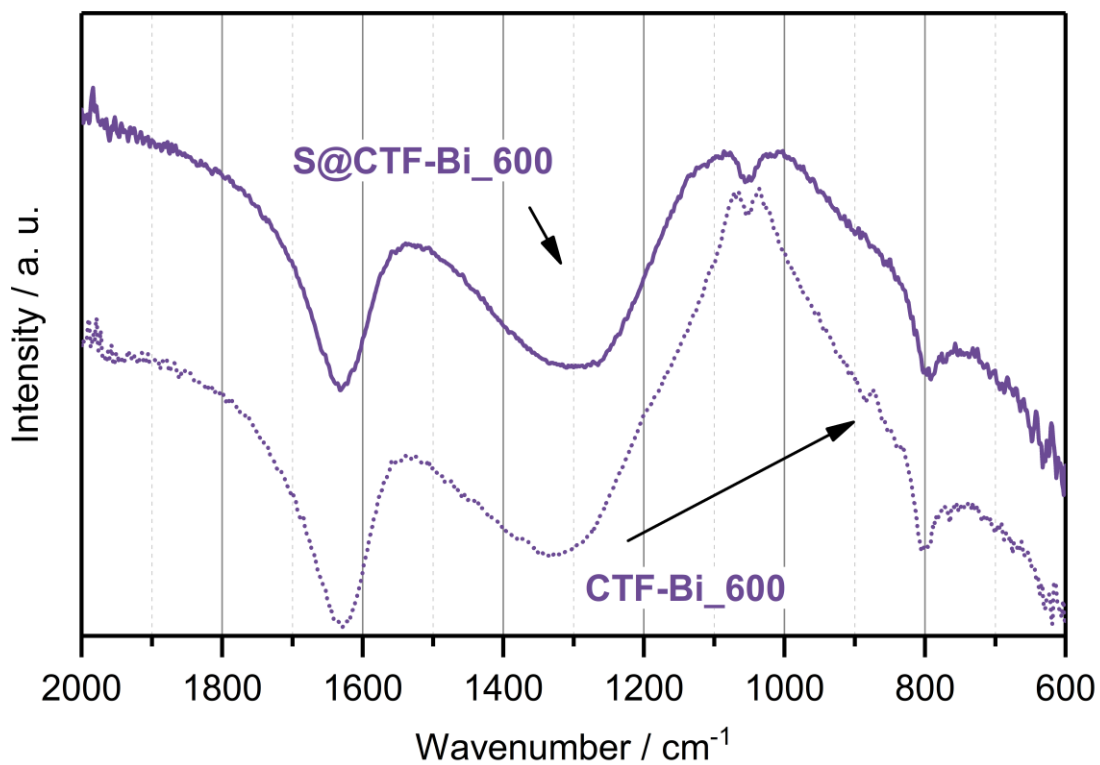


Figure A50 FT-IR spectra of CTF-Mono<sub>600</sub> and S@CTF-Mono<sub>600</sub>. The spectra shown here are normalised and an offset was applied for better visibility.

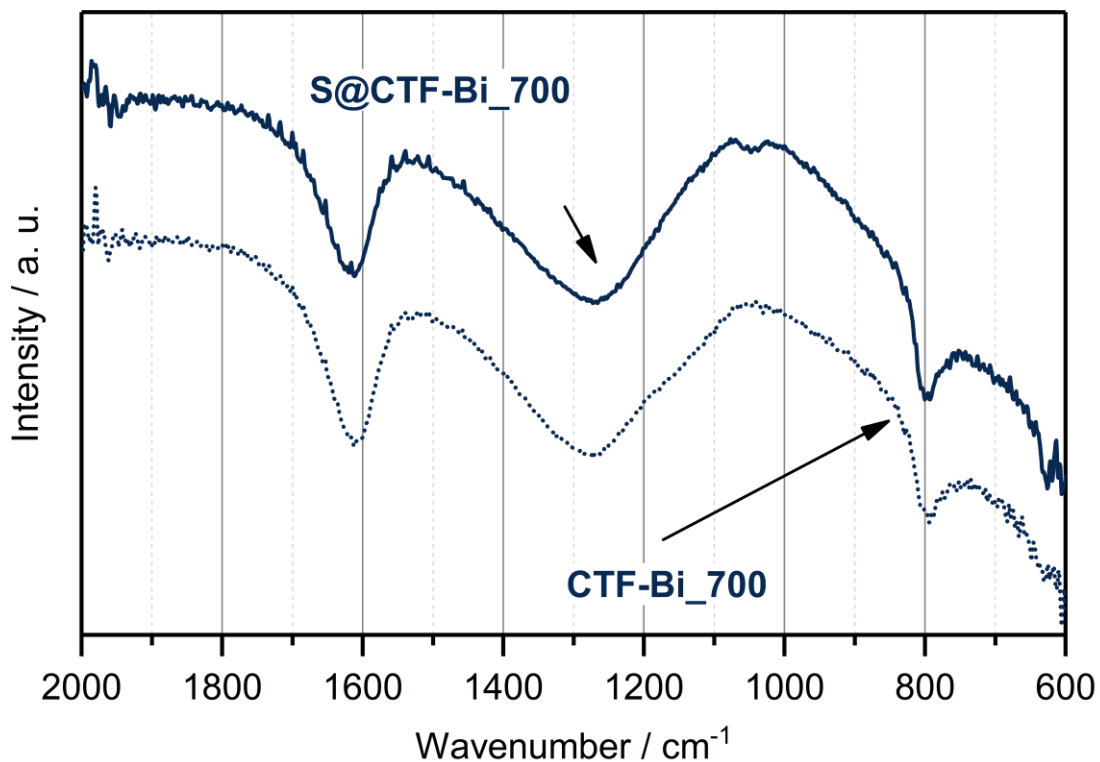




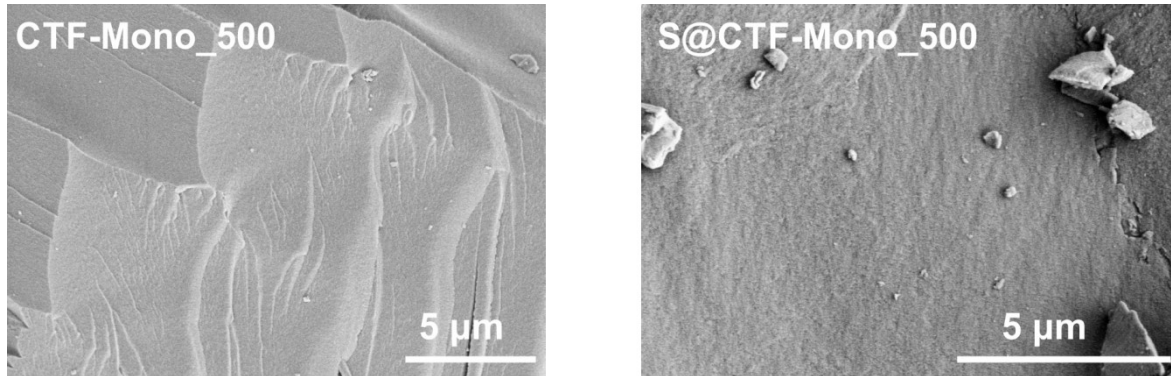
**Figure A51** FT-IR spectra of CTF-Mono\_700 and S@CTF-Mono\_700. The spectra shown here are normalised and an offset was applied for better visibility.



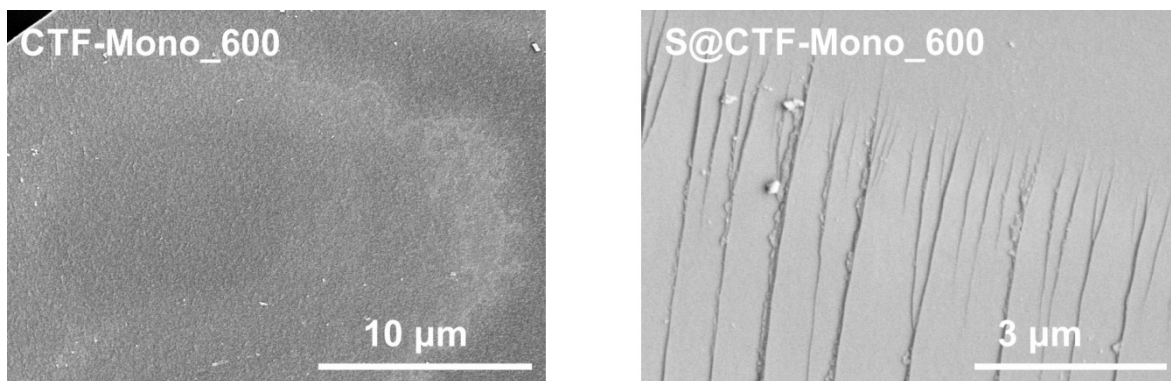
**Figure A52** FT-IR spectra of CTF-Bi\_600 and S@CTF-Bi\_600. The spectra shown here are normalised and an offset was applied for better visibility.



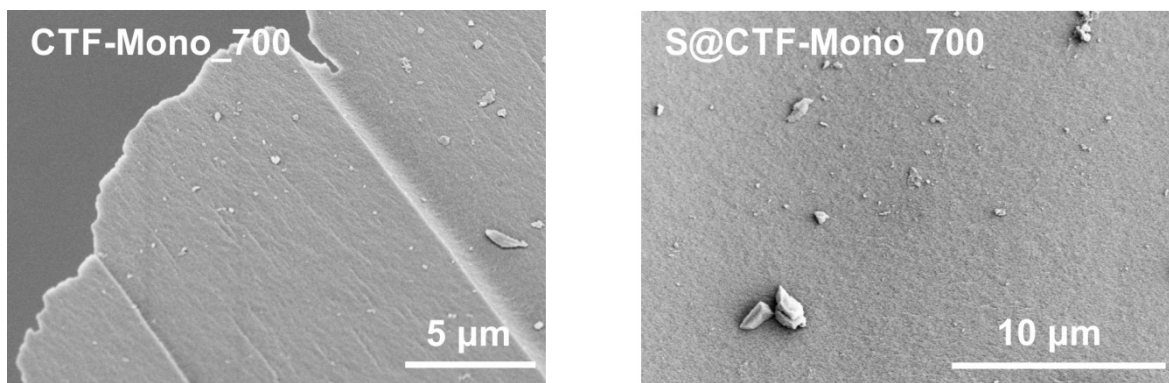
**Figure A53** FT-IR spectra of CTF-Bi\_700 and S@CTF-Bi\_700. The spectra shown here are normalised and an offset was applied for better visibility.



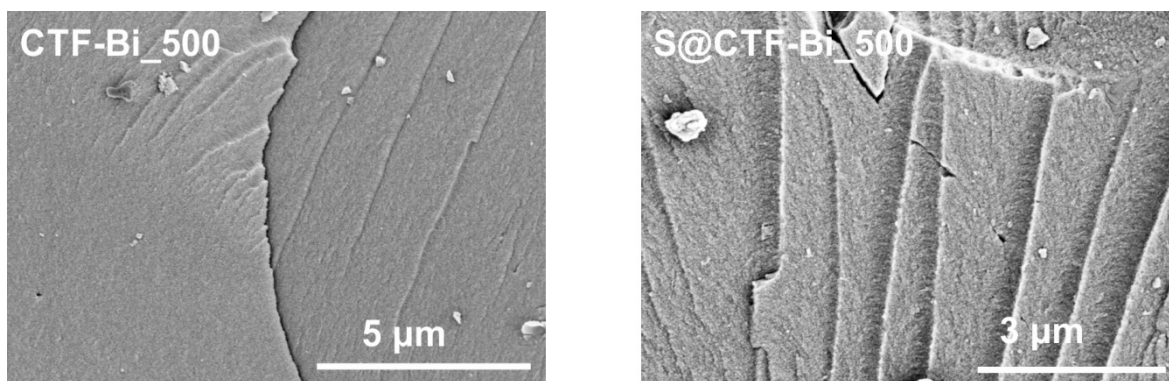
**Figure A54** SEM images of CTF-Mono\_500 (left) and S@CTF-Mono\_500 (right).



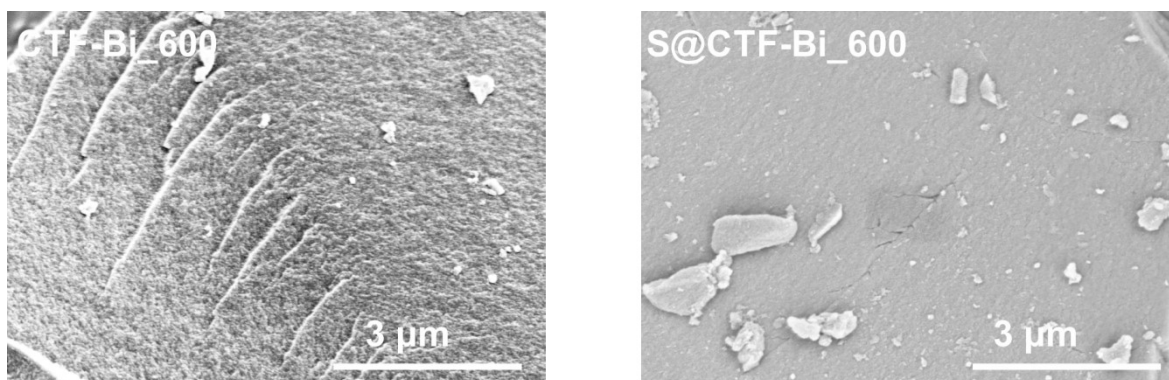
**Figure A55** SEM images of CTF-Mono\_600 (left) and S@CTF-Mono\_600 (right).



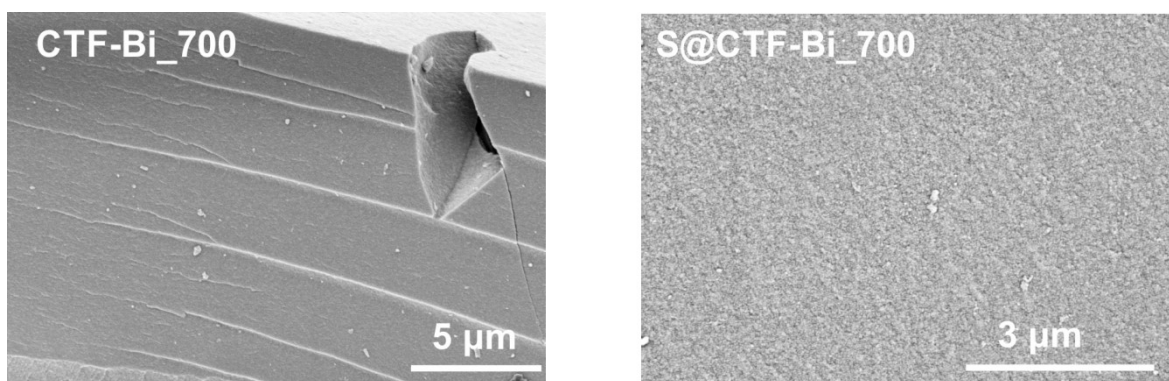
**Figure A56** SEM images of CTF-Mono\_700 (left) and S@CTF-Mono\_700 (right).



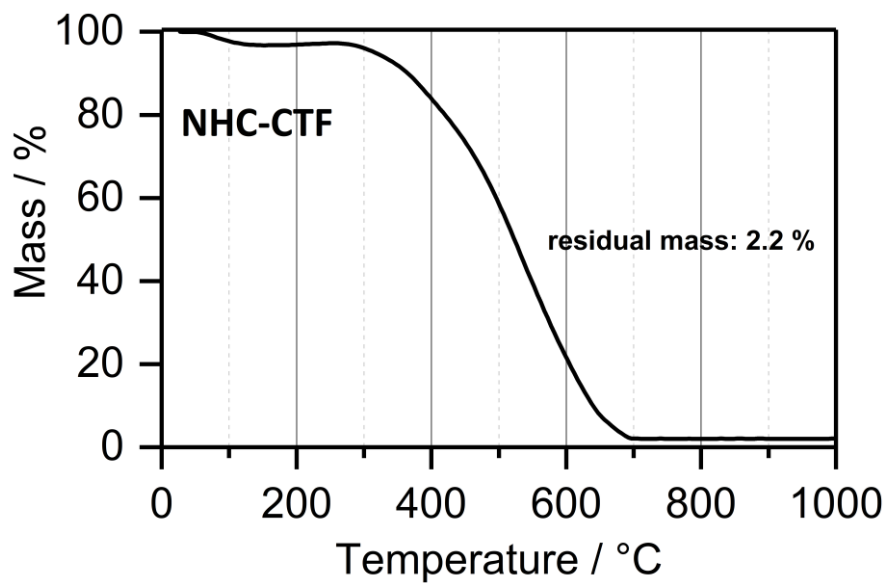
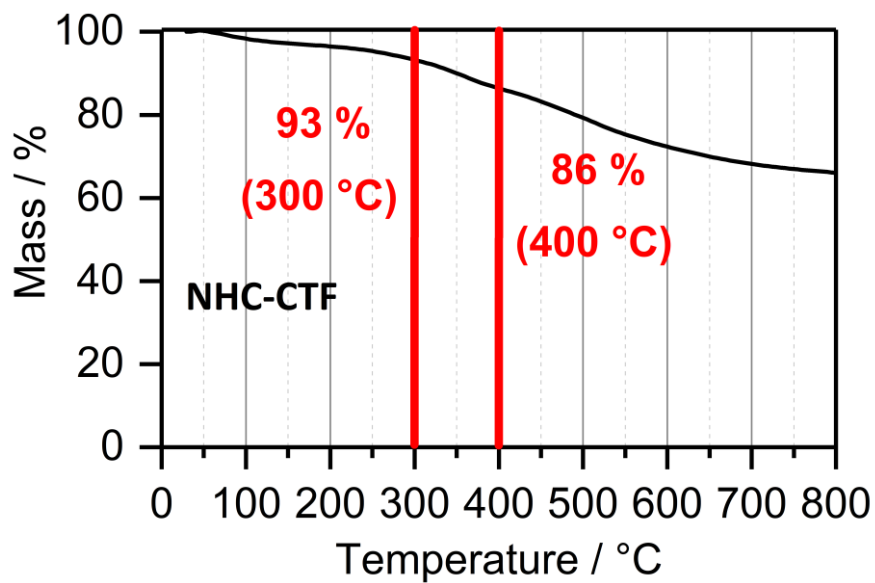
**Figure A57** SEM images of CTF-Bi\_500 (left) and S@CTF-Bi\_500 (right).



**Figure A58** SEM images of CTF-Bi\_600 (left) and S@CTF-Bi\_600 (right).



**Figure A59** SEM images of CTF-Bi\_700 (left) and S@CTF-Bi\_700 (right).

**NHC-CTF****Figure A60** TGA of NHC-CTF in air.**Figure A61** TGA NHC-CTF in argon.

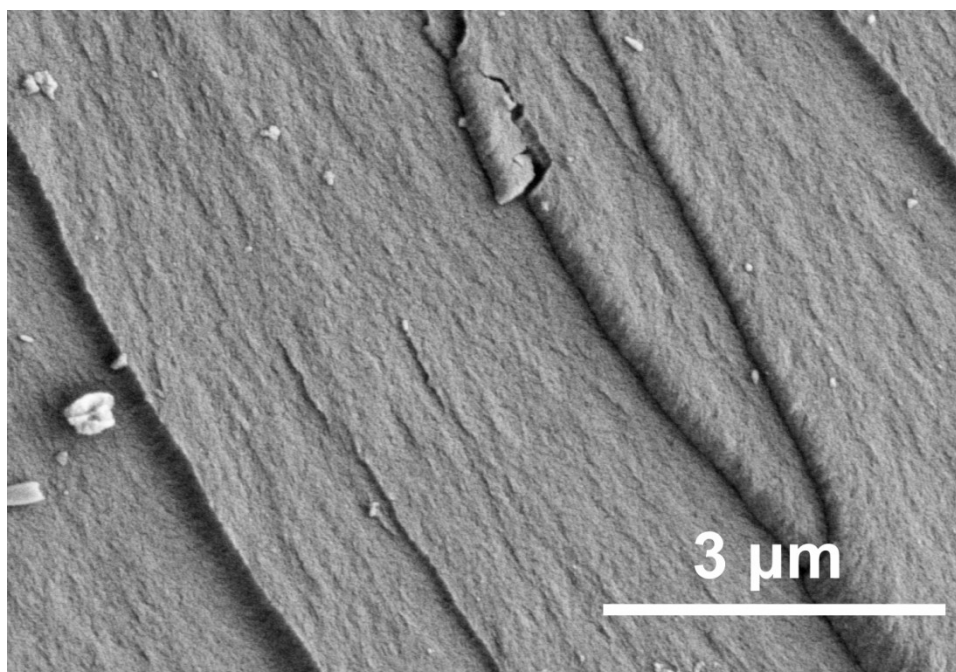


**Figure A62** SEM picture of NHC-CTF.

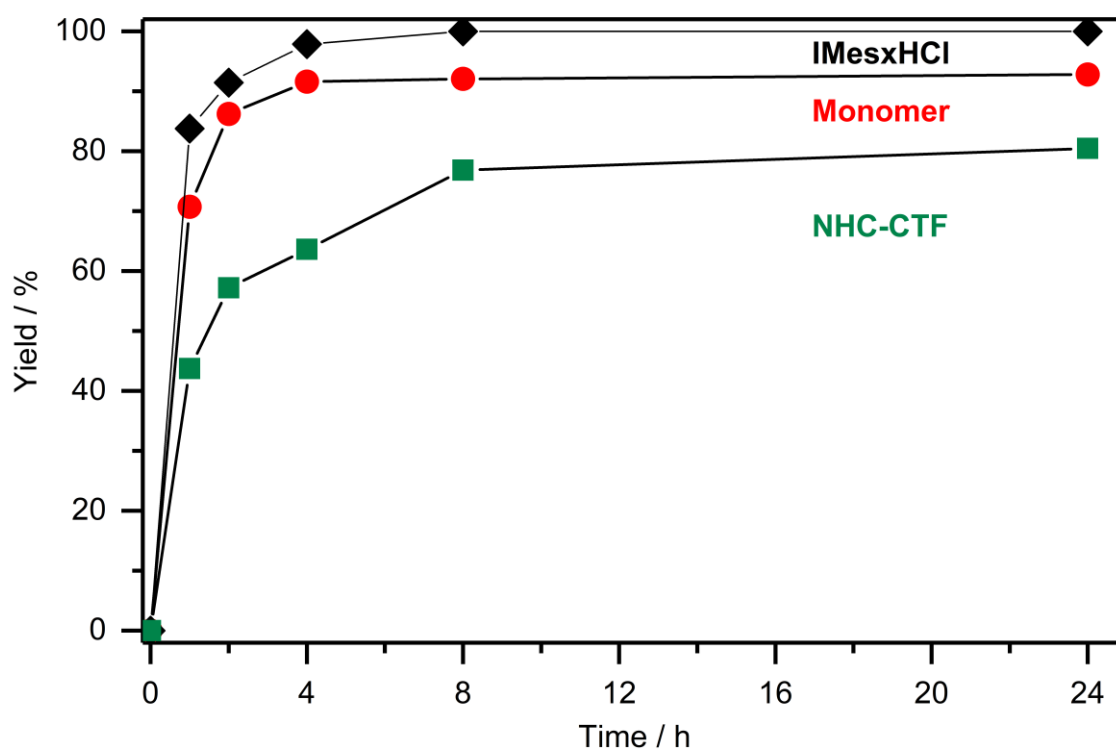


**Figure A63** Kinetic data of the NHC-CTF and homogeneous analogues (monomer and conventionally used NHC catalyst). T = 70 °C, 15 mol% of catalyst with respect to *trans*-cinnamaldehyde.

## List of tables

Table 1	Significant reactions employed in the metal-catalysed (-mediated) synthesis of NPOPs. ....	18
Table 2	Synopsis of applied methods to synthesise CTF materials and their respective main features including the highest reported surface areas for each method. ....	31
Table 3	List of applied chemicals. ....	51
Table 4	Solvents applied in this thesis ....	52
Table 5	Synthetic parameters of different mechanochemically synthesised CTF samples. ....	64
Table 6	Porosity data of the investigated CTF samples including their specific surface area, ultramicropore volume, supermicropore volume, mesopore volume, ratio of micropore and mesopore volume and total pore volume (at $p/p_0 = 0.95$ ). ....	77
Table 7	Porous CTFs of different monomers and their specific surface area (argon), total pore volume (at $p/p_0 = 0.95$ ) and yield (reaction time).....	89
Table 8	Comparison of BET surface areas regarding different monomers and the derived CTFs using classical ampoule syntheses ( $N_2$ BET surface area), Brønsted acid catalysed ( $N_2$ BET surface area) and the mechanochemically synthesised CTFs (Argon BET surface area). ....	91
Table 9	Porosity data of the investigated CTF samples including their specific surface area (argon), micropore volume, mesopore volume, ratio of micropore and mesopore volume and total pore volume (at $p/p_0 = 0.95$ ). ....	95
Table 10	Elemental analysis of 3,5-dicyanopyridine derived CTF materials. ....	96
Table 11	Raman fitting data of DCP-CTF-500, DCP-CTF-600 and DCP-CTF-700. ....	99
Table 12	Electrochemical data of 3,5-dicyanopyridine derived CTF materials determined by galvanostatic charge- and discharge cycles at $1 \text{ Ag}^{-1}$ . ....	103
Table 13	Porosity data of all CTF samples and their sulfur treated analogues (from Nitrogen adsorption at 77 K). ....	107
Table 14	Gravimetric powder resistivities of investigated sulfur treated CTF samples and CTF-1. ....	115
Table 15	Elemental analyses of NHC-CTF and samples obtained at 320 °C and 330 °C. ....	121
Table 16	Results of catalytic testing and comparison of NHC-CTF with samples synthesised at higher temperature and homogeneous analogues. ....	126



## List of schemes

Scheme 1	Schematic representation of different pores sizes in porous solids (according to IUPAC). <sup>4</sup> .....	9
Scheme 2	Comparison of two opposite concepts to create porosity in nanoporous organic polymers: a) porosity as a result of ineffective packing of polymer chains <sup>15</sup> and b) porosity as a result of a modular construction principle yielding organic frameworks. <sup>16</sup> .....	11
Scheme 3	Classification of the most prominent representatives of nanoporous organic polymers according to their synthesis concept (organic vs. polymeric), the requirement of metals for their synthesis (metal-free condensation vs. metal-catalysed/-mediated) and the degree of reversibility (reversible vs. irreversible) provided by their synthesis protocol. Figures adapted from reference: PIMs [15]; COFs [16]; HCPs [18]; CMPs [19]; CTFs [20]; PAFs [21]......	12
Scheme 4	Synthesis of PIM-1 by a condensation reaction to yield the spirocyclic bis(phthalonitrile) (1) which undergoes tetramerisation to form phthalocyanine-based PIM-1. <sup>9</sup> .....	13
Scheme 5	Synthesis of COF-1 obtained by a condensation of 1,4-diboronic acid and COF-5 obtained by co-condensation of 1,4-diboronic acid and hexahydroxy triphenylene. <sup>28</sup> .....	14
Scheme 6	Significant reversible reactions for the synthesis of covalent organic frameworks. All reactions belong to the group of condensation reactions except for the formation of azodioxy compounds. Red atoms indicate atoms that form water in course of the reaction.....	15
Scheme 7	Synthesis of borazine linked polymer (a) presented by Reich <i>et al.</i> <sup>45</sup> and synthesis of a nanoporous organic polymer by cyclotrimerization of aromatic bi-acetyl compounds (b) from Kaskel and co-workers. <sup>47</sup> .....	16
Scheme 8	Schematic synthesis of a hypercrosslinked polymer (adapted from reference [18]).....	19
Scheme 9	Isorecticular synthesis of CMPs with varying tecton length by Cooper and co-workers. <sup>60</sup> .....	20
Scheme 10	Synthesis of porous aromatic framework (PAF-1) starting from tetrakis(4-bromophenyl-methane). <sup>21</sup> .....	22
Scheme 11	Ionothermal trimerization reaction to synthesise CTF-1 from 1,4-dicyanobenzene. ....	24
Scheme 12	Representative aromatic nitrile monomers which have been applied for the ionothermal synthesis of CTF materials and the respective reference of first report. For a complete overview find more information in a very recent review that has summarised all applied nitrile monomers until 2016. <sup>94</sup> .....	26

---

Scheme 13	Different synthetic procedures towards CTF materials including a) ionothermal synthesis in molten $\text{ZnCl}_2$ / <sup>81</sup> microwave, <sup>95</sup> b) Brønsted acid catalysed trimerization (solution/microwave) <sup>96</sup> c) $\text{P}_2\text{O}_5$ triggered dehydration and consequent trimerization, <sup>20</sup> d) Friedel-Crafts reaction, <sup>97</sup> e) Yamamoto homo-coupling <sup>98</sup> and f) Sonogashira-Hagihara cross-coupling. <sup>99</sup> .....	27
Scheme 14	Synthesis of ordered CTF materials starting from aromatic amides according to Yu <i>et al.</i> <sup>20</sup> .....	30
Scheme 15	Synthesis of HAT-CTF and incorporation of oxygen in the structure by <i>in situ</i> cleavage of methoxy-groups as proposed by Zhu <i>et al.</i> <sup>110</sup> .....	32
Scheme 16	Schematic representation of Lennard-Jones potentials in different pore types. ....	37
Scheme 17	Classification of physisorption isotherms according to IUPAC (adapted from reference [4]). ....	39
Scheme 18	Schematic representation of the processes occurring while degassing a flexible nanoporous organic polymer and the change of pore morphology upon adsorption (adapted with slight modification from [153]). ....	44
Scheme 19	The basic principle of an XPS experiment: An irradiated surface emits electrons via the photoelectric effect (according to reference [155]). Other relevant quantities present in a real setup such as the work function are omitted in this scheme.....	45
Scheme 20	Schematic representation of an XPS spectrometer (adapted from reference [155]). ....	48
Scheme 21	Salt templating procedure for the synthesis of hierarchical CTFs. ....	73
Scheme 22	Mechanochemical syntheses of porous covalent triazine frameworks by Friedel-Crafts alkylation of different aromatic monomers with cyanuric chloride.....	81
Scheme 23	Synthesis of CTF-Mono (derived from 1,4-dicyanobenzene) and CTF-Bi (4,4'-dicyano-1,1'-biphenyl) and corresponding temperature protocol for the CTF synthesis. ....	105
Scheme 24	Possible application of CTF materials as heterogeneous catalyst including: a) CTF as catalyst support for deposited metal nanoparticles (M), b) coordination of catalytically active metal complexes, c) application of basic properties of triazinic nitrogen atoms.....	117
Scheme 25	Application of NHC-CTF as heterogeneous catalyst in carbene-catalysed conjugated Umpolung reaction.....	124



## List of figures

Figure 1	Temperature protocol for salt templated CTF samples. ....	60
Figure 2	Temperature protocol for the synthesis of CTF-Mono and CTF-Bi.....	65
Figure 3	Temperature protocol for the synthesis of 3,5-dicyanopyridine derived CTF.....	68
Figure 4	Temperature protocol for the synthesis of NHC-CTF.....	70
Figure 5	Temperature protocol applied for the synthesis of salt templated CTFs (a); FT-IR spectra of salt template CTF samples and reference (b).....	74
Figure 6	Influence of different ZnCl <sub>2</sub> : NaCl ratios on the porosity of the resulting CTF material.....	74
Figure 7	Argon physisorption isotherm (87 K) of salt templated CTF samples and reference (a); Pore size distribution (QSDFT) of respective samples (b).....	76
Figure 8	SEM pictures of CTF-1_450 (a), CTF-1_LiCl (b), CTF-1_NaCl (c) and CTF-1_KCl (d).....	78
Figure 9	Carbon to nitrogen ratio derived from elemental analysis of investigated CTF samples.....	78
Figure 10	a) picture of CTF-CBZ, b) nitrogen physisorption isotherm (77 K) of CTF-CBZ. ....	82
Figure 11	a) FT-IR spectra of carbazole-CTF (CTF-CBZ), carbazole and cyanuric chloride, b) <sup>13</sup> C CP/MAS NMR spectra of CTF-CBZ and carbazole.....	83
Figure 12	C 1s XPS spectrum of CTF-CBZ (c), N 1s XPS spectrum of CTF-CBZ (d).....	84
Figure 13	Argon physisorption isotherm (87 K) of CTF-CBZ (a), Pore size distributed (QSDTF) (b).....	85
Figure 14	PXRD data of CTF-CBZ revealing traces of tungsten carbide (a); Thermogravimetric analysis of CTF-CBZ under synthetic air (b).....	85
Figure 15	a) Evolution of porosity and yield of the polymerisation reaction for the synthesis of CTF-CBZ, b) <i>in situ</i> analysis of temperature and pressure in the milling jar.....	87
Figure 16	(a) <sup>1</sup> H NMR spectra of samples taken after 5 minutes and 10 minutes. § EtOAc, * DMSO, # EtOH; (b) <sup>13</sup> C NMR spectra of samples taken after 5 minutes and 10 minutes. Deuterated solvent: DMSO-d <sub>6</sub> .....	87
Figure 17	<sup>1</sup> H/ <sup>13</sup> C-HMBC spectrum of CTF-CBZ reaction mixture after 10 min reaction time. Main component is unreacted carbazole. Peaks corresponding to the main product (3-substituted carbazole) are marked.....	88
Figure 18	MALDI-TOF spectra of CTF-CBZ samples taken at different times from the polymerisation reaction. ....	88
Figure 19	Argon physisorption isotherm (87 K) of mechanochemically synthesised CTFs from benzene (a), naphthalene (b), anthracene (c), triphenylbenzene (d) and tetraphenylmethane (e).....	90

---

Figure 20	Synthesis of 3,5-dicyanopyridine and derived covalent triazine frameworks.....	93
Figure 21	(a) Argon physisorption (87 K) isotherms revealing a temperature induced evolution of porosity. b) Pore size distribution (QSDFT). .....	94
Figure 22	Water vapour adsorption isotherms measured at 298 K.....	95
Figure 23	High resolution N 1s XPS spectra of 3,5-dicyanopyridine derived CTF materials (a); High resolution C 1s XPS spectra of 3,5-dicyanopyridine derived CTF materials (b). .....	97
Figure 24	Survey XPS spectra of 3,5-dicyanopyridine derived CTF materials. ....	98
Figure 25	Raman spectra of the investigated 3,5-dicyanopyridine derived CTF materials.....	98
Figure 26	SEM pictures of DCP-CTF-700 comparing an unwashed (left) and washed sample (right). .....	100
Figure 27	a) Nyquist plot; b) Cyclic voltammograms at 10 mVs <sup>-1</sup> ; c) Galvanostatic charge- and discharge cycles at 1 A g <sup>-1</sup> .....	102
Figure 28	Nitrogen physisorption isotherms (77 K) of CTF materials synthesised at different temperatures and derived materials containing covalently bound sulfur obtained from a) 1,4-dicyanobenzene (CTF-Mono) and b) 4,4'-dicyano-1,1'-biphenyl (CTF-Bi). $\Delta V_P$ represents the percental decrease of the total pore volume after sulfur attachment.....	106
Figure 29	Nitrogen physisorption isotherm (77 K) of CTF-Bi_500 and a ball milled reference sample. After ball milling, no loss of porosity is observed. Therefore, the isotherms can be considered as identical.....	108
Figure 30	Elemental analyses and the respective C/H molar ratios of CTF-Mono samples (a) and CTF-Bi samples (b) obtained at different temperatures. Sulfur content with respect to the synthesis temperature for S@CTF-Mono (a) and S@CTF-Bi (b) samples. ....	109
Figure 31	Powder X-ray diffraction data of a) S@CTF-Mono and b) S@CTF-Bi.....	110
Figure 32	Survey XPS spectra of CTF-Mono and CTF-Bi samples.....	111
Figure 33	High resolution S 2p XPS spectra of S@CTF-Mono_600 and S@CTF-Bi_600. Resulting peaks were obtained by adding p <sub>1/2</sub> and p <sub>3/2</sub> component fit and subtracting the background. ....	112
Figure 34	a) High resolution C 1s XPS spectra of CTF-Mono_600 and S@CTF-Mono_600, b) High resolution N 1s spectra of the same samples.....	113
Figure 35	FT-IR spectra of CTF-Mono/CTF-Bi_500 and the sulfur treated analogues revealing an additional C=S stretching mode. The spectra shown here are normalised and an offset was applied for better visibility. ....	114
Figure 36	Gravimetric powder resistivities of investigated sulfur treated CTF samples and CTF-1.....	115
Figure 37	Integration of an N-heterocyclic carbene precursor into a covalent triazine framework and its application as heterogeneous organocatalyst for carbene-catalysed Umpolung reaction (see Scheme 25).....	118
Figure 38	Thermogravimetric analysis of imidazolium monomer in argon. The red horizontal line indicates the mass loss at 400 °C.....	119

---

---

Figure 39	a) $^1\text{H}$ solid-state MAS NMR spectra of imidazolium-monomer and corresponding NHC-CTF; b) Deconvoluted N 1s XPS spectrum of NHC-CTF; and c) FT-IR spectra of imidazolium-monomer and corresponding NHC-CTF.....	120
Figure 40	PXRD data of NHC-CTF reflecting interlayer stacking.....	122
Figure 41	a) Nitrogen physisorption isotherm (77 K) of NHC-CTF; b) Carbon dioxide physisorption isotherm (273 K) of NHC-CTF.....	123
Figure 42	Vapour adsorption isotherms (MeCN, EtOH, toluene) of NHC-CTF.....	124
Figure 43	a) Comparison of obtained yields using different solvents in heterogeneous catalysis; b) Kinetic data and heterogeneity testing of NHC-CTF. Red horizontal line illustrates no further product formation after removal of the catalyst. Reaction conditions: $T = 70\text{ }^\circ\text{C}$ , 15 mol% of catalyst with respect to <i>trans</i> -cinnamaldehyde.....	125
Figure 44	Recyclability of NHC-CTF investigated over five runs in MeCN. Reaction conditions: $T = 70\text{ }^\circ\text{C}$ , 15 mol% of catalyst with respect to <i>trans</i> -cinnamaldehyde.....	126

## List of publications of Erik Troschke

- [1] Yahaya, N. P.; Appleby, K. M.; Teh, M.; Wagner, C.; Troschke, E.; Bray, J. T. W.; Duckett, S. B.; Hammarback, L. A.; Ward, J. S.; Milani, J.; Pridmore, N. E.; Whitwood, A. C.; Lynam, J. M.; Fairlamb, I. J. S. Manganese(I)-catalyzed C–H activation: the key role of a 7-Membered manganacycle in H-Transfer and reductive elimination. *Angew. Chem., Int. Ed.* **2016**, *55*, 12455–12459.  
<https://doi.org/10.1002/ange.201606236>
- [2] Troschke, E.; Grätz, S.; Borchardt, L.; Haubold, D.; Senkovska, I.; Eychmueller, A.; Kaskel, S. Salt templated synthesis of hierarchical covalent triazine frameworks. *Microporous and Mesoporous Materials* **2017**, *239*, 190–194.  
<https://doi.org/10.1016/j.micromeso.2016.10.002>
- [3] Troschke, E.; Grätz, S.; Lübken, T.; Borchardt, L. Mechanochemical Friedel-Crafts alkylation – a sustainable pathway towards porous organic polymers. *Angew. Chem., Int. Ed.* **2017**, *56*, 6859–6863.  
<https://doi.org/10.1002/anie.201702303>
- [4] Grätz, S.; Oltermann, M.; Troschke, E.; Paasch, S.; Krause, S.; Brunner, E.; Borchardt, L. Solvent-free synthesis of a porous thiophene polymer by mechanochemical oxidative polymerization. *J. Mater. Chem. A* **2018**, *6*, 21901–21905.  
<https://doi.org/10.1039/C8TA03684E>
- [5] Haase, F.; Troschke, E.; Savasci, G.; Banerjee, T.; Duppel, V.; Dörfler, S.; Grundei, M. M. J.; Burow, A. M.; Ochsenfeld, C.; Kaskel, S.; Lotsch, B. V. Topochemical conversion of an imine- into a thiazole-linked covalent organic framework enabling real structure analysis. *Nat. Commun.* **2018**, *9*, 2600.  
<https://doi.org/10.1038/s41467-018-04979-y>
- [6] Troschke, E.; Nguyen, K. D.; Paasch, S.; Schmidt, J.; Nickerl, G.; Senkovska, I.; Brunner, E.; Kaskel, S. Integration of an N-heterocyclic carbene precursor into a covalent triazine framework for organocatalysis. *Chem. Eur. J.* **2018**.  
<https://doi.org/10.1002/chem.201804373>
- [7] Dörfler, S.; Strubel, P.; Jaumann, T.; Troschke, E.; Hippauf, F.; Kensy, C.; Schoekel, A.; Althues, H.; Giebeler, L.; Oswald, S.; Kaskel, S. On The Mechanistic Role of Nitrogen-Doped Carbon Cathodes in Lithium-Sulfur Batteries with Low Electrolyte Weight Portion. *Nano Energy* **2018**, *54*, 116–128.  
<https://doi.org/10.1016/j.nanoen.2018.09.065>

## **Conference participations of Erik Troschke**

- 03/2018            **30. Deutsche Zeolith Tagung; Kiel**, poster presentation: „Mechanochemical Friedel-Crafts alkylation – a sustainable pathway towards porous organic polymers “
- 10/2017            **EuroMOF 2017; Delft/NL**, poster presentation: „Mechanochemical Friedel-Crafts alkylation – a sustainable pathway towards porous organic polymers “
- 03/2017            **29. Deutsche Zeolith Tagung; Frankfurt a. M.**, poster presentation: „Salt templated synthesis of hierarchical covalent triazine frameworks“
- 03/2016            **28. Deutsche Zeolith Tagung; Gießen**
- 10/2015            **EuroMOF 2015; Potsdam**
- 02/2015            **27. Deutsche Zeolith Tagung; Oldenburg**

## Erklärung

Hiermit versichere ich, dass ich die vorliegende Arbeit ohne unzulässige Hilfe Dritter und ohne Benutzung anderer als der angegebenen Hilfsmittel angefertigt habe; die aus fremden Quellen direkt oder indirekt übernommenen Gedanken sind als solche kenntlich gemacht.

Die Arbeit wurde bisher weder im Inland noch im Ausland in gleicher oder ähnlicher Form einer anderen Prüfungsbehörde vorgelegt.

Die vorliegende Arbeit wurde am Institut für Anorganische Chemie der Technischen Universität Dresden im Zeitraum von März 2015 bis August 2018 unter wissenschaftlicher Betreuung von Herrn Prof. Dr. S. Kaskel angefertigt.

Dresden, 20.11.2018, Erik Troschke

